Experimental Study of Early Solar System Processes aboard the International Space Station

Dissertation
zur Erlangung des Doktorgrades
der Naturwissenschaften

vorgelegt beim Fachbereich 11, Geowissenschaften/Geographie
der Johann Wolfgang Goethe-Universität
in Frankfurt am Main

von
Tamara Elisabeth Koch
aus Hanau

Frankfurt 2021
(D30)

vom Fachbereich 11 Geowissenschaften/Geographie der

Johann Wolfgang Goethe-Universität Dissertation angenommen.

Dekan: Prof. Dr. Jürgen Runge

Gutachter: Prof. Dr. Frank E. Brenker und Prof. Dr. Björn Winkler

Datum der Disputation: 11. Februar 2022

Abstract

The formation of terrestrial planets was a complex process which begun in the very early stage of the Solar System in the protoplanetary disk (PPD). Chondrites are fragments of planet precursors, which have never experienced differentiation and can help to reconstruct the first processes leading to planet formation. The main components of chondrites are chondrules, calcium-aluminum-rich inclusions (CAIs), amoeboid olivine aggregates (AOAs), metals and fine-grained material. Each of these components formed by a complex mechanism involving aggregation and/or melting. Previous research has already provided an overall view of the formation of these objects, however, there are still open questions regarding the aggregation behavior of particles, the heating mechanism(s) and the thermal history of CAIs, AOAs and chondrules. For instance, the involvement of flash-heating events and electrostatics in the aggregation and melting of these objects has been a keen topic of discussion.

The aim of this doctoral thesis was to develop and carry out an experiment to study various early Solar System processes under long-term microgravity. In the project with the acronym EXCISS (Experimental Chondrule Formation aboard the ISS), free-floating, $126 \pm 23\,\mu$m-sized Mg_2SiO_4 dust particles were exposed to electric fields and electric discharges.

The experimental set-up was installed inside a $10 \times 10 \times 15\,cm^3$-sized container and consisted of an arc generation unit connected to the sample chamber, a camera with an optical system, a power supply unit with lithium-ion batteries and the EXCISS mainboard with a Raspberry Pi Zero and mass storage devices. The sample chamber was manufactured from quartz glass and the experiments were filmed. The complete experiment container was subsequently returned to the Goethe University and the samples were analyzed with scanning electron microscopy, electron backscatter diffraction and synchrotron micro-CT.

Video analysis has shown that particles, which were agitated by electric discharges, align in chains within the electric field with their longest axis parallel to the electric field lines. Consequently, electric fields could have influenced the inner structure and porosity of particle aggregates in the PPD.

The discharge experiments produced fused aggregates and individual melt spherules. The fused aggregates share many morphological characteristics with natural fluffy-type CAIs and some igneous CAIs found in chondrites. Consequently, CAIs could have formed by the aggregation of particles with various degrees of melting. Further, a small amount of melting could have supplied the required stability for such fractal structures to have survived transportation and aggregation to, and subsequent compaction within, developing planetesimals.

Some initial particles were completely melted by the arc discharges and formed melt spherules. The newly formed olivines crystallized with a preferred orientation of the [010] axis perpendicular to the surface of the spherule. Similar preferred orientations have been found in natural chondrules. However, the microstructure differs from the results of previous experiments on Earth, which show, for example, crystal settling on one side of the sample because of the influence of gravity. Furthermore, the melt spherules show evidence for an interaction of the melt with the surrounding hot gas. Therefore, microgravity experiments with more advanced experimental parameters bear great potential for future chondrule formation experiments.

Contents

List of Figures

List of Tables

CHAPTER 1

Introduction & Outline

The formation of the terrestrial planets of our Solar System begun more than 4.56 Ga ago, when the Solar System consisted of a proto sun and a surrounding nebula of gas and dust particles, which is called the protoplanetary disk (PPD) (Boss, 2007). This protoplanetary disk was the setting for the formation of planet precursors such as chondritic parent bodies. These objects, which are still present in our Solar System in form of asteroids in the asteroid belt, are most likely the result of multistage aggregation processes and thermal procession in the PPD (e.g. Dominik et al., 2007; Russel et al., 2018).

Fragments from these asteroids can be found on Earth in form of specific meteorites, which are called chondrites. These meteorites are thought to be the key to understand the first processes in the PPD (Russel et al., 2018). Chondrites are aggregates of calcium-aluminum-rich inclusions (CAIs), amoeboid olivine aggregates (AOAs), spherical objects called chondrules, metal and fine-grained material (Russel et al., 2018).

The different steps in the early evolution of the PPD, which formed the components of chondrites and planet precursors are displayed in the schematic sketch in Figure 1.1. First of all, CAIs were formed by evaporation and condensation from the nebula in a region close to the sun (A) (e.g. Krot, 2019). CAIs in chondrites often show fractal structures, which could have been formed during condensation or are the result of aggregation by collisions of different CAI nodules (B) (e.g. Rubin, 2012; Russell and Howard, 2013). The second type of refractory inclusions in meteorites are AOAs (Ruzicka et al., 2012b). They condensed from the nebula after CAI condensation in a region more distant to the sun (C) and formed aggregates (D). These aggregates probably never experienced intense melting (Marrocchi et al., 2019b). These materials were subsequently transported outwards within the PPD. A certain amount of CAIs was melted and formed igneous CAIs (E) (e.g. Krot, 2019). AOAs and probably further, not yet defined materials, were melted by transient heating events and formed spherical objects, which are called chondrules (E) (Marrocchi et al., 2019a). Some chondrules as well as CAIs show evidence for several heating events and material recycling (F) (Krot et al., 2018). Chondrules accreted with other components to chondritic parent bodies (G) and some of them evolved to differentiated planets (H) (Johansen et al., 2015).

However, the formation of the different components of chondrites together with the aggregation of chondritic bodies is still full of open questions. For example, it is unclear how the different CAI types were formed (Russell and Howard, 2013). Furthermore, the aggregation of particles under microgravity conditions, which is important for the formation of CAIs, AOAs and chondrites including collision velocities, maximum aggregate sizes and porosity reduction is not fully resolved (Blum and Wurm, 2008). In addition, the precursor material

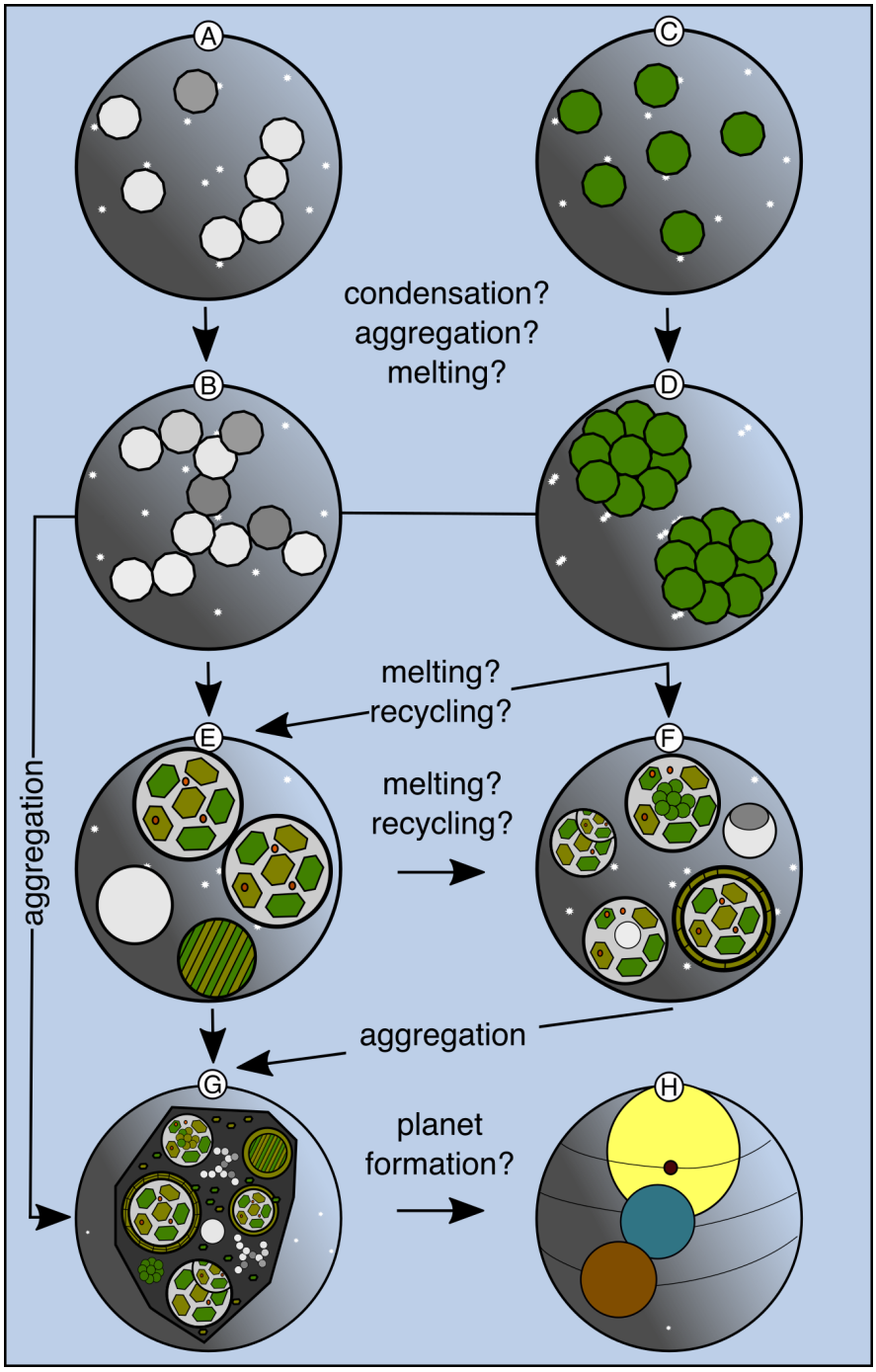

Figure 1.1: Simplified sketch of processes in the early Solar System. (A) CAIs were formed by evaporation and condensation from the nebula in a region close to the sun. (B) CAIs in chondrites often have fractal structures, which could formed during condensation or are the results of aggregation by collisions of different CAI nodules (e.g. Rubin, 2012; Russell and Howard, 2013). (C) The second type of refractory inclusions in meteorites are AOA (Ruzicka et al., 2012b). They condensed from the nebula after CAI condensation in a region more distant to the sun and probably aggregate to AOAs, which never experienced melting (Marrocchi et al., 2019b) (D). (E) The material was transported outwards in the PPD and transient heating events transformed parts of CAIs, AOAs, and other material. A certain amount of CAIs was melted and formed igneous CAIs. AOAs and probably further, not yet defined material, was melted and formed spherical objects, which are called chondrules (Marrocchi et al., 2019a). (F) Some chondrules as well as CAIs show evidence for several heating events and material recycling (Krot et al., 2018). (G) Chondrules accreted with other components to chondritic parent bodies and some of them evolved to differentiated planets (H) (Johansen et al., 2015).

of chondrules and the nature of transient heating events, which melted CAIs and formed chondrules, has not been resolved. For instance, different scenarios such as shock waves (Ciesla and Hood, 2002; Desch and Connolly Jr., 2002), lightning (Desch and Cuzzi, 2000; Johansen and Okuzumi, 2018) or collisions of protoplanets (Ebel et al., 2018; Sanders and Scott, 2018) were proposed for chondrule formation. However, none of these theories can explain all characteristics observed in chondrules.

Experiments are a useful tool to test proposed processes in the PPD. Particle aggregation experiments are well established in astrophysics and often carried out at microgravity conditions, mostly in drop towers (e.g. Blum and Wurm, 2008; Beitz et al., 2011; Steinpilz et al., 2020). Chondrule formation experiments have been only carried out under gravity conditions with the aim to reproduce chondrule textures and gain information about cooling rates and other formation conditions (Hewins and Fox, 2004). The most successful experiments to reproduce chondrule textures were carried out using furnaces as heating source with fixed sample pellets (Connolly Jr. and Love, 1998; Hewins and Fox, 2004; Villeneuve et al., 2015). Only a few experiments used flash-heating mechanisms such as laser-heating or electric arc discharges which melted samples, which were not statically mounted (Hewins et al., 2000; Güttler et al., 2008; Morlok et al., 2012).

The aim of the project presented in this thesis was the implementation of an experiment, which combined these experimental approaches to study aggregation together with melting under long-term microgravity conditions aboard the International Space Station (ISS). In this experiment with the acronym EXCISS (**Ex**perimental **C**hondrule Formation aboard the **ISS**), freely floating Mg_2SiO_4 dust particles were observed under microgravity conditions while being exposed to electric fields and electric discharges. With this type of experiment, a variety of processes could be observed, which can be used to increase the knowledge of early Solar System processes. The results of the experiment were presented in four articles which were published in "peer-reviewed" journals, which are part of this cumulative thesis:

Publication I: A chondrule formation experiment aboard the ISS: Experimental set-up and test experiments

This publication describes the experimental set-up and test experiments on Earth.

Publication II: Mg_2SiO_4 particle aggregation aboard the ISS — Influence of electric fields on aggregation behavior, particle velocity and shape-preferred orientation

The behavior of freely floating particles while being exposed to electric discharges and the influence of electric field on particle aggregates, which probably influenced aggregation processes in the PPD, is described in this article.

Publication III: Formation of fused aggregates under long-term microgravity conditions aboard the ISS with implications for early Solar System particle aggregation

This publication includes the analysis of fused aggregates which were formed in the experiment aboard the ISS. These aggregates can be related to natural CAIs.

Publication IV: Formation of chondrule analogs aboard the International Space Station

This article shows the analysis of formed single melt droplets, which represent chondrule analogs.

CHAPTER 2

Early Solar System Processes

The formation of the terrestrial planets started more than 4.56 Ga ago in the protoplanetary disk (Weidenschilling and Cuzzi, 2006; Dominik et al., 2007; Blum and Wurm, 2008; Johansen et al., 2015). The main constraints on the early evolution of our Solar System arise from the observation and spectral analyses of protoplanetary disks in other planetary systems (e.g. Sicilia-Aguilar et al., 2016), from the analysis of meteorites (reviewed in Russel et al., 2018) and from experiments (e.g. Desch et al., 2012; Hewins et al., 2005; Blum and Wurm, 2008). Figure 2.1 shows a schematic sketch of the current understanding of different processes at different times and locations in the protoplanetary disk (PPD), which are probably the first processes leading to planet formation.

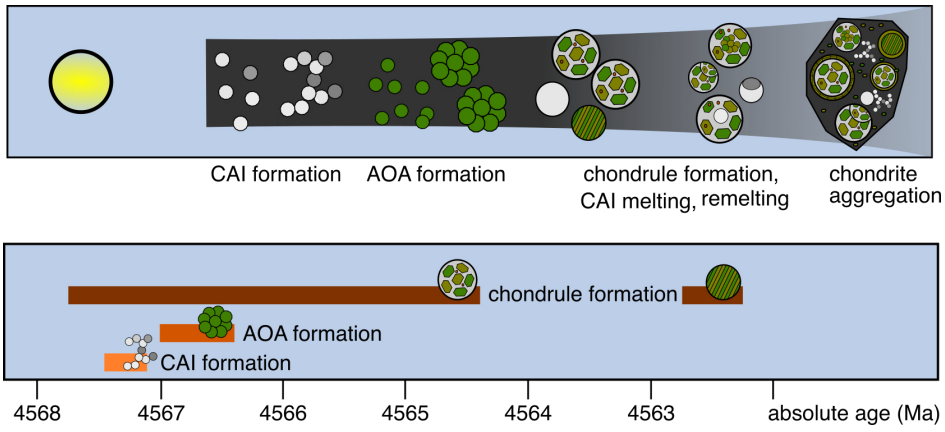

Figure 2.1: Schematic sketch of the most important milestones during the early evolution of the protoplanetary disk which include condensation and aggregation of refractory inclusions such as CAIs and AOAs, chondrule formation, material recycling and aggregation to planet precursors. The different materials were formed at different times and different distances from the sun. The age data of CAIs and chondrules are taken from Connelly and Bizzarro (2018), ages of AOAs from Itoh et al. (2002).

The first solids which condensed from the hot nebula are calcium-aluminum-rich phases (Ebel and Rivers, 2007). These objects formed aggregates which can be found in many meteorites and are called Ca,Al-rich inclusions (CAIs). About 0.4 Ma later, olivine condensed from the nebula and also formed aggregates, the so called amoeboid olivine aggregates (AOAs) (Itoh et al., 2002). A heating event probably transformed AOAs to chondrules (Marrocchi et al., 2019b) and melted some CAIs. However, other studies proposed that chondrule formation started simultaneously to CAI formation (Connelly et al., 2012; Connelly and Bizzarro,

2018). At last, all these components aggregated together with matrix material to chondritic bodies, which probably represent planet precursor. Collisions of protoplanets were probably responsible for a second chondrule formation event approx. 2–4 Ma after the main chondrule formation period (e.g. Krot et al., 2005; Bollard et al., 2015).

However, a complete model, which is in accordance with all expected and observed constrains, has not been developed (Weidenschilling and Cuzzi, 2006; Russel et al., 2018). The current understanding and controversies of the processes expected for the early stage of our Solar System, which were studied with the experiments of this thesis, are summarized in this chapter.

2.1 Particle aggregation

The aggregation of particles to larger objects occurred in many different episodes and locations in the protoplanetary disk (e.g. Blum and Wurm, 2008; Dominik et al., 2007). The first particles in the Solar System are thought to be submicron-sized dust particles (e.g. Dominik et al., 2007 and references therein). Particles in this size range are coupled to gas molecules, which means that their movement is in equilibrium with the gas movement (Cuzzi and Weidenschilling, 2006). However, these dust particles can also move with relative velocities to each other due to, for instance, Brownian motion, sedimentation towards the midplane, and gas turbulences (Weidenschilling, 1977; Okuzumi, 2009). Brownian motion describes the random particle motion in a liquid or gas which is induced by the thermal movement of molecules (Einstein, 1905). It was probably the driving force for micrometer-sized particles which induces particle velocities in the range of $0.1\,\mathrm{cm\,s^{-1}}$ (Zsom et al., 2010).

When particles or particle aggregates collide, they can stick together (Blum et al., 2008). This depends on different parameters such as the adhesion force between particles (Van der Waals, molecular dipole interactions, electrostatic or magnetic forces) and the collision velocity (Blum and Wurm, 2008). Uncharged and non-magnetic grains adhere by Van-der-Waals forces. These collisions result in fractal aggregates. The fractal morphology is the consequence of the effect, that these particles are resistant to rolling movements (Dominik et al., 2007). Figure 2.2 shows the growth of fractal aggregates produced in hit and stick collisions. Fractal aggregates grow by collisions until they reach the centimeter-size (Suyama et al., 2008). Studies which modeled the size evolution of aggregates in the PPD came to the conclusion, that particles grew rapidly to centimeter-sized dust aggregates in about 1000 y (Weidenschilling, 1977, 1980; Dullemond and Dominik, 2005; Ormel et al., 2007).

Larger fractal aggregates must have undergone some sort of compaction, which played an important role in planetesimal formation. Different scenarios, such as collisions of similar-sized dust aggregates, static compression by disk gas or by self-gravity have been proposed to increase the volume filling factor (Dominik and Tielens, 1997; Ormel et al., 2007; Suyama et al., 2008; Kataoka et al., 2013). Collisions can change the morphology and porosity of the aggregates, however, too high collision energies result in the loss of particles and fragmentation of the aggregates (Dominik and Tielens, 1997; Blum and Wurm, 2000a). Critical velocities for fragmentation are in the range of $>100\,\mathrm{cm\,s^{-1}}$ (Dominik and Tielens, 1997; Blum and Wurm, 2000b, 2008). However, even compacted aggregates have porosities of >65%, which is still higher than the porosity of meteorites and their components, which is approx. 20% (Consolmagno et al., 2008; Kataoka, 2017; Kataoka et al., 2013; Kataoka et al., 2013).

Centimeter-sized objects decouple from the gas and settle vertically and drift radially (Blum and Wurm, 2008). Different forces, such as central gravity forces and outward drift caused by a radial pressure gradient, induced the formation of a particle-rich, dense midplane layer in the PPD, which was the environment for the processes leading to planet formation

(Dominik et al., 2007).

Particles in the millimeter to centimeter-size range, which represent the dimensions of chondrules, rather bounce than stick together after collisions (Zsom et al., 2010). This effect is called the bouncing barrier. The high abundance of chondrule-bearing asteroids shows, that aggregation in this size range is of special importance regarding planet formation. Several mechanisms which could have improved the sticking capability of chondrules have been proposed, for example dust coating of chondrules (Beitz et al., 2011) or electrical charging (Love et al., 2014; Jungmann et al., 2018; Steinpilz et al., 2020). The latter is discussed in more detail in Section 2.6.1 and was also studied with the experiments of this thesis project.

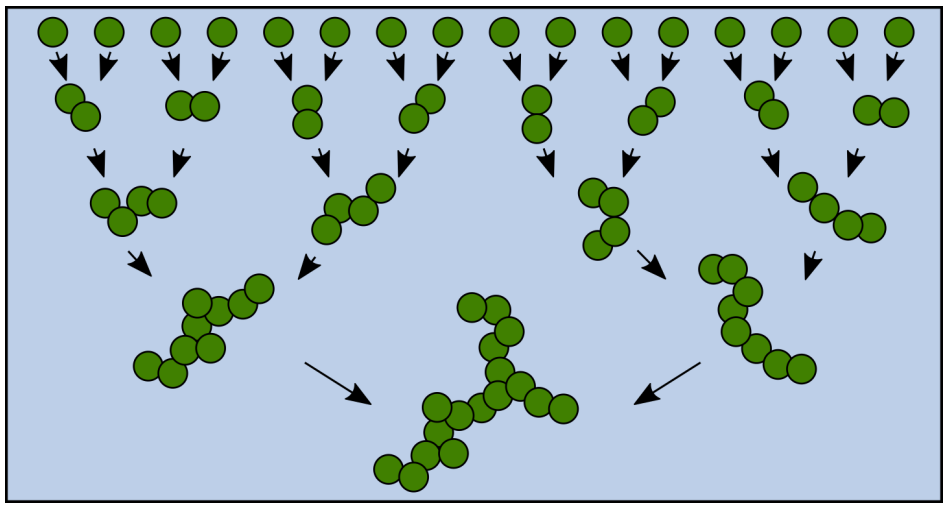

Figure 2.2: Schematic sketch of the fractal aggregate growth by hit and stick collisions, modified from Blum and Wurm (2008).

2.2 Classification of chondrites

Chondrites are fragments from primitive asteroids, which have never experienced planetary processes (e.g. Weisberg et al., 2006; Krot et al., 2009). Chondrites are classified based on a variety of characteristics, for instance their mineralogy and petrography, and their whole-rock chemical and O-isotopic compositions. Figure 2.3 shows the generally used classification scheme of chondrites (Weisberg et al., 2006). They are mainly divided into three classes: carbonaceous (C), ordinary (O), and enstatite (E) chondrites (Weisberg et al., 2006).

Chondrites sharing the same class show similar properties in terms of broadly similar refractory lithophile-element abundances that are enriched, depleted or equal to solar abundances. The chondritic classes are divided into 15 groups. Eight of them belong to the class of carbonaceous chondrites (CI, CM, CO, CV, CK, CR, CH, CB), three to ordinary chondrites (H, L, LL), two to enstatite chondrites (EH, EL), and the remaining to R and K chondrites. However, several chondrites cannot be assigned to any of these groups, and they may represent new groups. CI chondrites define the best approximation of the composition of the solar photosphere (Anders and Grevesse, 1989). Meteorites in the same group are considered to originate from the same parental body. Different kinds of processes on the parent body of a single group of meteorites result in the subdivision of a group into subgroups. The chondritic clan describes a classification order between class and group. They represent chondritic groups and ungrouped chondrites with chemical and mineralogical similarities. A clan consists of one or more groups that may have "closely similar refractory lithophile-element

abundances, plot on the same O-isotopic mixing line, share an isotopic anomaly or have some similarities in petrologic characteristics" (Weisberg et al., 2006). Due to their experienced thermal and aqueous alteration, chondrites are divided into petrologic types 1–6 (Schmus and Wood, 1967).

Another classification scheme of meteorites which has become more and more important in the last decade is the differentiation in non-carbonaceous (NC) and carbonaceous (CC) meteorites (Warren, 2011; Budde et al., 2016; Kleine et al., 2020). This classification, called the NC-CC dichotomy, arises from the fact that meteorites can be divided in two groups regarding their isotopic compositions. These compositions are probably the relict from presolar matter, which was heterogeneously distributed in the PPD. The relatively volatile-rich CC meteorites were probably formed in the outer Solar System, while the relatively volatile-poor NC meteorites formed in the inner Solar System. The two different reservoirs were probably separated by Jupiter (Kruijer et al., 2017; Kleine et al., 2020). This classification can be applied to any meteorite type, also for metal meteorites and achondrites. The meteorite classes and groups which belong to the carbonaceous meteorites according to this new classifications are marked with green in Figure 2.3, the non-carbonaceous with red.

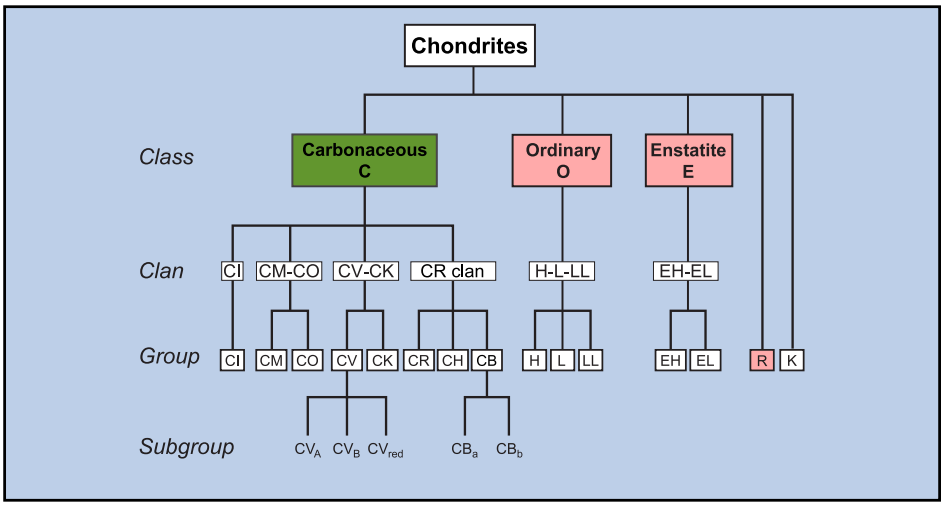

Figure 2.3: Classification scheme of chondrites, modified from Weisberg et al., 2006. The carbonaceous meteorites are marked with green, the non-carbonaceous with red, according to (Kleine et al., 2020).

2.3 Refractory inclusions

Chondritic meteorites include refractory inclusions in form of calcium-aluminum-rich inclusions (CAIs) and amoeboid olivine aggregates (AOAs). These inclusions are among the main components of carbonaceous chondrites (0.1–3% of the area of representative sections of these meteorites), while their abundance in CI chondrites and ordinary chondrites is very rare with <0.1% of the studied area of these meteorites (Hezel et al., 2008; Krot, 2019). They represent direct nebular condensates and can help to understand the conditions of the early PPD (Connelly et al., 2012; Ruzicka et al., 2012b).

2.3.1 Calcium-Aluminum-rich inclusions (CAIs)

CAIs are very heterogeneous and diverse objects which consist of refractory minerals such as Ca, Al, Mg or Ti oxides and silicates (reviewed e.g. in MacPherson, 2003 and Krot, 2019).

They are mostly in the size range of <1 mm, but some can reach up to 3 cm (MacPherson, 2003).

CAIs have formed 4567.30 ± 0.16 Ma ago in a hot environment (approx. 1300 K) near the proto-sun and are considered as the oldest material of the Solar System (Connelly et al., 2012). Their formation history is complex and includes "evaporation, condensation and aggregation" (MacPherson, 2003; Rubin, 2012; Russell and Howard, 2013; Krot, 2019). CAI formation was probably an episodic event (Krot, 2019; Larsen et al., 2020) and they remained in their formation region for a few thousand years until they were periodically ejected to the outer regions of the PPD (Taillifet et al., 2014). Many CAIs underwent melting and deformation, probably in their formation region as well as after radial transportation (Krot, 2019).

CAIs are divided regarding their texture, mineralogy, bulk composition as well as trace element and isotopic compositions (e.g. Krot, 2019; MacPherson, 2003 and references therein). First, they are broadly distinguished between "fine-grained" (spinel-rich, nodular texture) and "coarse-grained" (melted) CAIs (Grossmann, 1975). CAIs in CV chondrites are divided regarding their mineralogy in type A (Al-rich melilite-spinel-rich), B (melilite-rich), and C (anorthite-pyroxene-rich). Type A CAIs are further subdivided in compact CAIs (CTA), which have spheroidal shapes and experienced melting, and in fluffy CAIs, which were not melted and have irregular, fluffy morphologies. Type B CAIs are divided in type B1, which have a melilith mantle and type B2 that have no melilith mantle. In other chondritic groups, the CAIs were mainly named according to their mineralogy. Figure 2.4 shows some images of representative CAIs with different characteristics.

The different morphologies of CAIs, such as the nearly spherical morphology of igneous CAIs or the fractal morphology of fluffy-type CAIs might be the result from processes after their condensation. For example, fluffy-type CAIs represent aggregates of several CAI nodules (Figs. 2.4a,b,c). It is not clear if these proto CAIs aggregated during condensation (Russell and Howard, 2013) or during a secondary process (Rubin, 2012). Some studies suggested a simultaneously formation of igneous and fluffy-type CAIs. For example, Rubin (2012) suggested, that CTAs collided and aggregated in the CV aggregation region prior to chondrule formation and experienced melting and evaporation. Fluffy-type A CAIs were also formed by aggregation of CTA which experienced a smaller amount of melting.

Type B CAIs were melted in an event which was probably related to the chondrule formation event (Desch et al., 2010). CAIs have reached a peak temperature of approx. 1700 K and were cooled with 0.5–50 $\mathrm{K\,h^{-1}}$ (e.g. MacPherson et al., 1985; Beckett et al., 2006). Some CAIs have experienced incomplete melting, which was interpreted to be the result from a flash-heating event (Russell and Howard, 2013). Other CAIs, such as compound CAIs, are composed of CAIs with different lithologies. They are probably the result of collisions of different CAI nodules with various degrees of melting (Aléon et al., 2013; Ivanova et al., 2015).

Many CAIs are surrounded by several tens of micrometer thick mineralic layers, the so-called Wark-Lovering rims (Wark and Lovering, 1977; Krot, 2019). These layers probably formed after CAI formation; however the origin of these rims is still under discussion. Different scenarios, such as condensation (Wark and Lovering, 1977; MacPherson et al., 1985; Bolser et al., 2016) or flash-heating have been proposed (Han et al., 2020; Wark and Boynton, 2001). It is also unclear, whether WLRs formed immediately after CAI formation or about 1 Ma after the formation of the latter, since isotopic studies give conflicting information. However, these different isotopic compositions could also arise from "isotopic disturbances in the Nebula" after their formation (Han et al., 2020). Furthermore, many CAIs are surrounded by a layer of fine-grained rims which did not experience melting (MacPherson et al., 1985; MacPherson and Grossman, 1984), similar to fine-grained rims around chondrules (see

Sec. 2.4.1).

Some igneous Type B CAIs have a disk- or bowl-shaped morphology (Ivanova et al., 2008). Some studies suggested that these shapes are the result of aerodynamical deformation and shock-flattening (Lorenz et al., 2019), or a more complex scenario including ejection from the inner Solar System and remelting during re-entry at hypersonic speed (Liffman et al., 2016). Furthermore, the most recent study of Zhang et al. (2021) showed that many CAIs and AOAs have an elongated or a bent fractal morphology, which was also interpreted to be the result from motion, for example induced by radial drift.

Furthermore, CAI relicts can be found in chondrules (Krot et al., 2018). This observation supports the assumption that CAIs were formed prior to chondrules, were transported to the chondrule formation region and remelted in the chondrule formation event. Therefore, CAIs were probably among chondrule precursors, especially for Al-rich chondrules (Krot, 2019).

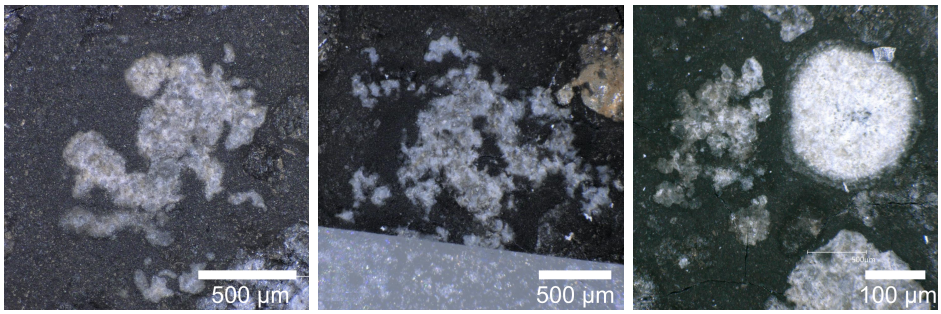

(a) (b) (c)

Figure 2.4: Optical microscopy images of representative CAIs from Northwest Africa 13656. (*a*) A fluffy-type, irregularly shaped CAI. (*b*) A very fractal fluffy-type CAIs. (*c*) A fluffy-type CAI (left) next to a round igneous CAI. The single nodules as well as the igneous CAI are covered by rims.

2.3.2 Amoeboid olivine aggregates (AOAs)

AOAs represent fine-grained, irregular-shaped, mostly porous aggregates consisting of <2 to 10 µm-sized olivines, Fe,Ni-metal and CAI-like material (Weber and Bischoff, 1996; Krot et al., 2002; Krot et al., 2004a and references therein). Similar to CAIs, they have a condensation origin but probably formed approx. 0.1–0.5 Ma after CAI formation in a greater distance from the sun compared to CAIs (Itoh et al., 2002).

AOAs can reach up to a few millimeters and can be divided into porous and compact AOAs (Sugiura et al., 2010). Figure 2.5 shows representative images of the two types of AOAs. Porous AOAs are fine-grained (Fig. 2.5a) and never experienced intense melting, which makes them suitable to gain more information, such as pressure, temperature and isotopic composition of the early PPD. Compact aggregates (Fig. 2.5b) are coarse-grained and rounded, which is probably the result of annealing, recrystallization or melting of porous AOAs (Sugiura et al., 2010; Krot et al., 2004a), but could be also the result of very slow cooling during condensation (Sugiura et al., 2010).

Figure 2.6 shows a schematic sketch of the recently proposed formation scenario from Marrocchi et al. (2019b). This model assumes that local heating evaporated parts of the present CAI-like material beyond the nominal olivine condensation front and that the remaining seeds influenced the olivine condensation. The single AOA components condensed in a short time of days to weeks. Subsequently, the grains aggregated within a year. Afterwards, the aggregates were either evaporated or migrated outwards while being thermally annealed.

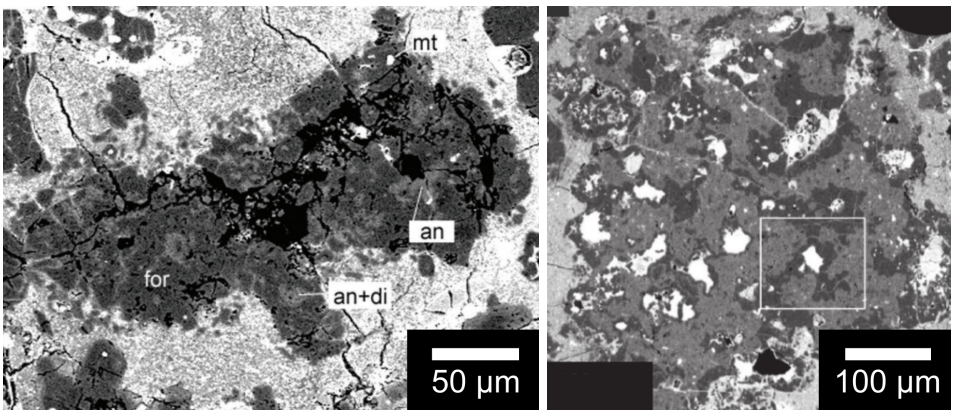

(a) (b)

Figure 2.5: Backscattered electron microscopic images of representative amoeboid olivine aggregates. (*a*) Porous AOA in Yamamoto 81020 consisting of forsterite (for) with some anorthite (an), diopside(di) and some metal grains (mt) (Sugiura et al., 2010). (*b*) Compact AOA from Yamamoto 81020 (Komatsu et al., 2015).

AOAs are genetically related to CAIs (Weber and Bischoff, 1996; Krot et al., 2004a; Krot et al., 2004b) but they share more similarities to chondrules (Krot et al., 2004a; Marrocchi et al., 2019a). Therefore, they are considered to be chondrule precursors (Marrocchi et al., 2019a).

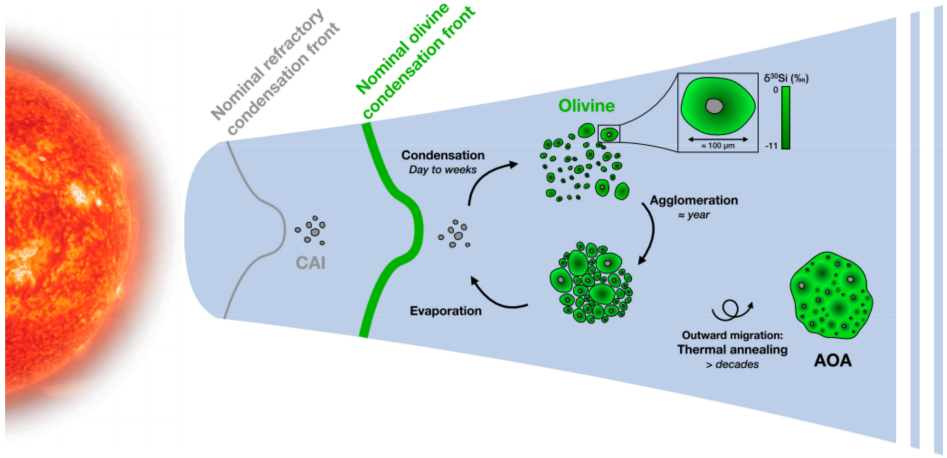

Figure 2.6: Schematic sketch of the recently proposed AOA formation scenario. CAI-like material evaporated and during subsequent cooling, they started to grow olivine within days to weeks. The single AOA nodules aggregated over a period of a year to amoeboid olivine aggregates. AOAs drifted outwards, were thermally annealed and incorporated in chondritic bodies. (Marrocchi et al., 2019b)

2.4 Chondrules

2.4.1 Chondrule characteristics

Chondrules are spherical objects which represent a main component of chondritic meteorites (except for CI). Their abundances vary between the different chondritic group and can reach up to 80vol% in ordinary chondrites (e.g. Scott and Krot, 2014; Russel et al., 2018). Chondrules were also called the "building blocks" of terrestrial planets (Bollard et al., 2017),

however their formation conditions are still not resolved (e.g. Alexander and Ebel, 2012). Recently, the current understanding and controversies of chondrules have been intensively reviewed in Russel et al. (2018).

The main components of chondrules are olivine, pyroxene, metal, sulfides and mesostasis (remaining liquid) (Russel et al., 2018). The most obvious characteristics to distinguish between different chondrules is their texture. They can be divided into:

- porphyritic (P): porphyritic olivine (PO) or porphyritic pyroxene (PP)
- micro porphyritic (MP): micro porphyritic olivine (PO) or micro porphyritic pyroxene (PP)
- barred (B): barred olivine (BO) or barred pyroxene (BP)
- radiating (R): radiating olivine (RO) or radiating pyroxene (RP)
- cryptocrystalline chondrules (CC)

Representative photographs of the different chondrule types are shown in Figure 2.7. Porphyritic chondrules (Figs. 2.7a,b) are the most common chondrule type (84% in ordinary chondrites) (Gooding and Keil, 1981). They consist mostly of olivine or pyroxene crystals with mesostasis. Barred chondrules (4% of chondrules in ordinary chondrites) (Gooding and Keil, 1981) show parallel lamella of olivine or pyroxene crystals (Figs. 2.7c,d). Cryptocrystalline chondrules (Fig. 2.7e) are characterized by their tiny grain sizes and radial chondrules have textures with thin lamellae radiating from one nucleation point (radiating chondrules make approx. 8% in ordinary chondrites) (Gooding and Keil, 1981). The different chondrule types are often thought to be a function of different formation parameters which are explained in Section 2.4.2.

Furthermore, a high percentage of all chondrules (e.g. 50% in CV chondrites, 10% in H-LL-L3 meteorites, and $\leq$1% in CO3 chondrites (Rubin, 1984)) are surrounded by a layer of matrix-like dust particles, which are called fine-grained rims (FGRs) (Rubin, 1984; Metzler et al., 1992; Morfill et al., 1998; Bland et al., 2011) or by igneous rims (Morris and Garvie, 2013; Matsuda et al., 2019). FGRs are more likely the result of dust aggregation in the Solar nebula (Bland et al., 2011) rather than from parent body processes (Trigo-Rodríguez et al., 2006). Igneous rims are probably former FGRs, which were melted by the same mechanism which melted the chondrule precursors (Rubin, 1984; Krot and Wasson, 1995; Morris and Garvie, 2013).

Chondrules are further classified into type I (FeO-poor, Fe-metal bearing, dominant in carbonaceous chondrites, generally micro porphyritic) and type II (FeO-rich, Fe-metal bearing, dominant in ordinary chondrites, generally porphyritic) chondrules (Jones et al., 2005; Villeneuve et al., 2015). The relation between type I and type II chondrules is still under discussion. Some studies assume different reservoirs for the origin of type I and type II chondrules (e.g. Jones et al., 2005). Another idea suggests that type I and type II chondrules formed contemporary and that type I chondrules transformed to type II chondrules by evaporation and reduction induced by heating (Leroux et al., 2003; Jones et al., 2005; Villeneuve et al., 2009; Ruzicka et al., 2012a). Experiments also showed that type II chondrules could have formed by reaction of the melted type I chondrules with the surrounding gas (Villeneuve et al., 2015).

About 15% of chondrules from ordinary chondrites contain relict grains, which were not melted in the chondrule formation event and can help to reconstruct the chondrule precursor material (Jones, 1996). Some relict grains consist of coarse olivine or orthopyroxene, which are

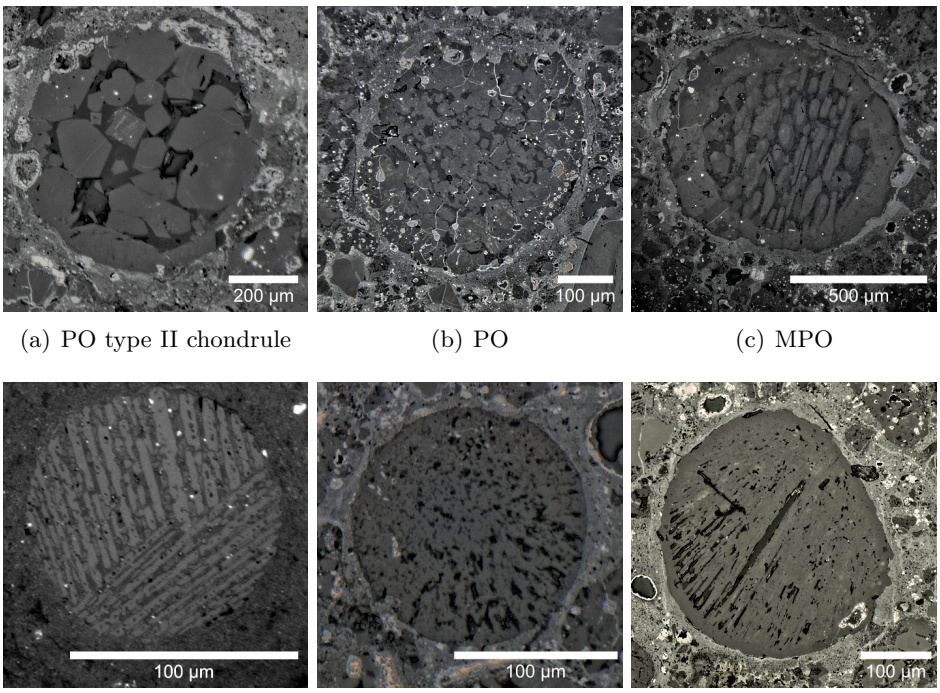

(a) PO type II chondrule (b) PO (c) MPO

(d) BO (e) CC (f) R

Figure 2.7: Optical microscopy images of chondrules with different textures. (*a*) Porphyritic chondrules from NWA 11542. (*b*) Porphyritic chondrules from NWA 11542. (*c*) Barred olivine chondrule from NWA 11542 surrounded by an igneous rim. (*d*) Barred olivine chondrule from NWA 1906. (*e*) Cryptocrystalline chondrule from NWA 11542. (*f*) Radial chondrule from NWA 11542. All images are contrast enhanced.

often termed as "dusty" olivines (e.g. Rambaldi, 1981; Jones, 1996; Jones and Danielson, 1997; Leroux et al., 2003). Further, chondrules include relict chondrules of an earlier generation and CAIs (Jones, 1996; Krot et al., 2018), which implies that the chondrule formation event was a repeated event and that material was recycled.

Approximately 2.6–5% of all chondrules are compound chondrules (Wasson et al., 1995; Hewins, 1997; Ciesla et al., 2004). These are composite objects consisting of several fused (sub-)chondrules (Wasson et al., 1995). Most of the compound chondrules consist of 2–3 individual chondrules, but they can also occur as very complex objects formed from 16 individual chondrules (Bischoff et al., 2017). Compound chondrules can help to reconstruct processes in the Solar System, for instance the number of heating events which chondrules experienced (Wasson et al., 1995; Ciesla et al., 2004; Bischoff et al., 2017). The most likely scenario of their formation is that chondrules collided shortly after their formation while being plastic with temperatures above 1400 K (Hewins, 1997; Ciesla et al., 2004), or as super cooled liquids (Arakawa and Nakamoto, 2016). However, another idea assumes that these chondrules were "fused cold", which means that solid chondrules have collided and stuck together and were heated afterwards (Hubbard, 2015). Compound chondrules can also help to estimate local particle densities in the chondrule forming region. For example, the particle to gas ratios in the chondrule formation region was calculated to be 0.005 (Ciesla et al., 2004), however, the formation of multi-compound chondrules require ratios of >1000 (Bischoff et al., 2017).

2.4.2 Thermal history of chondrules

The thermal history of chondrules is one of the most decisive aspect to find a plausible chondrule formation mechanism because it has to be in accordance with the physics of the proposed heating mechanism. The thermal history includes the number of heating events, the heating rate, the peak temperature, the duration at high temperatures and the cooling path of chondrules. This topic was recently reviewed in detail by Jones et al. (2018). There are plenty of chondrule properties that can be used as thermal history indicators, for instance the chondrule microstructure, chemical zoning, relict grains, partitioning coefficients, diffusion profiles, exsolution lamellae and crystal defects (Jones et al., 2018). However, these indicators also lead to many contradictions.

The texture of chondrules is probably the most important indicator for the thermal history of chondrules, since the preservation or destruction of crystal nuclei during the heating pulse probably influenced the crystal growth (Jones et al., 2018). Figure 2.8 shows the most established thermal paths for the different chondrule types. Most studies agree, that chondrules were melted in a single event and heated from <673 K to temperatures of approx. 1673–2000 K. The formation of radial and cryptocrystalline chondrules was interpreted to be the result of heating over the liquidus range, which destroyed all crystal nuclei, followed by a quick quenching (Hewins et al., 2005). Barred olivine chondrules exceed the liquidus slightly and cooled with 500 to 2500 K h^{-1}. Porphyritic textures were heated to a peak temperature below the liquidus and were cooled slowly with 10 to 500 K h^{-1}. Chemical zoning

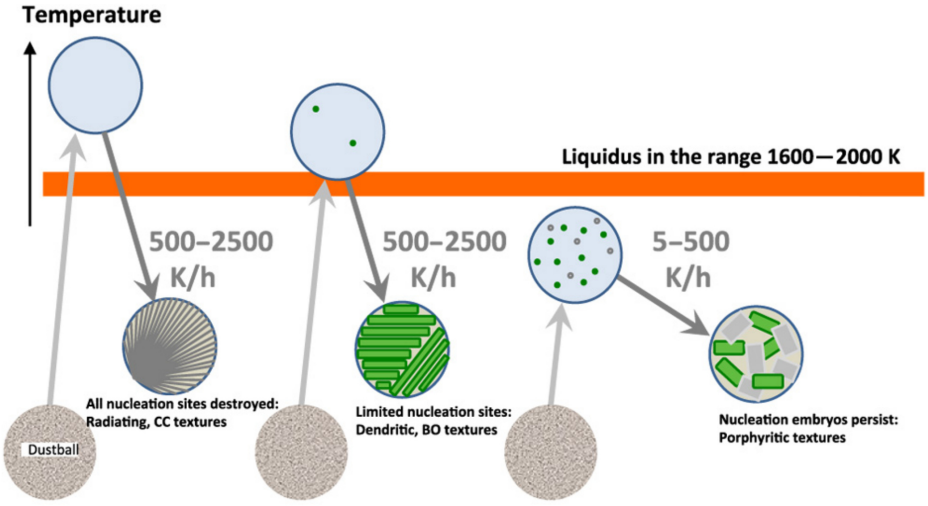

Figure 2.8: The most accepted model of the thermal history of the different chondrule textures as a function of the peak temperature and cooling rate (Fig. from Libourel and Portail, 2018).

in olivine and pyroxene of type IIA and IIAB chondrules are also used as an indicator for the thermal history. It implies that these chondrules were melted in a single event and cooled slowly with 10–1000 K h^{-1} (Jones et al., 2018 and references therein). However, a new experimental study could reproduce chemical zoning in porphyritic chondrules with cooling rates of 3000–6000 K h^{-1} (Greenwood and Herbst, 2021).

The presence of large phenocrysts in type II chondrules was also discussed to be the result of cooling rates of <50 K h^{-1}, which could be reproduced with experiments (Jones et al., 2018). In contrast, the presence of relict olivine grains in chondrules which survived the heating event were interpreted to be the result of very fast cooling at high temperature and/or a very short heating pulse (Hewins et al., 2005; Jones et al., 2018). New experiments confirmed this assumption (Villeneuve et al., 2015; Soulié et al., 2017).

The cooling path is not always considered as a linear cooling. Slower cooling rates at lower temperature were also induced by for instance the crystallization of plagioclase, trace element zoning in metal and exsolution lamellae in clinopyroxene (Jones et al., 2018). In addition, reaction of the chondrule melt with the surrounding gas was also considered to influence the crystallization of chondrules. Libourel and Portail (2018) presented an alternative model for the thermal history of the different chondrule types based on the presence of metal inclusions and gas-melt interactions. They suggested that the precursor material was heated above the liquidus temperature and started crystallizing at high temperatures around 1800 K in reaction with the surrounding gas (max. few tens of minutes), with subsequent fast cooling at rates of up to $10^6\,\mathrm{K\,h^{-1}}$. The formation of porphyritic textures is favored by the incorporation of Fe-Ni metal which served as crystal seeds and by gas-melt interaction at high temperature. Figure 2.9 illustrates this alternative thermal history.

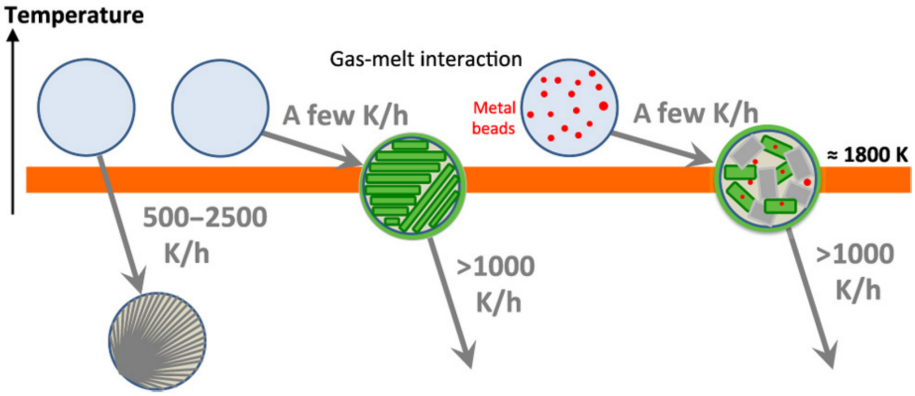

Figure 2.9: A new model of the thermal history for different chondrule types (Libourel and Portail, 2018). The different chondrule types cooled with similar, two stage cooling rates. Porphyritic chondrule textures formed due to the incorporation of Fe-Ni metal which works as crystal seeds and by gas-melt interaction at high temperatures (Libourel and Portail, 2018).

2.4.3 Chondrule formation theories

Chondrule formation scenarios must explain how a certain precursor material was transformed to chondrules with the observed characteristics. Furthermore, the heating event has to be plausible in the astrophysical context. However, the exact chondrule precursor material as well as the formation process have not been resolved yet.

Up to now, numerous different formation scenarios were proposed. In general, the proposed scenarios are divided into formation in the nebular environment (e.g. Túnyi et al., 2003; Johansen and Okuzumi, 2018; Desch and Connolly Jr., 2002; Morris and Desch, 2010; Hubbard and Ebel, 2018) or in the planetary setting (e.g. Connolly Jr. and Hewins, 1995; Krot et al., 2005; Johnson et al., 2015; Lichtenberg et al., 2018).

Most chondrule formation theories assume that a solid chondrule precursor material was melted by at least one transient heating event in the PPD (Krot et al., 2018). The precursor material in this setting for chondrule formation was mostly assumed to be dust balls of submicron sized particles in the form of a mixture of CAIs, AOAs and matrix materials (Floss, 2010). The region of the solar nebular in which the chondrules formed was probably relatively cold (<1000 K), with a size of approx. $>10^2$–10^3 km in extent and in 2–3 AU distance from the sun (e.g. reviewed in Desch et al., 2010). Further, it was dust-rich with 1–10 chondrule-sized particles per cubic meter (Wasson et al., 1995; Cuzzi and Alexander, 2006). The gas was a hydrogen-rich atmosphere with a pressure of approx. 0.1 to 0.001 mbar (Connolly Jr. et al., 2006).

In the last years, some formation scenarios have been proposed to be more plausible than others, for example shock waves (e.g. Connolly Jr. and Love, 1998; Desch and Connolly Jr., 2002; Morris and Desch, 2010; Morris et al., 2012), formation by lightning (Whipple, 1966; Horányi et al., 1995; Desch and Cuzzi, 2000; Túnyi et al., 2003; Johansen and Okuzumi, 2018), by collisions of planetesimals (Connolly Jr. and Hewins, 1995; Krot et al., 2005; Johnson et al., 2015; Lichtenberg et al., 2018), by X-winds (Shu and Shang, 1996; Desch et al., 2010) and magneto hydrodynamic turbulences (McNally et al., 2013). However, each hypothesis and theory has weaknesses. For decades, it was the intention to find a single mechanism, which explains all of the observed chondrule properties, however, it has been more and more accepted that several mechanisms could form chondrules at different times and different settings (Morris and Boley, 2018)

Formation by shock waves The formation of shock waves was proposed by Wood (1963) and has become the most accepted chondrule formation scenario so far (Desch and Connolly Jr., 2002; Ciesla and Hood, 2002; Morris and Desch, 2010). The shock waves were probably induced by "gravitational instabilities that drive spiral shocks" or "bow shock around planetesimals on eccentric orbits" (Desch et al., 2005; Desch et al., 2010). The latter seems to be more realistic, but requires that planetesimals were formed prior to chondrule formation (Desch et al., 2012). The shock wave model is in agreement with the most accepted thermal history and the assumption that chondrules and matrix were formed at the same location where chondritic bodies aggregated (chondrule-matrix complementarity, see Sec. 2.5 and Hezel et al., 2017). However, the shock wave model is not in agreement with the formation of compound chondrules in dense regions of the nebula (Bischoff et al., 2017) or with solid-gas reactions during chondrule formation (Libourel and Portail, 2018).

Formation by nebular lightning The formation of chondrules by nebular lightning assumes that chondrules were formed by the energy of an electric discharge in the PPD (Whipple, 1966; Horányi et al., 1995; Desch and Cuzzi, 2000; Túnyi et al., 2003; Güttler et al., 2008; Johansen and Okuzumi, 2018). Melting induced by lightning could have occurred directly in the plasma channel, but also for instance by the emitted thermal radiation (Wasson, 1996) or by "thermal exchange with the heated gas" (Desch and Cuzzi, 2000).

The generation of lightnings in the PPD occurred probably in different steps (Desch and Cuzzi, 2000). First, the particles were charged by a certain mechanism in correlation to their grain size, e.g. by triboelectric charging (Desch and Cuzzi, 2000) or by the decay of ^{26}Al (Johansen and Okuzumi, 2018). Subsequently, the particles were separated by their different charging. This charge separation generates an electric field which finally discharged by lightning bolts.

The formation of chondrules by localized lightnings is in agreement with the chondrule-matrix complementary (Hezel et al., 2017) and could leave the matrix material unprocessed (Pilipp et al., 1992). However, it is argued that melting by electric arc discharges is very inefficient. Further, the gas to dust ratio has to be about two times higher than the usually expected ratio (Hubbard and Ebel, 2015). Another important argument against the formation by lightning are the high cooling rates, which contradict the commonly accepted thermal history of chondrules, especially for porphyritic chondrules (Desch et al., 2010).

Formation by planetary collisions The so called non-canonical view of chondrule formation assumes that chondrules have formed in the setting of planet formation and deprives chondrules of their status as the building blocks of terrestrial planets (Burkhardt et al., 2008;

Asphaug et al., 2011; Sanders and Scott, 2012; Kruijer et al., 2014; Lichtenberg et al., 2018; Sanders and Scott, 2018; Ebel et al., 2018).

This theory is derived from different observations which imply that differentiated planets existed prior to chondrule formation (Hutcheon and Hutchison, 1989). For example, the Pb-Pb ages of metal meteorites, which are believed to be fragments from cores of differentiated planets, imply that these meteorites are older than chondrules (Kruijer et al., 2014). Further, fragments of planetary igneous rocks, which must have crystallized under gravity, have been found in chondrites (Kennedy et al., 1992; Libourel and Krot, 2007). In addition, impacts of planetesimals in the Solar System are, in contrast to shock waves, lightnings and other supposed scenarios in the PPD, a regular occurrence (Davison et al., 2013).

Furthermore, the rare group of metal-rich CB chondrites shows evidence for a formation by planetary collisions (Weisberg et al., 2001). The chondrules of these meteorites formed approximately 4–5 Ma after the main chondrule formation event, when the solar nebular was probably empty (Krot et al., 2005). CB chondrules probably condensed from an impact plume induced by the collision of two protoplanets, whereby one was metal-rich (Krot et al., 2005; Fedkin et al., 2015; Oulton et al., 2016).

There are several scenarios how non-CB chondrules might have formed in this setting, which are reviewed in Sanders and Scott (2018) and Ebel et al. (2018). The first idea is that chondrules crystallized from impact melt formed by high velocity collisions, which is called the "impact jetting" model (Pierazzo et al., 1997; Ebel et al., 2018). The "molten planetesimal splashing models" assume, that chondrules "sprayed out" from molten interiors of colliding planetesimals as liquid droplets (Asphaug et al., 2011).

These models are in accordance with the cooling rates proposed for chondrule formation (Johnson et al., 2015), however, there are many observations of chondrules which cannot be explained by a formation by planetary collisions. For example, iron-rich chondrules are rare, the presence of Fe-Ni metal within chondrules is hard to explain, splashing of planetesimals cannot explain the chemical and isotopic diversity of individual chondrules within the same chondrite and it seems unlikely that molten and differentiated material can produce chondrules with primitive compositions (Sanders and Scott, 2012). Further, the chondrule-matrix complementary was probably not achieved when chondrules and matrix were formed by planetary collisions (Budde et al., 2016).

2.5 Formation of chondritic parent bodies

Chondrules and refractory inclusions aggregated together with matrix material to planet precursors (Weidenschilling and Cuzzi, 2006; Johansen et al., 2015; van Kooten et al., 2019). However, there are still many open questions regarding this process, for instance regarding the mass transportation in the PPD, how different material aggregated and underwent porosity reduction, about the relationship between matrix and chondrules or the formation of the different chondritic groups (e.g. Dominik et al., 2007; Ebel et al., 2016; van Kooten et al., 2019).

Chondrules within the same meteorite show different ages and isotopic signatures which led to the assumption that they were formed in different settings at different times until they were transported to the region where they aggregated (Olsen et al., 2016; Van Kooten et al., 2016; Bizzarro et al., 2017). However, although the chondrules and matrices of several types of chondrites have different element ratios (Mg/Si, Al/Ca, Al/Ti, Fe/Mg) and isotope ratios, small pieces of the bulk meteorite always have the element ratio of CI chondrites (Hezel and Palme, 2010; Ebel et al., 2016; Hezel et al., 2017). This observation is called the chondrule-matrix complementarity. It implies, that chondrules and matrix were formed from the same

CI-like material and excludes mixing of material from different regions of the PPD. However, this idea is not completely accepted and other studies proposed that complementarity arose for instance from secondary alteration (Alexander, 2005; Bizzarro et al., 2017; Zanda et al., 2018).

Furthermore, the different chondrule groups show different average chondrule sizes, for example 0.3 mm in H chondrites, 0.5 mm in L and LL chondrites and 0.1–1 mm in carbonaceous chondrites (Cuzzi et al., 2001). Size-sorting was probably the result of "aerodynamical sorting" during the aggregation of chondritic bodies (Johansen et al., 2015).

The aggregation process itself, which means that spherules in the millimeter-range stuck together, has not been resolved, since spherules in this size range rather bounce than stick together after collisions (bouncing barrier) (Zsom et al., 2010). Several mechanisms, which could have improved the sticking capability of chondrules have been proposed, for example dust coating of chondrules (Beitz et al., 2011) or electrical charging (Love et al., 2014; Jungmann et al., 2018; Steinpilz et al., 2020).

The recently developed model of van Kooten et al. (2019) explains how chondrules were formed in different settings together with complementary and size-sorting of chondrules in different chondrites. The chondrule-matrix complementary arose because chondrules form layers of metal and sulfides. The chondrules were then transported outwards and accreted a layer of CI-like matrix material. Aqueous alteration caused an oxidation of the metal layer which enriched the matrix material. Physical erosion of the metal rims and mixing with the matrix material was also proposed as a possible origin for the complementary chemistry of chondrules and matrix. The authors also suggested, that chondrules were accreted in "rubble pile" objects, which were stored in pressure traps, probably caused by the growth of Jupiter, which caused the size sorting. At the end, the "rubble pile" objects were "cemented" by gravitational collapses to the parent bodies of chondritic meteorites.

2.6 Experimental approaches to study early Solar System processes

This section gives a brief overview of the different technical approaches of experiments regarding early planet formation processes. The first kind of experiments deals with the aggregation of dust particles in the PPD (Blum and Wurm, 2000a; Blum et al., 2008; Weidling et al., 2012; Beitz et al., 2012; Steinpilz et al., 2020; Wurm and Teiser, 2021). These experiments are designed either to understand the aggregation of the first solids of the Solar System, or to understand how objects like chondrules aggregated to larger objects. Most of these experiments have been carried out under microgravity conditions (Blum and Wurm, 2000a,b; Blum et al., 2000; Wurm and Teiser, 2021). There are different possibilities to achieve a microgravity environment which have been used for planetary science experiments:

- drop towers (up to 9 s of microgravity) (e.g. Weidling et al., 2012; Steinpilz et al., 2020)
- parabolic flights (approx. 30 s) (e.g. Heißelmann et al., 2007)
- Space Shuttle (several hours) (e.g. Blum et al.; Colwell, 2002; 2003)
- International Space Station (ISS) (up to years) (e.g. Love et al., 2014; Brisset et al., 2017)

The second type of experiments in early Solar System research deals with the formation of chondrules. These experiments are focused on the parameters such as thermal evolution and (gas-)reactions in order to reproduce the chemical and textural characteristics of chondrules

(Whipple, 1975; Lofgren, 1996; Nelson et al., 1972; Hewins et al., 2000; Güttler et al., 2008; Morlok et al., 2012; Villeneuve et al., 2015). Chondrule formation experiments are generally carried out in laboratories on Earth. They can be divided in furnace heating experiments (e.g. Hewins et al., 2000; Hewins et al., 2005; Villeneuve et al., 2015), which are the most common experimental type, and "flash-heating" experiments, which use arc discharges, plasma arcs or laser as heating mechanism (Wdowiak, 1983; Whipple, 1975; Horányi, 1997; Hewins et al., 2000; Güttler et al., 2008; Morlok et al., 2012).

2.6.1 Collision and aggregation experiments

Experiments with freely floating dust particles are carried out to study the particle behavior under microgravity conditions (Blum and Wurm, 2008). These experiments are carried out to understand the physics of colliding particles (e.g. Blum and Wurm, 2008; Blum, 2006; Dominik and Tielens, 1997; Güttler et al., 2010; Kataoka et al., 2013; Kataoka et al., 2013; Kataoka, 2017).

For instance, electrostatic forces strongly affect the behavior of dust particles (e.g., Shinbrot, 2014; Siu et al., 2015), and therefore they have been considered as a possible mechanism that influenced particle aggregation in the protoplanetary disk (e.g., Poppe et al., 2000; Marshall et al., 2005; Konopka et al., 2005; Okuzumi, 2009; Love et al., 2014; Jungmann et al., 2018; Steinpilz et al., 2020). Different experiments at microgravity have followed this experimental approach (Marshall et al., 2005; Konopka et al., 2005; Love et al., 2014; Jungmann et al., 2018; Steinpilz et al., 2020). For example, it was experimentally demonstrated that charged 500 µm-sized glass spherules stick together after collisions even if they have higher velocities than uncharged spherules (Jungmann et al., 2018). Another experiment at microgravity conditions aboard a Space Shuttle showed that 400 µm-sized quartz spherules formed centimeter-sized, stable aggregates, where the spherules aligned in parallel chains within the aggregates (Marshall et al., 2005). This observation was called coaxial alignment of the spherules and was interpreted to be the result of an alignment of the quartz dipole axis. These aggregates also attracted freely levitating particles. Furthermore, informal experiments aboard the International Space Station (ISS) have shown that electrostatic forces can lead to the formation of dense, spheroidal aggregates of sucrose (Love et al., 2014). Most recently, drop tower experiments using approx. 430 µm-sized SiO_2 glass spherules which were charged by a plate capacitor, showed that charged particles form aggregates with sizes beyond the bouncing barrier with collision velocities of $>10\,\mathrm{cm\,s^{-1}}$ (Fig. 2.10) (Steinpilz et al., 2020).

Another experimental approach to form aggregates beyond the bouncing barrier was demonstrated by the drop tower experiments of Beitz et al. (2012). This experiment has shown that dust rimmed spherules and dust aggregates have an enhanced sticking behavior even at velocities, where uncoated spherules bounce off each other. Consequently, fine-grained rims around chondrules (FGRs) could have influenced the aggregation of chondritic parent bodies.

2.6.2 Chondrule formation experiments

Furnace heating

Furnace heating experiments represent the most successful experiments to reproduce chondrule textures. In most of these experiments, a solid pellet was connected to Pt wires at 1 atm pressure under controlled oxygen fugacity (fO_2) (Hewins et al., 2005). The advantage of these experiments is that the experimental parameters are very flexible which enables to vary heating and cooling rate, peak temperature, rate of melting, starting composition, re-

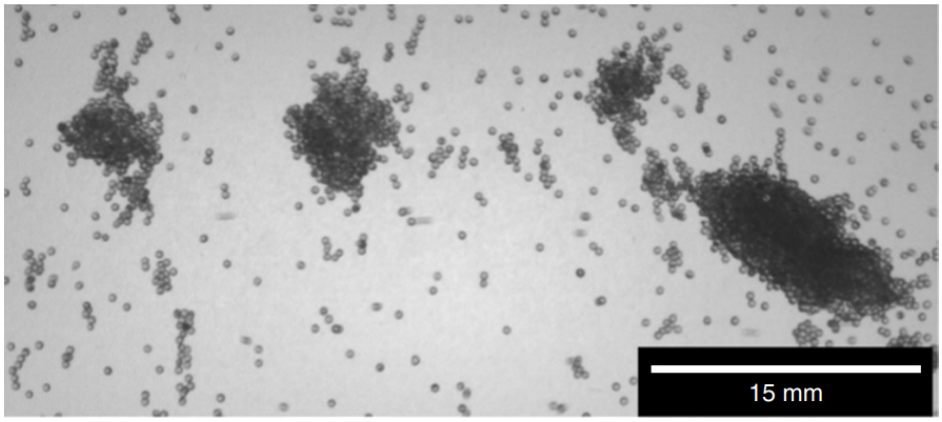

Figure 2.10: Particle aggregation experiment with charged particles which lead to the formation of agglomerates in the cm-range (Steinpilz et al., 2020).

actions and interactions between the melt and solid or melt and gas (Lofgren, 1996; Hewins and Connolly Jr., 1996; Connolly Jr. and Love, 1998; Hewins et al., 2005; Villeneuve et al., 2015). Consequently, most of the constrains for chondrule formation were derived from this kind of experiments. However, many experiments have shown that the same cooling rate can produce different chondrule textures with a different combination of heating time and peak temperature (Connolly Jr. and Love, 1998; Desch and Connolly Jr., 2002; Lofgren, 1996).

Another important parameter which may influence the chondrule formation and which could be studied with furnace heating experiments is the interaction of melt with the surrounding gas (Libourel and Portail, 2018; Libourel et al., 2006; Marrocchi and Chaussidon, 2015; Marrocchi et al., 2018; Tissandier et al., 2002; Villeneuve et al., 2015). These experiments have questioned whether the formation of porphyritic chondrules requires slow cooling rates, and proposed faster cooling rates after gas-melt reactions at high temperatures (Libourel and Portail, 2018). Furthermore, these experiments could gain new information about the relation between type I and II chondrules (Villeneuve et al., 2015). However, these experiments are influenced by gravity, for instance show gravitationally-induced settling of crystals on one side of the sample (Radomsky and Hewins, 1990).

"Flash-heating" experiments

"Flash-heating" experiments were carried out with different heating sources and materials. Many of these experiments worked with non-statically mounted samples (Güttler et al., 2008; Poppe et al., 2010; Mishra et al., 2020). However, most of these experiments were not as successful as furnace experiments and therefore often used to argue against a flash-heating mechanism for chondrule formation.

Electric arc discharges were used in chondrule formation experiments following the Nebular lightning hypothesis. However, only a few experiments with electric discharges have been carried out (Wdowiak, 1983; Whipple, 1975; Horányi, 1997) and only under gravity conditions. Figure 2.11 shows sketches of different experimental set-ups of experiments using electrical discharges and a plasma arc.

In the early study of Wdowiak (1983), millimeter-sized aggregates consisting of particles from the ground Allende meteorite were exposed to discharges between two electrodes (Fig. 2.11a). The sample was hanging on a thread between the two electrodes, was hit by a 5 kJ discharge and cooled in free fall at 5 mbar. Most of the material remained unprocessed, however a few spherules in the size range of 10 to 200 µm containing bubbles in the interior

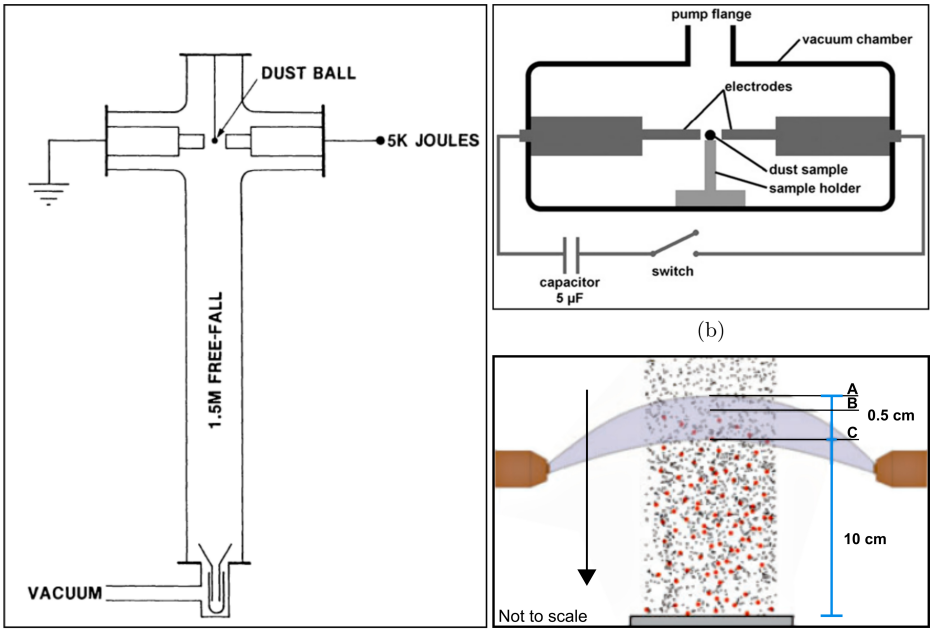

Figure 2.11: Experimental set-ups of different chondrule formation experiments using arc discharges as heating source. (*a*) Schematic sketch of the experimental set-up of the arc discharge experiments from Wdowiak (1983). (*b*) Experimental set-up of the discharge experiment from Güttler et al. (2008) (*c*) Sketch of the experiment from Morlok et al. (2012), where dust particles were falling through a plasma arc.

and on the surface were produced. He concluded that chondrules did not form by lightning because at that time, it was generally assumed, that chondrules do not contain any voids. The experiment of Güttler et al. (2008) used a similar experimental set-up (Fig. 2.11b). In this experiment, millimeter-sized dust aggregates consisting of micrometer-sized particles of different materials (fayalite, nickel, iron, San Carlos olivine, silica) were placed statically between two electrodes. They used discharge energies of 150–500 J at a gas pressure of 10–10^5 Pa, which resulted in a maximum temperature of 6500 K. Most of the aggregates fragmented, however a few sintered aggregates and small spherules were produced. Figures 2.12a–d show some of the experimental outcome. The authors argued against the formation of chondrules within lightning bolts, because lightnings are inefficient and the formed spherules were smaller than natural chondrules with a higher porosity. However, they did not exclude that chondrules could be melted by the radiation of lightnings.

The plasma arc experiment from Morlok et al. (2012) was designed in order to simulate the hot plasma produced by a shock wave. The sample material consisted of dust particles with various chemical compositions (silicates, metal, sulfide) which fell through the plasma arc (Fig. 2.11c). The experiments were carried out in air at atmospheric pressure. The plasma temperature was measured as 2973.15 ± 2.00 K and the sample material was maintained inside the plasma for approximately 0.02 s. The experiment produced different spherules with a grain size ranging from a few microns to up to approx. 100 µm which the authors called chondrule analogue objects (CAO) (Figs. 2.12e,f). However, the produced spherules represent only less than 0.1 vol% of the total sample material which was used in the experiments. The authors also recognized mixing between the different starting materials which led to the assumption that the particles reached at least the olivine eutectic temperature of 1539.15 K. One of the presented samples resembled a compound chondrule (Fig. 2.12e). Proofs for a direct crystallization of olivine from the melt has not been found. The CAOs have cooled within <0.15 s which results in cooling rates of approx. 10^7 K h^{-1}.

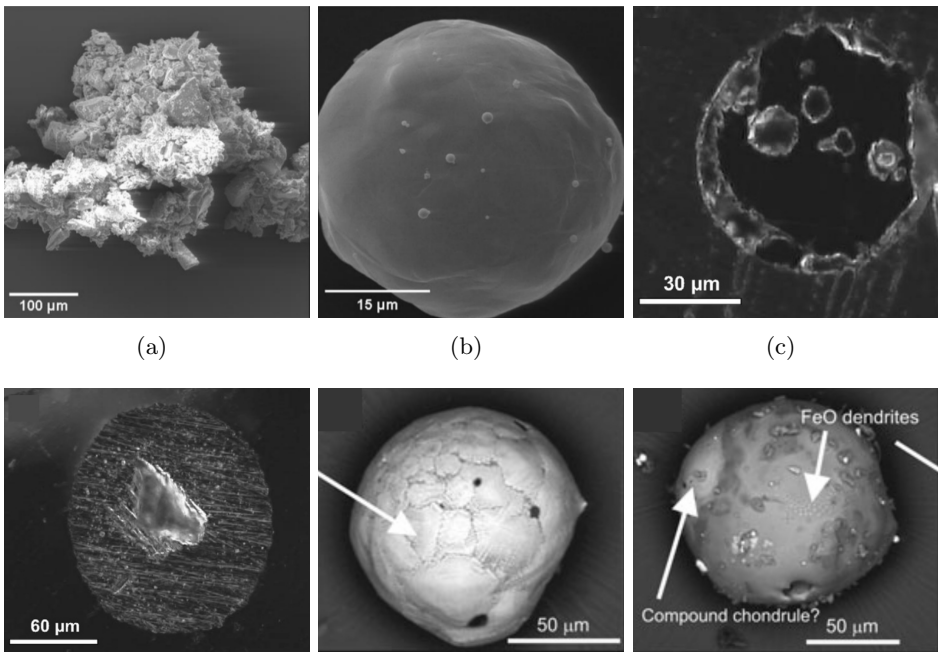

Figure 2.12: Experimental outcome of different chondrule formation experiment using electric discharges. (*a*) Fayalite aggregate from the experiment of Güttler et al. (2008). (*b*) A melt spherule of iron (center) from the experiment of Güttler et al. (2008). (*c*) Embedded and polished fayalite spherules includes pores from the experiment of Güttler et al. (2008). (*d*) Embedded and sectioned nickel spherules from the experiment of Güttler et al. (2008). (*e*) Two objects fused together similar to compound chondrules from the experiment of Morlok et al. (2012). (*f*) Spherule dominated by FeO-rich dendrites from the experiment of Morlok et al. (2012).

The experiments of Poppe et al. (2010) heated different sample materials such as peridotite, fayalite and albite with a laser for several seconds. In some cases, the sample holder was tilted, and the sample could solidify in free fall. Figure 2.13a and b show images of polished melt spherules produced by laser heating. They have shown that laser heating is a more efficient heating source than the arc discharges used in the previous experiment. They concluded that radiative heating, even after discharges, could eventually formed chondrules.

The most recent crystallization experiments on Earth carried out laser heating of Mg_2SiO_4 spherules, which were levitated on a gas jet (Mishra et al., 2020). The experiments were filmed using a high-speed camera. Best approximation of chondrule textures were formed from an undercooled forsterite melt droplets at 50 mbar with a cooling rate of approx. $10^6\,\mathrm{K\,h^{-1}}$. However, the formed dendritic microstructure is still distinct from the majority of chondrule textures (Fig. 2.13c).

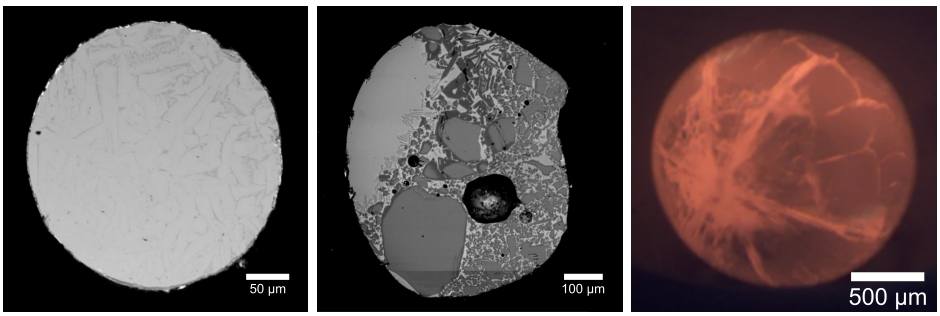

(a) (b) (c)

Figure 2.13: Experimental outcome of different chondrule formation experiments using laser heating (Poppe et al., 2010). (*a*) A polished forsterite spherule which was heated for 8 s subsequently cooling in free fall. (*b*) Polished spherules produced with laser heating (25 s) and of a mantle rock sample which cooled on the sample holder. The microstructure is probably influenced by the sample holder and gravity (Poppe et al., 2010). (*c*) A laser heated forsterite melt spherule approx. 22 ms after the beginning of solidification and cooled levitating with a cooling rate of approx. 10^6 kh at 50 mbar (Mishra et al., 2020).

2.6.3 The EXCISS experiment

The EXCISS (**Ex**perimental **C**hondrule Formation aboard the **ISS**) project was developed to combine the different experimental approaches (1) particle aggregation under microgravity and (2) melting. Figure 2.14 shows a schematic sketch of the experiment idea. Freely floating particles were exposed to electric arc discharges at long-term microgravity conditions aboard the International Space Station. With this experiment, it was possible to observe the particles under different circumstances which can be related to early Solar System processes. First, the aggregation of agitated particles in electric fields could be observed which expands our knowledge of charge-influenced particle aggregation and can be applied to understand processes like CAI, AOA and chondritic body aggregation. Furthermore, the particles were exposed to flash-heating events in form of electric arc discharges, which was proposed to be involved in CAI and chondrule formation. Videos from the experiments were recorded and the sample material was analyzed prior to and after the experiments aboard the ISS, which is part of this thesis. EXCISS represents, at least to my knowledge, the first experiment of this type which was carried out at microgravity.

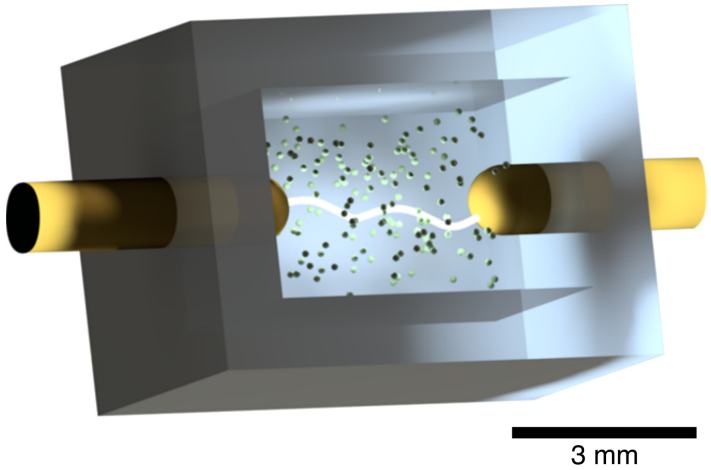

Figure 2.14: First sketch of the experiment idea of the EXCISS experiment. Freely floating dust particles were exposed to electric arc discharges. Sketch developed together with D. Merges.

CHAPTER 3

Methods & Materials

3.1 Analytical methods

3.1.1 Scanning electron microscopy (SEM)

Scanning electron microscopy (SEM) was applied as a tool to study the microstructure and chemical composition of the sample materials. A detailed description of this technique is given in Goldstein et al. (2003). Backscattered (BSE) and secondary electrons (SE) were used for imaging and the characteristic energies of X-rays were used for the chemical analysis (EDX).

Imaging and EDX analysis were carried out at a Phenom World ProX desktop SEM equipped with an electron backscatter detector in the Crystallographic Laboratory of the Geoscience Institute at the Goethe University. The advantage of this instrument is that non-coated, non-polished samples could be analyzed easily under low-vacuum conditions. More information about the analytical parameters are given in the methods section in the publications.

3.1.2 Electron backscatter diffraction (EBSD)

Electron backscatter diffraction (EBSD) is an electron diffraction technique which can be carried out using a SEM (Schwartz et al., 2000; Engler and Randle, 2010). In geoscience, this technique is used for phase identification, to study the orientation and substructure of crystals and for grain size analyses of terrestrial and extraterrestrial samples (e.g. Prior et al., 2009; Tkalcec et al., 2013). These data can help to understand for example deformation and crystallization processes as well as early Solar System processes (Prior et al., 2009; Bland et al., 2011; Tkalcec et al., 2013).

Figure 3.1 shows a schematic sketch of the basic principle of EBSD, which is explained in more detail in Schwartz et al. (2000). Secondary electrons are inelastically scattered on the lattice planes of the crystals in the sample. The angle between the primary beam and the polished sample surface must be small (approx. 20°) to increase the number of scattered electrons. If the Bragg conditions $\lambda = 2d \sin\theta$, where λ is the wavelength, d the spacing between lattice planes and θ the diffraction angle, are applied for scattered electrons, the positive interference leads to the formation of a pattern which can be detected on a plate detector (Bragg and Bragg, 1913). The obtained electron backscatter pattern, also called Kikuchi pattern, displays all the angle relations of the crystal structures which is related to the crystal symmetry. Intersections of these Kikuchi bands correspond to high symmetry

orientations, also called zone axis, and intersections of more than two bands to major zone axis. These patterns are specific for a certain crystal structure and orientation.

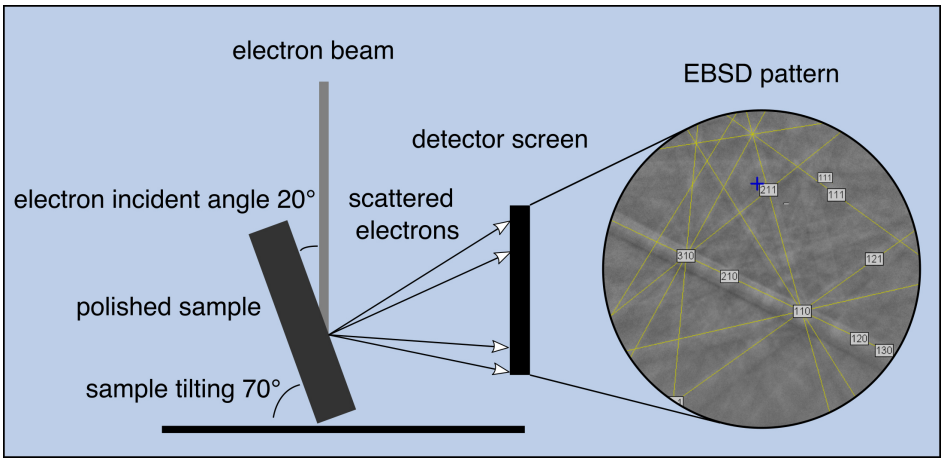

Figure 3.1: Schematic sketch of electron backscatter diffraction. The angle between the primary beam and the polished sample surface must be small (approx. 20°). The electron beam hit the tilted sample and if the Bragg condition is applied, the positive interference lead to the formation of a pattern which can be detected on a plate detector. The obtained electron backscatter pattern, also called Kikuchi pattern, displays the angle relations of the crystal structure.

The most common operation mode in EBSD is mapping. These orientation maps reveal the grain boundaries, twin boundaries, the orientation of the crystals and precipitation. Two different types of maps are shown in this thesis. EBSD phase contrast maps show the distribution of the diffraction pattern quality. The phase boundaries in these maps are visible as areas where patterns could not be indexed. The second type of EBSD map is called all-Euler angle maps. The Euler angle describes the crystal orientation with respect to a reference orientation. These all-Euler angle maps show the indexed data points which are displayed in different colors in dependence to their crystal structure and/or crystal orientation. Crystals displayed in the all-Euler angle maps with similar colors have similar orientations.

In order to display the three dimensional EBSD data of a sample in two dimensions, they are mostly displayed in stereographic projections, also called pole figures. Figure 3.2 shows a schematic sketch of how the crystal orientation is transformed into stereographic projection representative for a cubic unit cell. First, the plane normal of the unit cell are projected on the surface of a sphere (Fig. 3.2b). The sphere is then divided by a plane parallel to the surface of the sample. The intersections between the plane normal and the surface of the sphere on opposite sides are joined (Fig. 3.2c). The sphere can then be oriented along the different orientations (Fig. 3.2d).

Each collected data point or one data point per grain (ppg) can be displayed as one data point in the pole figure. The pole figures are usually contoured using multiples of uniform distributions (m.u.d.). Preferred orientations of grains in a sample can be recognized by clustering or symmetrical distributions of data points on the pole figures.

Electron backscatter diffraction was performed in the laboratory of the Geoscience Institute at Goethe University Frankfurt with a Jeol scanning electron microscope JSM 6490. The SEM is equipped with a Nordlys II phosphor screen EBSD detector with Channel 5 software from Oxford Instruments and HKL Technology. The working conditions are described in the method sections of Publication III and IV.

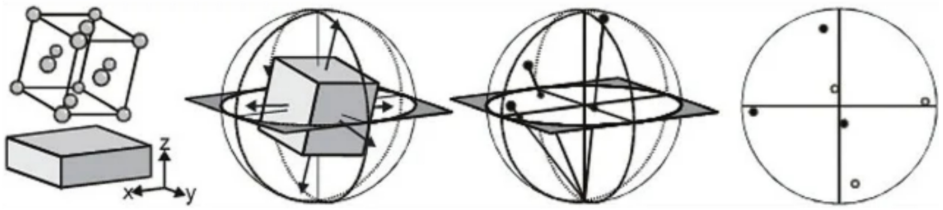

Figure 3.2: Schematic sketch of the transformation of the crystal orientation to stereographic projections. (*a*) The six {100} plane normal of the cubic unit cell are projected on the surface of a sphere. (*b*) The sphere is divided by a plane parallel to the surface of the sample. (*c*) The intersections between the {100} plane normals and the surface of the sphere on opposite sides are joined. However, the pole figures in this thesis only who the data points of one hemisphere. (*d*) The view parallel the surface of the sample is displayed in the pole figures. Image from NanoAnalysis (Retrieved on October 04, 2021).

3.1.3 Synchrotron micro-CT

Synchrotron micro-CT is a non-destructive, three-dimensional imaging technique (reviewed in Bonse and Busch, 1996). This technique allows to study the morphology of a sample as well as its interior, without the need to polish the material.

The main operating principle of synchrotron micro-CT is based on the collection of two-dimensional radiograms of the sample, which were then reconstructed to a three dimensional projection (Radon, 1917; Bonse and Busch, 1996). The radiograms show either the absorption contrast due to the different absorption coefficients of the materials in the sample or the phase contrast, which arises from the refracted or scattered synchrotron rays. The synchrotron micro-CT analysis was performed at PETRA III (DESY) in Hamburg, Germany. All data was collected on the micro tomography beamline P05 (Haibel et al., 2010; Ogurreck et al., 2013; Wilde et al., 2016), operated by Helmholtz-Zentrum Hereon. The working conditions are described in the method sections of Publications I, III and IV. The projections were visualized using Drishti (Limaye, 2012).

3.2 Sample description & preparation

3.2.1 Initial sample pellet

The dust particles which were used for the experiments were produced from a synthetic Mg_2SiO_4 (forsterite) pellet. The melting point of forsterite is approx. 2200 K (Bowen and Schairer, 1925). Figure 3.3 shows three SEM secondary electron images of the non-polished, non-coated pellet. The pellet consists of Mg_2SiO_4 grains with diameters from 1 to 20 µm. The grain boundaries intersect at 120° triple junctions.

3.2.2 Powder preparation

The pellet was ground sifted to prepare the dust particles which were used in the experiment. The power preparation is described in Section 4.2.1. SEM and micro-CT images of the single grains are shown in Publication I (Figs. 4.6, 4.7 and 4.8), in Publication III (Fig. 6.1) and in Publication IV in (Fig. 7.2).

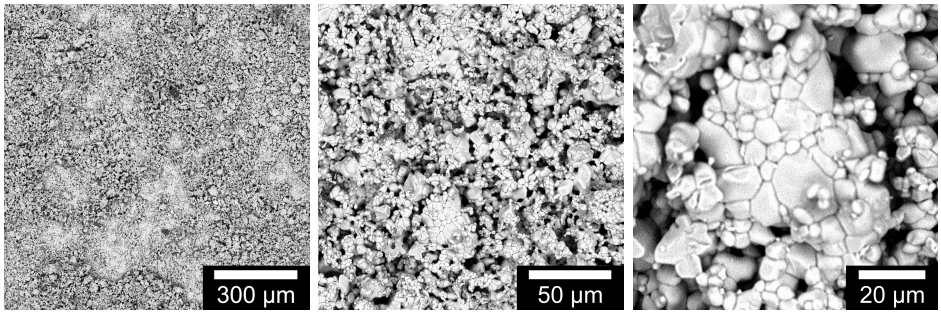

(a) (b) (c)

Figure 3.3: Secondary electron images with different magnifications of the pressed Mg_2SiO_4-pellet showing the grains sizes from 1 to 20 µm which intersects at 120° triple junctions.

3.2.3 Porosity determination

The particles are highly porous and the cavities inside the particles show a wide heterogeneity of volume and shape of pores and cracks. The porosity was quantified with BSE images of polished and unreacted sample material using ImageJ (Rueden et al., 2017). Figure 3.4 shows a BSE image of a representative grain and its corresponding threshold image. With this method, the two dimensional porosity was determined to be 7.6 ± 0.6 vol% ($n = 3$).

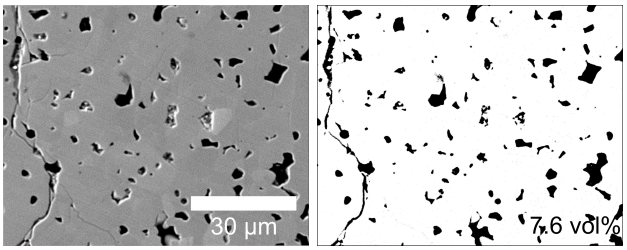

(a) (b)

Figure 3.4: (*a*) SEM BSE images of representative initial, polished grains. (*b*) Color threshold to visualize the pore volume.

3.2.4 Size distribution

The irregular and heterogeneous shapes and sizes of the grains challenged the determination of a size distribution. For the size analyses, the particles were evenly distributed in a petri dish. Several photographs were captured under an optical microscopy and the contrast of the images was then enhanced. The particles were analyzed using the particle analyzing tool of ImageJ (Rueden et al., 2017). Figure 3.5a shows a representative close-up of a high contrast photograph of the particles which were used for the size distribution analysis. The area sizes of the different grains were captured and counted by the particle analysis tool (Fig. 3.5b) and in addition, the particles were approximated as ellipsoids in order to measure the longest and shortest diameter of the grain (Fig. 3.5c). The data was binned with Gnuplot and was fitted with a normal distribution function $F(x, A, \mu, \sigma^2)$ (Bryc, 1995):

$$F(x; A, \mu, \sigma^2) = \frac{A}{\sigma\sqrt{2\pi}} \cdot exp\left(-\frac{(x-\mu)^2}{2\sigma^2}\right) \tag{3.1}$$

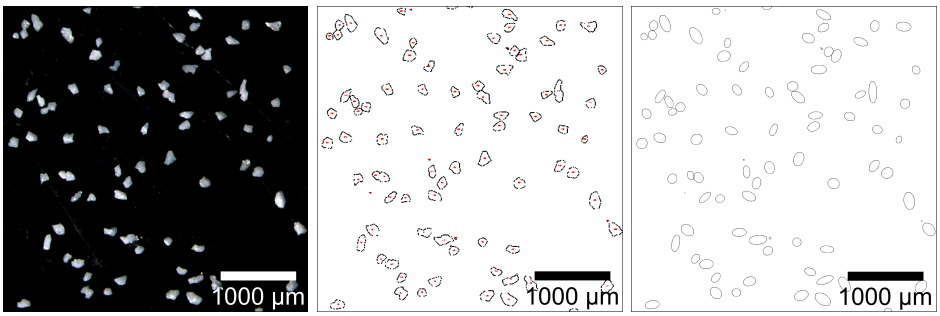

(a) (b) (c)

Figure 3.5: Different processing steps for grain size analysis. (*a*) High contrast photograph. (*b*) Outlines determined by ImageJ. (*c*) Best-fit ellipses determined by ImageJ.

where A is the amplitude, a weighting factor for the normalized peak shape, μ is the mean of the distribution, σ the standard deviation and x the values of the grain sizes. The size distribution of the particles was displayed in several diagrams and histograms which are shown in Publication III (Fig. 6.1) and in Publication IV (Figs. 7.2). The size distribution of the experimental results and natural CAIs were determined in the same way and shown in Publication III (Figs. 6.4 and 6.13).

3.2.5 Number of particles inside the sample chamber

The number of particles inside the sample chamber is used to quantify the changes of particles of the experiment. However, this number can only be roughly estimated due to the heterogenic shape and size distributions.

The sample chamber was loaded with 30 mg of Mg_2SiO_4 dust particles. With a density of $\rho_{Mg_2SiO_4} = 3.275\,\mathrm{g\,cm^{-3}}$ (Anthony et al., 2018), the total volume V_{total} of 30 mg bulk Mg_2SiO_4 is:

$$V_{\mathrm{total}} = 0.009297\,\mathrm{cm}^3 \tag{3.2}$$

The grains were assumed as spheres with a diameter of 126.6 µm. This leads to a sphere volume V_{sphere} of:

$$V_{\mathrm{sphere}} = 1.06 \cdot 10^{-6}\mathrm{cm}^3 \tag{3.3}$$

The pore volume of approx. 7.6% has to be taken into account in order to calculate the intrinsic number of particles. Consequently, the volume of a single particle excluding the pore volume $V_{\mathrm{without\ pores}}$ results in:

$$V_{\mathrm{without\ pores}} = 0.98 \cdot 10^{-6}\mathrm{cm}^3 \tag{3.4}$$

As a result, the total number n of dust particles based on this rough calculation is determined as:

$$n = 9.297 \cdot 10^{-3} \div 0.98 \cdot 10^{-6} = 9486 \approx 10^4 \tag{3.5}$$

However, the error of this number is strongly influenced by the heterogeneity of the grain sizes and shapes, the fraction of particles with a diameter of <30 µm and the error in the estimated pore volume. The number can be considered as a minimum number and the total number of particles could include up to 3000 more particles. Consequently, the number of particles inside the sample chamber will be referred to approx. 10^4 particles in the following publications.

3.2.6 Sample preparation for analysis

After the return of the experiment, the sample chamber was opened with a thread saw at the narrow tail of the sample chamber. The particles were carefully transported with weighing paper into two petri dishes. First, the sample material was studied with the optical microscope and the samples that would merit further investigation were separated from the unreacted dust particles.

For the first analyses at PETRA III, the initial samples grains and products from experiments on Earth were completely embedded in two component epoxy adhesive UHU Plus Endfest 300 placed on 50 µm Kapton foil. The epoxy was cured under vacuum by heating it up to 333 ± 2 K. Since the UHU Endfest 300 showed some bubble growth in the electron beam, the following samples were prepared in a different way.

After sample return, some of the samples were immediately prepared for synchrotron micro-CT analysis. The aggregates and melt spherules were embedded in araldite epoxy on custom-made sample holder for the sample system at beamline P05. Figure 3.6a shows the sample holder with the plateau made of araldite which includes a sample. The araldite has transformed from clear to yellow due to radiation damage from the synchrotron beam. Some of the CT samples were polished with Syton polish and thinly C-coated for SEM and EBSD analysis. Figure 3.6b shows a close-up of a polished sample before the C-coating. Other aggregates and melt spherules were embedded with araldite epoxy in brass or plastic rings and also polished with Syton and coated with carbon (Fig. 3.6c).

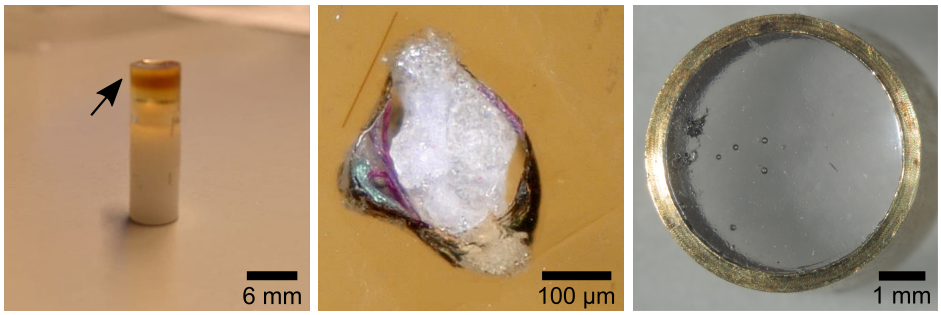

(a) (b) (c)

Figure 3.6: Different sample holders for CT and SEM analyses. (*a*) Sample holder for synchrotron micro-CT, the plateau of araldite epoxy includes the sample. The orange color is due to beam damage. (*b*) Embedded and polished sample. The pink thread is from the polishing disk. (*c*) Brass ring with embedded melt spherules. Bubbles have grown next to the samples.

Bibliography

Aléon, J., Marin-Carbonne, J., Taillifet, E., Mckeegan, K., Charnoz, S., and Baillie, K. 2013. Igneous CAI growth by coagulation and partial melting of smaller proto-CAIs: Insights from a compact type A CAI and from modeling. In *44th Lunar and Planetary Science Conference*. (abstract #2530).

Alexander, C. 2005. Re-examining the role of chondrules in producing the elemental fractionations in chondrites. *Meteoritics & Planetary Science*, 40:943–965.

Alexander, C. M. O. and Ebel, D. 2012. Questions, questions: Can the contradictions between the petrologic, isotopic, thermodynamic, and astrophysical constraints on chondrule formation be resolved? *Meteoritics & Planetary Science*, 47:1157–1175.

Anders, E. and Grevesse, N. 1989. Abundances of the elements: Meteoritic and solar. *Geochimica and Cosmochimica Acta*, 53:197–214.

Anthony, J. W., Bideaux, R. A., Bladh, K. W., and Nichols, M. C., editors. *Handbook of Mineralogy*. Mineralogical Society of America, 2018.

Arakawa, S. and Nakamoto, T. 2016. Compound chondrule formation via collision of supercooled droplets. *Icarus*, 276:102–106.

Asphaug, E., Jutzi, M., and Movshovitz, N. 2011. Chondrule formation during planetesimal accretion. *Earth and Planetary Science Letters*, 308:369–379.

Beckett, J., Connolly Jr., H. C., and Ebel, D. 2006. Chemical processes in igneous calcium-aluminum-rich inclusions: A mostly cmas view of melting and crystallization. In Lauretta, D. S. and McSween, H. Y., editors, *Meteorites and the Early Solar System II*, pages 399–429. The University of Arizona Press.

Beitz, E., Blum, J., Mathieu, R., Pack, A., and Hezel, D. 2011. Experimental investigation of nebular formation of chondrule rims and the formation of chondrite parent bodies. *Geochimica et Cosmochimica Acta*, 116:41–51.

Beitz, E., Guettler, C., Weidling, R., and Blum, J. 2012. Free collisions in a microgravity many-particle experiment-II: The collision dynamics of dust-coated chondrules. *Icarus*, pages 701–706.

Bischoff, A., Wurm, G., Chaussidon, M., Horstmann, M., Metzler, K., Weyrauch, M., and Weinauer, J. 2017. The Allende multicompound chondrule (ACC)—Chondrule formation in a local super-dense region of the early solar system. *Meteoritics & Planetary Science*, 52:906–924.

Bizzarro, M., Connelly, J. N., and Krot, A. N. 2017. Chondrules: Ubiquitous chondritic solids tracking the evolution of the solar protoplanetary disk. In Pessah, M. and Gressel, O., editors, *Formation, Evolution, and Dynamics of Young Solar Systems*, pages 161–195, Cambridge, 2017. Springer International Publishing.

Bland, P. A., Howard, L. E., Prior, D. J., Wheeler, J., Hough, R. M., and Dyl, K. A. 2011. Earliest rock fabric formed in the Solar System preserved in a chondrule rim. *Nature Geoscience*, 4:244–247.

Blum, J. 2006. Dust agglomeration. *Advances in Physics*, 55:881–947.

Blum, J. and Wurm, G. 2000a. Experiments on sticking, restructuring, and fragmentation of preplanetary dust aggregates. *Icarus*, 143:138–146.

Blum, J. and Wurm, G. 2000b. Experiments on sticking, restructuring, and fragmentation of preplanetary dust aggregates. *Icarus*, 143:138–146.

Blum, J., Wurm, G., Kempf, S., Poppe, T., Klahr, H., Kozasa, T., Rott, M., Jena, T., Dorschner, J., Schräpler, R., Keller, H., Markiewicz, W., Mann, I., Gustafson, B., Giovane, F., Neuhaus, D., Fechtig, H., Grün, E., Feuerbacher, B., and Ip, W.-H. 10 2000. Growth and form of planetary seedlings: Results from a microgravity aggregation experiment. *Physical review letters*, 85:2426–2429.

Blum, J., Wurm, G., Poppe, T., Kempf, S., and Kozasa, T. 2002. First results from the cosmic dust aggregation experiment CODAG. *Advances in Space Research*, 29:497–503.

Blum, J., Levasseur-Regourd, A.-C., Muñoz, O., Slobodrian, R. J., and Vedernikov, A. 2008. Dust in space. *Europhysics News*, 39:27–29.

Blum, J., Schräpler, R., Poppe, T., and Borst, G. 2008. Handling of particulate solids on the international space station. *Granular Matter*, 10:323–328.

Blum, J. and Wurm, G. 2008. The growth mechanisms of macroscopic bodies in protoplanetary disks. *Annual Review of Astronomy and Astrophysics*, 46:21–56.

Bollard, J., Connelly, J. N., and Bizzarro, M. 2015. Pb-Pb dating of individual chondrules from the CBa chondrite Gujba: Assessment of the impact plume formation model. *Meteoritics & Planetary Science*, 50: 1197–1216.

Bollard, J., Connelly, J. N., Whitehouse, M. J., Pringle, E. A., Bonal, L., Jørgensen, J. K., Nordlund, Å., Moynier, F., and Bizzarro, M. 2017. Early formation of planetary building blocks inferred from Pb isotopic ages of chondrules. *Science Advances*, 3.

Bolser, D., Zega, T. J., Asaduzzaman, A., Bringuier, S., Simon, S. B., Grossman, L., Thompson, M. S., and Domanik, K. J. 2016. Microstructural analysis of Wark-Lovering rims in the Allende and Axtell CV3 chondrites: Implications for high-temperature nebular processes. *Meteoritics & Planetary Science*, 51: 743–756.

Bonse, U. and Busch, F. 1996. X-ray computed microtomography (µCT) using synchrotron radiation (SR). *Progress in Biophysics and Molecular Biology*, 65(1):133–169.

Boss, A. P. The solar nebula. In Holland, H. D. and Turekian, K. K., editors, *Treatise on Geochemistry*, pages 1–23. Pergamon, Oxford, 2007.

Bowen, N. L. and Schairer, J. F. 1925. The system MgO-FeO-SiO_2. *American Journal Science*, 29:151–217.

Bragg, W. H. and Bragg, W. L. 1913. The reflection of x-rays by crystals. *Proceedings of the Royal Society of London A: Mathematical, Physical and Engineering Sciences*, 88:428–438.

Brisset, J., Colwell, J., Dove, A., and Maukonen, D. 2017. NanoRocks: Design and performance of an experiment studying planet formation on the International Space Station. *Review of Scientific Instruments*, 88:074502.

Bryc, W. *The normal distribution-Characterizations with applications*. Springer-Verlag New York, 1995.

Budde, G., Burkhardt, C., Brennecka, G. A., Fischer-Gödde, M., Kruijer, T. S., and Kleine, T. 2016. Molybdenum isotopic evidence for the origin of chondrules and a distinct genetic heritage of carbonaceous and non-carbonaceous meteorites. *Earth and Planetary Science Letters*, 454:293–303.

Burkhardt, C., Kleine, T., Bourdon, B., Palme, H., Zipfel, J., Friedrich, J. M., and Ebel, D. S. 2008. Hf-W mineral isochron for Ca,Al-rich inclusions: Age of the solar system and the timing of core formation in planetesimals. *Geochimica et Cosmochimica Acta*, 72:6177–6197.

Ciesla, F. J. and Hood, L. L. 2002. The nebular shock wave model for chondrule formation: Shock processing in a particle-gas suspension. *Icarus*, 158:281–293.

Ciesla, F. J., Lauretta, D. S., and Hood, L. L. 2004. The frequency of compound chondrules and implications for chondrule formation. *Meteoritics & Planetary Science*, 39:531–544.

Colwell, J. E. 2003. Low velocity impacts into dust: results from the collide-2 microgravity experiment. *Icarus*, 164:188–196.

Connelly, J. N. and Bizzarro, M. 2018. The absolute Pb–Pb isotope ages of chondrules insights into the dynamics of the solar protoplanetary disk. In Russell, S. S., Connolly Jr., H. C., and Krot, A. N., editors, *Chondrules: Records of Protoplanetary Disk Processes*, Cambridge Planetary Science, pages 300–323. Cambridge University Press.

Connelly, J. N., Bizzarro, M., Krot, A. N., Nordlund, Å., Wielandt, D., and Ivanova, M. A. 2012. The absolute chronology and thermal processing of solids in the solar protoplanetary disk. *Science*, 338:651–655.

Connolly Jr., H. C. and Hewins, R. H. 1995. Chondrules as products of dust collisions with totally molten droplets within a dust-rich nebular environment: An experimental investigation. *Geochimica et Cosmochimica Acta*, 59:3231–3246.

Connolly Jr., H. C. and Love, S. G. 1998. The formation of chondrules: Petrologic tests of the shock wave model. *Science*, 280:62–67.

Connolly Jr., H. C., Desch, S., Ash, R. D., and Jones, R. H. Transient heating events in the protoplanetary nebula. In Lauretta, D. S. and McSween, H. Y., editors, *Meteorites and the Early Solar System II*, pages 19–52. University of Arizona Press, 2006.

Consolmagno, G., Britt, D., and Macke, R. 2008. What density and porosity tell us about meteorites. In *39th Lunar and Planetary Science Conference*. (abstract #1582).

Cuzzi, J. N. and Alexander, C. M. O. 2006. Chondrule formation in particle-rich nebular regions at least hundreds of kilometres across. *Nature*, 441:483–485.

Cuzzi, J. N. and Weidenschilling, S. J. 2006. Particle-Gas Dynamics and Primary Accretion. In Lauretta, D. S. and McSween, H. Y., editors, *Meteorites and the Early Solar System II*, pages 353–381. The University of Arizona Press.

Cuzzi, J. N., Hogan, R. C., Paque, J. M., and Dobrovolskis, A. R. 2001. Size-selective concentration of chondrules and other small particles in protoplanetary nebula turbulence. *Astrophysical Journal*, 546:496.

Davison, T. M., O'Brien, D. P., Ciesla, F. J., and Collins, G. S. 2013. The early impact histories of meteorite parent bodies. *Meteoritics & Planetary Science*, 48:1894–1918.

Desch, S. J. and Connolly Jr., H. C. 2002. A model of the thermal processing of particles in solar nebula shocks: Application to the cooling rates of chondrules. *Meteoritics & Planetary Science*, 37:183–207.

Desch, S. J. and Cuzzi, J. N. 2000. The generation of lightning in the solar nebula. *Icarus*, 143:87–105.

Desch, S. J., Ciesla, F. J., Hood, L. L., and Nakamoto, T. 2005. Heating of Chondritic Materials in Solar Nebula Shocks. In Krot, A. N., Scott, E. R. D., and Reipurth, B., editors, *Chondrites and the Protoplanetary Disk*, volume 341 of *Astronomical Society of the Pacific Conference Series*, pages 849–872.

Desch, S. J., Morris, M. A., Connolly Jr., H. C., and Boss, A. P. 2010. A critical examination of the x-wind model for chondrule and calcium-rich, aluminum-rich inclusion formation and radionuclide production. *The Astrophysical Journal*, 725:692–711.

Desch, S. J., Morris, M. A., Connolly Jr., H. C., and Boss, A. P. 2012. The importance of experiments: Constraints on chondrule formation models. *Meteoritics & Planetary Science*, 47:1139–1156.

Dominik, C. and Tielens, A. G. G. M. 1997. The physics of dust coagulation and the structure of dust aggregates in space. *The Astrophysical Journal*, 480:647–673.

Dominik, C., Blum, J., Cuzzi, J. N., and Wurm, G. 2007. Growth of dust as the initial step toward planet formation. In Reipurth, B., Jewitt, D., and Keil, K., editors, *Protostars and Planets V*, pages 257–263.

Dullemond, C. P. and Dominik, C. Apr 2005. Dust coagulation in protoplanetary disks: A rapid depletion of small grains. *Astronomy & Astrophysics*, 434:971–986.

Ebel, D., Alexander, C., and Libourel, G. 2018. Formation of chondrules by planetesimal collisions. In Johnson, B. C., Ciesla, F. J., Dullemond, C. P., and Melosh, H. J., editors, *Chondrules: Records of Protoplanetary Disk Processes*, Cambridge Planetary Science, pages 343–360. Cambridge University Press.

Ebel, D. S. and Rivers, M. L. 2007. Meteorite 3-D synchrotron microtomography: Methods and applications. *Meteoritics & Planetary Science*, 42:1627–1646.

Ebel, D. S., Brunner, C., Konrad, K., Leftwich, K., Erb, I., Lu, M., Rodriguez, H., Crapster-Pregont, E. J., Friedrich, J. M., and Weisberg, M. K. 2016. Abundance, major element composition and size of components and matrix in cv, co and acfer 094 chondrites. *Geochimica et Cosmochimica Acta*, 172:322–356.

Einstein, A. 1905. Über die von der molekularkinetischen Theorie der Wärme geforderte Bewegung von in ruhenden Flüssigkeiten suspendierten Teilchen. *Annalen der Physik*, 322:549–560.

Engler, O. and Randle, V. *Introduction to texture analysis: Macrotexture, microtexture and orientation mapping*. CRC Press 488 p., 2 edition, 2010.

Fedkin, A. V., Grossman, L., Humayun, M., Simon, S. B., and Campbell, A. J. 2015. Condensates from vapor made by impacts between metal-, silicate-rich bodies: Comparison with metal and chondrules in CB chondrites. *Geochimica et Cosmochimica Acta*, 164:236–261.

Floss, C. 2010. Protoplanetary dust: Astrophysical and cosmochemical perspectives. *Meteoritics & Planetary Science*, 45:913–914.

Goldstein, J., Newbury, D. E., Joy, D. C., Lyman, C. E., Echlin, P., Lifshin, E., Sawyer, L., and Michael, J. R. *Scanning Electron Microscopy and X-Ray Microanalysis*. Springer Verlag, 3 edition, 2003.

Gooding, J. L. and Keil, K. 1981. Relative abundances of chondrule primary texture types in ordinary chondrites and their bearing on chondrule formation. *Meteoritics & Planetary Science*, 16:17–43.

Greenwood, J. P. and Herbst, W. 2021. New constraints on chondrule formation from experimental reproduction of aluminum and titanium zoning in chondrule olivine. In *52th Lunar and Planetary Science Conference*. (abstract #1617).

Grossmann, L. 1975. Petrography and mineral chemistry of Ca-rich inclusions in the Allende meteorite. *Geochimica et Cosmochimica Acta*, 39:433–454.

Güttler, C., Poppe, T., Wasson, J. T., and Blum, J. 2008. Exposing metal and silicate charges to electrical discharges: Did chondrules form by nebular lightning? *Icarus*, 195:504–510.

Güttler, C., Blum, J., Zsom, A., Ormel, C. W., and Dullemond, C. P. 2010. The outcome of protoplanetary dust growth: pebbles, boulders, or planetesimals? I. Mapping the zoo of laboratory collision experiments. *Astronomy & Astrophysics*, 513:A56.

Haibel, A., Ogurreck, M., Beckmann, F., Dose, T., Wilde, F., Herzen, J., Müller, M., Schreyer, A., Nazmov, V., Simon, M., last, A., and Mohr, J. 2010. Micro- and nano-tomography at the GKSS imaging beamline at PETRA III. In *Developments in X-ray tomography VII*, page 78040B. SPIE.

Han, J., Keller, L. P., Liu, M.-C., Needham, A. W., Hertwig, A. T., Messenger, S., and Simon, J. I. 2020. A coordinated microstructural and isotopic study of a Wark-Lovering rim on a Vigarano CAI. *Geochimica et Cosmochimica Acta*, 269:639–660.

Heißelmann, D., Fraser, H. J., and Blum, J. 2007. Experimental studies on the aggregation properties of ice and dust in planet-forming regions. In *58th International Astronautical Congress*. (abstract #IAC-07-A2.1.02).

Hewins, R., Connolly Jr., H. C., and Libourel, G. 2005. Experimental constraints on chondrule formation. *Chondrites and the Protoplanetary Disk*, 341:286.

Hewins, R. H. and Connolly Jr., H. C. 1996. Peak temperatures of flash-melted chondrules. In Hewins, R. H., Jones, R. H., and Scott, E. R. D., editors, *Chondrules and the Protoplanetary Disk*, pages 197–204.

Hewins, R. H. and Fox, G. E. 2004. Chondrule textures and precursor grain size: an experimental study. *Geochimica et Cosmochimica Acta*, 68:917–926.

Hewins, R. H., Zanda, R. H., Horányi, M., Robertson, S., Den Hartog, D. J., and Fiksel, G. 2000. The trouble with flash heating. In *31st Lunar and Planetary Science Conference*. (abstract #1675).

Hewins, R. H. 1997. Chondrules. *Annual Review of Earth and Planetary Sciences*, 25:61–83.

Hezel, D. and Palme, H. 05 2010. The chemical relationship between chondrules and matrix and the chondrule matrix complementarity. *Earth and Planetary Science Letters*, 294:85–93.

Hezel, D., Palme, H., Bland, P., and Jacquet, E. 2017. The chondrule-matrix complementarity. In *Workshop on Chondrules and Protoplanetary Disk*. (abstract #2007).

Hezel, D. C., Russell, S. S., Ross, A. J., and Kearsley, A. T. 2008. Modal abundances of cais: Implications for bulk chondrite element abundances and fractionations. *Meteoritics & Planetary Science*, 43:1879–1894.

Horányi, M. 1997. Lightning and shock heating as candidate processes for chondrule formation. In *Workshop on Parent-Body and Nebular Modification of Chondritic Materials*. (abstract #1499).

Horányi, M., Morfill, G., Goertz, C. K., and Levy, E. H. 1995. Chondrule formation in lightning discharges. *Icarus*, 114:174–185.

Hubbard, A. 2015. Compound chondrules fused cold. *Icarus*, 254:56–61.

Hubbard, A. and Ebel, D. S. 2015. Semarkona: Lessons for chondrule and chondrite formation. *Icarus*, 245: 32–37.

Hubbard, A. and Ebel, D. S. 2018. Evaluating non-shock, non-collisional models for chondrule formation. In Russell, S. S., Connolly Jr., H. C., and Krot, A. N., editors, *Chondrules: Records of Protoplanetary Disk Processes*, Cambridge Planetary Science, page 400–426. Cambridge University Press.

Hutcheon, I. and Hutchison, R. 1989. Evidence from the Semarkona ordinary chondrite for ^{26}Al heating of small planets. *Nature*, 337:238–241.

Itoh, A., Rubin, A. E., Kojima, H., Wasson, J. T., and Yurimoto, H. 2002. Amoeboid olivine aggregates and aoa-bearing chondrule from y-81020 co3.0 chondrite: Distribution of oxygen and magnesium isotopes. In *52th Lunar and Planetary Science Conference*. (abstract #1490).

Ivanova, M. A., Kononkova, N. N., Krot, A. N., Greenwood, R. C., Franchi, I. A., Verchovsky, A. B., Trieloff, M., Korochantseva, E. V., and Brandstätter, F. 2008. The Isheyevo meteorite: Mineralogy, petrology, bulk chemistry, oxygen, nitrogen, carbon isotopic compositions, and ^{40}Ar-^{39}Ar ages. *Meteoritics & Planetary Science*, 43:915–940.

Ivanova, M. A., Lorenz, C. A., Krot, A. N., and MacPherson, G. J. 2015. A compound Ca-, Al-rich inclusion from CV3 chondrite Northwest Africa 3118: Implications for understanding processes during CAI formation. *Meteoritics & Planetary Science*, 50:1512–1528.

Johansen, A. and Okuzumi, S. 2018. Harvesting the decay energy of ^{26}Al to drive lightning discharge in protoplanetary discs. *Astronomy and Astrophysics*, 609:1–22.

Johansen, A., Low, M.-M. M., Lacerda, P., and Bizzarro, M. 2015. Growth of asteroids, planetary embryos, and kuiper belt objects by chondrule accretion. *Science Advances*, 1:1–16.

Johnson, B. C., Minton, D. A., Melosh, H. J., and Zuber, M. T. 2015. Impact jetting as the origin of chondrules. *Nature*, 517:339–341.

Jones, R., Villeneuve, J., and Libourel, G. 2018. Thermal histories of chondrules. In Russell, S. S., Connolly Jr., H. C., and Krot, A. N., editors, *Chondrules: Records of Protoplanetary Disk Processes*, Cambridge Planetary Science, pages 57–90. Cambridge University Press.

Jones, R. H. 1996. Feo-rich, porphyritic pyroxene chondrules in unequilibrated ordinary chondrites. *Geochimica et Cosmochimica Acta*, 60:3115–3138.

Jones, R. H. and Danielson, L. R. 1997. A chondrule origin for dusty relict olivine in unequilibrated chondrites. *Meteoritics and Planetary Science*, 32:753–760.

Jones, R. H., Grossman, J., and Rubin, A. 2005. Chemical, mineralogical and isotopic properties of chondrules: Clues to their origin. *Chondrites and the Protoplanetary Disk*, 341:251.

Jungmann, F., Steinpilz, T., Teiser, J., and Wurm, G. 2018. Sticking and restitution in collisions of charged sub-mm dielectric grains. *Journal of Physics Communications*, 2:095009.

Kataoka, A. 2017. Dust coagulation with porosity evolution. In Pessah, M. and Gressel, O., editors, *Formation, Evolution, and Dynamics of Young Solar Systems*, pages 143–159, Cambridge, 2017. Springer International Publishing.

Kataoka, A., Tanaka, H., Okuzumi, S., and Wada, K. 2013. Static compression of porous dust aggregates. *Astronomy & Astrophysics*, 554:A4.

Kataoka, A., Tanaka, H., Okuzumi, S., and Wada, K. 2013. Fluffy dust forms icy planetesimals by static compression. *Astronomy & Astrophysics*, 557:L4.

Kennedy, A. K., Hutchison, R., Hutcheon, I. D., and Agrell, S. O. 1992. A unique high mn/fe microgabbro in the parnallee (ll3) ordinary chondrite: nebular mixture or planetary differentiate from a previously unrecognized planetary body? *Earth and Planetary Science Letters*, 113:191–205.

Kleine, T., Budde, G., Burkhardt, C., Kruijer, T. S., Worsham, E. A., Morbidelli, A., and Nimmo, F. 2020. The Non-carbonaceous-Carbonaceous Meteorite Dichotomy. *Space Science Reviews*, 216:55.

Komatsu, M., Fagan, T. J., Mikouchi, T., Petaev, M. I., and Zolensky, M. E. 2015. LIME silicates in amoeboid olivine aggregates in carbonaceous chondrites: Indicator of nebular and asteroidal processes. *Meteoritics & Planetary Science*, 50:1271–1294.

Konopka, U., Mokler, F., Ivlev, A. V., Kretschmer, M., Morfill, G. E., Thomas, H. M., Rothermel, H., Fortov, V. E., Lipaev, A. M., Molotkov, V. I., Nefedov, A. P., Baturin, Y. M., Budarin, Y., Ivanov, A. I., and Roth, M. 2005. Charge-induced gelation of microparticles. *New Journal of Physics*, 7:227–227.

Krot, A. N. 2019. Refractory inclusions in carbonaceous chondrites: Records of early solar system processes. *Meteoritics & Planetary Science*, 54:1647–1691.

Krot, A. N. and Wasson, J. T. 1995. Igneous rims on low-FeO and high-FeO chondrules in ordinary chondrites. *Geochimica et Cosmochimica Acta*, 59:4951–4966.

Krot, A. N., Meibom, A., Weisberg, M. K., and Keil, K. 2002. The CR chondrite clan: Implications for early Solar System processes. *Meteoritics & Planetary Science*, 37:1451–1490.

Krot, A. N., Petaev, M. I., Russell, S. S., Itoh, S., Fagan, T. J., Yurimoto, H., Chizmadia, L., Weisberg, M. K., Komatsu, M., Ulyanov, A. A., and Keil, K. 2004a. Amoeboid olivine aggregates and related objects in carbonaceous chondrites: records of nebular and asteroid processes. *Geochemistry*, 64:185–239.

Krot, A. N., Petaev, M. I., and Yurimoto, H. 2004b. Amoeboid olivine aggregates with low-ca pyroxenes: a genetic link between refractory inclusions and chondrules? *Geochimica et Cosmochimica Acta*, 68:1923–1941.

Krot, A. N., Amelin, Y., Cassen, P., and Meibom, A. 2005. Young chondrules in CB chondrites from a giant impact in the early solar system. *Nature*, 436:989–992.

Krot, A. N., Amelin, Y., Bland, P., Ciesla, F., Connelly, J., Davis, A. M., Huss, G. R., Hutcheon, I., Makide, K., Nagashima, K., Nyquist, L., Russell, S., Scott, E. R. D., Thrane, K., Yurimoto, H., and Yin, Q.-Z. 2009. Origin and chronology of chondritic components: A review. *Geochimica et Cosmochimica Acta*, 73: 4963–4997.

Krot, A. N., Nagashima, K., Libourel, G., and Miller, K. E. 2018. Multiple mechanisms of transient heating events in the protoplanetary disk: Evidence from precursors of chondrules and igneous ca, al-rich inclusions. In Russell, S. S., Connolly Jr., H. C., and Krot, A. N., editors, *Chondrules: Records of Protoplanetary Disk Processes*, Cambridge Planetary Science, page 11–56. Cambridge University Press.

Kruijer, T. S., Touboul, M., Fischer-Gödde, M., Bermingham, K. R., Walker, R. J., and Kleine, T. 2014. Protracted core formation and rapid accretion of protoplanets. *Science*, 344:1150–1154.

Kruijer, T. S., Burkhardt, C., Budde, G., and Kleine, T. 2017. Age of jupiter inferred from the distinct genetics and formation times of meteorites. *Proceedings of the National Academy of Sciences*, 114:6712–6716.

Larsen, K. K., Wielandt, D., Schiller, M., Krot, A. N., and Bizzarro, M. 2020. Episodic formation of refractory inclusions in the Solar System and their presolar heritage. *Earth and Planetary Science Letters*, 535:116088.

Leroux, H., Libourel, G., Lemelle, L., and Guyot, F. 2003. Experimental study and TEM characterization of dusty olivines in chondrites: Evidence for formation by in situ reduction. *Meteoritics & Planetary Science*, 38:81–94.

Libourel, G. and Krot, A. N. 2007. Evidence for the presence of planetesimal material among the precursors of magnesian chondrules of nebular origin. *Earth and Planetary Science Letters*, 254:1–8.

Libourel, G. and Portail, M. 2018. Chondrules as direct thermochemical sensors of solar protoplanetary disk gas. *Science Advances*, 4:eaar3321.

Libourel, G., Krot, A. N., and Tissandier, L. 2006. Role of gas-melt interaction during chondrule formation. *Earth and Planetary Science Letters*, 251:232–240.

Lichtenberg, T., Golabek, G. J., Dullemond, C. P., Schönbächler, M., Gerya, T. V., and Meyer, M. R. 2018. Impact splash chondrule formation during planetesimal recycling. *Icarus*, 302:27–43.

Liffman, K., Cuello, N., and Paterson, D. 2016. A unified framework for producing CAI melting, Wark–Lovering rims and bowl-shaped CAIs. *Monthly Notices of the Royal Astronomical Society*, 462: 1137–1163.

Limaye, A. 2012. Drishti: A volume exploration and presentation tool. In *Developments in X-ray tomography VIII*, volume 8506, pages 1–9. SPIE.

Lofgren, G. E. 1996. A dynamic crystallization model for chondrule melts. In Hewins, R. H., Jones, R. H., and Scott, E. R. D., editors, *Chondrules and the Protoplanetary Disk*, pages 187–196.

Lorenz, C., Ivanova, M., Krot, A., and Shuvalov, V. 2019. Formation of disk- and bowl-shaped igneous Ca,Al-rich inclusions: Constraints from their morphology, textures, mineralogy and modelling. *Geochemistry*, 79: 125523.

Love, S. G., Pettit, D. R., and Messenger, S. R. 2014. Particle aggregation in microgravity: Informal experiments on the International Space Station. *Meteoritics & Planetary Science*, 49:732–739.

MacPherson, G. J. 2003. Calcium-Aluminum-rich Inclusions in Chondritic Meteorites. *Treatise on Geochemistry*, 1:201–246.

MacPherson, G. J. and Grossman, L. 1984. "Fluffy" Type A Ca-, Al-rich inclusions in the Allende meteorite. *Geochimica et Cosmochimica Acta*, 48:29–46.

MacPherson, G. J., Hashimoto, A., and Grossman, L. 1985. Accretionary rims on inclusions in the Allende meteorite. *Geochimica et Cosmochimica Acta*, 49:2267–2279.

Marrocchi, Y. and Chaussidon, M. 2015. A systematic for oxygen isotopic variation in meteoritic chondrules. *Earth and Planetary Science Letters*, 430:308–315.

Marrocchi, Y., Villeneuve, J., Batanova, V., Piani, L., and Jacquet, E. 2018. Oxygen isotopic diversity of chondrule precursors and the nebular origin of chondrules. *Earth and Planetary Science Letters*, 496: 132–141.

Marrocchi, Y., Euverte, R., Villeneuve, J., Batanova, V., Welsch, B., Ferrière, L., and Jacquet, E. 2019a. Formation of cv chondrules by recycling of amoeboid olivine aggregate-like precursors. *Geochimica et Cosmochimica Acta*, 247:121–141.

Marrocchi, Y., Villeneuve, J., Jacquet, E., Piralla, M., and Chaussidon, M. 2019b. Rapid condensation of the first solar system solids. *Proceedings of the National Academy of Sciences*, 116:23461–23466.

Marshall, J. R., Sauke, T. B., and Cuzzi, J. N. 2005. Microgravity studies of aggregation in particulate clouds. *Geophysical Research Letter*, 32:L11202.

Matsuda, N., Sakamoto, N., Tachibana, S., and Yurimoto, H. 2019. Heating duration of igneous rim formation on a chondrule in the Northwest Africa 3118 CV3oxA carbonaceous chondrite inferred from micro-scale migration of the oxygen isotopes. *Geochemistry*, 79:125524.

McNally, C. P., Hubbard, A., Mac Low, M.-M., Ebel, D. S., and D'Alessio, P. 2013. Mineral processing by short circuits in protoplanetary disks. *The Astrophysical Journal*, 767:L2.

Metzler, K., Bischoff, A., and Stöffler, D. 1992. Accretionary dust mantles in CM chondrites: Evidence for solar nebula processes. *Geochimica et Cosmochimica Acta*, 56:2873–2897.

Mishra, B., Manvar, P., Choudhury, K., Karagadde, S., and Srivastava, A. 2020. Experiments to understand crystallization of levitated high temperature silicate melt droplets under low vacuum conditions. *Scientific Reports*, 10:20910.

Morfill, G. E., Durisen, R. H., and Turner, G. W. 1998. An accretion rim constraint on chondrule formation theories. *Icarus*, 134:180–184.

Morlok, A., Sutton, Y. C., Braithwaite, N. S. J., and Grady, M. M. 2012. Chondrules born in plasma? Simulation of gas-grain interaction using plasma arcs with applications to chondrule and cosmic spherule formation. *Meteoritics & Planetary Science*, 47:2269–2280.

Morris, M. and Boley, A. C. 2018. Formation of chondrules by shock waves. In Russell, S. S., Connolly Jr., H. C., and Krot, A. N., editors, *Chondrules: Records of Protoplanetary Disk Processes*, Cambridge Planetary Science, pages 375–399. Cambridge University Press.

Morris, M. and Garvie, L. 2013. New constraints on the formation of igneous rims around chondrules. In *44th Lunar and Planetary Science Conference*. (abstract #2852).

Morris, M. A. and Desch, S. J. 2010. Thermal histories of chondrules in solar nebula shocks. *The Astrophysical Journal*, 722:1474–1494.

Morris, M. A., Boley, A. C., Desch, S. J., and Athanassiadou, T. 2012. Chondrule formation in bow shocks around eccentric planetary embryos. *The Astrophysical Journal*, 752:1–17.

NanoAnalysis, O. I. Generating orientation maps to present EBSD data. AZoM. https://www.azom.com/article.aspx?ArticleID=11775, Retrieved on October 04, 2021.

Nelson, L. S., Blander, M., Skaggs, S. R., and Keil, K. 1972. Use of a co_2 laser to prepare chondrule-like spherules from supercooled molten oxide and silicate droplets. *Earth and Planetary Science Letters*, 14: 338–344.

Ogurreck, M., Wilde, F., Herzen, J., Beckmann, F., Nazmov, V., Mohr, J., Haibel, A., Müller, M., and Schreyer, A. 2013. The nanotomography endstation at the PETRA III Imaging Beamline. *Journal of Physics: Conference Series*, 425:182002.

Okuzumi, S. 2009. Electric charging of dust aggregates and its effect on dust coagulation in protoplanetary disks. *The Astrophysical Journal*, 698:1122–1135.

Olsen, M. B., Wielandt, D., Schiller, M., Van Kooten, E. M. M. E., and Bizzarro, M. 2016. Magnesium and ^{54}Cr isotope compositions of carbonaceous chondrite chondrules – Insights into early disk processes. *Geochimica et Cosmochimica Acta*, 191:118–138.

Ormel, C. W., Spaans, M., and Tielens, A. G. G. M. 2007. Dust coagulation in protoplanetary disks: porosity matters. *Astronomy & Astrophysics*, 461:215–232.

Oulton, J., Humayun, M., Fedkin, A., and Grossman, L. 2016. Chemical evidence for differentiation, evaporation and recondensation from silicate clasts in Gujba. *Geochimica et Cosmochimica Acta*, 177:254–274.

Pierazzo, E., Vickery, A. M., and Melosh, H. J. 1997. A reevaluation of impact melt production. *Icarus*, 127 (2):408–423.

Pilipp, W., Hartquist, T. W., and Morfill, G. E. 1992. Large Electric Fields in Acoustic Waves and the Stimulation of Lightning Discharges. *The Astrophysical Journal*, 387:364–371.

Poppe, T., Blum, J., and Henning, T. 2000. Analogous experiments on the stickiness of micron-sized preplanetary dust. *The Astrophysical Journal*, 533:454–471.

Poppe, T., Güttler, C., and Springborn, T. 2010. Thermal metamorphoses of cosmic dust aggregates: Experiments by furnace, electrical gas discharge, and radiative heating. *Earth, Planets and Space*, 62:53–56.

Prior, D. J., Mariani, E., and Wheeler, J. 2009. Ebsd in the earth sciences: Applications, common practice, and challenges. In Schwartz, A. J., Kumar, M., Adams, B. L., and Field, D. P., editors, *Electron backscatter diffraction in materials science*, Cambridge Planetary Science, pages 345–360, Boston, MA, 2009. Springer US.

Radomsky, P. M. and Hewins, R. H. 1990. Formation conditions of pyroxene-olivine and magnesian olivine chondrules. *Geochimica et Cosmochimica Acta*, 54:3475–3490.

Radon, J. 1917. Über die Bestimmung von Funktionen durch ihre Integralwerte längs gewisser Mannigfaltigkeiten. *Akademie der Wissenschaft*, 69:262–277.

Rambaldi, E. R. 1981. Relict grains in chondrules. *Nature*, 293:558–561.

Rubin, A. 2012. A new model for the origin of Type-B and Fluffy Type-A CAIs: Analogies to remelted compound chondrules. *Meteoritics & Planetary Science*, 47:1062–1074.

Rubin, A. E. 1984. Coarse-grained chondrule rims in type 3 chondrites. *Geochimica et Cosmochimica Acta*, 48:1779–1789.

Rueden, C. T., Schindelin, J., Hiner, M. C., DeZonia, B. E., Walter, A. E., Arena, E. T., and Eliceiri, K. W. ImageJ2: ImageJ for the next generation of scientific image data. *BMC Bioinformatics* 18:529, 2017.

Russel, S. S., Connolly Jr., H. C., and Krot, A. N., editors. *Chondrules: Records of Protoplanetary Disk Processes*. Cambridge Planetary Science. Cambridge University Press 450 p., 2018.

Russell, S. S. and Howard, L. 2013. The texture of a fine-grained calcium–aluminium-rich inclusion (CAI) in three dimensions and implications for early solar system condensation. *Geochimica et Cosmochimica Acta*, 116:52–62.

Ruzicka, A., Floss, C., and Hutson, M. 2012a. Agglomeratic olivine (AO) objects and Type II chondrules in ordinary chondrites: Accretion and melting of dust to form ferroan chondrules. *Geochimica et Cosmochimica Acta*, 76:103–124.

Ruzicka, A., Floss, C., and Hutson, M. 2012b. Amoeboid olivine aggregates (AOAs) in the Efremovka, Leoville and Vigarano (CV3) chondrites: A record of condensate evolution in the solar nebula. *Geochimica et Cosmochimica Acta*, 79:79–105.

Sanders, I. S. and Scott, E. R. D. 2012. The origin of chondrules and chondrites: Debris from low-velocity impacts between molten planetesimals? *Meteoritics & Planetary Science*, 47:2170–2192.

Sanders, I. S. and Scott, E. R. D. 2018. Making chondrules by splashing molten planetesimals. In Johnson, B. C., Ciesla, F. J., Dullemond, C. P., and Melosh, H. J., editors, *Chondrules: Records of Protoplanetary Disk Processes*, Cambridge Planetary Science, pages 361–374. Cambridge University Press.

Schmus, W. V. and Wood, J. A. 1967. A chemical-petrologic classification for the chondritic meteorites. *Geochimica et Cosmochimica Acta*, 31:747–765.

Schwartz, A., Kumar, M., and Adams, B., editors. *Electron backscatter diffraction in material science*. Springer US 403p., Boston, Massachusetts, 2 edition, 2000.

Scott, E. R. D. and Krot, A. N. 2014. Chondrites and Their Components. In Davis, A. M., editor, *Meteorites and Cosmochemical Processes*, volume 1, pages 65–137.

Shinbrot, T. 2014. Granular electrostatics: Progress and outstanding questions. *The European Physical Journal Special Topics*, 223:2241–2252.

Shu, F. H. and Shang, T., H.and Lee. 1996. Toward an astrophysical theory of chondrites. *Science*, 271: 1545–1552.

Sicilia-Aguilar, A., Banzatti, A., Carmona, A., Stolker, T., Kama, M., Mendigutía, I., Garufi, A., Flaherty, K., van der Marel, N., Greaves, J., and et al. 2016. A 'rosetta stone' for protoplanetary disks: The synergy of multi-wavelength observations. *Publications of the Astronomical Society of Australia*, 33:e059.

Siu, T., Pittman, W., Cotton, J., and Shinbrot, T. 2015. Nonlinear granular electrostatics. *Granular Matter*, 17:165–175.

Soulié, C., Libourel, G., and Tissandier, L. 2017. Olivine dissolution in molten silicates: An experimental study with application to chondrule formation. *Meteoritics & Planetary Science*, 52:225–250.

Steinpilz, T., Joeris, K., Jungmann, F., Wolf, D., Brendel, L., Teiser, J., Shinbrot, T., and Wurm, G. 2020. Electrical charging overcomes the bouncing barrier in planet formation. *Nature Physics*, 16:225–229.

Sugiura, N., Petaev, M., Kimura, M., Miyazaki, A., and Hiyagon, H. 01 2010. Nebular history of amoeboid olivine aggregates. *Meteoritics & Planetary Science*, 44:559–572.

Suyama, T., Wada, K., and Tanaka, H. 2008. Numerical simulation of density evolution of dust aggregates in protoplanetary disks. I. Head-on collisions. *The Astrophysical Journal*, 684:1310–322.

Taillifet, E., Baillié, K., Charnoz, S., and Aléon, J. 2014. Origin of Refractory Inclusion Diversity by Turbulent Transport in the Inner Solar Nebula. In *45th Lunar and Planetary Science Conference*. (abstract #2086).

Tissandier, L., Libourel, G., and Robert, F. 2002. Gas-melt interaction and their bearing on chondrule formation. *Meteoritics & Planetary Science*, 37:1377–1389.

Tkalcec, B. J., Golabek, G. J., and Brenker, F. E. 2013. Solid-state plastic deformation in the dynamic interior of a differentiated asteroid. *Nature Geoscience*, 6:93–97.

Trigo-Rodríguez, J., Rubin, A., and Wasson, J. 2006. Non-nebular origin of dark mantles around chondrules and inclusions in cm chondrites. *Geochimica et Cosmochimica Acta*, 70:1271–1290.

Túnyi, I., Guba, P., Roth, L. E., and Timko, M. 2003. Electric discharges in the protoplanetary nebula as a source of impulse magnetic fields to promote dust aggregation. *Earth Moon Planets*, 93:65–74.

Van Kooten, E. M. M. E., Wielandt, D., Schiller, M., Nagashima, K., Thomen, A., Larsen, K. K., Olsen, M. B., Nordlund, Å., Krot, A. N., and Bizzarro, M. 2016. Isotopic evidence for primordial molecular cloud material in metal-rich carbonaceous chondrites. *Proceedings of the National Academy of Sciences*, 113: 2011–2016.

van Kooten, E. M. M. E., Moynier, F., and Agranier, A. 2019. A unifying model for the accretion of chondrules and matrix. *Proceedings of the National Academy of Sciences*, 116:18860–18866.

Villeneuve, J., Chaussidon, M., and Libourel, G. 2009. Homogeneous distribution of ^{26}al in the solar system from the mg isotopic composition of chondrules. *Science*, 325:985–988.

Villeneuve, J., Libourel, G., and Soulié, C. 2015. Relationships between type i and type ii chondrules: Implications on chondrule formation processes. *Geochimica et Cosmochimica Acta*, 160:277–305.

Wark, D. and Boynton, W. V. 2001. The formation of rims on calcium-aluminum-rich inclusions: Step I—Flash heating. *Meteoritics & Planetary Science*, 36:1135–1166.

Wark, D. and Lovering, J. 1977. Marker events in the early evolution of the solar system: Evidence from rims on Ca-Al-rich inclusions in carbonaceous chondrites. *Lunar and Planetary Science Conference Proceedings*, 1:95–112.

Warren, P. H. 2011. Stable-isotopic anomalies and the accretionary assemblage of the Earth and Mars: A subordinate role for carbonaceous chondrites. *Earth and Planetary Science Letters*, 311:93–100.

Wasson, J. T. 1996. Chondrule formation energetics and length scales. In Hewins, R. H., Jones, R. H., and Scott, E. R. D., editors, *Chondrules and the Protoplanetary Disk*, pages 45–55.

Wasson, J. T., Krot, A. N., Lee, M. S., and Rubin, A. E. 1995. Compound chondrules. *Geochimica et Cosmochimica Acta*, 59:1847–1869.

Wdowiak, T. J. 1983. Experimental investigation of electrical discharge formation of chondrules. In King, E. A., editor, *Chondrules and their origins*, pages 279–283. Lunar and Planetary Institute, Houston.

Weber, D. and Bischoff, A. 1996. Refractory inclusions in the CR chondrite Acfer 059-El Djouf 001: Petrology, chemical composition, and relationship to inclusion populations in other types of carbonaceous chondrites. *Chemie der Erde*, 57:1–24.

Weidenschilling, S. J. 1977. Aerodynamics of solid bodies in the solar nebula. *Monthly Notices of the Royal Astronomical Society*, 180:57–70.

Weidenschilling, S. J. 1977. Aerodynamics of solid bodies in the solar nebula. *Monthly Notices of the Royal Astronomical Society*, 143:57–70.

Weidenschilling, S. J. and Cuzzi, J. N. 2006. Accretion dynamics and timescales: Relation to chondrites. In *Meteorites and the Early Solar System II*, pages 473–485. The University of Arizona Press.

Weidenschilling, S. 1980. Dust to planetesimals: Settling and coagulation in the solar nebula. *Icarus*, 44: 172–189.

Weidling, R., Güttler, C., and Blum, J. 2012. Free collisions in a microgravity many-particle experiment. I. Dust aggregate sticking at low velocities. *Icarus*, 218:688–700.

Weisberg, M. K., Prinz, M., Clayton, R. N., Mayeda, T. K., Sugiura, N., Zashu, S., and Ebihara, M. 2001. A new metal-rich chondrite grouplet. *Meteoritics & Planetary Science*, 36:401–418.

Weisberg, M. K., McCoy, T. J., and Krot, A. N. 2006. Systematics and Evaluation of Meteorite Classification. In Lauretta, D. S. and McSween, H. Y., editors, *Meteorites and the Early Solar System II*, pages 19–52. University of Arizona Press.

Whipple, F. L. 1966. Chondrules: Suggestion Concerning the Origin. *Science*, 153:54–56.

Whipple, F. L. 1975. Comments. In Field, G. B. and Cameron, A. G. W., editors, *The Dusty universe: proceedings of a symposium honoring Fred Lawrence Whipple on his retirement as director of the Smithsonian Astrophysical Observatory, October 17-19, 1973*, pages 293–310. New York: N.Watson.

Wilde, F., Ogurreck, M., Greving, I., Hammel, J. U., Beckmann, F., Hipp, A., Lottermoser, L., Khokhriakov, I., Lytaev, P., Dose, T., Burmester, H., Müller, M., and Schreyer, A. 2016. Micro-CT at the imaging beamline P05 at PETRA III. *AIP Conference Proceeding*, 1741:030035.

Wood, J. A. 1963. On the origin of chondrules and chondrites. *Icarus*, 2:152–180.

Wurm, G. and Teiser, J. 2021. Understanding planet formation using microgravity experiments. *Nature Reviews Physics*, 3(6):405–421.

Zanda, B., Lewin, E., and Humayun, M. 2018. The chondritic assemblage. In Russell, S. S., Connolly Jr., H. C., and Krot, A. N., editors, *Chondrules: Records of Protoplanetary Disk Processes*, Cambridge Planetary Science, pages 122–150. Cambridge University Press.

Zhang, M., Clark, B., King, A. J., Russell, S. S., and Lin, Y. 2021. Shape and porosity of refractory inclusions in CV3 chondrites: A micro-computed tomography (µCT) study. *Meteoritics & Planetary Science*, 56: 500–514.

Zsom, A., Ormel, C. W., Güttler, C., Blum, J., and Dullemond, C. P. 2010. The outcome of protoplanetary dust growth: pebbles, boulders, or planetesimals? II. Introducing the bouncing barrier. *Astronomy & Astrophysics*, 513:A57.

CHAPTER 4

Publication I

A Chondrule Formation Experiment Aboard the ISS: Experimental Set-up and Test Experiments

ICARUS **350**:113898 (2020)

D. Spahr[a], T. E. Koch[a], D. Merges[a] A. A. Beck[a] B. Bohlender[b], J. M. Carlsson[c], O. Christ[a] S. Fujita[d], P.-T. Genzel[a] J. Kerscher[d], T. Knautz[b], M. Lindner[a] D. Mederos-Leber[a] V. Milman[c], W. Morgenroth[a] F. Wilde[e], F. E. Brenker[a,f] and B. Winkler[a]

[a]Institute of Geosciences, Goethe-Universität Frankfurt, Altenhöferallee 1, 60438 Frankfurt, Germany
[b]Institute of Applied Physics, Goethe-Universität Frankfurt, Max-von-Laue-Str. 1, 60438 Frankfurt, Germany
[c]Dassault Systèmes BIOVIA, 335 Cambridge Science Park Rd, Cambridge, United Kingdom
[d]HackerSpace FFM e.V., Ludwig-Erhard-Str. 32, 61440 Oberursel, Germany
[e]Helmholtz-Zentrum Hereon, Max-Planck Strasse 1, 21502 Geesthacht, Germany
[f]Hawai'i Institute of Geophysics and Planetology, School of Ocean and Earth Science and Technology, University of Hawai'i at Mānoa, 1680 East-West Road, Honolulu, HI 96822, USA

Abstract

The formation of chondrules in the solar nebula is still an enigmatic process. In order to reconstruct this process, we performed a chondrule formation experiment aboard the International Space Station (ISS), called EXCISS. The purpose of the EXCISS experiment is to acquire new insights in chondrule formation by "nebular lightnings". During the experiment forsterite (Mg_2SiO_4) particles were repeatedly exposed to arc discharges under long-term microgravity conditions. The purpose of this paper is to describe the experimental set-up and establish and benchmark approaches for the analysis of the samples once they are returned from the ISS. We produced aggregates of fused Mg_2SiO_4 particles in our Earth-based experiment which we studied by SEM and X-ray microtomography. The results of our preliminary Earth-based experiments indicate that the chosen experimental parameters will likely lead to melting of Mg_2SiO_4 particles and the formation of aggregates. The results from the first experiments aboard the ISS revealed that the EXCISS experiment is fully operational.

4.1 Introduction

4.1.1 Chondrules and their formation

Chondrules are small spherical objects of varying sizes which can be found in many primitive meteorites (Russel et al., 2018). While most of them have diameters in the sub-mm range, also cm-sized chondrules have been found (Weisberg et al., 2001). Chondrules belong, together with calcium-aluminium-rich inclusions, to the oldest material of our solar system. Most of the models for planet and planetesimal formation consider chondrules as the building blocks of our solar system (Russel et al., 2018). Despite their great abundance and numerous studies carried out for over 150 years, the processes leading to the formation of chondrules are still disputed controversially (Boss, 1996; Kerr, 2013; Connolly and Jones, 2016).

The textures of chondrules indicate that they crystallized from a melt. A realistic model for chondrule formation should be consistent with their typical microstructures, indicating high peak temperatures of 1600–2000 K, and fast cooling rates of 10–10 000 $\mathrm{K\,h^{-1}}$ (Libourel and Portail, 2018). Also, there is a complementarity in the distribution of refractory elements between chondrules and matrix, i.e. while chondrules and matrix have different compositions, the bulk composition is that of CI chondrites, which a realistic model should be able to explain (Hewins and Connolly, 1996; Alexander et al., 2000; Desch and Connolly Jr., 2002; Hezel and Palme, 2010; Palme et al., 2015; Budde et al., 2016; Libourel and Portail, 2018).

Most chondrule formation models assume that the formation occurred in the early solar nebula environment (Youdin and Shu, 2002; Morris et al., 2012; Johansen and Okuzumi, 2018). In the last decades, the formation of chondrules by shock waves (Connolly and Love, 1998; Ciesla and Hood, 2002) or by nebular lightnings (Whipple, 1966; Horányi et al., 1995; Desch and Cuzzi, 2000; Túnyi et al., 2003; Güttler et al., 2008; Johansen and Okuzumi, 2018) has been suggested. Alternatively, their formation by collisions of planetesimals (Krot et al., 2005; Asphaug et al., 2011; Johnson et al., 2015; Lichtenberg et al., 2018) has been proposed. The very young ages of chondrules found in CB chondrites (about 5 My younger than chondrules in CV chondrites) and their unique geochemical properties indicate that chondrules of this chondrite type might have formed at a different period and setting during the evolution of our solar system (Krot et al., 2005).

The main strength of the "nebular lightning" theory is the explanation of the inferred fast cooling rates and the strongly varying thermal histories of different chondrules in the same meteorite sample. It is, however, uncertain if lightnings occurred in the solar nebula, and it has been debated whether they have provided enough energy to melt mm-sized particles. Recently, Johansen and Okuzumi (2018) published a study where they conclude that the escape of positrons released in the decay of the short-lived radionuclide ^{26}Al would lead to charging of dust particles in the solar nebula, which would discharge through lightnings. The amount of energy in this case would be sufficient to melt almost all chondrules.

Figure 4.1 shows a schematic illustration of a possible chondrule formation process in the solar nebula by several heating events according to Scott (2007). The suggested multiple heatings may have been caused by lightnings.

4.1.2 Previous chondrule formation experiments

The number of experiments studying chondrule formation is rather limited (Wdowiak, 1996; Lofgren, 1996; Connolly et al., 1998; Hewins et al., 2000; Hewins and Fox, 2004; Güttler et al., 2008; Morlok et al., 2012; Imae and Isobe, 2017). Most of the experimental work focused on changes of textural and geochemical properties as a function of cooling rates (Lofgren, 1996; Connolly et al., 1998; Hewins and Fox, 2004). These experiments reproduced many prop-

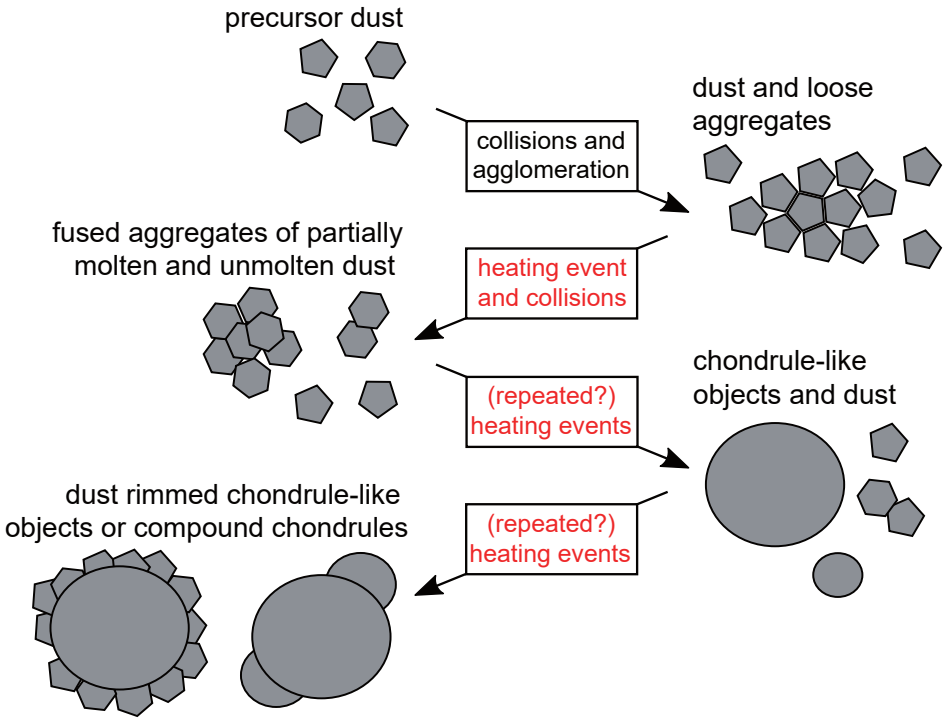

Figure 4.1: Schematic illustration of the chondrule formation process. Dust particles were exposed to several electrical discharges. The chondrules grow by agglomeration and (partial-)melting of agglomerated particles (adopted from Scott, 2007).

erties of chondrules, but of course suffered from the influence of gravity. Wdowiak (1996) was the first to expose chondrules from the Allende meteorite to lightnings, while Güttler et al. (2008) subjected dust aggregates to electrical discharges. Both experimental studies did not show compelling evidence for the formation of chondrules due to lightning, but the relevance of these findings is limited due to the influence of gravity and the specific experimental parameters (e.g. energy, duration of the lightnings, gas pressure), which preclude a generalisation of their results. Morlok et al. (2012) accelerated a mixture of silicate, sulphide and metal particles (100–500 µm) into a fixed arc plasma, thus studying the role of heated gas produced by a shock wave. The experiment produced a small amount of round, molten objects of different phases with diameters ranging from a few microns to about 100 µm.

4.1.3 Preparation of the EXCISS experiment

Our experiment is designed to study the behavior of Mg_2SiO_4 (forsterite) particles in a long-term microgravity environment aboard the ISS while they are exposed to repeated arc discharges. Forsterite was chosen as it is the most abundant mineral phase in natural chondrules (Russel et al., 2018). Here we describe the development of the experimental set-up, first laboratory-based experiments, aimed to establish optimal parameters for the ISS-based experiments, and the sample characterization. While our experiments resemble those of Güttler et al. (2008), we assume that by using energies lower by two orders of magnitude and substantially longer duration of the arc discharges we will avoid the fragmentation of aggregates, but will rather observe their fusion. Because of the microgravity conditions aboard the ISS, the particles can move, collide and fuse induced only by the lightning and its radiation without the influence of gravity or a directed movement caused by e.g. a gas flow. The experimental set-up described below fulfills all NASA safety requirements. Sample characterization

included Raman spectroscopy, X-ray powder diffraction, scanning electron microscopy and synchrotron based X-ray microtomography. We also studied natural porphyric chondrules in order to demonstrate that it is possible to visualize the inner structure of chondrules.

4.2 Experimental

4.2.1 Sample preparation

We used two types of sample material in our experiments, namely synthetic forsterite and natural chondrules.

Synthetic forsterite

We synthesized Mg_2SiO_4 pellets from the oxides as sample material. They were ground mechanically for a few seconds in an agate mortar. The resulting powder was elutriated with distilled water to remove particles with a grain size much smaller than 80 µm. After drying the powder in an oven at atmospheric conditions at 353 ± 1 K it was sifted with sieves having 80 µm and 120 µm mesh size respectively. The particles which passed through the 120 µm but not the 80 µm sieve were used for the experiment. The sample material was finally washed with isopropyl alcohol and dried again. The melting point of the forsterite end-member is approx. 2200 K (Bowen and Schairer, 1925).

Natural chondrules

Individual chondrules were separated from a fragment of the carbonaceous chondrite Allende (CV3) (Clarke Jr. et al., 1971). We used the high-voltage electrical pulse fragmentation system selFrag-Lab from Ammann Schweiz AG to crush the chondrite fragment. The electrical pulse fragmentation technique allows to separate components of rocks along their grain boundaries without being abrasive. The selected chondrite fragment had a dimension of $1 \times 1 \times 0.5\,cm^3$. It was placed on a sieve in a vessel filled with water, so the fragmented sample material could sink down and would not be exposed to further discharges. We used a pulse voltage of 110 kV with a repetition rate of 5 Hz for 10 seconds. The distance between both electrodes was 15 mm. The suspension was filtered and the retrieved fragments were dried at 353 ± 1 K.

4.2.2 Sample characterization

Powder diffraction and Raman spectroscopy

The synthetic Mg_2SiO_4 powder was analyzed by X-ray powder diffraction with a PANalytical X'Pert Pro powder diffractometer in Bragg–Brentano geometry. We used a PANalytical PIXcel^{3D} detector and a X-ray tube with a copper anode in combination with a Johansson monochromator to obtain Cu $K_{\alpha 1}$ radiation. All instrument parameters were obtained by measuring and refining a Si-standard (99.999% purity). The sample measurements were performed with 1/4° fixed divergence slits in a range of $10° < 2\Theta < 110°$ with a scan speed of 0.04° min^{-1} on an oriented Si single crystal sample holder. Rietveld refinement (Rietveld, 1969) was carried out using the software package GSAS-II (Toby and Von Dreele, 2013).

The Mg_2SiO_4 powder was further characterized by Raman spectroscopy with a set-up described in Bayarjargal et al. (2018). The set-up consists of an OXXIUS S.A. LaserBoxx

LMX532 laser ($\lambda = 532.14\,\text{nm}$) and a Pixis256E CCD camera mounted on a Princeton Instruments ACTON SpectraPro 2300i spectrograph. Theoretical Raman spectra were calculated by DFT-based model calculations using the CASTEP-package (Clark et al., 2005).

Scanning electron microscopy

Scanning electron microscopy (SEM) was performed with a Phenom World ProX desktop SEM using an electron backscatter detector (BSE). Energy dispersive X-ray spectroscopy (EDX) was carried out with an integrated silicon drift detector for a semi-quantitative characterization of the composition. The samples were mounted without coating using sticky carbon tape on aluminum stubs. They were measured under low vacuum conditions to reduce charging effects on the sample. For imaging we used an acceleration voltage of 10 kV while for EDX analysis a voltage of 15 kV was employed. Multiple BSE images were acquired with different focal planes and combined afterwards with the Helicon Focus 7 Pro (Kozub et al., 2018) software from Helicon Soft to obtain images with an improved depth of field using the depth map rendering method with radius 8 (size of the analysed area around each pixel) and smoothing 4 (value determines how depth map will be smoothed out). EDX data were analyzed using the Phenom Pro Suite software.

Synchrotron-based microtomography

Synchrotron-based microtomography was performed at PETRA III (DESY) in Hamburg, Germany. All data were collected on the micro tomography beamline P05 (Wilde et al., 2016; Ogurreck et al., 2013), operated by Helmholtz-Zentrum Geesthacht, using a 15 keV beam monochromatized by a double crystal monochromator. The images were acquired using a 24× objective lens with a CMOS camera resulting in a $1.8 \times 1.8\ \text{mm}^2$ field of view. We used an acquisition time of 350 ms. A binning factor of 2×2 pixel resulted in a binned pixel size of approx. $0.61 \times 0.61\ \mu\text{m}^2$. The Mg_2SiO_4 particles and the experimental products from the discharge experiments were embedded in two component epoxy adhesive UHU Plus Endfest 300 placed on 50 µm Kapton foil. The epoxy was cured under vacuum by heating it up to 333 ± 2 K. The Kapton foil was glued with Henkel LOCTITE 493 on the sample holder. The natural chondrules were directly mounted with LOCTITE 493. Data pre-processing, including tomographic reconstruction was performed using MATLAB scripts provided by Moosmann et al. (2014). The microtomography reconstructions were visualized with the volume exploration software tool Drishti (Limaye, 2012).

4.3 Experimental set-up

We designed two different experimental set-ups, one for Earth-based experiments (sample chamber type I) and one for ISS-based experiments (sample chamber type II). Both set-ups allowed us to expose Mg_2SiO_4 particles to arc discharges. The experiments on Earth were carried out to design and calibrate the experimental set-up for the ISS experiment. A list of materials (Table 4.1) and figures of the experimental set-up can be found in the supplementary material section. Further, a detailed description of the calibration of the experimental set-up is provided there.

4.3.1 Sample chamber I

Sample chamber I (Fig. 4.14) was designed to allow a variation of the experimental conditions, such as gas composition and pressure or electrode material and shape. It consists of two

KF-16 cross vacuum flanges connected to a vacuum pump and a gas supply. We used two different types of electrodes, W-electrodes similar to the ISS experiment (Fig. 4.16) and Cu-electrodes to allow a spectroscopic determination of the plasma temperature. Their distance was adjusted to be approx. 3 mm. Optical characterization of the arc discharge was enabled by a transparent window. Most experiments were carried out in a 100 ± 1 mbar Ar atmosphere. A Ar/H_2 gas mixture at the same pressure was used for the temperature and electron density measurements. The forsterite dust particles were placed inside a 5 mm quartz glass tube mounted between the tips of the electrodes for the melting experiments.

4.3.2 Sample chamber II

Sample chambers of type II (Fig. 4.15, Fig. 4.2 left) made of quartz glass were developed for the ISS-based experiment. W-electrodes were embedded into the glass on opposite sides with approx.2–3 mm distance between the tips. A vacuum tight connection between electrodes and glass was achieved by a copper galvanization of the electrodes' surface. The Ar gas pressure inside the sample chambers was adjusted to be 100 ± 1 mbar before sealing. They were loaded with 30 ± 1 mg of synthetic Mg_2SiO_4 particles.

4.3.3 Arc discharge generation

The experimental set-ups of the Earth-based and ISS-based experiments are very similar. The differences will be explained in the subsequent sections. Figure 4.17 shows a schematic illustration of sample chamber I and a simplified circuit which includes the most relevant parts of the arc generation unit.

In order to meet the severe constraints for the ISS-based experiment (e.g. NASA safety requirements, limited space, power supply etc.), we developed an electronic circuit with a two-stage process to generate arc discharges. A DC-DC converter charges three parallel capacitors ($C_{arc} \mathrel{\widehat{=}} 450\,\mu F$). An ignition coil is protected from the charging voltage of C_{arc} by the diode D_{spark}. After C_{arc} has reached the target voltage, the ignition coil generates a high voltage peak up to 8 kV and produces an ionized channel between the electrodes (ignition spark). Diode D_{spark} becomes conductive while D_{arc} protects C_{arc} from the high voltage peak. After the electrical breakdown the voltage decreases instantaneously. When the voltage has dropped below the charging voltage of C_{arc}, the energy stored in C_{arc} is released into the existing ionized channel, causing a high energetic arc discharge. Figure 4.18 shows the arc generation unit used for the laboratory experiments on Earth. The circuit diagrams and the components will be available on GitHub

4.3.4 Discharge characterization

The discharges were characterized using the Earth-based experiment. We used a Tektronix TDS 2024B oscilloscope to measure current and voltage in order to quantify the energy of the arc discharges. A Testec TT-SI 50 10:1 test probe was connected to a 10 mΩ shunt in series with the spark gap for current measurements. The voltage across the gap was measured with a Testec HVP-15HF 1000:1 test probe and the charging voltage of the capacitor was measured with a Testec TT-SI 51 100:1 test probe. The configuration of the test probes is illustrated in Figure 4.17.

We used an ACTON SpectraPro 2500i spectrograph equipped with a Pixis256E CCD camera to measure the Cu-I emission lines from the electrodes and the H_β emission lines from the Ar/H_2 plasma in the sample chamber I. The spectrograph was connected with a 200 µm optical fiber to the window of sample chamber I.

We employed a pco.dimax HD camera for high-speed video recording of the arc discharge with a frame rate of 20 000 fps and a resolution of 288 × 248 pixel. Long-time exposure photography of the arc discharge was performed with a Nikon D7200 single-lens reflex camera.

4.3.5 Experimental set-up for the ISS-based experiments

The experiment aboard the ISS was carried out inside a 1.5 U NanoRacks NanoLab (e.g., Brisset et al., 2017). Figure 4.2 shows the NanoRacks NanoLab with a dimension of approx. $10 \times 10 \times 15\,\mathrm{cm}^3$ and the different components of the experimental set-up. This set-up is equipped with a sample chamber of type II loaded with 30 ± 1 mg of Mg_2SiO_4 particles. A camera in combination with a 2.5× objective and a tube lens was utilized to monitor the particle distribution, movement and interaction with the arc discharges and to inspect the condition of the electrodes aboard the ISS. The video recording was controlled by a Raspberry Pi Zero. All optical components were mounted on a microbench system and the focus was adjusted to the tip of the pointed electrode. The sample chamber was illuminated with one LED from the front and one from the back. The field of view (Fig. 4.16) is approx.$2.73 \times 3.63\,\mathrm{mm}^2$ with a resolution of 1640 × 1232 pixel when a 2 × 2 pixel binning is employed. Videos were recorded with a frame rate of 40 fps. The custom designed power supply unit was equipped with four lithium-ion batteries. The PCB design and the software developed here will be available on GitHub.

The NanoLab is connected with an USB3 B port (5 V, 900 mA) to the NanoRacks rack aboard the ISS for power supply and data transfer. We configured two 256 GB USB mass storage devices for redundant long-time data storage and a single 64 GB mass storage device for data transfer between our set-up and the NanoRacks rack. The experiment was designed to operate autonomously.

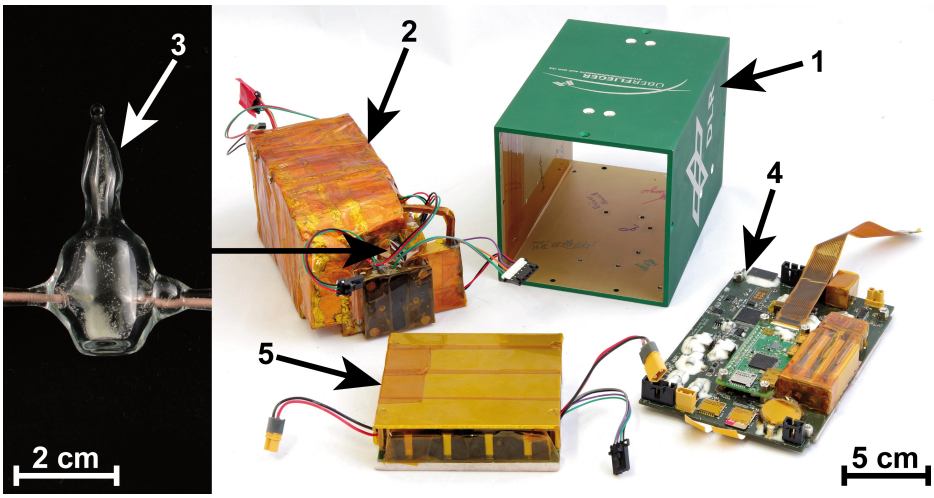

Figure 4.2: Experimental set-up of the ISS-based experiment with NanoRacks NanoLab housing (1), arc generation unit and Raspberry PI camera with optics (2), a sample chamber of type II (3), EXCISS mainboard with Raspberry Pi Zero and mass storage devices (4) and power supply unit with lithium-ion batteries (5).

4.3.6 Calibrating the experimental set-up

Energy of the arc discharge

The arc discharge generation in our sample chamber is initiated by an ignition spark (Fig. 4.3, $t = 0\,\mu s$) with a breakdown voltage of approx. 6–8 kV. The generation of an ignition spark takes approx. 4 µs (Fig. 4.19). The duration of the ignition spark is much shorter than the duration of the following arc discharge and the voltage maximum is two orders of magnitude higher than the burning voltage of the arc discharge. The energy released during the ignition spark can be neglected.

The energy released into the arc discharge in the ISS-based experiment can be varied between approx. 3.1–21 J (150–450 V) and for the Earth-based experiment between approx. 2.6–17 J. The energy of the arc discharge reaches its maximum approx. 5–10 µs after the ignition spark. At this time the voltage is decreasing from the charging voltage to the burning voltage of the arc (usually 60–80 V, see Fig. 4.20). The duration of an arc discharge varies between 400 µs and 600 µs. We adjusted the arc discharge to an energy level which was sufficient to melt and fuse the Mg_2SiO_4 particles, without wearing the electrodes down strongly. Figure 4.3 shows frames recorded by a high-speed camera of the arc discharge. The time interval between the frames is 50 µs and the first frame shows the weak ignition spark. In order to ensure the transferability of parameters between the different types of

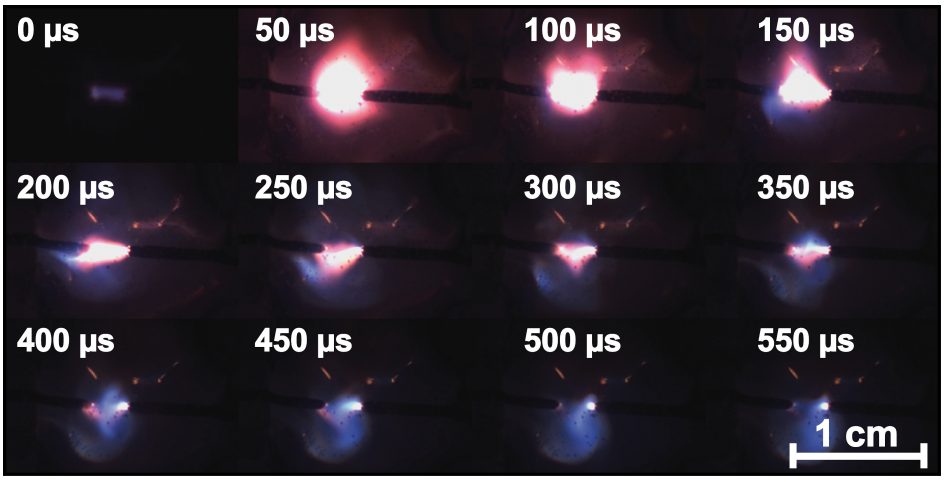

Figure 4.3: High-speed photographs of an arc discharge where the capacitors were charged to 450 V. Picture one (0 µs) shows the weak ignition spark.

sample chambers and the ISS- and Earth-based-laboratory set-ups, we performed discharge experiments as a function of charging voltages (Fig. 4.21). The calibration enables us to approximate the energy released into an arc discharge aboard the ISS for different voltages.

Electron density and temperature of the arc discharge

In addition to its energy the arc discharge can be characterized by its electron density n_e and temperature T_e. In the desired range of operation we determined an electron density of $n_e = 1.6(1) \times 1 \times 10^{-16}\,cm^3$ to $2.0(1) \times 1 \times 10^{-16}\,cm^3$ and an electron temperature of $k_B T_e \approx 6900 \pm 1000\,K$ (Fig. 4.23).

4.4 Results & Discussion

4.4.1 Characterization of the starting material

X-ray powder diffraction

The phase purity of the synthetic Mg_2SiO_4 powder was confirmed by Rietveld refinement and no secondary phase was detected within the experimental error limits of approx. 3% (Fig. 4.4). The diffraction pattern also shows that the sample material is very well crystallized.

The results of the Rietveld refinement are listed in the supplementary material section (Table S2). The refinement data confirmed the established structural model of forsterite (Cernik et al., 1990).

Raman spectroscopy

Powder Raman spectroscopy was performed on the Mg_2SiO_4 particles. The experimental Raman spectra are in very good agreement with theoretical data from DFT calculations (Fig. 4.5).

Based on the DFT-based calculations we were able to assign irreducible representations to all observed peaks. Following the factor group analysis (DeAngelis et al., 1972) 36 modes can be Raman active ($\Gamma_{\mathrm{Raman}} = 11A_g + 11B_{1g} + 7B_{2g} + 7B_{3g}$) and we observed all A_g modes experimentally. The experimental Raman data also confirmed the very good crystallinity of the Mg_2SiO_4 powder as the Raman peaks did not show any broadening.

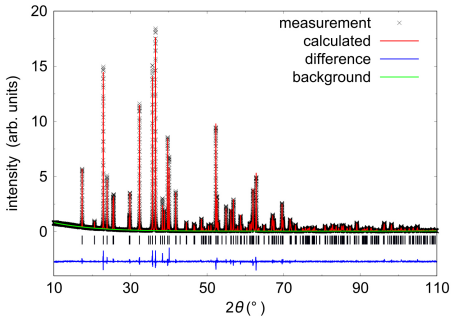

Figure 4.4: Rietveld refinement of synthetic Mg_2SiO_4 powder. The differences between measurement and refinement are represented by the blue line. The Bragg positions are indicated by tick marks.

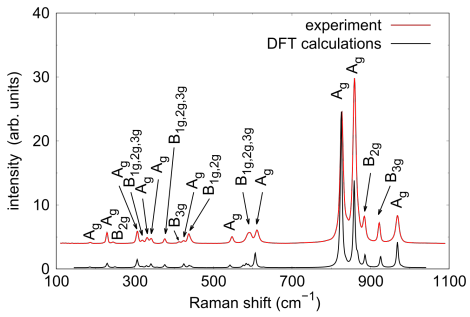

Figure 4.5: Experimental Raman spectra of synthetic Mg_2SiO_4 grains in comparison to DFT calculations for forsterite. The DFT spectrum was scaled by 5%. All Raman modes were assigned to irreducible representations.

SEM

The size, shape and micro-structure of the Mg_2SiO_4 grains before exposing them to arc discharges were examined by scanning electron microscopy. The SEM images confirm that all grains of the starting material with a diameter of $<80 \times 80\,\mu m^2$ and a diameter of $>120 \times 120\,\mu m^2$ were sorted out during the sample preparation (Fig. 4.6). The length of the third axis can differ from the range.

The Mg_2SiO_4 grains show an irregular shape and fractured surfaces. Some grains have approximately flat surfaces (Fig. 4.7a), while others have a rough surface (Fig. 4.7b). Furthermore, the roughness of the surface and the clearly visible cavities in the particles suggest that the grains are highly porous.

We confirmed the expected chemical composition of the Mg_2SiO_4 grains by EDX analysis (nominal vs. EDX in atom %): MgO: 66.7/68(5) and SiO_2: 33.3/32(2). No other elements were detected within experimental uncertainties.

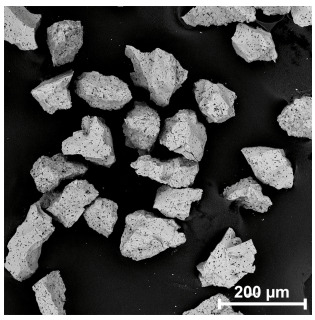

Figure 4.6: SEM image of multiple Mg_2SiO_4 grains after the sample preparation process.

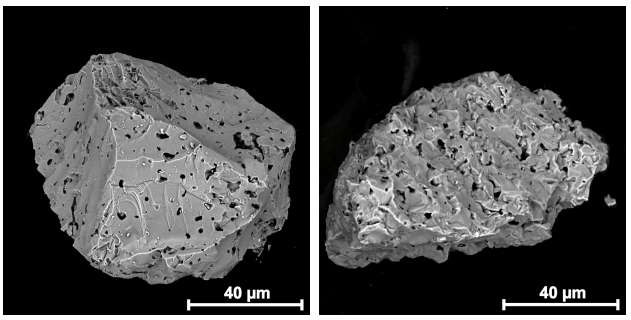

Figure 4.7: Close-up SEM images of Mg_2SiO_4 grains after the sample preparation process: Mg_2SiO_4 grain with flat surfaces (left) and grain with a rough surface (right).

X-ray microtomography

X-ray microtomography (CT) was performed on the starting material. The results show no density differences inside the Mg_2SiO_4 grains, which confirms the chemical homogeneity of the grains. Furthermore, the microtomography also confirms the porosity of the Mg_2SiO_4 grains (Fig. 4.8).

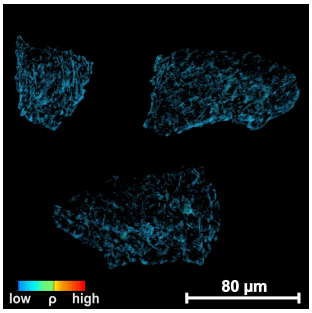

Figure 4.8: Synchrotron microtomography image of three Mg_2SiO_4 grains after the sample preparation process.

4.4.2 Aggregates formed by arc discharges

SEM analysis

We used both sample chambers to expose the Mg_2SiO_4 grains to arc discharges on Earth in order to estimate the energy which is sufficient to melt and fuse Mg_2SiO_4 particles. In sample chamber of type II the particles were located at the bottom of the chamber close to the electrodes and the turbulence of the arc discharge led to floating particles.

We were able to partially melt and fuse Mg_2SiO_4 grains and form aggregates of several grains by arc discharges in sample chamber I and II on Earth. The first melting and aggregation of Mg_2SiO_4 particles occurred in experiments with a charging voltage of 350 V (approx. 11 J). The SEM image (Fig. 4.9a shows a representative fused aggregate of Mg_2SiO_4 particles. The surface of the particles of the aggregate is much smoother and homogeneous,

the cavities in the surface and the sharp edges have disappeared. Figure 4.9b shows a close-up where the molten areas between the fused single grains can be clearly identified. Grain boundaries between the Mg_2SiO_4 particles cannot be identified any more. Figure 4.9c shows a small Mg_2SiO_4 melt droplet between unmolten grains. The surface of the nearly spherical melt droplet is smooth. We studied the aggregates by EDX map analysis to ensure that the Mg_2SiO_4 particles are not welded together by sputtered material from the electrode. The EDX spectra showed the absence of any tungsten contamination from the electrodes. An example of a tungsten contamination found in another aggregate is shown in Figure 4.9d. A molten tungsten particle from the electrodes impacted into Mg_2SiO_4 particles and lead to aggregate formation.

The number of aggregated particles increased with the charging voltage, but the erosion of the electrodes and the contamination of the sample material also increased. EDX analysis clearly shows an enhanced tungsten contamination at higher charging voltages of C_{arc} (450 V to 550 V).

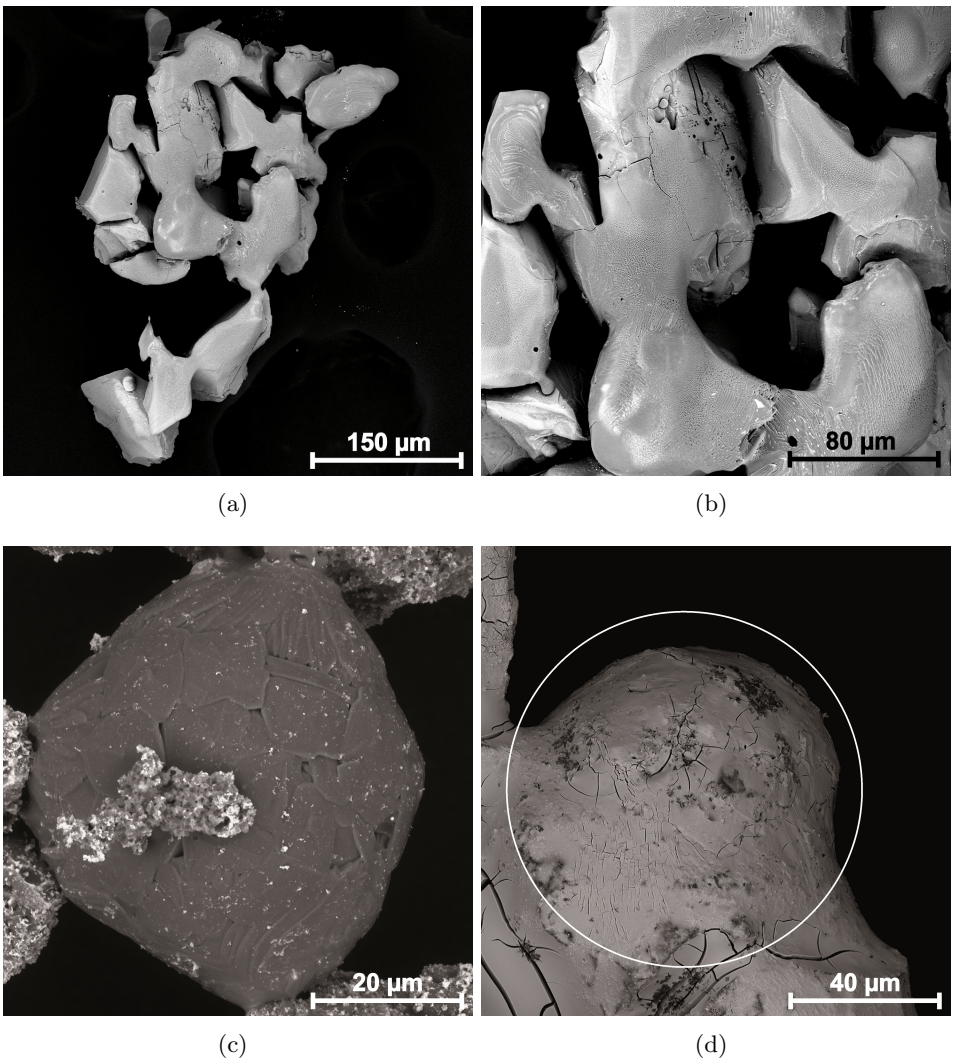

(a) (b)

(c) (d)

Figure 4.9: SEM image of an aggregate formed by fusion of multiple Mg_2SiO_4 grains with lower (*a*) and higher (*b*) magnification. The particles were exposed to several discharges with 450 V (approx. 22 J) in sample chamber II on Earth. Melt droplet between unmolten Mg_2SiO_4 grains (*c*) and impact of a tungsten particle from the electrodes (white circle) into Mg_2SiO_4 grains (*d*).

X-ray microtomography

We used microtomography to study the grain-grain contacts of the fused aggregates (Fig. 4.10). Figure 4.10a shows the contact of an elongated and partially molten grain to another unmolten Mg_2SiO_4 particle. The surface of the partially molten grain is rounded and the molten regions show a slightly higher density than the rest of the grain, especially in the contact area to the other grain. We observed no heavy element contamination in the surface area of the particles.

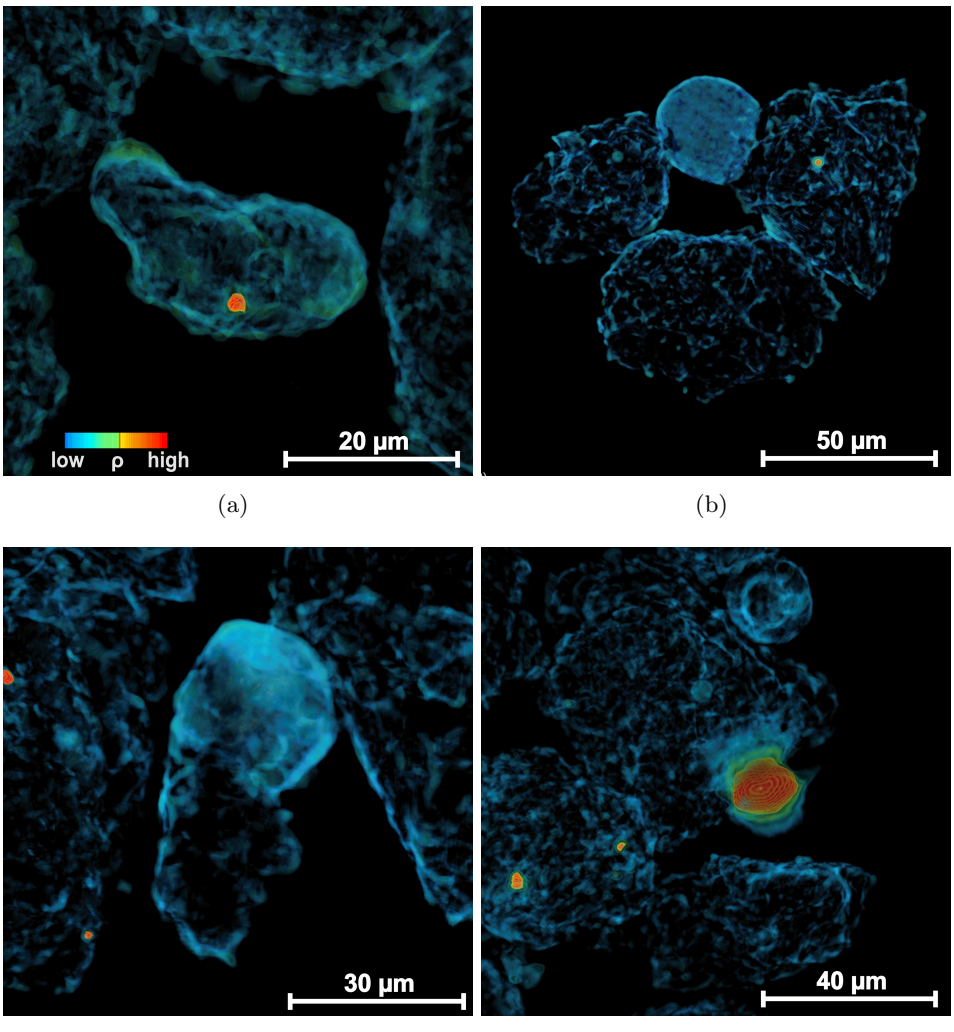

(a) (b)

(c) (d)

Figure 4.10: Synchrotron microtomography images of the fused aggregates obtained by Earth-based experiments: contact point between two grains (*a*), melt droplet between fused Mg_2SiO_4 grains (*b*), partially molten Mg_2SiO_4 grain fused to an aggregate (*c*) and melt droplet with heavy element contamination, probably tungsten from the electrodes (*d*).

Figures 4.10b and c show melt droplets with a size between 30–60 µm which fuse Mg_2SiO_4 precursor grains together. The microtomography images reveal that these melt droplets are less porous than the initial grains, based on the density contrast in comparison to the unmolten particles. Furthermore, the surface of the melt droplets is smoothed. Figure 4.10d shows a close-up of an aggregate with a Mg_2SiO_4 melt droplet and heavy element contamination (probably tungsten from the electrodes). We could clearly identify whether fused

aggregates were formed due to the impact of molten tungsten particles from the electrodes or by the arc discharge.

4.4.3 X-ray microtomography on natural chondrules

We studied two different types of chondrules from the Allende meteorite by X-ray microtomography to allow a comparison between the samples produced by arc discharges and natural chondrules. The first chondrule has a diameter of about approx. 935 µm and is nearly spherical with a flat side (Fig. 4.11). The chondrule shows a porphyric texture with grain diameters from 48 µm to 196 µm. The grain size increases towards the edges. Metal inclusions are rare and have diameters of less than 40 µm. The structure of these porphyric chondrules is caused by incomplete melting of the chondrule precursors (Connolly et al., 1998; Lofgren, 1996).

The second chondrule represents a compound chondrule (Fig. 4.12). Compound chondrules consist of two chondrules fused together and represent 4–5% of all chondrules (Gooding and Keil, 1981). This material is of special interest for our studies as the interfaces between the single chondrules of a compound chondrule can provide information about the temperature and velocities during their fusion. Whether or not collisions of liquid or cooled chondrules lead to the formation of compound chondrules is still discussed controversially (Hubbard, 2015; Arakawa and Nakamoto, 2016).

In the studied compound chondrule, the dominant chondrule has a diameter of 250 µm, while the small one has a size of approx. 95 µm. The dominant chondrule shows two regions with distinct textures. The predominant texture type of the chondrule is porphyric. The small chondrule and the interstitial region between the two primary chondrules have a texture typical for a quickly quenched melt. Furthermore, the main chondrule contains a significant amount of spherical metallic inclusions with diameters up to approx. 44 µm.

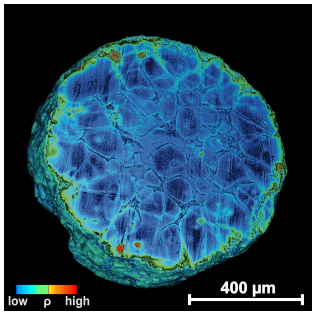

Figure 4.11: Virtual slice through a single porphyric chondrule obtained by synchrotron microtomography. The chondrule was separated from the Allende meteorite by the selFrag technique.

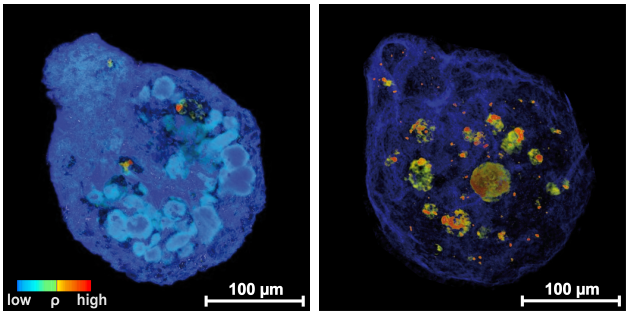

Figure 4.12: Visualization of a microtomography scan of a compound chondrule separated from the Allende meteorite by the selFrag technique: texture of the silicate crystals inside the chondrule (*a*) and transparency adjusted to visualize the metallic inclusions (*b*).

4.4.4 Start of the experiments aboard the ISS

The experiment was initially activated on November 27th 2018 and communication in the daily data transfer time window was possible. In the first weeks we were able to obtain preliminary image and video data which confirmed that we can operate the camera and the micro computers remotely. In addition, we performed ignition sparks without charging the capacitors to test our arc generation unit (Fig. 4.13). Furthermore, the log files showed that

the power supply aboard the ISS worked as planned. Consequently the received images, videos and log files confirmed that the experimental set-up was fully operational.

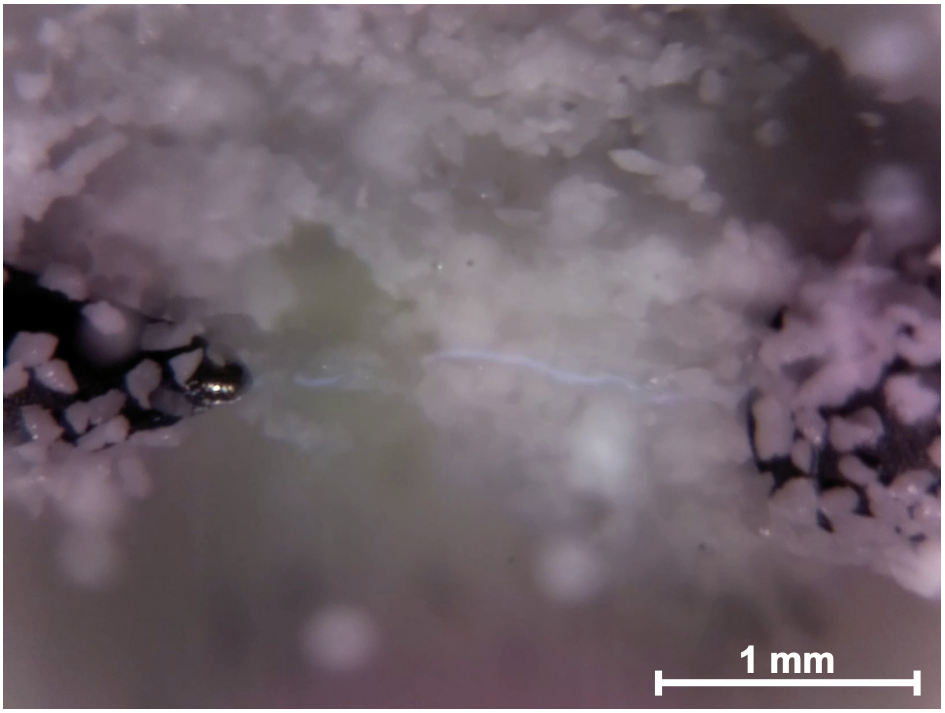

Figure 4.13: Ignition spark between the electrodes in sample chamber II aboard the ISS, without charging C_{arc}. Agglomerated Mg_2SiO_4 particles are levitating between the electrodes and many particles are sticking on the electrodes. Field of view with a resolution of 1640×1232 pixel.

4.5 Conclusion & Outlook

We have developed an experimental set-up for a chondrule formation experiment aboard the ISS to investigate if chondrule formation via nebular lightning is a viable process. With our laboratory-based experiments on Earth we were able to find appropriate experimental settings for the experiment aboard the ISS. We will start the experiments aboard the ISS with an energy of approx. 2.6 J (150 V) and afterwards increase the released energy to 13–21 J (350–450 V) which was appropriate to fuse and melt particles in the Earth-based test experiments. Therefore, while our experiments resemble those of Güttler et al. (2008), we anticipate that by using energies lower by two orders of magnitude and substantially longer duration of the arc discharges we will avoid the fragmentation of aggregates, but will rather observe the fusion of freely floating particles.

We have established benchmarks for the characterization of the samples once they have been returned, and shown that synchrotron-based microtomography data are very well suited to detect the density difference due to partial melting. The CT images obtained from the natural Allende chondrules clearly show their complex inner structure and we therefore anticipate that we will be able to study our synthetic samples in similar detail.

The preliminary images received from the ISS show that Mg_2SiO_4 particles agglomerate and accumulate between electrodes in microgravity. While finalizing this manuscript, we performed about 80 electrical discharges aboard the ISS and acquired approximately 16 hours of video material and 15000 pictures. Sample return was scheduled with SpaceX CRS-17 and took place on the 3rd June 2019. The samples are now studied with the techniques described

above and will then be compared to the results of the laboratory-based experiments on Earth and a variety of natural chondrules.

Acknowledgements

We gratefully acknowledge the technical help from the HackerSpace FFM e. V., Rainer Haseitl and Solveigh Matthies. Furthermore, we acknowledge Prof. Horst Marschall for access to the selFrag system. We are grateful for the technical help from Dr. Marcus Iberler and the whole Institute of Applied Physics (Plasmaphysics) Frankfurt of Prof. J. Jacoby. The authors are grateful for financial support by the Dr. Rolf M. Schwiete Stiftung, DFG (Wi1232/44-1), the BMWi (50JR1704), the the BMBF (05K16RFB), the German Aerospace Center (DLR), ZEISS, BIOVIA, DreamUp, NanoRacks and Nordlicht. We acknowledge DESY (Hamburg, Germany), a member of the Helmholtz Association HGF, for the provision of experimental facilities. Parts of this research were carried out at PETRA III.

4.6 Supplementary Material

4.6.1 Experimental set-up

Insulation in the ISS-based experiment

The heat radiating and vibration-sensitive components on all PCBs were covered with thermally conductive epoxy and the PCB surfaces were conformally coated so that no conductor was left exposed. The bottom of the PCBs were covered with thermal conductive pads to ensure a heat transfer from the PCBs to the chassis. All parts in the arc discharge generation unit were insulated with epoxy adhesive. Further conducting surfaces in the experimental set-up were covered with Kapton for insulation. Table 4.1 shows the specific material information.

Sample chamber I and II

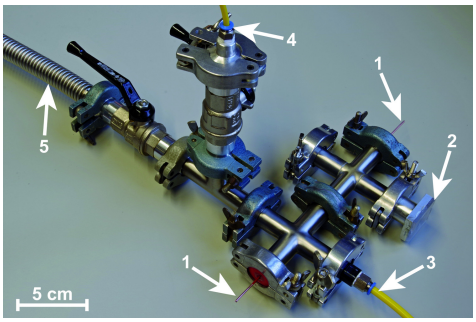

Figure 4.14: Sample chamber I with electrodes (1), polycarbonate glass window (2), connection to manometer (3), gas purge (4) and connection to vacuum pump (5).

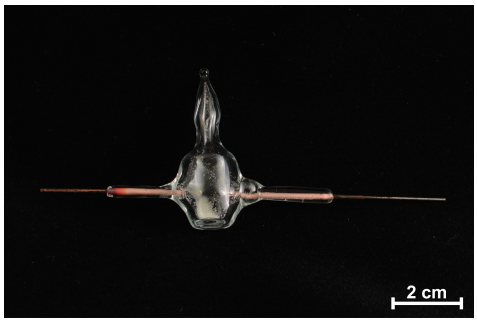

Figure 4.15: A sample chamber of type II made of quartz glass and manufactured by Nordlicht GmbH. Two W-electrodes are embedded into the glass on opposite sides, one is pointed while one is rounded. The sample chamber is loaded with 30 mg Mg_2SiO_4 particles.

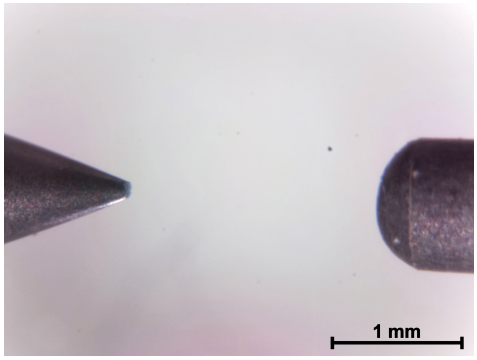

Figure 4.16: Field of view in sample chamber of type II mounted in the ISS-based experiment with a resolution of 1640 × 1232 pixel. Two W-electrodes are embedded on opposite sides with a distance of approx. 2 mm.

Discharge generation

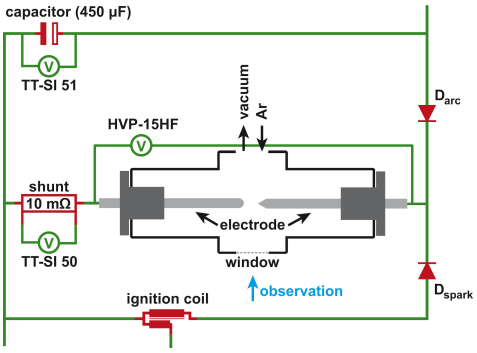

Figure 4.17: Schematic illustration of the most relevant parts of the arc generation unit connected to sample chamber I.

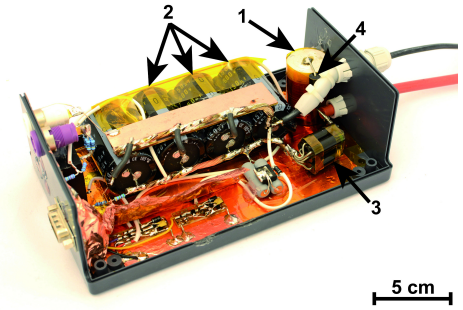

Figure 4.18: Arc generation unit in an enclosure for the laboratory experiment on Earth with three connected capacitors in parallel (C_{arc}) (1), ignition coil (2), diodes D_{arc} (3) and D_{spark} (4).

List of materials

Table 4.1: List of the main materials used in the different parts of experimental set-up: sample chambers, arc discharge generation and in the ISS-based experiment.

component	manufacturer	type
sample chamber		
W-electrodes	Technolit GmbH	Wigstar Longlife (1 mm)
electrode mount	custom made	polyoxymethylene lid
glass window	custom made	polycarbonate glass
manometer	GHM GROUP — Greisinger	HMH 3100
gas	Messer Group GmbH	CANGas Argon 5.0
gas	Messer Group GmbH	CANGas 2% H_2 in Ar
sample chamber II	Nordlicht GmbH	-
arc discharge generation		
DC-DC converter	XP Power GmbH	G06
capacitor C_{arc}	Nichicon Corporation	4 × LGN2X151MELB5 (150 µF)
diode D_{spark}	Diotec Semiconductor AG	BY16
diode D_{arc}	Diotec Semiconductor AG	6 × BY16
ignition coil	Paaschburg & Wunderlich GmbH	4054783027989
ISS-based experiment		
camera	Raspberry Pi Foundation	Raspberry Pi Camera v2.1
single-board computer	Raspberry Pi Foundation	Raspberry Pi Zero
objective	Carl Zeiss AG	EC Epiplan Neofluar 2.5×/0.06
microbench system	Qioptiq Photonics GmbH	LINOS
LED	LUMITRONIX GmbH	CreeXM-L2T2
lithium-ion batteries	LG Electronics Inc.	INR18650MJ1
thermally conductive epoxy	3M Company	TC-2810
epoxy adhesive	3M Company	EC-2216
Kapton tape	3M Company	polyimide film tape 5413
conformal coating	Dow Corning Inc.	3145 RTV
thermal pads	The Bergquist Company Inc.	Gap Pad VO Ultra Soft

4.6.2 Calibration of the set-up

Ignition spark

The energy released during an ignition spark is negligible in comparison to the energy released in an arc discharge due to the low current and its very short duration.

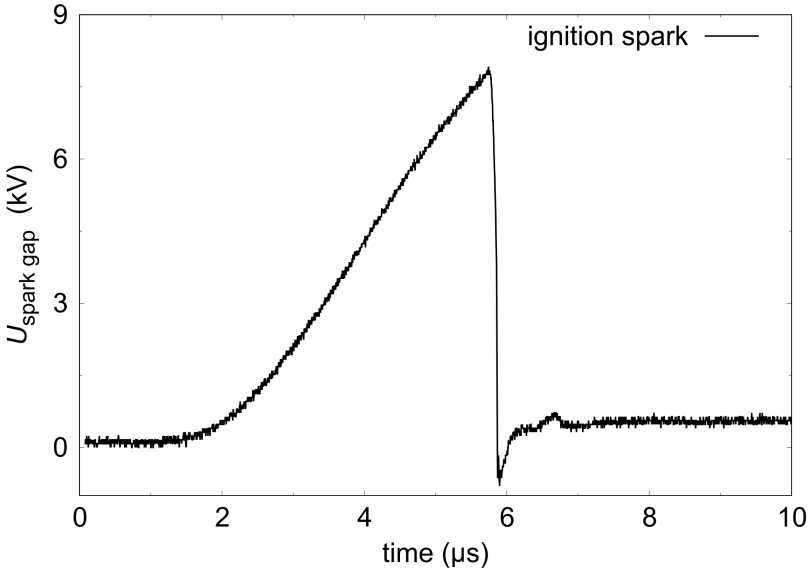

Figure 4.19: Voltage measurement of an ignition spark between the electrodes in sample chamber I.

Energy of the arc discharge

The energy and duration of the arc discharge can be varied by several parameters. The main parameters to adjust the energy of the arc discharge are the capacitance of C_{arc}, its charging voltage and the gas pressure in the sample chamber. A higher argon pressure leads to a higher charge carrier density in the arc. The energy stored in a capacitor ($W_{C_{arc}}$) can be described by equation (4.1), where C is the capacitance of C_{arc} and V its charging voltage. The stored energy increases quadratically with the charging voltage. Our experimental set-up allows discharges with $W_{C_{arc}}$ between approx. 2.3 J (100 V) and 68 J (550 V).

$$W_{C_{arc}} = \frac{1}{2} \cdot C \cdot V^2 \tag{4.1}$$

The energy released into an arc discharge ($W_{t_1-t_2}$) can be calculated from the time-dependent change of the current I and voltage U during the arc discharge using equation (4.2).

$$W_{t_1-t_2} = \int_{t_1}^{t_2} U \cdot I \mathrm{d}t \tag{4.2}$$

Figure 4.20 shows the voltage between and the current through the electrodes in the sample chamber I during an ignition where C_{arc} was charged to 450 V. After this ignition, approx. 17 J were released into the arc discharge, while 46 J were stored in the capacitor. The energy difference is mainly caused by transformation into thermal energy in the diodes and in the resistance of the capacitors.
The experiments with the ISS set-up were performed with a sample chamber of type II. This sample chamber belonged to the same batch of sample chambers as the one used on the ISS. The arc discharge energy increases with increasing charging voltage of the capacitor C_{arc} (Eq.

4.1). The arc discharge energies of the laboratory and the ISS-based set-up are similar for small charging voltages, but increasingly differ with increasing charging voltage (Fig. 4.21). The deviation between the discharge energies may be caused by the shorter connections between the arc generation unit and the sample chamber for the ISS-based experiment, or a variation in the electrode distance.

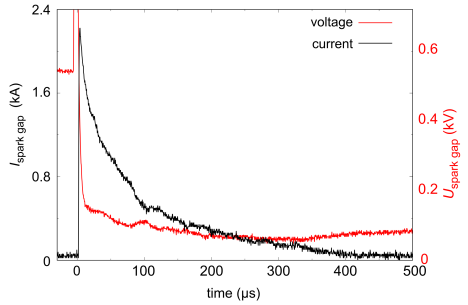

Figure 4.20: Current (black) and voltage (red) measurement over the spark gap between the electrodes in sample chamber I during an arc discharge. C_{arc} was charged to 450 V. The charging state of the capacitors before the ignition spark is also shown in the left upper corner and the high voltage of the ignition spark is out of the accessible range.

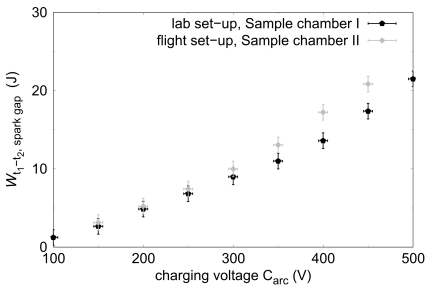

Figure 4.21: Energy $W_{t_1-t_2}$ release into an arc discharge as a function of the charging voltage of C_{arc}. The Earth-based laboratory arc generation unit was measured with sample chamber I and the ISS-based set-up with a sample chamber of type II.

Electron density and temperature

We measured the electron density n_e and temperature T_e as a function of the charging voltage with sample chamber I using Cu-electrodes. We expect slightly higher temperatures for the ISS-based experiment because of the differences in energies described above (Fig. 4.21). We used long-time exposure photographs to characterize the emitted light during an arc discharge to estimate the shape, homogeneity and time-integrated brightness distribution of the arc discharge (Fig. 4.22).

The brightest area of the discharge has approximately the same diameter as the electrodes (approx. 1 mm). The image suggests that the intensity of the discharge decreases rapidly in the first 1–2 mm away from the discharge axis. In comparison to the outer region it seems that the core part of the arc discharge consists of a homogeneous plasma with approx. 1 mm diameter. This is in good agreement with the theory for the positive column of arc discharges.

The Stark broadening of spectral lines can be used to estimate the electron density in a plasma. We used the broadening of the hydrogen H_β line which can be described by a Voigt-function. The half width of the Lorentzian profile $\Delta\lambda_S$ increases with increasing electron density while the Gaussian profile part can be considered constant. A correlation between n_e and $\Delta\lambda_S$ is given by equation (4.3) (Gigosos et al., 2003):

$$\Delta\lambda_S = 4.8\,\text{mm}\,\left(\frac{n_e}{10^{17}\,\text{cm}^{-3}}\right)^{0.68116} \tag{4.3}$$

In the expected operating range of the experiment between 350 V (approx. 13 J) and 450 V (approx. 17 J) we calculated an electron density between $1.6(1)\times1\times10^{-16}\,\text{cm}^3$ and $2.0(1)\times1\times10^{-16}\,\text{cm}^3$ for the Earth-based experiment using sample chamber I (Fig. 4.23).

The determination of the electron temperature was based on the dependence of the emissivity ϵ_{pq} of an emmission line on T_e (Griem, 2005; Kunze, 2009):

$$\epsilon_{pq} \propto \frac{A_{pq}g_p}{\lambda_{pq}}\,\exp\left(-\frac{E_p-E_q}{k_B T_e}\right) \tag{4.4}$$

where

$$k_{\mathrm{B}}T_{\mathrm{e}} = -\frac{E_2 - E_1}{\ln\left(\frac{\lambda_1 g_2 A_2}{\lambda_2 g_1 A_1}\frac{I_1}{I_2}\right)} \tag{4.5}$$

We used the relative intensities of the Cu-I lines at 510.697 nm and 515.467 nm. The parameters E_i, A_i, g_i and λ_i were taken from the NIST database (Kramida et al., 2018). Equation (4.5) may only be used to determine T_{e} if the upper states of the used lines are at least in a partial local thermal equilibrium (pLTE) and the plasma is optically thin. The plasma used in this experiment can be considered optically thin due to the low working pressure and electron temperatures. The measured electron density, electron temperature and the long burning duration (Fig. 4.20) support the assumption of a pLTE during an arc discharge (Fujimoto and McWhirter, 1991).
In the desired range of operation of the ISS-based experiment we determined an electron density of $n_{\mathrm{e}} = 1.6(1) \times 1 \times 10^{-16}\,\mathrm{cm}^3$ to $2.0(1) \times 1 \times 10^{-16}\,\mathrm{cm}^3$ and an electron temperature of $k_{\mathrm{B}}T_{\mathrm{e}} \approx 6900 \pm 1000\,\mathrm{K}$ (Fig. 4.23).

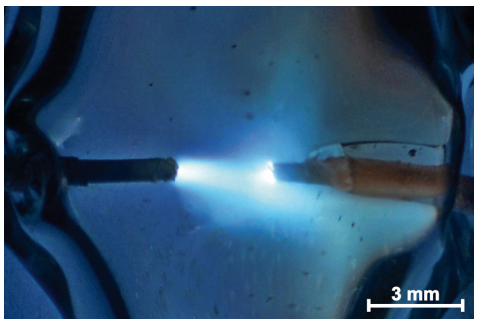

Figure 4.22: Long-time exposure photograph of an arc discharge in a sample chamber of type II with C_{arc} charged to 450 V.

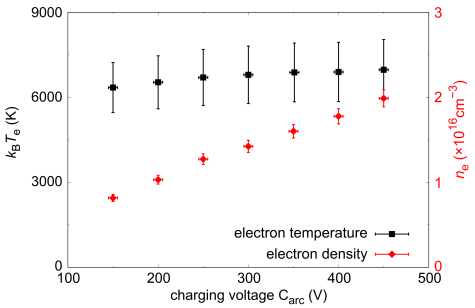

Figure 4.23: Electron temperature $k_{\mathrm{B}}T_{\mathrm{e}}$ and electron density n_{e} dependence on the charging voltage of C_{arc} in sample chamber I.

4.6.3 Rietveld refinement data

Table 4.2: Structural parameters of Mg_2SiO_4, obtained by Rietveld refinement in comparison to synchrotron X-ray powder data from Cernik et al. (1990). Mg_2SiO_4 crystallized in the orthorhombic space group *Pbnm* with $Z = 4$.

	experiment	**reference**
Crystal data		
a (Å)	4.75463(1)	4.7533(1)
b (Å)	10.20281(2)	10.2063(1)
c (Å)	5.98424(1)	5.9841(1)
V (Å^3)	290.299(1)	290.31(1)
ρ (g cm^{-3})	3.219	3.219
Refinement		
R_{p} (%)	7.0	5.8
R_{wp} (%)	9.7	7.4
No. of reflections	222	302
No. of parameters	39	-

Bibliography

Alexander, C. M. O., Grossmann, J. N., Wang, J., Zanda, B., Bourot-Denise, M., and Hewins, R. H. 2000. The lack of potassium-isotopic fractionation in Bishunpur chondrules. *Meteoritics & Planetary Science*, 35: 859–868.

Arakawa, S. and Nakamoto, T. 2016. Compound chondrule formation via collision of supercooled droplets. *Icarus*, 276:102–106.

Asphaug, E., Jutzi, M., and Movshovitz, N. 2011. Chondrule formation during planetesimal accretion. *Earth and Planetary Science Letters*, 308:369–379.

Bayarjargal, L., Fruhner, C.-J., Schrodt, N., and Winkler, B. 2018. $CaCO_3$ phase diagram studied with Raman spectroscopy at pressures up to 50 GPa and high temperatures and DFT modeling. *Physics of the Earth and Planetary Interiors*, 281:31–45.

Boss, A. P. 1996. A concise guide to chondrule formation models. In Hewins, R. H., Jones, R. H., and Scott, E. R. D., editors, *Chondrules and the Protoplanetary Disk*, pages 257–263.

Bowen, N. L. and Schairer, J. F. 1925. The system MgO-FeO-SiO_2. *American Journal of Science*, 29:151–217.

Brisset, J., Colwell, J., Dove, A., and Maukonen, D. 2017. NanoRocks: Design and performance of an experiment studying planet formation on the International Space Station. *Rev. Sci. Instrum.*, 88:074502.

Budde, G., Burkhardt, C., Brennecka, G. A., Fischer-Gödde, M., Kruijer, T. S., and Kleine, T. 2016. Molybdenum isotopic evidence for the origin of chondrules and a distinct genetic heritage of carbonaceous and non-carbonaceous meteorites. *Earth and Planetary Science Letters*, 454:293–303.

Cernik, R. J., Murray, P. K., Pattison, P., and Fitch, A. N. 1990. A two-circle powder diffractometer for synchrotron radiation with a closed loop encoder feedback system. *Journal of Applied Crystallography*, 23: 292–296.

Ciesla, F. J. and Hood, L. L. 2002. The nebular shock wave model for chondrule formation: Shock processing in a particle–gas suspension. *Icarus*, 158:281–293.

Clark, S. J., Segall, M. D., Pickard, C. J., Hasnip, P. J., Probert, M. I. J., Refson, K., and Payne, M. C. 2005. First principles methods using CASTEP. *Zeitschrift für Kristallogrographie*, 220:567–570.

Clarke Jr., R. S., Jarosewich, E., Mason, B., Nelen, J., Gomez, M., and Hyde, J. R. 1971. The Allende, Mexico, Meteorite shower. *Smithsonian Contributions to the Earth Sciences*, 5:1–53.

Connolly, H. C. and Jones, R. H. 2016. Chondrules: The canonical and noncanonical views. *Journal of Geophysical Research: Planets*, 121:1885–1899.

Connolly, H. C. and Love, S. G. 1998. The formation of chondrules: Petrologic tests of the shock wave model. *Science*, 280:62–67.

Connolly, H. C., Jones, B. D., and Hewins, R. H. 1998. The flash melting of chondrules: an experimental investigation into the melting history and physical nature of chondrule precursors. *Geochimica et Cosmochimica Acta*, 62(15):2725–2735.

DeAngelis, B. A., Newnham, R. E., and White, W. B. 1972. Factor group analysis of the vibrational spectra of crystals: A review and consolidation. *American Mineralogist*, 57:255–268.

Desch, S. J. and Connolly Jr., H. C. 2002. A model of the thermal processing of particles in solar nebula shocks: Application to the cooling rates of chondrules. *Meteoritics & Planetary Science*, 37:183–207.

Desch, S. J. and Cuzzi, J. N. 2000. The generation of lightning in the solar nebula. *Icarus*, 143:87–105.

Fujimoto, T. and McWhirter, R. W. P. 1991. Validity criteria for local thermodynamic equilibrium in plasma spectroscopy. *Physical Review A*, 42:6588–6601.

Gigosos, M. A., González, M. A., and noso, V. C. 2003. Computer simulated balmer-alpha, -beta and -gamma stark line profiles for non-equilibrium plasmas diagnostics. *Spectrochimica Acta Part B*, 58(8):1489–1504.

Gooding, J. L. and Keil, K. 1981. Relative abundances of chondrule primary texture types in ordinary chondrites and their bearing on chondrule formation. *Meteoritics & Planetary Science*, 16:17–43.

Griem, H. R. *Principles of Plasma Spectroscopy*. Cambridge University Press, 2005. doi: 10.1017/CBO9780511524578.

Güttler, C., Poppe, T., Wasson, J. T., and Blum, J. 2008. Exposing metal and silicate charges to electrical discharges: Did chondrules form by nebular lightning? *Icarus*, 195:504–510.

Hewins, R. H. and Connolly, H. C., Jr. 1996. Peak temperatures of flash-melted chondrules. In Hewins, R. H., Jones, R. H., and Scott, E. R. D., editors, *Chondrules and the Protoplanetary Disk*, pages 197–204.

Hewins, R. H. and Fox, G. E. 2004. Chondrule textures and precursor grain size: an experimental study. *Geochimica et Cosmochimica Acta*, 68(4):917–926.

Hewins, R. H., Zanda, R. H., Horanyi, M., Robertson, S., Den Hartog, D. J., and Fiksel, G. 2000. The trouble with flash heating. *Lunar and Planetary Science Conference*, 31:1675 (abstract).

Hezel, D. C. and Palme, H. 2010. The chemical relationship between chondrules and matrix and the chondrule matrix complementarity. *Earth and Planetary Science Letters*, 294:85–93.

Horányi, M., Morfill, G., Goertz, C. K., and Levy, E. H. 1995. Chondrule formation in lightning discharges. *Icarus*, 114:174–185.

Hubbard, A. 2015. Compound chondrules fused cold. *Icarus*, 254:56–61.

Imae, N. and Isobe, H. 2017. An experimental study of chondrule formation from chondritic precursors via evaporation and condensation in Knudsen cell: Shock heating model of dust aggregates. *Earth and Planetary Science Letters*, 473:256–268.

Johansen, A. and Okuzumi, S. 2018. Harvesting the decay energy of ^{26}Al to drive lightning discharge in protoplanetary discs. *Astronomy & Astrophysics*, 609:1–22.

Johnson, B. C., Minton, D. A., Melosh, H. J., and Zuber, M. T. 2015. Impact jetting as the origin of chondrules. *Nature*, 517:339–341.

Kerr, R. A. 2013. Meteorite mystery edges closer to an answer — Or the end of a field. *Science*, 341:126–127.

Kozub, D., Khmelik, V., Shapoval, J., Chentsov, V., Yatsenko, S., Litovchenko, B., and Starikh, V. Helicon Focus 7.0.2 Pro. Helicon Soft Ltd. Available: `https://www.heliconsoft.com/heliconsoft-products/helicon-focus/` [2018, Septemper 27]., 2018.

Kramida, A., Ralchenko, Y., Reader, J., and NIST ASD Team. NIST Atomic Spectra Database (ver. 5.6.1), [Online]. Available: `https://physics.nist.gov/asd` [2015, April 16]. National Institute of Standards and Technology, Gaithersburg, MD., 2018.

Krot, A. N., Amelin, Y., Cassen, P., and Meibom, A. 2005. Young chondrules in CB chondrites from a giant impact in the early Solar System. *Nature*, 436:989–992.

Kunze, H.-J. *Introduction to Plasma Spectroscopy*. Springer Berlin Heidelberg, 2009. doi: 10.1007/978-3-642-02233-3.

Libourel, G. and Portail, M. 2018. Chondrules as direct thermochemical sensors of solar protoplanetary disk gas. *Science Advances*, 4(7):eaar3321.

Lichtenberg, T., Golabek, G. J., Dullemond, C. P., Schönbächler, M., Gerya, T. V., and Meyer, M. R. 2018. Impact splash chondrule formation during planetesimal recycling. *Icarus*, 302:27–43.

Limaye, A. 2012. Drishti: A volume exploration and presentation tool. In *Developments in X-ray tomography VIII*, volume 8506, pages 1–9. SPIE.

Lofgren, G. 1996. A dynamic crystallization model for chondrule melts. In Hewins, R. H., Jones, R. H., and Scott, E. R. D., editors, *Chondrules and the Protoplanetary Disk*, pages 187–196.

Moosmann, J., Ershov, A., Weinhardt, V., Baumbach, T., Prasad, M. S., LaBonne, C., Xiao, X., Kashef, J., and Hofmann, R. 2014. Time-lapse X-ray phase-contrast microtomography for *in vivo* imaging and analysis of morphogenesis. *Nature Protocols*, 9:294–304.

Morlok, A., Sutton, Y. C., Braithwaite, N. S. J., and Grady, M. M. 2012. Chondrules born in plasma? Simulation of gas–grain interaction using plasma arcs with applications to chondrule and cosmic spherule formation. *Meteoritics & Planetary Science*, 47:2269–2280.

Morris, M. A., Boley, A. C., Desch, S. J., and Athanassiadou, T. 2012. Chondrule formation in bow shocks around eccentric planetary embryos. *The Astrophysical Journal*, 752:1–17.

Ogurreck, M., Wilde, F., Herzen, J., Beckmann, F., Nazmov, V., Mohr, J., Haibel, A., Müller, M., and Schreyer, A. 2013. The nanotomography endstation at the PETRA III Imaging Beamline. *Journal of Physics: Conference Series*, 425(18):182002.

Palme, H., Hezel, D. C., and Ebel, D. S. 2015. The origin of chondrules: Constraints from matrix composition and matrix-chondrule complementarity. *Earth and Planetary Science Letters*, 411:11–19.

Rietveld, H. M. 1969. A profile refinement method for nuclear and magnetic structures. *Journal of Applied Crystallography*, 2:65–71.

Russel, S., Connolly Jr., H. C., and Krot, A. N., editors. *Chondrules: Records of Protoplanetary Disk Processes*, Cambridge Planetary Science, 2018. Cambridge University Press.

Scott, E. R. D. 2007. Chondrites and the protoplanetary disk. *Geochimica et Cosmochimica Acta*, 59: 1847–1869.

Toby, B. H. and Von Dreele, R. B. 2013. *GSAS-II*: the genesis of a modern open-source all purpose crystallography software package. *Journal of Applied Crystallography*, 46:544–546.

Túnyi, I., Guba, P., Roth, L. E., and Timko, M. 2003. Electric discharges in the protoplanetary nebula as a source of impulse magnetic fields to promote dust aggregation. *Earth Moon Planets*, 93:65–74.

Wdowiak, T. J. 1996. Experimental investigation of electrical discharge formation of chondrules. Lunar and Planetary Institute, Houston. In King, E. A., editor, *Chondrules and their originsk*, pages 279–283.

Weisberg, M. K., Prinz, M., Clayton, R. N., Mayeda, T. K., Sugiura, N., Zashu, S., and Ebihara, M. 2001. A new metal-rich chondrite grouplet. *Meteoritics & Planetary Science*, 36(3):401–418.

Whipple, F. L. 1966. Chondrules: Suggestion Concerning the Origin. *Science*, 153:54–56.

Wilde, F., Ogurreck, M., Greving, I., Hammel, J. U., Beckmann, F., Hipp, A., Lottermoser, L., Khokhriakov, I., Lytaev, P., Dose, T., Burmester, H., Müller, M., and Schreyer, A. 2016. Micro-CT at the imaging beamline P05 at PETRA III. *AIP Conference Proceedings*, 1741:030035.

Youdin, A. N. and Shu, F. H. 2002. Planetesimal Formation by Gravitational Instability. *The Astrophysical Journal*, 580:494–505.

CHAPTER 5

Publication II

Mg_2SiO_4 particle aggregation aboard the ISS — Influence of electric fields on aggregation behavior, particle velocity and shape-preferred orientation

Astronomy & Astrophysics **651**:A1 (2021)

T. E. Koch[a], D. Spahr[a], D. Merges[a], B. Winkler[a] and F. E. Brenker[a,b]

[a]Institute of Geosciences, Goethe-Universität Frankfurt, Altenhöferallee 1, 60438 Frankfurt, Germany
[b]Hawai'i Institute of Geophysics and Planetology, School of Ocean and Earth Science and Technology, University of Hawai'i at Mānoa, 1680 East-West Road, Honolulu, HI 96822, USA

Abstract

Context: Particle aggregation in the solar nebula played a major role in the framework of planet formation; for example, primitive meteorites and their components formed by different aggregation processes. These processes are still not completely understood.
Aims: Electrostatic forces probably influenced particle aggregation in the early Solar System. We developed an experiment that was carried out under long-term microgravity conditions aboard the International Space Station (ISS) to expand the knowledge of charge-influenced particle aggregation.
Methods: Aggregation of freely floating, elongated, angular, and polycrystalline Mg_2SiO_4-particles was observed under long-term microgravity conditions while being exposed to electric fields as well as low- and high-energy electric discharges.
Results: Nearly all of the particles formed an aggregate, which freely floated in the sample chamber prior to the discharge experiments. The aggregate was attracted by the electrodes and partly disintegrated by low-energy electric discharges. High-energy arc discharges accelerated the particles, which reassembled in chains parallel to the field lines of the subsequent electric field between the electrodes. A strong shape-preferred orientation of the longest grain axis parallel to the field lines was observed in the Mg_2SiO_4-particles. With increasing strength of the electric field, the particle chains narrowed, leading to the formation of a compact aggregate.
Conclusion: In microgravity conditions, electrostatic forces influence the aggregation process in terms of aggregate growth rate, morphology, packing density, and particle orientation. These observations help us to better understand the formation and compaction mechanism of early Solar System aggregates.

5.1 Introduction

Aggregation of particles in the early stage of the Solar System is considered to be one of the first and most important processes leading to planet formation (Cuzzi and Weidenschilling, 2006; Weidenschilling and Cuzzi, 2006; Dominik et al., 2007; Blum and Wurm, 2008). For example, primitive meteorites and their components, including amoeboid olivine aggregates (AOAs); calcium-aluminum-rich inclusions (CAIs); matrix material; and chondrules, which probably represent planet precursors, are the result of different early aggregation processes (Russel et al., 2018).
The aggregation behavior of particles in the early Solar System and the internal structure of particle aggregates depend on numerous parameters, and there are still many unsolved questions (Dominik and Tielens, 1997; Poppe et al., 2000; Blum, 2006; Blum and Wurm, 2008; Dominik et al., 2007; Güttler et al., 2010). For instance, the evolution of the porosity and the compaction of aggregates influenced the structure of the protoplanetary disk, for example, the formation of a dense mid-plane layer (Ormel et al., 2007; Kataoka et al., 2013; Kataoka, 2017) and different processes such as collisions and compaction by gas and by self-gravity have been proposed as mechanisms for compaction (Dominik and Tielens, 1997; Dominik et al., 2007; Blum and Wurm, 2008). However, the estimated porosity of aggregates formed by these processes is higher than porosities usually observed in extraterrestrial samples (Weidenschilling and Cuzzi, 2006; Forman et al., 2016). Another enigma is the coagulation of chondrule-sized objects to larger, centimeter-to-meter-sized objects, since experimental work has shown that chondrule-sized objects bounce off each other rather than sticking together after collisions, due to the so-called bouncing barrier (Zsom et al., 2010; Güttler et al., 2010; Kruss et al., 2017; Steinpilz et al., 2020).
Electrostatic forces strongly affect the behavior of dust particles (e.g., Shinbrot, 2014; Siu et al., 2015), and therefore they have been considered as a possible mechanism that influenced particle aggregation in the protoplanetary disk (e.g., Poppe et al., 2000; Marshall et al., 2005; Konopka et al., 2005; Okuzumi, 2009; Love et al., 2014; Jungmann et al., 2018; Steinpilz et al., 2020). For example, it was experimentally demonstrated that charged 500 µm-sized glass spherules stick together after collisions even if they have higher velocities than uncharged spherules (Jungmann et al., 2018). Another experiment in microgravity conditions showed that 400 µm-sized quartz spherules formed centimeter-sized, stable aggregates, where the spherules formed parallel chains within the aggregates (Marshall et al., 2005). The coaxial alignment of these spherules was interpreted as the result of an alignment of the quartz dipole axis. These aggregates also attracted freely levitating particles. Furthermore, informal experiments aboard the International Space Station (ISS) have shown that electrostatic forces can lead to the formation of dense, spheroidal aggregates of sucrose (Love et al., 2014). Most recently, experiments with charged, approx. 430 µm-sized SiO_2 glass spherules, showed that charged particles form aggregates with sizes beyond the bouncing barrier with collision velocities of $>10\,\mathrm{cm\,s^{-1}}$ (Steinpilz et al., 2020).
We carried out an experiment aboard the ISS, which was primarily developed to examine chondrule formation by arc discharges (Spahr et al., 2020). In this experiment, freely floating Mg_2SiO_4 (forsterite) particles were exposed to electrical discharges in order to simulate chondrule formation under reasonably realistic conditions. In the framework of this experiment, we could also study particle aggregation in electric fields and their response to electric discharges, which expands our knowledge of charge-influenced particle aggregation. These observations can potentially offer new constraints on aggregation processes, adhesive forces, and the texture and microstructure of chondrule precursors.

5.2 Methods

5.2.1 Experimental set-up & sample material

The experiment was performed aboard the International Space Station (ISS) inside a $10 \times 10 \times 15\,\mathrm{cm}^3$-sized NanoRacks NanoLab (Spahr et al., 2020). Two types of electrical discharges were induced: ignition sparks and arc discharges. Ignition sparks represent short (approx. 4 µs), low-energy ($Q \ll 0.01\,\mathrm{J}$) discharges, while arc discharges have a longer discharge duration (approx. 300–400 µs) with higher energies ($Q = 5$–$8\,\mathrm{J}$). Figure 5.1a shows a schematic circuit diagram of the discharge generation electronics. First, a DC-DC converter charged three parallel capacitors ($C_{arc} \mathrel{\widehat{=}} 450\,\mu\mathrm{F}$) to apply the electric field between the electrodes. The short ignition sparks were then induced by the ignition coil. An electric field between the electrodes remained up to 60 s after the ignition sparks. In order to generate longer, high-energy arc discharges, the energy stored in C_{arc} was released into the ionized channel generated by the ignition coil. The capacitors were subsequently charged in preparation for the next arc discharge.
Figure 5.1b shows a photograph of the sample chamber. It was manufactured from quartz glass and two tungsten electrodes with a diameter of 1 mm and a spark gap of approx. 2 mm were fused into the glass. The sample chamber was loaded with 100 ± 1 mbar Argon gas and the sample material. The sample material consisted of 30 ± 1 mg Mg_2SiO_4 particles, which corresponds to approx. 10^4 particles. The particles vary in size from 80–180 µm (mean diameter 126 ± 32 µm) and were polycrystalline, highly porous, angular, and often slightly elongated (Spahr et al., 2020). The behavior of the Mg_2SiO_4 particles in the sample chamber was observed with a Raspberry Pi V2 camera with a field of view (FOV) of $2.73 \times 3.63\,\mathrm{mm}^2$. The resolution was 1232×1640 pixel with a frame rate of 40 fps. The focal depth is approx. 1 mm. For more details on the experimental set-up and the sample material we refer the reader to Spahr et al. (2020) or the GitHub repository[1].

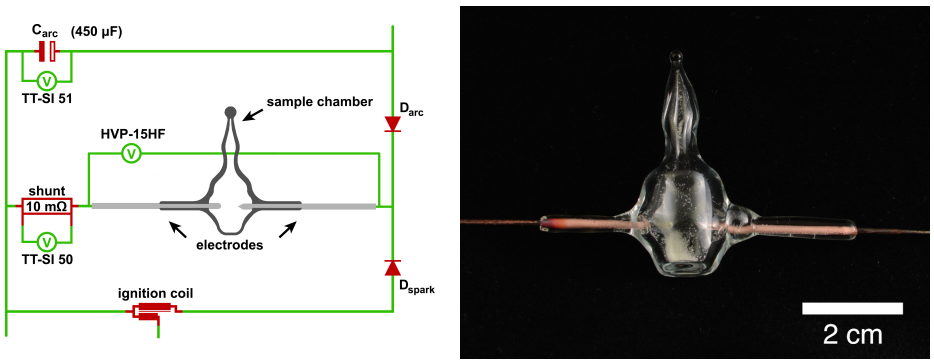

(a) (b)

Figure 5.1: Experimental set-up. (*a*) Schematic illustration of the most relevant parts of the arc generation circuit connected to the sample chamber. A DC-DC converter charged three parallel capacitors ($C_{arc} \mathrel{\widehat{=}} 450\,\mu\mathrm{F}$). The ignition coil was protected from the charging voltage of C_{arc} by the diode D_{spark}. After C_{arc} had reached the target voltage, the ignition coil generated a high-voltage peak up to 8 kV and produced an ionized channel between the electrodes (ignition spark). Diode D_{spark} became conductive, while C_{arc} was protected by D_{arc} from the high-voltage peak. After the electrical breakdown, the voltage decreased instantaneously. When the voltage had dropped below the charging voltage of C_{arc}, the energy stored in C_{arc} was released into the existing ionized channel, causing a high-energy arc discharge. (*b*) Sample chamber made of quartz glass. Two tungsten electrodes were embedded into the glass on opposite sides. The sample chamber was loaded with 30 mg of Mg_2SiO_4 particles.

[1] https://github.com/geowissenschaften/exciss

5.2.2 Experimental stages

The experiment is divided into three different operational stages:

I: **Initial situation and particles in the electric field**
First, videos and photographs were collected prior to any operational command. Subsequently, the capacitor C_{arc} was charged to $U = 110$–$160\,V$ to apply an electric field between the electrodes.

II: **Ignition spark experiments**
C_{arc} was charged to voltages in the range of $U = 110$–$160\,V$ over a duration of $60\,s$, which applied an electric field between the electrodes. The capacitor voltage was kept constant for another $60\,s$, and the ignition spark was subsequently induced by the ignition coil. An electric field that was strong enough to affect particles remained over a duration of approx. $60\,s$ after the discharge. The complete charging process and the ignition spark were filmed.

III **Arc discharge experiments**
C_{arc} was charged to an adjustable target voltage of $U = 150$–$190\,V$ for approx. $60\,s$. The capacitor voltage was kept constant for another $60\,s$ until the arc discharge was released between the electrodes. C_{arc} was subsequently charged in preparation for the next arc discharge. The complete charging process and the arc discharges were filmed.

5.2.3 Velocity analysis

Video analysis was performed using the *Tracker – Video Analysis and Modelling Tool* software (Brown, 2008). The particle positions (x, y) were determined for each particle on each frame of the video to determine the particle trajectories and velocities, beginning from the discharge event ($t = 0\,s$). The program calculated the velocities from the position-time data with the average velocity over a two-step interval. The relatively low frame rate of the camera and the rather poor contrast limited the precision of the particle position analysis and the particle positions could not always be determined for each frame. The particle velocities in the approximately first ten frames were determined from the length of particle traces during an exposure. The error in the velocity determination can be estimated to be in the range of 0.1–$2\,mm\,s^{-1}$, which is due to the limited frame rate, the contrast conditions of the images and because the third dimension was neglected.

5.3 Results

5.3.1 Stage I: Initial situation and particles in the electric field

The first set of videos received from the ISS showed that within the limited field of view in the center of the experimental chamber, a few particles stuck to the electrodes and the sample chamber wall (Fig. 5.2a). Ten days after the rocket launch, the capacitors were charged for the first time, which led to the appearance of a particle aggregate in the corner of the field of view. With increased charge, the aggregate moved toward the center of the field of view before settling between the electrodes (Fig. 5.2b). The aggregate had an approximate size of $2 \times 2 \times 4\,mm^3$, which presumably contained nearly all approx. 10^4 particles inside the sample chamber. It is densely packed and has an approximately ellipsoidal morphology (Fig. 5.2b). At this stage of the experiment, the aggregates appeared frequently whenever the capacitors were charged. The long axis of the ellipsoidal aggregate aligned itself between the two

electrodes. As soon as the electric field was turned off, the aggregate moved out of the field of view with a velocity of approx. $0.7 \pm 0.1\,\mathrm{mm\,s^{-1}}$. This aggregate represents the initial situation before the discharge experiments started.

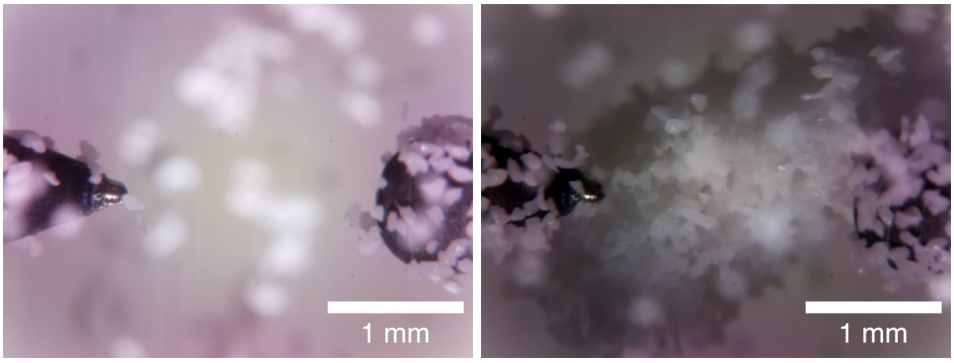

(a) (b)

Figure 5.2: Field of view of the camera aboard the ISS. (*a*) The first image captured aboard the ISS. The electrodes are on the left- and right-hand sides of the image. Some particles stuck to the electrodes and the sample chamber wall. (*b*) A spheroidal, dense aggregate levitating between the electrodes.

5.3.2 Stage II: Ignition spark experiments

Some ignition sparks were induced while the aggregate was levitating between the electrodes; in other cases, the space between the electrodes was empty. Figure 5.3a shows the aggregate immediately before the ignition spark was induced, and Figure 5.3b shows the situation inside the sample chamber 0.3 s after the ignition spark. The particles in the impacted volume flew in various directions, while the main part of the aggregate stayed intact (Video S1). The aggregate itself stayed attached to the electrodes but revolved around the electrode, as indicated by the arrows in Figure 5.3b. Some ignition sparks separated the aggregate in two main parts, where one part moved instantly out of the field of view with a velocity of $3.1 \pm 0.5\,\mathrm{mm\,s^{-1}}$, while the other part stayed attached to one of the electrodes. Immediately after the discharge, many of the dispersed particles reunited with the aggregate. After several ignition sparks and with increased charging of C_{arc} in preparation for stage III, the aggregate disappeared.
The trajectories and the resulting velocities of the particles after ignition sparks were analyzed in detail for a few representative cases. Figure 5.4a shows the particle trajectories after an ignition spark. The direction of the particle motion was influenced by an attraction to the electrodes. Figure 5.4b shows the velocities of particles after different ignition spark events. A few particles reached velocities of $>25\,\mathrm{mm\,s^{-1}}$. Most particles moved with velocities between 0.1 and $10\,\mathrm{mm\,s^{-1}}$. Their velocities increased after approx. 1 s after the discharge when they were attracted by the electrodes.

5.3.3 Stage III: Arc discharge experiments

The generation of high-energy arc discharges caused a higher degree of random particle motion in the sample chamber. Although the first two arc discharges were induced when the space between the electrodes was almost empty, the arc discharges led to a random particle motion inside the sample chamber (Fig. 5.5a). The electric field prior to the third arc discharge was applied while the particles were still in motion. The moving particles were deflected from their path by the attraction of the electrodes and formed chains parallel to the field lines of

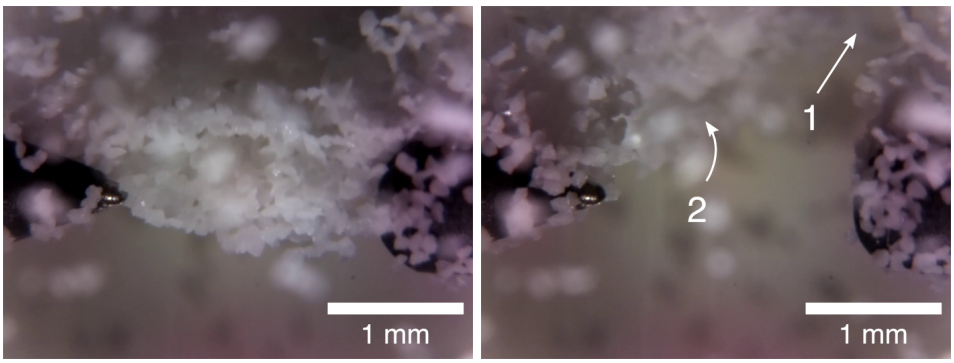

(a) (b)

Figure 5.3: Aggregate before and immediately after the impact of an ignition spark. (*a*) Aggregate levitating between the electrodes while the capacitors were charged. (*b*) Situation inside the sample chamber 0.3 s after the ignition spark. The arrows show the direction in which the aggregate parts moved. The right part of the aggregate was destroyed (1), whereas the main part of the aggregates moved to the left side (2).

the electric field between the electrodes (Fig. 5.5b, Video S2). The particles moved with velocities of approx. $1\,\mathrm{mm\,s^{-1}}$ toward the electrodes and reached up to approx. $4\,\mathrm{mm\,s^{-1}}$ before they stopped at their final position in the chain. A few particles, which were levitating closer to the left electrode, were attracted by the right electrode and vice versa. Fig. 5.5c shows a close-up of the particle chains that reveals that the particles aligned with their longest axis parallel to the electrodes, which is also parallel to the field lines of the electric field. With increasing charging voltage, the vertical distance between the particle chains decreased, which led to the formation of a more closely packed aggregate (Fig. 5.5d). A subsequent arc discharge scattered these particles completely (Video S3). The electric field, which was applied when the capacitors were charged for the fourth arc discharge ($U = 170\,\mathrm{V}$), again caused the formation of particle chains parallel to the field lines between the electrodes. However, the number of particle chains, which accumulated between the electrodes, decreased with further arc discharges.

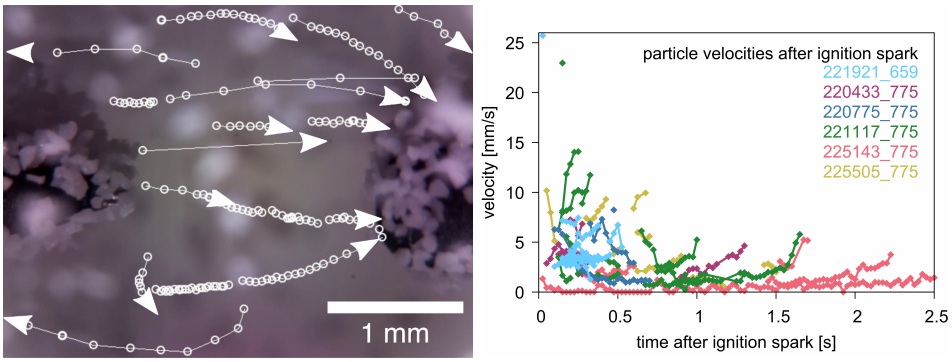

(a) (b)

Figure 5.4: Velocity analysis of particles after ignition sparks. (*a*) Particle trajectories over 1.7 s after a representative ignition spark, which was induced without the aggregate between the electrodes. White circles mark the position of the particles in the single frames. The directions of movement of the particles were influenced by the electrostatic attraction of the electrodes. (*b*) Velocities of particles after an ignition spark ($t = 0\,\mathrm{s}$). The numbers in the top right-hand corner represent different discharge events. The first two ignition sparks (221921_659, 220433_775) were induced while the aggregate was levitating between the electrodes. The other ignition sparks were induced when the space between the electrodes was empty, but the electrode tips were covered with particles. The velocity increase is caused by the attraction of the electrodes.

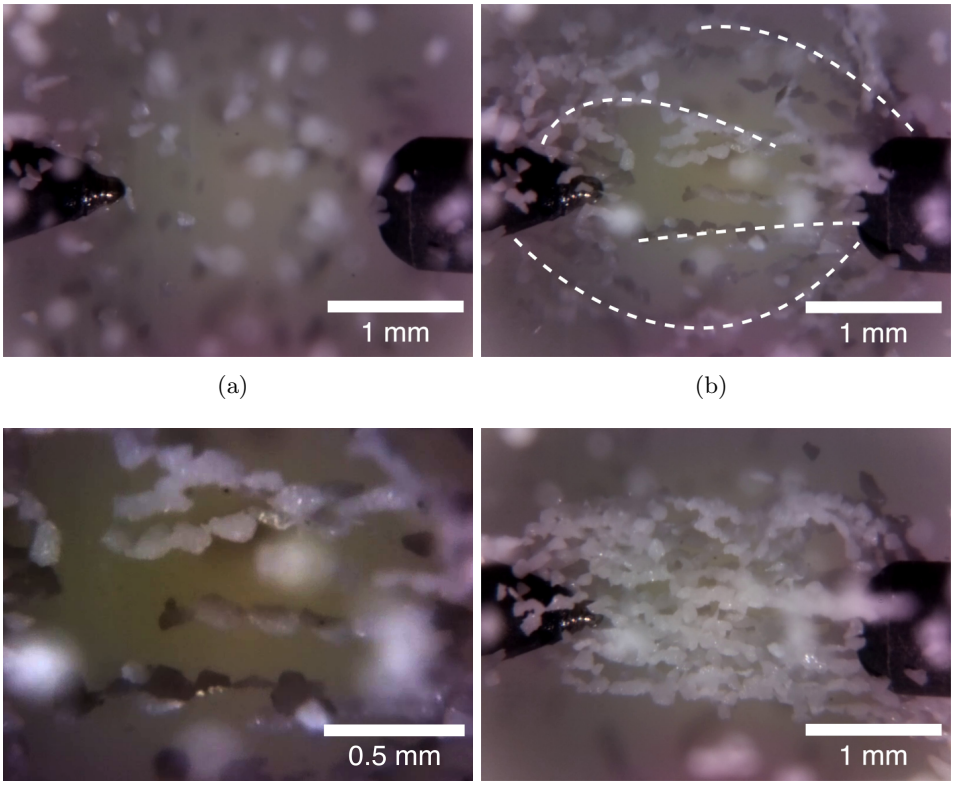

(a) (b)

(c) (d)

Figure 5.5: Particle aggregation in the electric field. (*a*) Particles were in motion inside the sample chamber; screenshot from approx. 0.7 s after the second arc discharge. (*b*) Electric field that was applied prior the third arc discharge ($U = 170$ V) caught the particles that aligned along chains parallel to the field lines; photograph approx. 110 s after the second arc discharge. The dashed white lines better visualize some chains of particles. The longest particle axis aligned itself parallel to the field lines. (*c*) Close-up of (*b*) with enhanced contrast. The particles aligned with their longest axes parallel to the field lines. (*d*) With increasing charging voltage, the vertical distance between the particle chains decreased, which led to the formation of a more closely packed aggregate; screenshot taken approx. 130 s after the second arc discharge.

Figure 5.6a shows the trajectories of particles after the last high-energy arc discharges ($Q \approx 8$ J). In contrast to particles after ignition sparks, the particle trajectories do not show any specific direction. Many particles reached velocities of $>60\,\mathrm{mm\,s^{-1}}$, which were calculated from the length of the particle traces on a single frame. Higher velocities are probable. Figure 5.6b shows the velocities versus time after arc discharge that we were able to calculate from the particle positions. The particles reached velocities $>25\,\mathrm{mm\,s^{-1}}$. The particle velocity decreased exponentially within the first 0.5 s after the discharge event.
A least-squares fit of the solution to the equation of motion with Stokes' gas drag (Stokes, 1851) and constant external force to the experimental data was performed, which can be expressed as follows:

$$v(t) = a \cdot e^{-t/b} + c, \tag{5.1}$$

where v is the velocity of the particle at time t, a is essentially the starting velocity at $t = 0$ s (discharge event), b represents the gas-grain coupling time, and c is the velocity of the particle after the deceleration. The fitting results are summarized in Table 5.1. The widespread distribution of the maximum velocity of the particles after an arc discharge a could be the result of different particle trajectories before the particle position could be tracked. The mean gas-grain coupling time for all analyzed particles was determined to be $b = 0.14 \pm 0.10$ s, which matches the calculated gas-grain coupling time with Stokes' law (Stokes, 1851) using

the viscosity of Ar at 100 mbar $\mu \approx 2 \times 10^{-5}\,\mathrm{kg\,m\,s^{-1}}$ (Kestin and Leidenfrost, 1959) for particles with a mean radius of $r = 63.5\,\mu\mathrm{m}$ and a mass of $3.28 \times 10^{-9}\,\mathrm{kg}$. The parameter c describes the particle response to the electric field and the attraction of the electrodes without the influence of gas motion.

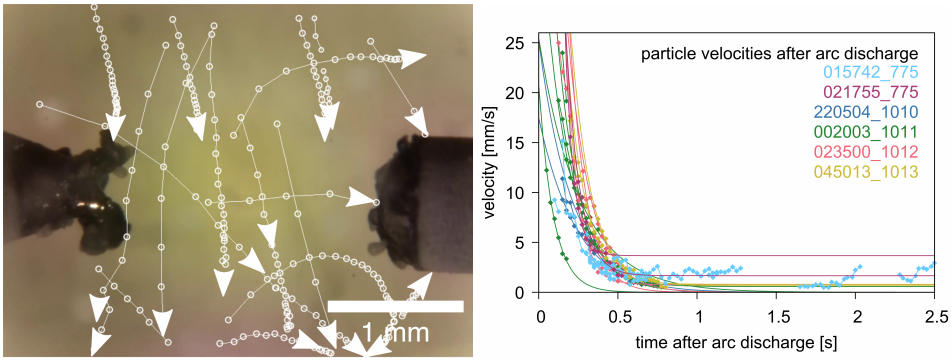

(a) (b)

Figure 5.6: Velocity analysis of particles after arc discharges. (*a*) Particle trajectories of different particles during the first 1.3 s after an arc discharge. White circles mark the position of the particles in single frames; however, the particle position could not be observed for every frame due to low contrast conditions. The distances between the circles are not always equivalent for the velocity. (*b*) Particle velocities after high-energy arc discharges. The velocity decreased exponentially after the arc discharge. The arc discharges 220504_1010, 002003_1011, 023500_2012, and 045013_1013 represent arc discharges with $Q \approx 8\,\mathrm{J}$, which were induced while the space between the electrodes was empty. The arc discharges 015742_775 and 021755_775 represent arc discharges that hit the aggregate with $Q \approx 6.5\,\mathrm{J}$. The acceleration after 1.5 s is due to the attraction of the electrode.

Table 5.1: Fitting results of the solution to the equation of motion with Stokes' gas drag and constant external force to the experimental data.

a [$\mathrm{mm\,s^{-1}}$]	b [s]	c [$\mathrm{mm\,s^{-1}}$]	Q [J]
503 ± 212	0.05 ± 0.01	3.7 ± 0.7	6.5
234 ± 28	0.08 ± 0.01	0.7 ± 0.2	7.9
187 ± 100	0.08 ± 0.02	1.7 ± 0.6	6.5
170 ± 30	0.10 ± 0.01	0	7.9
124 ± 37	0.13 ± 0.01	0.7 ± 0.2	7.9
105 ± 15	0.12 ± 0.01	0.8 ± 0.3	7.9
93 ± 11	0.14 ± 0.01	0	7.9
58 ± 9	0.14 ± 0.10	0.6 ± 0.2	7.8
39 ± 3	0.17 ± 0.03	0	7.8
25 ± 3	0.17 ± 0.01	0	7.8
25 ± 2	0.21 ± 0.01	0	7.8
21 ± 1	0.09 ± 0.01	0	7.8

a is the starting velocity at $t = 0\,\mathrm{s}$ (discharge event), b represents the gas-grain coupling time, and c is the velocity of the particle after the deceleration. Q is the discharge energy.

5.4 Discussion

The starting condition of the experiment (stage I) was a densely packed aggregate, which was probably held together due to attractive forces such as Van-der-Waals or electrostatic forces due to tribocharging prior to the experiment during transportation. In microgravity conditions, the aggregate was attracted by the electrodes until it placed and aligned itself between the electrodes. The electric field may have polarized the complete aggregate. The aggregate morphology is similar to the initial situation of other particle aggregation experiments at microgravity (e.g., Steinpilz et al., 2019), to the cm-sized aggregates observed by Marshall et al. (2005) of 400 µm-sized spherical quartz particles and to aggregates of sucrose formed by experiments aboard the ISS by Love et al. (2014). The maximal size of the aggregates in the experiment was limited by the number of dust particles in the sample chamber.
During experimental stage II, we observed that short ignition sparks disintegrated the part of the aggregates that was transversed by the spark, and the sputtered particles were attracted by the surviving aggregate. The observation that dust aggregates can attract particles due to electrostatic attraction was also made by Marshall et al. (2005). Consequently, aggregates of charged particles in protoplanetary disk have a higher stability regarding any disturbances, which is in accordance with previous observations (Marshall et al., 2005; Love et al., 2014). Furthermore, the trajectories of the particle motions triggered by the ignition sparks were mainly influenced by the attraction of the electrodes.
In experimental stage III, high-energy arc discharges accelerated the particles, which subsequently aggregated in particle chains parallel in the electric field lines. With increasing charging voltages, these chains formed an aggregate with coaxial shape-alignment of most particles. It is not clear if the particles were polarized prior to the experiments; however, it is most likely that the particle behavior is caused by dielectrophoresis (e.g., Pohl, 1978; LaMarche et al., 2010; Shinbrot, 2014). The electric field has probably induced dipoles parallel the longest grain axis, which caused the alignment of the dipole axis parallel to the field lines and the formation of particle chains.
The formation of particle chains in aggregates by alignment of the quartz dipole axis of quartz spherules was observed in the experiment of Marshall et al. (2005). In the scope of our experiment, we show that an alignment can also occur when multi-grain particles have an elongated morphology. Furthermore, the electronic polarizability of forsterite is more than twice the polarizability of quartz (Lasaga and Cygan, 1982), and experiments have shown that olivine-bearing basalt spheres charge more strongly than glass spherules (Steinpilz et al., 2020). Therefore, forsterite represents a highly recommendable and realistic material for future aggregation experiments.
The porosity reduction of protoplanetary dust aggregates plays an important role in planetesimal formation and different scenarios, such as collisions of similar-sized dust aggregates, static compression by disk gas or by self-gravity have been proposed to increase the volume filling factor (Dominik and Tielens, 1997; Ormel et al., 2007; Suyama et al., 2008; Kataoka et al., 2013). In addition to these mechanisms, we have shown that electric fields can help to reduce the porosity of particle aggregates, which was further enhanced by the elongated morphology of the grains. A pre-alignment of particles also changes the magnitude and intensity required for compression events on aggregates and young planetary bodies.
The pressure and particle density in the sample chamber (approx. $1.6 \times 10^{-3}\,\mathrm{g\,cm^{-3}}$) differ from the parameters, which are assumed for the overall planet forming region of the Solar Nebula by a factor of 10^5–10^8 (Zsom et al., 2010; Weidenschilling, 1977; Hayashi, 1981). However, locally higher densities in the Nebula could be reached by turbulences (Love et al., 2014; Cuzzi et al., 2001). Centimeter-sized aggregates grown by hit-and-stick collision could

have formed over a period of approx. 1000 to several thousands of years (Blum and Wurm (2008) and references therein). The results of the experiment suggest that even at lower particle densities, electrostatic forces could substantially decrease aggregation times, since particles can be attracted over greater distances than previously assumed.

5.5 Conclusion

We studied the behavior of dust particles under long-term microgravity conditions aboard the ISS under the influence of electric fields and their response to electrical discharges. We show that electrostatic forces, the presence of an electric field, and electric discharges influence the aggregation process and aggregate morphology, the packing density in the aggregate, and the particle trajectories. Electric fields can also lead to strong shape-preferred orientation effects and porosity reduction in particle aggregates, which is an important process in the evolution of planet precursors.

Acknowledgements

This project was realized with the help of A.A. Beck, O. Christ, P.-T. Genzel and D. Mederos Leber. We thank the Hackerspace Ffm e. V., especially S. Fujita and J. Kerscher, R. Haseitl and S. Matthies for the help with the technical implementation and the software development. We thank J. Weppler and the German Aerospace Center DLR for taking care of the organization of this project. We thank NanoRacks LLC and DreamUp for the payload opportunity. We also thank the astronauts aboard the ISS under the commandant of A. Gerst for the implementation of the experiment. Funding: We are grateful for financial support provided by the Dr. Rolf M. Schwiete Stiftung, the German Aerospace center DLR, NanoRacks LLC, DreamUp, Biovia, the BmWi (50JR1704) and DFG (BR2015/35-1; Wi1232/44-1), Nordlicht GmbH and ZEISS. This manuscript benefitted from the comments and suggestions of an anonymous reviewer. This project was realized with the help of A.A. Beck, O. Christ, P.-T. Genzel and D. Mederos Leber. We thank the Hackerspace Ffm e. V., especially S. Fujita and J. Kerscher, R. Haseitl and S. Matthies for the help with the technical implementation and the software development. We thank J. Weppler and the German Aerospace Center DLR for taking care of the organization of this project. We thank NanoRacks LLC and DreamUp for the payload opportunity. We also thank the astronauts aboard the ISS under the commandant of A. Gerst for the implementation of the experiment. Funding: We are grateful for financial support provided by the Dr. Rolf M. Schwiete Stiftung, the German Aerospace center DLR, NanoRacks LLC, DreamUp, Biovia, the BmWi (50JR1704) and DFG (BR2015/35-1; Wi1232/44-1), Nordlicht GmbH and ZEISS. This manuscript benefitted from the comments and suggestions of an anonymous reviewer.

Bibliography

Blum, J. 2006. Dust agglomeration. *Advances in Physics*, 55:881–947.

Blum, J. and Wurm, G. 2008. The growth mechanisms of macroscopic bodies in protoplanetary disks. *Astronomy & Astrophysics*, 46:21–56.

Brown, D. Tracker video analysis and modeling tool. https://physlets.org/tracker/, 2008.

Cuzzi, J. N. and Weidenschilling, S. J. 2006. Particle-Gas Dynamics and Primary Accretion. In Lauretta, D. S. and McSween, H. Y., editors, *Meteorites and the Early Solar System II*, page 353.

Cuzzi, J. N., Hogan, R. C., Paque, J. M., and Dobrovolskis, A. R. 2001. Size-selective concentration of chondrules and other small particles in protoplanetary nebula turbulence. *The Astrophysical Journal*, 546: 496–508.

Dominik, C. and Tielens, A. G. G. M. 1997. The physics of dust coagulation and the structure of dust aggregates in space. *The Astrophysical Journal*, 480:647–673.

Dominik, C., Blum, J., Cuzzi, J. N., and Wurm, G. 2007. Growth of dust as the initial step toward planet formation. In Reipurth, B., Jewitt, D., and Keil, K., editors, *Protostars and Planets V*, pages 257–263.

Forman, L. V., Bland, P. A., Timms, N. E., Collins, G. S., Davison, T. M., Ciesla, F. J., Benedix, G. K., Daly, L., Trimby, P. W., Yan, L., and Ringer, S. P. 2016. Hidden secrets of deformation: Impact-induced compaction within a cv chondrite. *EPSL*, 452:133–145.

Güttler, C., Blum, J., Zsom, A., Ormel, C. W., and Dullemond, C. P. 2010. The outcome of protoplanetary dust growth: pebbles, boulders, or planetesimals? i. mapping the zoo of laboratory collision experiments. *Astronomy & Astrophysics*, 513:A56.

Hayashi, C. 1981. Structure of the solar nebula, growth and decay of magnetic fields and effects of magnetic and turbulent viscosities on the nebula. *Progress of Theoretical Physics Supplements*, 70:35–53.

Jungmann, F., Steinpilz, T., Teiser, J., and Wurm, G. 2018. Sticking and restitution in collisions of charged sub-mm dielectric grains. *Journal of Physics Communications*, 2:095009.

Kataoka, A. Dust coagulation with porosity evolution. In Pessah, M. and Gressel, O., editors, *Formation, evolution, and dynamics of young Solar Systems*, pages 143–159. Springer International Publishing, 2017.

Kataoka, A., Tanaka, H., Okuzumi, S., and Wada, K. 2013. Static compression of porous dust aggregates. *Astronomy & Astrophysics*, 554:A4.

Kestin, J. and Leidenfrost, W. 1959. An absolute determination of the viscosity of eleven gases over a range of pressures. *Physica*, 25:1033–1062.

Konopka, U., Mokler, F., Ivlev, A. V., Kretschmer, M., Morfill, G. E., Thomas, H. M., Rothermel, H., Fortov, V. E., Lipaev, A. M., Molotkov, V. I., Nefedov, A. P., Baturin, Y. M., Budarin, Y., Ivanov, A. I., and Roth, M. 2005. Charge-induced gelation of microparticles. *New Journal of Physics*, 7:227–227.

Kruss, M., Teiser, J., and Wurm, G. 2017. Growing into and out of the bouncing barrier in planetesimal formation. *Astronomy & Astrophysics*, 600:A103.

LaMarche, K. R., Muzzio, F. J., Shinbrot, T., and Glasser, B. J. 2010. Granular flow and dielectrophoresis: The effect of electrostatic forces on adhesion and flow of dielectric granular materials. *Powder Technology*, 199:180–188.

Lasaga, A. C. and Cygan, R. T. 1982. Electronic and ionic polarizabilities of silicate minerals. *American Mineralogy*, 67:328–334.

Love, S. G., Pettit, D. R., and Messenger, S. R. 2014. Particle aggregation in microgravity: Informal experiments on the International Space Station. *Meteoritics & Planetary Science*, 49:732–739.

Marshall, J. R., Sauke, T. B., and Cuzzi, J. N. 2005. Microgravity studies of aggregation in particulate clouds. *Geophysical Research Letter*, 32:L11202.

Okuzumi, S. 2009. Electric charging of dust aggregates and its effect on dust coagulation in protoplanetary disks. *The Astrophysical Journal*, 698:1122–1135.

Ormel, C. W., Spaans, M., and Tielens, A. G. G. M. 2007. Dust coagulation in protoplanetary disks: porosity matters. *Astronomy & Astrophysics*, 461:215–232.

Pohl, H. A., editor. *Dielectrophoresis: The behavior of neutral matter in nonuniform electric fields*. Cambridge University Press, 1978.

Poppe, T., Blum, J., and Henning, T. 2000. Analogous experiments on the stickiness of micron-sized preplanetary dust. *The Astrophysical Journal*, 533:454–471.

Russel, S., Connolly Jr., H. C., and Krot, A. N., editors. *Chondrules: Records of Protoplanetary Disk Processes*. Cambridge University Press, 2018.

Shinbrot, T. 2014. Granular electrostatics: Progress and outstanding questions. *The European Physical Journal Special Topics*, 223:2241–2252.

Siu, T., Pittman, W., Cotton, J., and Shinbrot, T. 2015. Nonlinear granular electrostatics. *Granular Matter*, 17:165–175.

Spahr, D., Koch, T. E., Merges, D., Beck, A. A., Bolender, B., Carlsson, J. M., Christ, O., Fujita, S., Genzel, P.-T., Kerscher, J., Knautz, T., Lindner, M., Mederos Leber, D., Milman, V., Morgenroth, W., Wilde, F., Brenker, F. E., and Winkler, B. 2020. A Chondrule Formation Experiment Aboard the ISS: Experimental Set-up and Test Experiments. *Icarus*, 350:113898.

Steinpilz, T., Musiolik, G., Kruss, M., Jungmann, F., Demirci, T., Aderholz, M., Kollmer, J. E., Teiser, J., Bila, T., Guay, E., and Wurm, G. 2019. Arise: A granular matter experiment on the international space station. *Review of Scientific Instruments*, 90:104503.

Steinpilz, T., Joeris, K., Jungmann, F., Wolf, D., Brendel, L., Teiser, J., Shinbrot, T., and Wurm, G. 2020. Electrical charging overcomes the bouncing barrier in planet formation. *Nature Physics*, 16:225–229.

Stokes, G. G. 1851. On the effect of the internal friction of fluids on the motion of pendulums. *Transactions of the Cambridge Philosophical Society*, 9:8–106.

Suyama, T., Wada, K., and Tanaka, H. 2008. Numerical simulation of density evolution of dust aggregates in protoplanetary disks. i. head-on collisions. *The Astrophysical Journal*, 684:1310–322.

Weidenschilling, S. J. 1977. Aerodynamics of solid bodies in the solar nebula. *Monthly Notices of the Royal Astronomical Society*, 180:57–70.

Weidenschilling, S. J. and Cuzzi, J. N. 2006. Accretion dynamics and timescales: Relation to chondrites. *Meteorites and the Early Solar System II*, pages 473–485.

Zsom, A., Ormel, C. W., Güttler, C., Blum, J., and Dullemond, C. P. 2010. The outcome of protoplanetary dust growth: pebbles, boulders, or planetesimals? II. Introducing the bouncing barrier. *Astronomy & Astrophysics*, 513:A57.

CHAPTER 6

Publication III

Formation of fused aggregates under long-term microgravity conditions aboard the ISS with implications for early Solar System particle aggregation

Meteoritics & Planetary Science **submitted 20th July** (2021)

T. E. Koch[a], D. Spahr[a], B. J. Tkalcec[a], O. Christ[a], P.-T. Genzel[a], M. Lindner, D. Merges[a], F. Wilde[c], B. Winkler[a] and F. E. Brenker[a,c]

[a]Institute of Geosciences, Goethe-Universität Frankfurt, Altenhöferallee 1, 60438 Frankfurt, Germany
[c]Helmholtz-Zentrum Hereon, Max-Planck Strasse 1, 21502 Geesthacht, Germany
[c]Hawai'i Institute of Geophysics and Planetology, School of Ocean and Earth Science and Technology, University of Hawai'i at Mãnoa, 1680 East-West Road, Honolulu, HI 96822, USA

Abstract

Calcium-aluminum-rich inclusions represent the oldest aggregates of condensed dust of our Solar System and occur in very different, sometimes quite fragile looking morphologies and variable sizes in primitive meteorites. Besides information about the condition of the Solar Nebula at the time of their condensation, they can provide knowledge about the processes regarding the circumstances of aggregation, secondary melting, recrystallization, compaction as well as Solar Nebula dynamics and material transportion. In order to gain further insights into early Solar System aggregation processes, we carried out an experiment on board the ISS which allowed us to study the behavior of dust particles exposed to electric arc discharges under long-term microgravity. The experiment led to the formation of robust, elongated, fluffy aggregates, which were studied by SEM, EBSD and synchrotron micro-CT. The morphologies of these aggregates strongly resemble the typical shapes of fractal „fluffy-type" CAIs. We conclude that a small amount of melting could have supplied the required stability for such fractal structures to have survived transportion and aggregation to and compaction within planetesimals. Other aggregates produced in our experiment have a massy morphology and contain relict grains, likely resulting from the collision of grains with different degrees of melting, also observed in some natural CAIs. Some particles are surrounded by igneous rims which remind in thickness and crystal orientation of Wark-Lovering rims, another aggregate shows similarities to disk-like CAIs. These results imply that a (flash-)heating event with subsequent aggregation could have been involved in the formation of different morphological CAI-characteristics.

6.1 Introduction

The aggregation of particles in the Solar Nebula is generally considered as the first process leading to planet formation (Blum and Wurm, 2008; Dominik et al., 2007). Refractory inclusions such as calcium-aluminum-rich inclusions (CAIs) and amoeboid olivine aggregates (AOAs) are considered to be the oldest material of our Solar System (Connelly et al., 2012; Krot et al., 2009) and likely witnesses of early aggregation processes. The chemical properties of CAIs and AOAs have been intensively studied in the past with regard to their condensation origin (e.g., Connelly et al., 2012; Han and Brearley, 2015; Krot et al., 2004a; Krot et al., 2004b; Krot et al., 2009; Sugiura et al., 2010). Their structural characteristics, such as morphologies, texture and porosity bear further knowledge about the processes regarding the circumstances of aggregation, reheating, annealing, recrystallization, compaction as well as Solar Nebula dynamics and material transportion (Komatsu et al., 2001, 2009; Rubin, 2012; Sugiura et al., 2010).
With ^{207}Pb-^{206}Pb ages of 4567.30 ± 0.16 Ma (Connelly et al., 2012), CAIs formed as the first solids of the Solar System, close to the sun and probably over a period of 0.3 Ma (Kita et al., 2013). The sojourn time of CAIs in their original condensation region was probably very short, ca. 2000 years, until they were either drawn into the Sun or transportationed outwards (Taillifet et al., 2014). Since several generations of CAIs have been recognized, CAI transportation to the outer regions of the disk, by a yet undefined process, must have been a frequent event (reviewed in Krot, 2019).
CAIs (especially in CV chondrites) are classified according to their mineralogy in types A, B and C (Krot, 2019) and further characterized by morphology, texture and microstructure. Type A CAIs occur either as spheroidal and compact CAIs (Compact Type A: CTA) that have experienced melting, or as irregularly shaped, non-moltenfluffy-type CAIs (fluffy-type A: FTA). Type B CAIs are usually interpreted to have formed by melting and fractional crystallization (Blander and Fuchs, 1975).
Fluffy-type CAIs have very irregular, fractal structures which resemble the structures formed from hit-and-stick collision experiments and modelling (e.g. Blum and Wurm, 2008; Blum and Wurm, 2000). Aggregation of micrometer particles to millimeter-sized objects by surface adhesion at 1 AU was probably a fast process of 10 to 100 years (Brauer et al., 2007; Charnoz and Taillifet, 2012). However, the question arises how these fragile, fractal structures could survive turbulences and transportation to the outer protoplanetary disk (PPD), chondrite aggregation and subsequent compaction. One explanation is that FTA CAIs potentially aggregated parallel to their condensation (Russel et al., 2018). Another theory assumes FTA CAIs result from hit-and-stick collisions of CTA CAIs and minor melting (Rubin, 2012).
Some CAIs consist of several nodules covered multimineral layers, the so-called Wark-Lovering rims (WLRs) (e.g. Lorenz et al., 2019; MacPherson et al., 1982; Wark and Lovering, 1977). Different formation scenarios have been proposed, such as condensation (Bolser et al., 2016; MacPherson et al., 1985; Wark and Lovering, 1977) or metasomatosis on the parent body (MacPherson et al., 1982). Other studies proposed that flash-heating, which melted the outer region of the PPD, could be involved in WLR formation (Han et al., 2020; Wark and Boynton, 2001). It is also unclear, whether WLRs formed immediately after CAI formation or about 1 millionyear after the formation of the latter, since isotopic studies give conflicting information, which, however, could also be due to later isotopic disturbances in the Nebula (Han et al., 2020).
Some igneous Type B CAIs have a disk- or bowl-shaped morphology (Ivanova et al., 2008), which was interpreted to result from areodynamical deformation and shock-flattening (Lorenz et al., 2019), or more complex scenarios which include ejection from the inner Solar System

and remelting during reentry at hypersonic speed (Liffman et al., 2016). Further relations between the morphology of CAIs and aerodynamical effects have been proposed in the most recent study of Zhang et al. (2021) in which the studied CAIs and AOAs have an elongated or a bent fractal morphology, interpreted as resulting from movement induced by e.g. radial drift.
Experiments can help to understand early Solar System processes and different experimental approaches have been established. Micro-gravity experiments regarding particle aggregation in the Solar Nebula are well established and have already delivered valuable findings (e.g. Beitz et al., 2012; Blum, 2010; Blum, 2010, Blum et al., 2002; Steinpilz et al., 2020, Wurm and Blum, 1998. Experiments addressing the process of thermal annealing of early Solar System materials, which are mostly focused on chondrule formation (Hewins et al., 2005), have so far only been carried out on Earth and have mostly involved static samples.
To complement these different types of experiments, we developed a proof-of-concept-experiment which was carried out under long-term microgravity conditions aboard the International Space Station (ISS) to combine aggregation, heating and thermal annealing of dust particles (Spahr et al., 2020). In this experiment, freely floating Mg_2SiO_4 dust particles were exposed to arc discharges inside a glass sample chamber with the aim to test how arc discharges influence the behavior of dust particles. A camera allowed the observation of the particles in real time and the sample material was analyzed after sample return to Earth. In the study presented here, we show the formation of aggregates using flash-heating under microgravity conditions which can be linked to the formation of refractory inclusions with regard to their morphology and microstructure.

6.2 Methods & Materials

6.2.1 ISS experiments

The experimental set-up is described in detail in Spahr et al. (2020). The experiment was set-up inside a $10 \times 10 \times 15\,\mathrm{cm}^3$-sized NanoRacks NanoLab, which was connected to the ISS by USB. The sample chamber consisted of quartz glass and two tungsten electrodes with a diameter of 1 mm were fused into the glass on opposite sides. The distance between the tips of the electrodes was approx. 2 mm. The sample chamber was loaded with 30 mg of the sample material and 100 ± 1 mbar Ar gas. A detailed description of the generation and calibration of the arc discharges is given in Spahr et al. (2020). In total, 81 arc discharges with energies of 5–8 J and durations between 300 and 500 µs per discharge were induced. The generation of the arc discharges also applied an electric field between the electrodes beginning approx. 2 min before the arc discharges. The area between the electrodes was filmed during the charging process and the arc discharges with a Raspberry Pi V2 camera with a field of view (FOV) of $2.73 \times 3.63\,\mathrm{mm}^2$.

6.2.2 Sample material

The initial sample material consisted of well-characterized synthetic forsterite particles (Spahr et al., 2020). Figure 6.1a shows a focus-stacked SEM BSE image of three representative initial particles. Fig. 6.1b shows several embedded and polished initial grains. Characteristics for the polished samples are numerous evenly distributed small pores. The grains are irregularly shaped with rough surfaces. EBSD analysis of the initial particles showed that the particles are fine-grained, consisting of crystals with (circular equivalent) diameters of 5–10 µm, with a few exceptions where larger crystals >20 µm are present (Koch et al., 2021b). In the initial sample material the crystals are randomly oriented within each grain. The grain size

analysis of the initial sample material was carried out using ImageJ (Rueden et al., 2017). Therefore, the grains were evenly distributed in a petri dish and photographed under an optical microscope. The photographs were transformed into black and white images, where the particles are displayed as black areas with the shape of the particles. This type of images will be called threshold images in the following text. Fig. 6.1c shows a histogram of the areas of a random sampling of 849 grains fitted with a normal distribution function. The mean area obtained from the fit is $0.012\,\mu m^2$ and, due to the heterogeneity of the particle shapes, the distribution is rather broad ($\sigma = 23$). Figure 6.1d shows the correlation of the major to the minor ellipse axes, likewise indicating the variability of the particle morphologies. The grain size analysis of the transformed samples was undertaken with the same method. The sample chamber was loaded with 30 mg of the sample material. Approximating the average volume of a single grain by a spherule with a diameter of 126 µm and a porosity of 10vol%, the total number of particles is in the range of 10^4 particles which represents a particle density of approx. $1.6 \times 10^{-3}\,g\,cm^{-3}$.

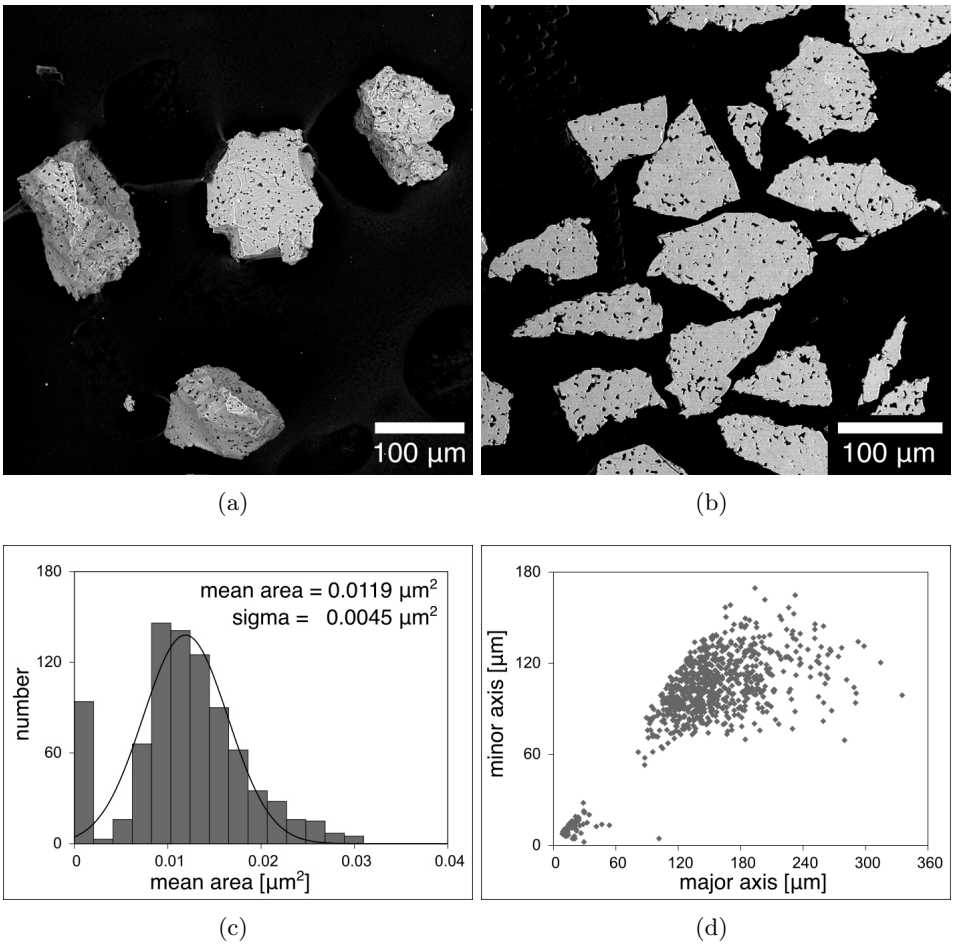

Figure 6.1: Initial sample material. (*a*) Focus-stacked representative porous initial dust particles used as starting material. (*b*) Polished grains of the initial starting material. The particles have highly heterogeneous morphologies and a large amount of evenly distributed small pores. (*c*) Histogram of the grain size distribution of a random sample containing 849 grains fitted with a normal distribution function. (*b*) Correlation between the minor and major axes of best-fit ellipses of the initial material.

6.2.3 Analytical procedure and sample preparation

Scanning electron microscopy (SEM) imaging was performed using a Phenom World ProX desktop SEM equipped with an electron backscatter detector (BSE) at the Geoscience Institute at the Goethe University. Energy dispersive X-ray spectroscopy (EDX) was carried out with an integrated silicon drift detector (SDD) for a semi-quantitative characterization of the chemical composition. The non-coated samples were measured under low vacuum conditions; the polished and carbon-coated samples were measured under high vacuum conditions. For imaging, we used an acceleration voltage of 10 kV while for EDX analysis a voltage of 15 kV was employed. Multiple BSE images were acquired with different focal planes and combined afterwards with the Helicon Focus 7 Pro (Kozub et al., 2018) software from Helicon. EDX data were analyzed using the Phenom Pro Suite software.
EBSD fabric analysis is especially suited to identify structural and textural properties of materials and is increasingly employed as an analytic tool to investigate the remnants of Solar Nebular processes in planetary materials (Bland et al., 2011; Tkalcec et al., 2013). EBSD was performed at the Geoscience Institute at Goethe University Frankfurt with a Jeol scanning electron microscope JSM 6490. The SEM is equipped with a Nordlys II phosphor screen EBSD detector with Channel 5 software from Oxford Instruments and HKL Technology. EBSD was performed with an acceleration voltage of 15 kV, a working distance of 20 mm and a Si-wafer as calibrant. EBSD data was acquired by automated mapping performed at step sizes of 0.8–1 µm with low gain, 2×2 pixel binning, and a mean angular deviation (MAD) limit of $< 1.3°$. Following data acquisition, no noise reduction at all was performed on the acquired EBSD data. Contoured pole figures are displayed as multiples of uniform density (m.u.d.), with a half width of 10°. The initial sample material as well as the experimental outcomes were embedded in Araldite epoxy resin, polished with Syton polish and thinly coated with carbon.
Synchrotron-based micro-CT was performed at PETRA III (DESY) in Hamburg, Germany. All data were collected on the micro tomography beamline P05 (Moosmann et al., 2014; Ogurreck et al., 2013; Wilde et al., 2016), operated by Helmholtz-Zentrum Hereon, using a 15 keV beam monochromatized by a double crystal monochromator. The images were acquired with a 24× magnification using a CMOS camera resulting in an approx. $1.8 \times 1.8\,\mathrm{mm}^2$ field of view. We used an acquisition time of 350 ms. A binning factor of 2×2 pixel resulted in a binned pixel size of approx. $0.61 \times 0.61\,\mathrm{mm}^2$. The samples were completely embedded in Araldite epoxy resin.

6.3 Results

6.3.1 Analysis of the video recording

The experiments were filmed and the videos could be analyzed in order to observe the behavior of particles in response to arc discharges. Figure 6.2a shows the field of view prior to the arc discharge experiments. The tips of the electrodes are visible on opposite sides of the image. The first two arc discharges were induced while the space between the electrodes was empty. The arc discharges agitated the particles inside the sample chamber. Subsequently, the moving particles were attracted by the electric field between the electrodes and formed chains parallel the electric field lines. The distance between the single chains of particles decreased with increasing charge build-up and the particles formed a dense aggregate levitating between the electrodes, which is shown in Fig. 6.2b. This aggregate was destroyed by the arc discharges and the particles were agitated to a random particle motion. The particles were then attracted by the electric field between the electrodes which was applied between two arc discharges

and formed again chains of particles. However, the number of particle chains which formed between the electrodes decreased with the number of arc discharges to approx. 2–3 chains of particles. In total, particle chains were present prior to 27 arc discharges. The first small aggregate (2–3 fused particles) was observed after the fourth arc discharge and the number of observed aggregates increased with increasing arc discharges. The aggregates were observed either when they crossed the field of view agitated by the discharges, or when they were attracted by the electrodes when the capacitors were charged. Selected frames from the video material showing some representative aggregates are shown in Figure 6.2c–g. The massy, approx. 300 µm-sized aggregate in Fig. 6.2c crossed the field of view after the 16^{th} arc discharge. Figure 6.2d shows an elongated aggregate attracted to the electrode after the 34th arc discharge. Fig. 6.2e is a frame shot from the video after the 75^{th} arc discharge, where three different aggregates levitated parallel the electric field lines between the electrodes similar to the particles in Figure 6.2b. One of these aggregates is elongated (top), while the other two aggregates show are curved. The elongated, bulbous aggregate in Figure 6.2f appeared after the last arc discharge. It was not possible to assign a specific aggregate to a specific discharge event or to distinguish whether the particles melted inside the plasma channel or by thermal radiation due to the frame rate. The focus plane of the camera objective was very small and many aggregates crossing the field of view were not in focus to allow subsequent identification (and discharge allocation) at the end of the experiment.

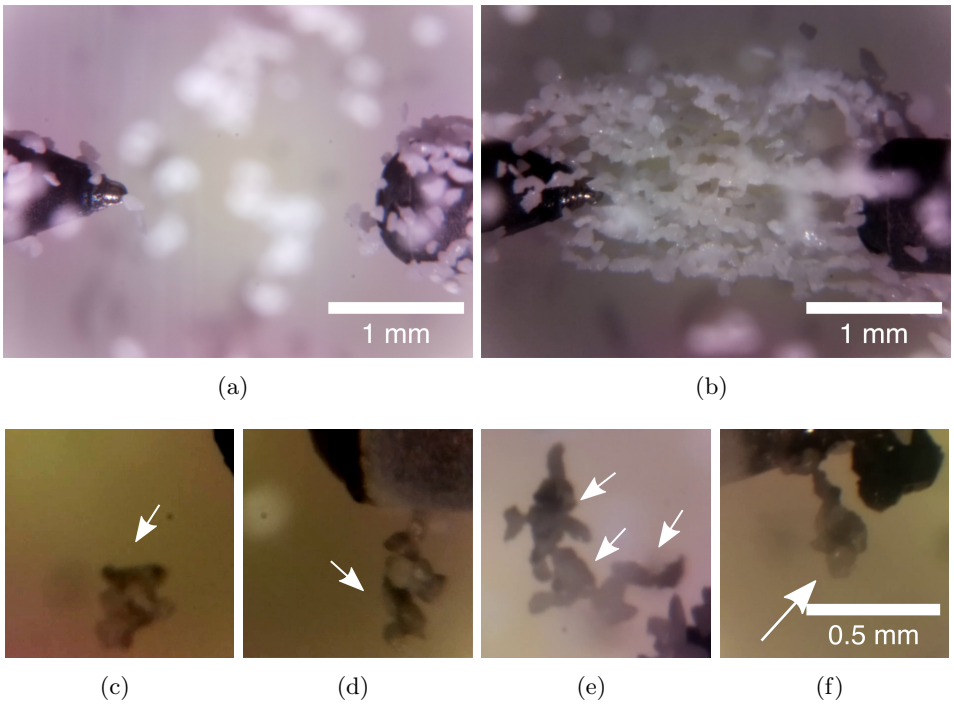

Figure 6.2: Selected frames from the video material and particle aggregation during the experiment. (*a*) The field of view prior to the arc discharge experiments. The tips of the electrodes are shown on opposite sides of the image. (*b*) The particles formed chains along the field lines between the two electrodes prior to the third arc discharge. (*c*) A massy aggregate (white arrows) which appeared after the 16th arc discharge (contrast enhanced). (*d*) An elongated aggregate (white arrows) appeared after the 34^{th} arc discharge (contrast enhanced). (*e*) Three fused aggregates after the 75th arc discharge (white arrows). (*f*) An elongated, bulbous aggregate (white arrow) detected after the 81^{st} arc discharge (contrast enhanced). Scale bar for (*c*)–(*g*) is displayed in (*f*).

6.3.2 Morphology analysis of fused aggregates

More than 100 newly formed objects including single spherules and fused aggregates could be detected after sample return. Due to the large amount of sample material in the recovered sample chamber, it seems likely that this number is underestimated for melt spherules and small aggregates and more are hidden in the remaining dust. The formed objects can be divided into different groups according to their characteristics. Fig. 6.3 shows the threshold images of the initial grains (*a*) and the experimentally transformed objects, the latter sorted into eight groups (B-I) according to their morphological characteristics. The coordinate numbers in this diagram are used as reference frame for identification of the specific aggregates described in the following text. The most abundant sample type group consists of 21 single melt spherules (group B and C) in addition to five melt spherules which are fused to other single particles (group C and D). This number is probably underestimated, because not all melt spherules could be detected among the high amount of initial particles. Another large group represents small aggregates consisting of 2–4 grains (group D and E). Group F shows aggregates with an elongated morphology. The most conspicuous morphology is displayed by the aggregates in rows G and H. Their morphology is characterized from curved fused chains of particles up to clear boomerang-shaped morphologies. Group I includes aggregates, which consist of several fused grains merged to one massy object, where the different initial grains could not be distinguished anymore. Some single grains were fused to the surface. To simplify, these aggregates will be called massy aggregates in the following text. The total area of all aggregates divided by a mean aggregate diameter of 126 µm results in approximately 300–400 reacted initial grains, which is 3–4% of the initially loaded sample amount.

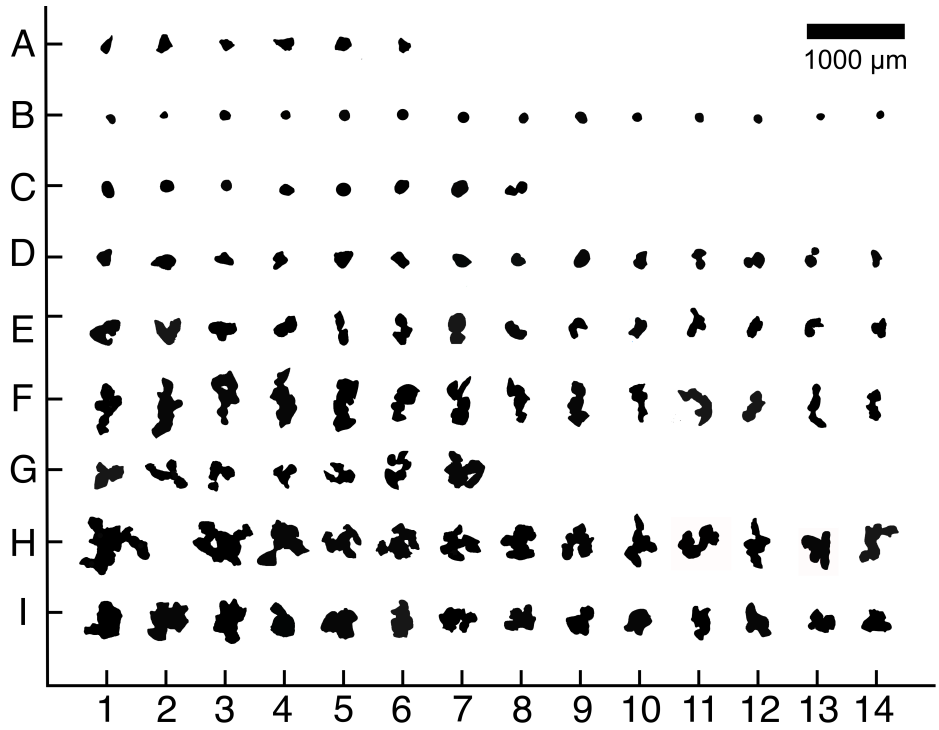

Figure 6.3: Threshold image of the initial grains and formed objects. Eight different types of experimental outcomes (Groups B-I) were detected. A: Representative initial sample grains. B & C: Melt spherules. D & E Small aggregates. F: Elongated aggregates. G: Small fluffy or three-winged aggregates. H: Fluffy aggregates with a three-winged boomerang-shapes morphology. I: Aggregates that are completely massy or have a massy center. The object numbers in this diagram serve for identification of the specific objects referred to in the following analysis.

The area sizes of the different aggregates are plotted in the histogram in Fig. 6.4a. There is a strong decrease in frequency towards larger sizes, especially considering the number of single melt spherules (morphology groups B and C) is probably underestimated. Figure 6.4b shows length of the major axis versus the minor axis of the approximated ellipsoids of the resulting material in comparison to the sizes of the initial material. Table 6.1 summarizes the ratios between the longest (b) and shortest dimension (c) of the 14 elongated aggregates of group F. The mean b/c ratio is 2.1(2).

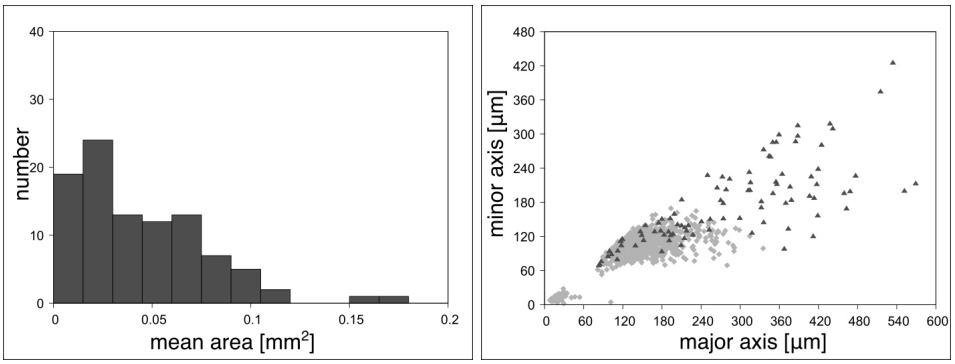

(a) (b)

Figure 6.4: Size analysis of the newly formed objects. (a) Histogram of the area size distribution. (b) Major axis versus the minor axis of the approximated ellipsoids of the resulting material (dark grey) in comparison to the sizes of the initial material (light grey).

Table 6.1: Ratio of the longest (b) versus shortest (c) dimensions of the elongated aggregates (Fig. 3 Group F).

no.	F1	F2	F3	F4	F5	F6	F7
b/c	1.9	1.9	1.9	2.2	2.1	1.9	2.1
no.	F8	F9	F10	F11	F12	F13	F14
b/c	2.3	2.0	2.2	1.7	1.8	2.3	2.3

6.3.3 Syncrotron micro-CT analysis

Some aggregates were studied with synchrotron micro-CT to study their morphology and internal structure. Figures 6.5a–c shows aggregates (from groups G and H), which have a more or less boomerang-shaped morphology, whereas Figures 5d and e show elongated aggregates (from group F). These aggregates consist of approximately 7–10 initial particles. The aggregate in Figure 6.5d consists mostly of angular grains with porous surfaces similar to the initial starting material. The surface of the aggregate in Figure 6.5e is mostly smooth. Figure 6.5f shows a virtual slice through the aggregate in 5e (grey box), revealing that at least three initial grains were fused. The grain boundaries (white arrows) are molten, displaying larger, spherical pores and a slightly higher density (brighter in the image) than in the unmolten areas. The three boundaries meet in the center in a triple junction (Fig. 6.5f, center).

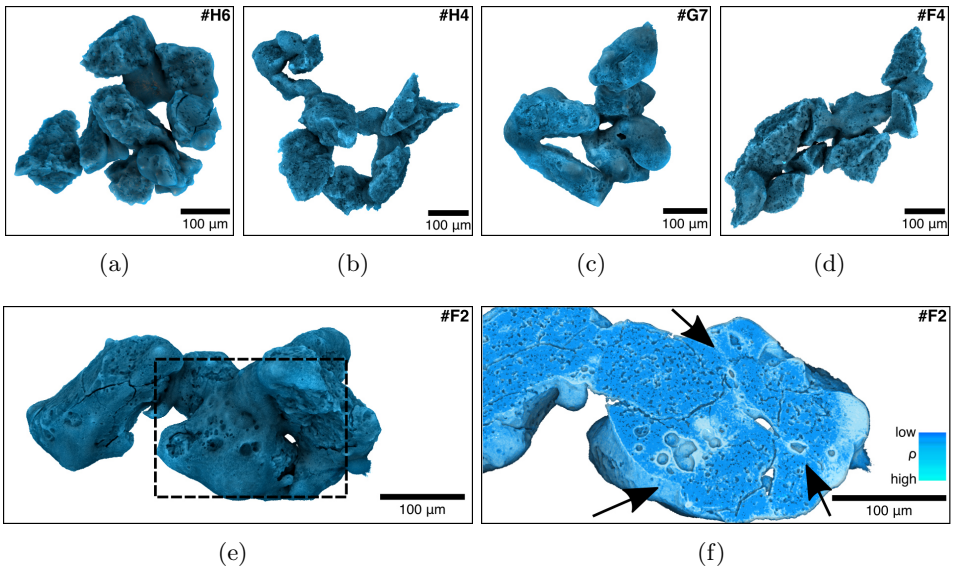

Figure 6.5: CT projection of some generated fused aggregates from morphology groups F, G and H. (a,b,c) show aggregates with a boomerang-shaped morphology. (*d*) and (*e*) show elongated aggregates. The aggregate in (*d*) consists mostly of grains with the initial angular and porous surface. The surface of the aggregate in (*e*) is mostly smooth with a few porous areas. (*f*) A virtual slice through the aggregate in (*e*) (black square) reveals a generally more porous interior. The triple junction in in the middle of the right part of the aggregate suggests that at least three grains were fused and form a triple junction. While the centers of the fused grains appear unprocessed, the interstitial areas (marked by arrows) have lost their original pore structure and instead, larger, spheroidal voids are present. Furthermore, these areas appear brighter which is indicative of a higher density and is probably due to tungsten precipitations. The outlines of the pores and cracks appear bright because of edge enhancement due to coherence.

6.3.4 SEM analysis

SEM analysis was also used to study the morphology and composition of the aggregates. The analysis of the single melt spherules was part of an earlier study (Koch et al., 2021b). Fig. 6.6 shows focus-stacked BSE images of some representative aggregates from morphology groups F (elongated) and H (boomerang-shaped). All aggregates consist of dust grains with various degrees of melting. Fig. 6.6a shows the largest formed object, which has formed from approximately 20 initial grains. The object has an almost perfectly symmetric, three-winged morphology with a diameter of approximately 720 µm. Figure Fig. 6.6b shows a close-up of the longest arm which consists of a bent chain of fused grains. A high percentage of the surface is molten material; however, the internal structure is visible through some cavities in the surface.

The molten surface shows fine lines of tungsten precipitation which appear bright in the BSE images. These precipitation arose from evaporation of the tungsten electrodes. However, since the aggregates were not carbon-coated prior to SEM analysis, surface charging may also be responsible for some bright artefacts. Fig. 6.6c shows one of the elongated aggregates with a length of 425 µm. The surface of the grains in the middle area of the aggregate was completely molten (Fig. 6.6d), the outer grains show the initial surface structure. The object in Fig. 6.6e has a length of approx. 500 µm. One part of the aggregate consists of a 170 µm-sized flat disk (Fig. 6.6f) displaying a very strong tungsten pattern on its surface.

Some aggregates were polished before SEM analysis (Fig. 6.7). The polishing reveals different thermal histories of particles in more detail and even grains that are directly fused to each other have experienced very different degrees of melting. Figure 6.7a shows a grain which

is only molten on the surface next to two nearly unprocessed initial particles. Figure 6.7b shows three or four fused grains. One grain was probably completely molten with very few tungsten inclusions on one side and some round pores. The elongated grain in the middle is interspersed by tungsten precipitations next to a nearly unprocessed particles. Figure 6.7c shows a grain from aggregate #E9, which was melted on the surface, while the inner structure of the grains underwent only light thermal annealing. Figure 6.7d shows a close-up of one of the fused grains of the fused aggregate #E1. The grain shows an igneous rim with a thickness of approx. 17–22 µm displaying the typical tungsten precipitation lines and spherical pores indicative of melting.

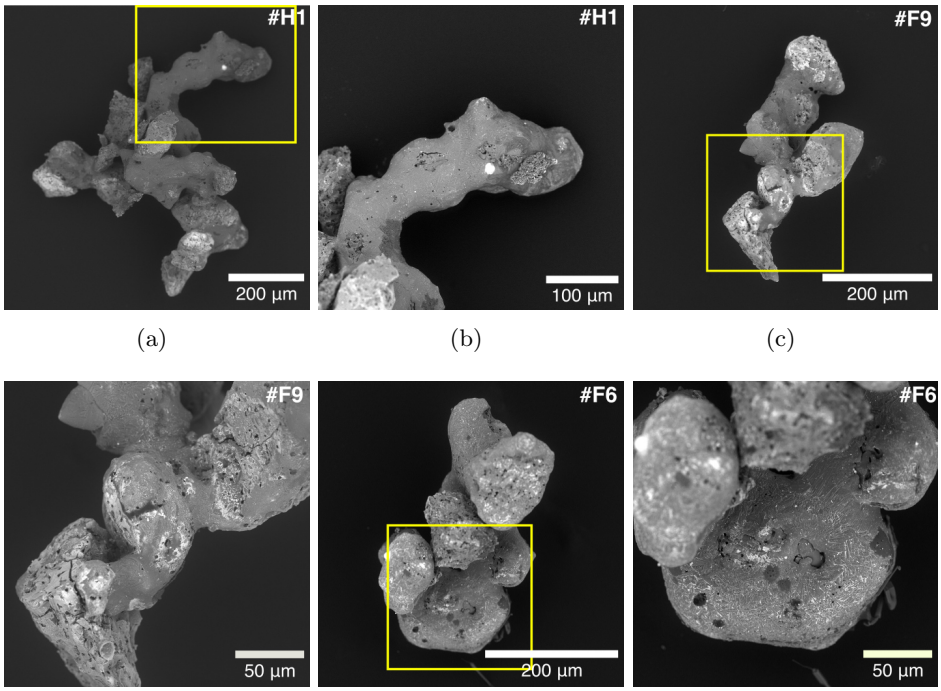

Figure 6.6: Focus-stacked SEM BSE images of representative fused aggregates from morphology groups H and F. (*a*) Aggregate with a nearly perfectly three-winged, boomerang-shaped morphology. (*b*) Close-up of the largest wing showing a molten surface with tungsten precipitation lines. Opening in the surface reveals a more porous interior. (*c*) Elongated aggregate. (*d*) Close-up of the aggregate in c showing completely molten inner region between particles. (*e*) Elongated aggregate with a flat, molten disk. (*f*) Close-up of the disk with tungsten precipitations. Yellow boxes in a, c, e and g denote the positions of the close-up images in b, d, f and h, respectively.

Fig. 6.8 shows the SEM and EBSD analysis of the polished aggregate #I12. The aggregate has a massy core and is droplet-shaped. Its size suggests that it fused from 4–6 initial grains. Fig. 6.8a shows an overview of the polished aggregate. Several areas with the original pore structures could be identified (yellow dashed lines). Figure 6.8b shows a close-up of the molten area between the initial areas. The molten area shows the typical tungsten precipitations pattern with parallel lamellae. This area was studied with EBSD in more detail and all indexed patterns were indexed as forsterite. Fig. 6.8c shows the band contrast image superimposed with an all-Euler angle map. The grain sizes identified in the band contrast image, displayed by black boundaries from the overlapping of two adjacent signals and defined by a misorientation threshold of 10°, are larger than those originally inferred from the tungsten precipitation patterns. This indicates that misorientation angles between the intragrain tungsten lamella are less than 10°. The all-Euler map confirms the presents of some

large grains, several of which display well-indexed interiors with negligible intragrain misorientation whereas others, for example the large center grain, reveal several non-indexed areas. In the latter case, however, all indexed points show the same uniform all Euler orientation confirming the single-grain identification shown by the grain boundaries of the sub-imposed band contrast map. The crystallographic orientations of these large forsterite grains are revealed by pole figures (Fig. 6.8d) contoured by multiples of uniform distribution (m.u.d.) set at maximum 12. Since no noise reduction at all was made on the raw data, the few tight point maxima (red) likely reflect duplication (non-adjacent points measured from the same large grain but identified as individual grains) in grains where indexing was not continuous. Thus, each large red m.u.d. maximum contour is interpreted as a single grain. The crystallographic [100] axes plot as broad N-S point maxima of several grains and the [010] axes possibly as a broad E-W girdle, although the latter should be seen with caution due to the small number of grains involved.

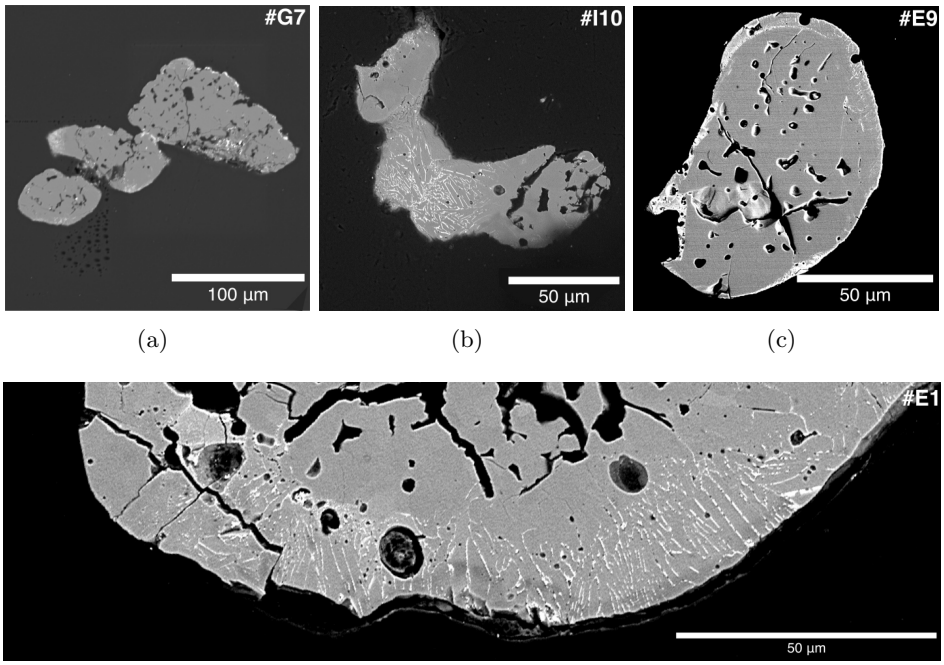

Figure 6.7: SEM analysis of polished aggregates. (*a*) Three grains which still reveal the original pore structure and were only fused on the surface. (*b*) Three fused aggregates with three different thermal histories. The center grain displays abundant tungsten precipitation lines and was probably completely molten. The upper grain has lost its initial pore structure but includes less tungsten. The third grain shows molten outer regions, but the initial pore structure in the interior regions. (*c*) Particle of aggregate #E9 which is completely surrounded by a tungsten bearing igneous rim. The inner part of the grain is nearly unprocessed, however the pores have slightly changed and appear more round than in the initial material. (*d*) Close-up of one of the fused grains of the fused aggregate #E1. The grain shows an igneous rim with a thickness of approx. 17–22 µm displaying the typical tungsten precipitation lines and spherical pores indicative of melting.

One of the igneous rims (particle #E1) was also studied with EBSD. The BSE image in Figure 6.9a reveals that the rim of particle #E1 is clearly different compared to the initial material. Tungsten precipitation is strongly present in the grain boundaries (Fig. 6.9a) and often form parallel lamellae perpendicular to the particle surface. In addition, a multitude of tiny tungsten spots that appear to be arranged in a linear layer parallel to (and about 14 µm inside) the particle rim. This tungsten layer runs perpendicular to the tungsten lamellae, which it appears to truncate, thus dividing each grain into the tungsten- lamellae-bearing

(TL) and tungsten-free (TF) zones. The corresponding EBSD all-Euler phase map reveals a number of large grains all aligned with their longest dimension perpendicular to the surface (Fig. 6.9c). The crystal directions of the grains plotted in the pole figures in Figure 6.9c confirm a strong crystallographic preferred orientation of all grains. The tungsten lamellae which are oriented perpendicular to the particle surface and parallel to the longest dimension of the grain in each case, dividing the part of the grain closest to the rim into parallel zones with negligible misorientation to one another.

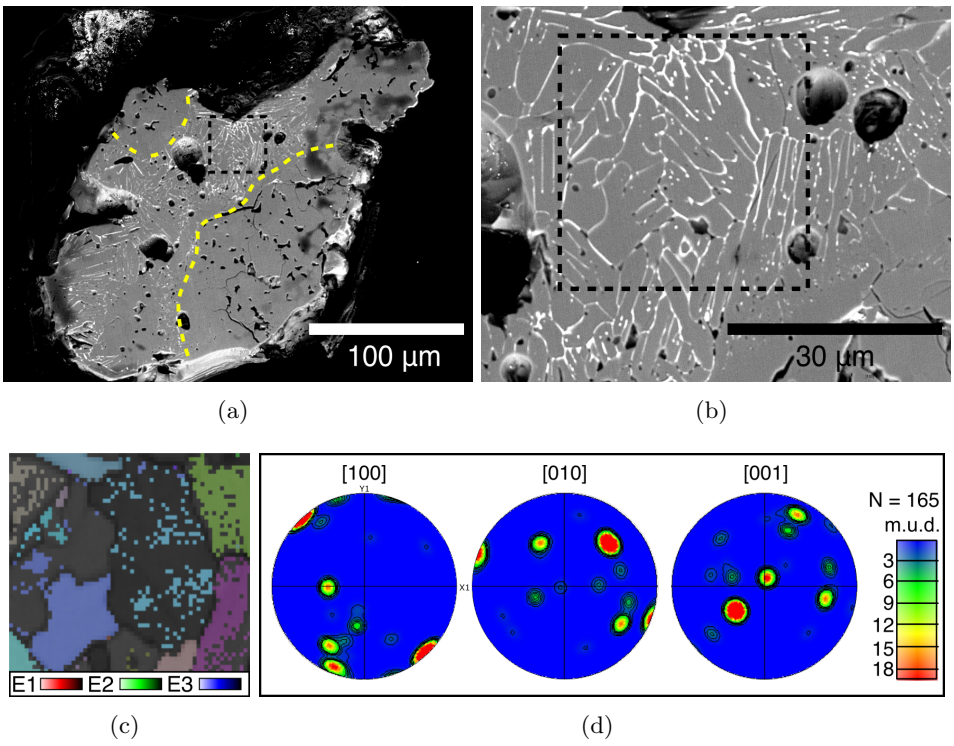

Figure 6.8: SEM and EBSD analysis of a polished massy aggregate #I12. (*a*) SEM BSE overview of the polished aggregate. The yellow dashed lines indicate the boundaries between molten and original sample material. (*b*) A close up of the molten area (black dashed square). The bright lines and inclusions represent tungsten precipitations. (*c*) EBSD band contrast image with overlying all Euler angle map of forsterite of the area marked by the dashed square in a and b. (*d*) Stereographic projections of EBSD data of the area shown in c.

6.3.5 Timescales of aggregation

The duration of aggregate formation in the experiments depended on the collision timescale and the cooling rates of the particles. The collision time t_{coll} describes the mean time of a grain between two collisions (Marrocchi et al., 2019; Nakagawa et al., 1981) and can be expressed as Equation 6.1:

$$t_{\mathrm{coll}} = \frac{1}{n_p 4\pi a^2 \Delta v_{\mathrm{coll}}}, \tag{6.1}$$

Where Δv_{coll} is the particle-particle velocity which is assumed to be similar to the collision velocity, a is the mean particle radius, n_p is the particle density (5500 particles per cm^3). The particle velocities v_{coll} after arc discharges were determined for different particles from the videos (see Koch et al., 2021a). The measured particle velocities are in the range of $>25\,\mathrm{mm\,s^{-1}}$ with a subsequent exponential deceleration due to gas drag. We calculated t_{coll}

for different velocity profiles using the fitting parameters from Koch et al. (2021a). Figure 6.10a shows some representative collision times of particles after arc discharges dependent on the time after the discharge events. Immediately after the arc discharge, the mean time between two collisions of a particle is in the range of 0.01 and 0.2 s Consequently, aggregates which consist of approx. 20 particles could have formed in 0.2–0.4 s. Furthermore, the particle size a will increase with ongoing collisions, which results in shorter collision times.

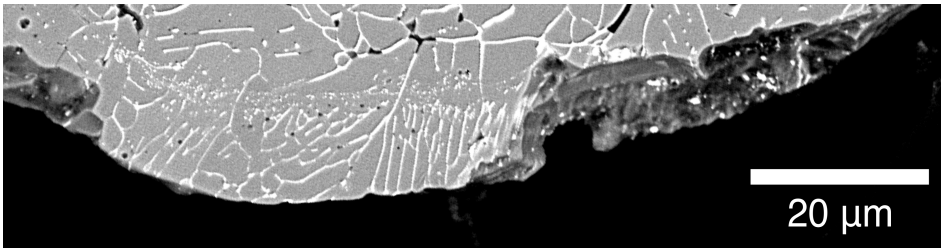

(a)

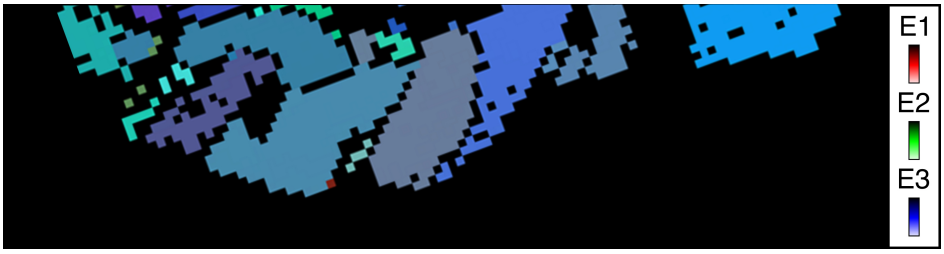

(b)

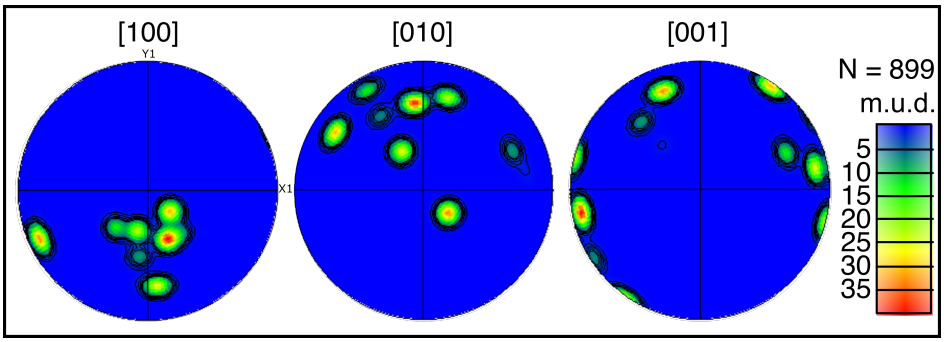

(c)

Figure 6.9: EBSD analysis of the igneous rim of an aggregate. (*a*) BSE image of the rim of one particle of aggregate #E1. The lines which appear white in the BSE image represent tungsten precipitations. Grains show a tungsten-lamellae (TL) and tungsten-free (TF) zone. (*b*) EBSD all-Euler map displaying the grain boundaries reveals that the observed sets of mostly parallel tungsten lamellae are intracrystal. (*c*) Stereographic projections of EBSD data of the rim. The grains show preferred orientation in all three crystallographic axes.

Another limitation for the duration of aggregate formation is the cooling rate of particles, because the particles have to be plastic to fuse in collisions. The lower temperature limit for the formation of compound chondrules was defined to be 1400 K, which represents the lowest temperature were silicate melts were present in chondrule melt (Bischoff et al., 2017; Ciesla et al., 2004). We used this temperature as a lower limit for the calculation of the timescale of aggregate formation in the experiment, because the used sample material consists of Mg_2SiO_4. The cooling rates of chondrules melted by lightning are usually modelled by radiative cooling

of a grey body (Eq. 6.2) (Morris and Desch, 2010). The temperature of the chondrule analogue after the arc discharge is given by the liquidus temperature of forsterite of 2.163 K (Bowen and Schairer, 1925) and the temperature aboard the ISS is estimated to be 290 K. Equation 2 gives the change of the internal energy U of a radiating spherical grey body with time:

$$\frac{\partial U}{\partial t} = \epsilon \cdot \sigma \cdot A \cdot (T^4_{\text{sample0}} - T^4_{\text{ISS}}), \tag{6.2}$$

Where U is the internal energy, t the time after the heating pulse in s, ϵ the emissivity (for reference, a black body has an emissivity of 1), σ the Stefan-Boltzmann constant, A the surface area of the spherule and T_{sample0} the temperature of the heated spherule at time 0 and T_{ISS} the temperature of the surrounding, both in K. ΔU for a short dt can be obtained using Equation (Eq. 6.3).

$$\Delta U = \epsilon \cdot \sigma \cdot A \cdot (T^4_{\text{sample}} - T^4_{\text{ISS}}) \cdot dt, \tag{6.3}$$

The change in U can also be described by means of the temperature dependent specific heat capacity $c_p(T)$ in $\mathrm{J\,mol^{-1}\,K^{-1}}$, the change in Temperature of the spherule ΔT in K and the amount of substance in mol (Equation 6.4). The amount of substance n is calculated for different spherule sizes using the volume of the spherule, the density of forsterite ($3.275\,\mathrm{g\,cm^{-3}}$, and the molar mass of forsterite ($140.693\,\mathrm{g\,mol^{-1}}$) (Anthony et al., 2018).

$$U = c_p(T) \cdot n \cdot (\Delta T), \tag{6.4}$$

Combining Equation 6.3 and 6.4 gives an expression for the change of temperature of the spherule during a short time of radiation (Eq. 6.5).

$$\Delta T = \frac{\epsilon \cdot \sigma \cdot A \cdot (T^4_{\text{sample0}} - T^4_{\text{ISS}}) \cdot dt}{c_p(T) \cdot n}, \tag{6.5}$$

The resulting ΔT is subtracted from T_{sample0} to derive the new temperature of the spherule T_{sample1}. Using this new temperature, the calculations are iterated N times until T_{sampleN} is sufficiently close to T_{ISS} (291 K in this case). The specific heat capacity $c_p(T)$ in Equation 6.3 is calculated for each iteration step with the data from the data from the NIST Standard Reference Database (see NIST in reference section) .
The cooling rates of the particles were determined to be 10^7–10^4 $\mathrm{Kh^{-1}}$ shortly after the arc discharges (Koch et al., 2021a). Figure 6.10b shows the temperature of the particles with different sizes after the discharge events. The particles were cooled to 1400 K in between 0.2 and 0.5 s. Thus, it is likely that aggregate formation in the experiment was a really fast process of <5 s after the discharge events, which is in accordance with the results from the collision time determination.

6.3.6 Morphology analysis of natural CAIs

To compare the morphology of the aggregates formed in the experiment with natural CAIs, a random sample of representative CAIs in the CV3 chondrite NWA 13656 were analyzed regarding their morphology. Figure 6.11 shows optical microscopic images of different types of fractal inclusions. Figure 6.11a shows an inclusion with 3–4 wings. Figures 6.11b and c show inclusions which have a massy center and several attached nodules. Figure 6.11d shows a very elongated inclusion.

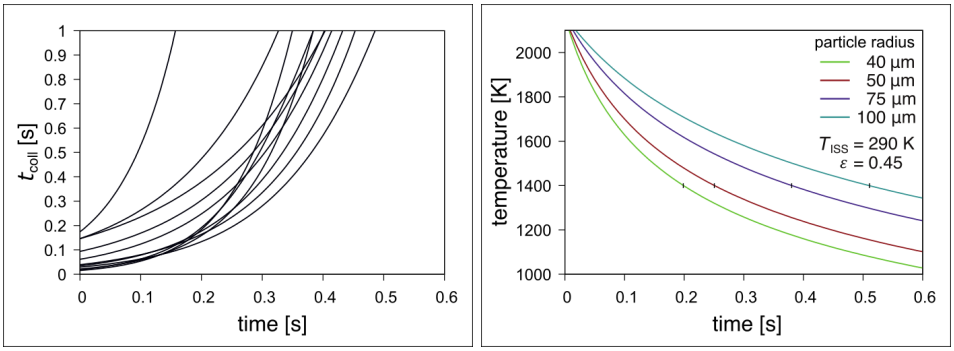

(a) (b)

Figure 6.10: Collision times t_{coll} of particles inside the sample chamber and cooling rates of the particles after arc discharges. (*a*) t_{coll} versus the time after the arc discharges is plotted for several grains after different arc discharges. (*b*) Calculated temperatures of particles with different radii versus time after the arc discharges inside the sample chamber.

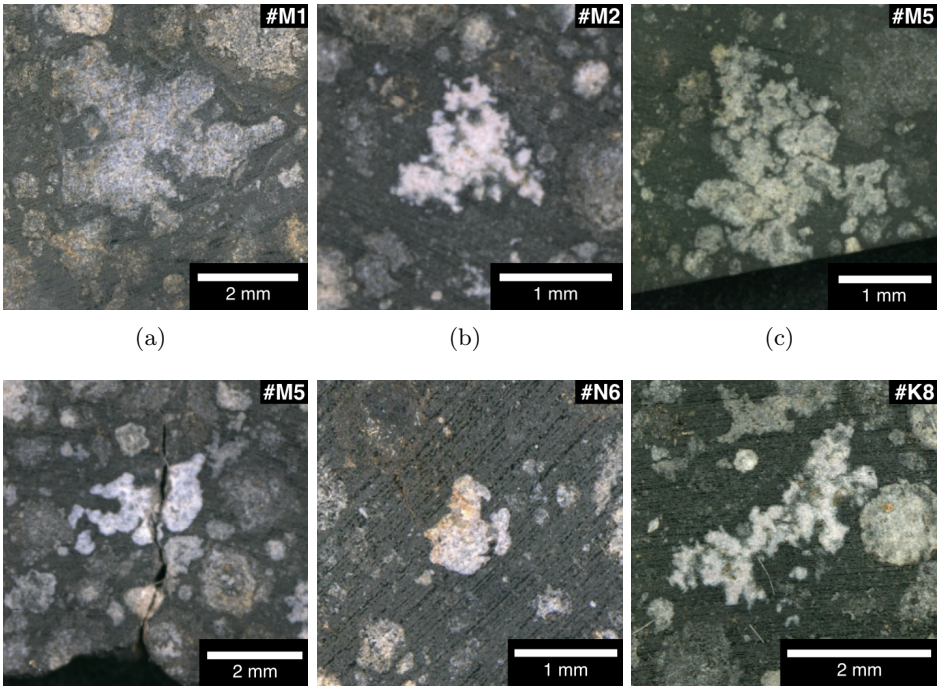

(a) (b) (c)

(d) (e) (f)

Figure 6.11: Photographs of irregular inclusions on slices of NWA 13656. (*a*) Inclusion with four wings. (*b*) Tringle-shaped inclusion (*c*) Three-winged inclusion. (*d*) Inclusion with a massy center and two attached nodular wings. (*e*) Inclusion with a massy center and several attached nodules. (*f*) Elongated inclusion.

Threshold images of the different inclusions in NWA 13656 were used for the morphology analysis. Figure 6.12 shows the threshold images of the NWA 13656 inclusions sorted by their morphologic inclusions. The inclusions can be divided into five different groups according to their morphology: small inclusions consisting of only a few singles nodules (J), elongated inclusions (K), bent fractal inclusions (L), fractal aggregates with four- and three-winged boomerang-shaped morphology (M) and inclusions with a massy center (N).
Figure 6.13 shows the size analysis of the natural inclusions. It is important to mention that we used a random sample of CAIs which resemble the three different aggregate type produced in the experiment. NWA 13656 includes also a wide range of spherical or completely molten CAIs in each size. The histogram in Figure 6.13a shows a heterogeneous distribution of the natural CAI sizes. However, this size distribution is biased due to the sample preparation which only displays a two dimensional image of the CAIs. Figure 6.13b shows the plotted minor versus major ellipsoid axis of the best-fit ellipsoids of the natural CAIs in comparison with the initial starting material of our experiment and the experimentally formed aggregates. The natural CAIs plot in the same range relative to the experimentally formed aggregates standardized by factor 5.
Table 6.2 shows the ratios between the longest (b) versus the shortest (c) direction of the natural CAIs. The values are generally in the same size range as those of the experimentally formed aggregates (Tab. 6.1) with some outliers of higher ratios >3 which could be a cutting effect. The mean value of the ratios excluding the outliers is 2.1(3).

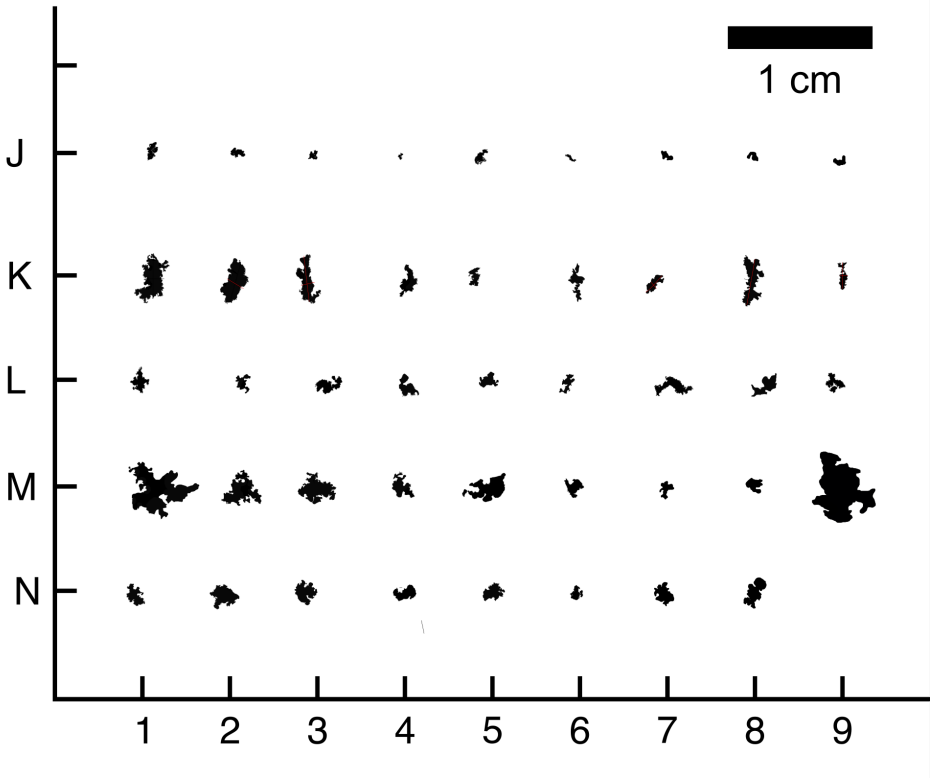

Figure 6.12: Threshold image of different natural fractal inclusions in NWA 13656. Different types of inclusions (Groups J–N) are observed. J: Small inclusions consisting of only a few singles nodules. K: Elongated inclusions. L Bent fractal inclusions. M: Fractal aggregates with four- and three-winged boomerang-shaped morphology. N: Inclusions with a massy center.

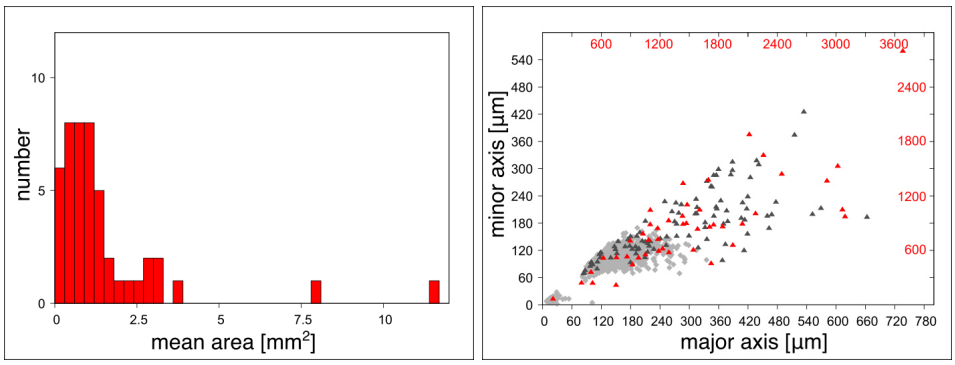

(a) (b)

Figure 6.13: Size analysis of irregular natural inclusions in NWA 13656. (*a*) Histogram of the area size distribution (*b*) Major axis versus minor axis of the approximated ellipsoids (red) in comparison to the sizes of the experimental initial starting material (light grey) and the experimentally formed aggregates (dark grey). The sizes of the irregular natural inclusions in NWA 13656 are referred to the red scale numbers since the natural CAIs have sizes of about a factor 5 larger than the experimentally formed aggregates (black-scale numbers).

Table 6.2: Ratio of the longest (*b*) versus shortest (*c*) dimensions of different natural CAIs in NWA 13656.

no.	J1	J2	K1	K2	K3	K5	K7
b/c	1.9	1.8	2.6	2.1	3.5	2.0	2.7
no.	K8	K9	N4	N8			
b/c	3.4	3.2	2.1	1.8			

6.4 Discussion

In the experiment aboard the ISS, two types of experimental outcome were produced, single melt droplets and fused aggregates. While the melt spherules have been already discussed to their role as chondrule analogs in a previous study (Koch et al., 2021b), we concentrate here on the fused aggregates.

6.4.1 Aggregate formation in the experiment

The main morphologies of aggregates produced in the experiments are: elongated aggregates; fluffy aggregates with curved and boomerang-shaped morphologies; and massy aggregates. The early appearance of aggregates also argues for a formation of these aggregates beginning during the first arc discharges. Some particles experienced different degrees of melting, collided with pristine and/or melted particles and stuck together. Still ductile, these aggregates moved with high velocities in various directions which caused some aggregates to form the typical boomerang-shape morphology. The calculated cooling rates and the collision times indicate an aggregate formation in <0.5 s which also implies the aggregates solidified while still in motion.
Aggregates with a massy center could have formed from collisions of several molten droplets. The analysis of single melt droplets showed that the experiment was able to completely melt single particles (Koch et al., 2021b). Some of these melt droplets could have collided with other completely molten grains, grains in the ductile state or initial particles and formed massy aggregates.

6.4.2 Relation to early Solar System processes

There are several similarities between the aggregates formed in our experiments and early Solar System aggregates. In general, many of the aggregates formed in our experiment aboard the ISS resemble fluffy-type CAIs (MacPherson et al., 1984a), both in size and in their irregular shaped morphologies. All different morphology types, for instance, elongated, three (four-)winged and massy aggregates can be found in a natural CV3 chondrite.
Furthermore, Zhang et al. (2021) performed CT-analysis of refractory inclusions of five CV3 meteorites to study their three dimensional morphology and found that among the six intact inclusions, three showed an elongated morphology with b/c ratios of 1.5–2.1 and two had a fractal and "swan-like" morphology. With 2.1(2), the mean b/c ratio of the aggregates formed in our experiment is similar to that observed for the natural refractory inclusions in the study of Zhang et al. (2021). Furthermore, the natural "swan-like" and bent inclusions shown in their study resemble aggregates formed in our experiment. The b/c ratio of the elongated, natural CAIs observed in NWA 13656 is also in accordance with the b/c ratio determined by Zhang et al. (2021) and the experimental outcomes of this study. It is also notable, that the largest aggregates formed in the experiment (Fig. 6.3 H) and most of the largest fluffy-type CAIs in NWA 13656 (Fig. 6.11a–c) have the three-winged morphology.
The fact that aggregates were formed in this experiment, even those that fused only superficially, and remained stable over the whole duration of this experiment and during subsequent return transportationat to Earth under gravity conditions, which should lead to friction and collisions with other particles, aggregates and the sample chamber walls, implies that aggregates which were fused in such short periods are able to survive even strong turbulences and collisions. In this regard we may note that CAIs observed in chondrites today have survived transportation from their formation region to the chondrite aggregation area by jets, turbulent diffusion, gravitational instabilities or advection due to disk expansion (e.g. Cuzzi et al., 2003; Cuzzi et al., 2005 Gounelle et al., 2001; Shu et al., 2001; Weidenschilling, 2003) which requires a certain amount of structural stability.
Melting has already been proposed to influence the formation and stability of fluffy CAIs (Rubin, 2012). However, it has been argued that the contact points of CAI nodules do not show evidence for melting or sintering (Russell and Howard, 2013). Yet we have shown that the interlocks between grains in the experiments have sometimes no visible melting zone. Furthermore, also fluffy-type CAIs show evidence for melting next to unprocessed material (Russell and Howard, 2013), similar to the adjacency of molten and unprocessed material produced in the presented experiment. The fluffy texture of the formed aggregates resembles that of those formed from low velocity hit-and stick collisions, but were formed by a flash-heating event in the sample chamber. Earlier studies have already shown that CAI aggregation induced by turbulences produces CAIs with the same size distribution as CAIs in chondrites (Charnoz et al., 2015; Taillifet et al., 2014). The combination of the different analytical and theoretical studies discussed above together with our experiment imply that collisions of (flash-)heated particles can reproduce the typical fluffy-type CAIs.
Some particles of the experimentally formed aggregates are surrounded by approx. 20 µm igneous rims. The thickness of the rims formed in our experiments is in the same size range as WLRs in natural CAIs (Bolser et al., 2016; Krot et al., 2017). The experimentally formed rims show a strong preferred orientation, which is similar to the orientation of the natural WLRs studied by Bolser et al. (2016) who explained the formation of WLRs by condensation from the nebular. However, Wark and Boynton (2001) suggested that flash-heating was involved in WLR formation and the recent study of Zhang et al. (2021) proposed that WLR formed by flash-heating followed by fast crystallization and gas solid reactions in a turbulent environment. Our results support the proposal that flash-heating could have

induced or influenced WLR formation. However, the typically observed mineral sequence in WLRs could not be reproduced in our experiment due to the single phase used as starting material. Future experiments involving multiphase starting material could address whether flash-heating could also lead to multilayered multimineral WLR analoges.
Disk or bowl-shaped aggregates have also been observed in chondrites and interpreted as the results of shock flattening (Lorenz et al., 2019). Although we could only detect one aggregate that consists of a flat, molten disk (#F6), it indicates that aerodynamical forces, which occur by the fast acceleration of the particles after the induced arc discharges, can also lead to a flattening of the molten droplet. The studied massy aggregates formed experimentally resemble natural igneous Type B CAIs, however they include many areas which did not experience melting. Aléon et al. (2013) reported an igneous CAI which shows evidence for partial melting, concluding that this CAI was the result of collisions of proto-CAIs which were partially molten. This interpretation is similar to our idea for the formation of massy aggregates in the experiment. It is also in agreement with the formation scenario for compound CAIs proposed by Ivanova et al. (2015). This aggregate type may represent a good example for CAI recycling during repeated events. Rubin (2012) suggested that type B CAIs formed from collisions of molten type A CAIs nodules that the difference during formation of fluffy-type CAIs and this specific CAI is that the grains had different degrees of melting. This idea is in accordance with our interpretation of the formation of the fractal aggregates and massy aggregates formed during the experiment aboard the ISS.
In the experiment aboard the ISS the different aggregates formed over a very short period of probably $<0.5\,\mathrm{s}$ with a very high cooling rate. The particle density in our sample chamber is approx. 10^5–10^8 higher than assumed for the natural CAI forming region of the protoplanetary disk (Zsom et al., 2010). The cooling rates of type B CAIs are generally thought to be much slower (approx. $50\,\mathrm{K\,h^{-1}}$, e.g. MacPherson et al., 1984a; MacPherson et al., 1984b) than the cooling rates determined for the particles in the experiments, however a slower cooling rate would be required to form aggregates in a less dust-rich environment.

6.5 Conclusion

We carried out an experiment at long-term microgravity conditions aboard the ISS where freely floating particles were exposed to arc discharges. The experiment produced fused aggregates which resemble many specific morphological CAI characteristics reported in the literature, such as the fluffy-type CAI morphologies, igneous CAIs textures with relict grains, disk-like CAIs and Wark-Lovering rims. The fractal structures formed in the experiment are very stable which could explain why the fractal structures of fluffy-type CAIs survived transportation to the chondrite accretion region and chondrite parent body formation. The high acceleration of particles would lead to disk and bowl-shaped CAIs. Collisions of CAI nodules with different degrees of melting can form igneous and compound CAIs. In summary, these results imply, that periodically repeated local (flash-)heating events with subsequent aggregation of particles could have been involved in CAI formation after their condensation.

Acknowledgments

This project was realized with the help of A.A. Beck and D. Mederos Leber. We thank the Hackerspace Ffm e. V., especially S. Fujita and J. Kerscher, R. Haseitl and S. Matthies for the help with the technical implementation and the software development. We thank J. Weppler and the German Aerospace Center DLR for taking care of the organization of this project. We thank NanoRacks LLC and DreamUp for the payload opportunity. We also thank the astronauts aboard the ISS under the commandant of A. Gerst for the implementation of the experiment. Funding: We are grateful for financial support provided by the Dr. Rolf M. Schwiete Stiftung, the German Aerospace center DLR, NanoRacks LLC, DreamUp, Biovia, the BmWi (50JR1704) and DFG (BR2015/35-1; Wi1232/44-1), Nordlicht GmbH and ZEISS. We acknowledge DESY (Hamburg, Germany), a member of the Helmholtz Association HGF, for the provision of experimental facilities. Parts of this research were carried out at PETRA III. BW is grateful for support through the BIOVIA Science Ambassador program.

Bibliography

Aléon, J., Marin-Carbonne, J., Taillifet, E., Mckeegan, K., Charnoz, S., and Baillie, K. 2013. Igneous CAI growth by coagulation and partial melting of smaller proto-CAIs: Insights from a compact type A CAI and from modeling. In *44th Lunar and Planetary Science Conference*. (abstract #2530).

Anthony, J. W., Bideaux, R. A., Bladh, K. W., and Nichols, M. C., editors. *Handbook of Mineralogy*. Mineralogical Society of America, 2018.

Beitz, E., Guettler, C., Weidling, R., and Blum, J. 2012. Free collisions in a microgravity many-particle experiment-II: The collision dynamics of dust-coated chondrules. *Icarus*, pages 701–706.

Bischoff, A., Wurm, G., Chaussidon, M., Horstmann, M., Metzler, K., Weyrauch, M., and Weinauer, J. 2017. The Allende multicompound chondrule (ACC)—Chondrule formation in a local super-dense region of the early solar system. *Meteoritics & Planetary Science*, 52:906–924.

Bland, P. A., Howard, L. E., Prior, D. J., Wheeler, J., Hough, R. M., and Dyl, K. A. 2011. Earliest rock fabric formed in the Solar System preserved in a chondrule rim. *Nature Geoscience*, 4:244–247.

Blander, M. and Fuchs, L. H. 1975. Calcium-aluminum-rich inclusions in the Allende meteorite: Evidence for a liquid origin. *Geochimica et Cosmochimica Acta*, 39:1605–1619.

Blum, J. 2010. Astrophysical microgravity experiments with dust particles. *Microgravity Science and Technology*, 22:517–527.

Blum, J. and Wurm, G. 2000. Experiments on sticking, restructuring, and fragmentation of preplanetary dust aggregates. *Icarus*, 143:138–146.

Blum, J., Wurm, G., Poppe, T., Kempf, S., and Kozasa, T. 2002. First results from the cosmic dust aggregation experiment CODAG. *Advances in Space Research*, 29:497–503.

Blum, J. and Wurm, G. 2008. The growth mechanisms of macroscopic bodies in protoplanetary disks. *Annual Review of Astronomy and Astrophysics*, 46:21–56.

Bolser, D., Zega, T. J., Asaduzzaman, A., Bringuier, S., Simon, S. B., Grossman, L., Thompson, M. S., and Domanik, K. J. 2016. Microstructural analysis of Wark-Lovering rims in the Allende and Axtell CV3 chondrites: Implications for high-temperature nebular processes. *Meteoritics & Planetary Science*, 51: 743–756.

Bowen, N. L. and Schairer, J. F. 1925. The system MgO-FeO-SiO_2. *American Journal Science*, 29:151–217.

Brauer, F., Dullemond, C. P., and Henning, T. 2007. Coagulation, fragmentation and radial motion of solid particles in protoplanetary disks. *Astronomy & Astrophysics*, 480:859–877.

Charnoz, S. and Taillifet, E. 2012. A method for coupling dynamical and collisional evolution of dust in circumstellar disks: The effect of a dead zone. *The Astrophysical Journal*, 753:119–148.

Charnoz, S., Aléon, J., Chaumard, N., Baillie, K., and Taillifet, E. 2015. Growth of calcium–aluminum-rich inclusions by coagulation and fragmentation in a turbulent protoplanetary disk: Observations and simulations. *Icarus*, 252:440–453.

Ciesla, F. J., Lauretta, D. S., and Hood, L. L. 2004. The frequency of compound chondrules and implications for chondrule formation. *Meteoritics & Planetary Science*, 39:531–544.

Connelly, J. N., Bizzarro, M., Krot, A. N., Nordlund, Å., Wielandt, D., and Ivanova, M. A. 2012. The absolute chronology and thermal processing of solids in the solar protoplanetary disk. *Science*, 338:651–655.

Cuzzi, J., Ciesla, F., Petaev, M., Krot, A., Scott, E., and Weidenschilling, S. 2005. Nebula evolution of thermally processed solids: Reconciling models and meteorites. *Chondrites and the Protoplanetary Disk*, 341:732–773.

Cuzzi, J. N., Davis, S. S., and Dobrovolskis, A. R. 2003. Blowing in the wind. ii. creation and redistribution of refractory inclusions in a turbulent protoplanetary nebula. *Icarus*, 166:385–402.

Dominik, C., Blum, J., Cuzzi, J. N., and Wurm, G. 2007. Growth of dust as the initial step toward planet formation. In Reipurth, B., Jewitt, D., and Keil, K., editors, *Protostars and Planets V*, pages 257–263.

Gounelle, M., Shu, F., Shang, H., Glassgold, A. E., Rehm, K. E., and Lee, T. 2001. Extinct radioactivities and protosolar cosmic rays: Self-shielding and light elements. *The Astrophysical Journal*, 548:1051–1070.

Han, J. and Brearley, A. J. 2015. Microstructural evidence for complex formation histories of amoeboid olivine aggregates from the ALHA77307 CO3.0 chondrite. *Meteoritics & Planetary Science*, 50:904–925.

Han, J., Keller, L. P., Liu, M.-C., Needham, A. W., Hertwig, A. T., Messenger, S., and Simon, J. I. 2020. A coordinated microstructural and isotopic study of a Wark-Lovering rim on a Vigarano CAI. *Geochimica et Cosmochimica Acta*, 269:639–660.

Hewins, R., Connolly Jr., H. C., and Libourel, G. 2005. Experimental constraints on chondrule formation. *Chondrites and the Protoplanetary Disk*, 341:286.

Ivanova, M. A., Kononkova, N. N., Krot, A. N., Greenwood, R. C., Franchi, I. A., Verchovsky, A. B., Trieloff, M., Korochantseva, E. V., and Brandstätter, F. 2008. The Isheyevo meteorite: Mineralogy, petrology, bulk chemistry, oxygen, nitrogen, carbon isotopic compositions, and ^{40}Ar-^{39}Ar ages. *Meteoritics & Planetary Science*, 43:915–940.

Ivanova, M. A., Lorenz, C. A., Krot, A. N., and MacPherson, G. J. 2015. A compound Ca-, Al-rich inclusion from CV3 chondrite Northwest Africa 3118: Implications for understanding processes during CAI formation. *Meteoritics & Planetary Science*, 50:1512–1528.

Kita, N. T., Yin, Q.-Z., MacPherson, G. J., Ushikubo, T., Jacobsen, B., Nagashima, K., Kurahashi, E., Krot, A. N., and Jacobsen, S. B. 2013. ^{26}Al-^{26}Mg isotope systematics of the first solids in the early solar system. *Meteoritics & Planetary Science*, 48:1383–1400.

Koch, T. E., Spahr, D., Merges, B., D. Winkler, and Brenker, F. E. 2021a. Mg_2SiO_4 particle aggregation aboard the ISS — Influence of electric fields on aggregation behavior, particle velocity and shape-preferred orientation. *Astronomy & Astrophysics*, 651:A1.

Koch, T. E., Spahr, D., Tkalcec, B. J., Lindner, M., Merges, D., Wilde, F., Winkler, B., and Brenker, F. E. 2021b. Formation of chondrule analogs aboard the international space station. *Meteoritics & Planetary Science*, 56:1669–1684.

Komatsu, M., Krot, A. N., Petaev, M. I., Ulyanov, A. A., Keil, K., and Miyamoto, M. 2001. Mineralogy and petrography of amoeboid olivine aggregates from the reduced CV3 chondrites Efremovka, Leoville and Vigarano: Products of nebular condensation, accretion and annealing. *Meteoritics & Planetary Science*, 36:629–641.

Komatsu, M., Mikouchi, T., and Miyamoto, M. 2009. High-temperature annealing of amoeboid olivine aggregates: Heating experiments on olivine–anorthite mixtures. *Polar Science*, 3:31–55.

Kozub, D., Khmelik, V., Shapoval, J., Chentsov, V., Yatsenko, S., Litovchenko, B., and Starikh, V. Helicon Focus 7.0.2 Pro. Helicon Soft Ltd. Available: `https://www.heliconsoft.com/heliconsoft-products/helicon-focus/` [2018, Septemper 27]., 2018.

Krot, A. N. 2019. Refractory inclusions in carbonaceous chondrites: Records of early solar system processes. *Meteoritics & Planetary Science*, 54:1647–1691.

Krot, A. N., Petaev, M. I., Russell, S. S., Itoh, S., Fagan, T. J., Yurimoto, H., Chizmadia, L., Weisberg, M. K., Komatsu, M., Ulyanov, A. A., and Keil, K. 2004a. Amoeboid olivine aggregates and related objects in carbonaceous chondrites: records of nebular and asteroid processes. *Geochemistry*, 64:185–239.

Krot, A. N., Petaev, M. I., and Yurimoto, H. 2004b. Amoeboid olivine aggregates with low-ca pyroxenes: a genetic link between refractory inclusions and chondrules? *eochimica et Cosmochimica Acta*, 68:1923–1941.

Krot, A. N., Amelin, Y., Bland, P., Ciesla, F., Connelly, J., Davis, A. M., Huss, G. R., Hutcheon, I., Makide, K., Nagashima, K., Nyquist, L., Russell, S., Scott, E. R. D., Thrane, K., Yurimoto, H., and Yin, Q.-Z. 2009. Origin and chronology of chondritic components: A review. *Geochimica et Cosmochimica Acta*, 73: 4963–4997.

Krot, A. N., Nagashima, K., van Kooten, E. M. M., and Bizzarro, M. 2017. High-temperature rims around calcium–aluminum-rich inclusions from the CR, CB and CH carbonaceous chondrites. *Geochimica et Cosmochimica Acta*, 201:155–184.

Liffman, K., Cuello, N., and Paterson, D. 2016. A unified framework for producing CAI melting, Wark–Lovering rims and bowl-shaped CAIs. *Monthly Notices of the Royal Astronomical Society*, 462: 1137–1163.

Lorenz, C., Ivanova, M., Krot, A., and Shuvalov, V. 2019. Formation of disk- and bowl-shaped igneous Ca,Al-rich inclusions: Constraints from their morphology, textures, mineralogy and modelling. *Geochemistry*, 79: 125523.

MacPherson, G. J., Grossman, L., Allen, J. M., and Beckett, J. R. 1982. Origin of rims on coarse-grained inclusions in the allende meteorite. *Lunar and Planetary Science Conference Proceedings*, 12:1079–1091.

MacPherson, G. J., Grossman, L., Hashimoto, A., Bar-Matthews, M., and Tanaka, T. 1984a. Petrographic studies of refractory inclusions from the murchison meteorite. *Journal of Geophysical Research: Solid Earth*, 89:C299–C312.

MacPherson, G. J., Paque, J. M., Stolper, E., and Grossman, L. 1984b. The Origin and significance of reverse zoning in melilite from Allende type B Inclusions. *The Journal of Geology*, 92:289–305.

MacPherson, G. J., Hashimoto, A., and Grossman, L. 1985. Accretionary rims on inclusions in the Allende meteorite. *Geochimica et Cosmochimica Acta*, 49:2267–2279.

Marrocchi, Y., Villeneuve, J., Jacquet, E., Piralla, M., and Chaussidon, M. 2019. Rapid condensation of the first solar system solids. *Proceedings of the National Academy of Sciences*, 116:23461–23466.

Moosmann, J., Ershov, A., Weinhardt, V., Baumbach, T., Prasad, M. S., LaBonne, C., Xiao, X., Kashef, J., and Hofmann, R. 2014. Time-lapse X-ray phase-contrast microtomography for *in vivo* imaging and analysis of morphogenesis. *Nature Protocols*, 9:294–304.

Morris, M. A. and Desch, S. J. 2010. Thermal histories of chondrules in solar nebula shocks. *The Astrophysical Journal*, 722:1474–1494.

Nakagawa, Y., Nakazawa, K., and Hayashi, C. 1981. Growth and sedimentation of dust grains in the primordial solar nebula. *Icarus*, 45:517–528.

NIST. https://webbook.nist.gov/cgi/cbook.cgi?ID=C10034943&Units=SI&Mask=2&Type=JANAFS&Plot=on, 06th June 2020.

Ogurreck, M., Wilde, F., Herzen, J., Beckmann, F., Nazmov, V., Mohr, J., Haibel, A., Müller, M., and Schreyer, A. 2013. The nanotomography endstation at the PETRA III Imaging Beamline. *Journal of Physics: Conference Series*, 425:182002.

Rubin, A. 2012. A new model for the origin of Type-B and Fluffy Type-A CAIs: Analogies to remelted compound chondrules. *Meteoritics & Planetary Science*, 47:1062–1074.

Rueden, C. T., Schindelin, J., Hiner, M. C., DeZonia, B. E., Walter, A. E., Arena, E. T., and Eliceiri, K. W. ImageJ2: ImageJ for the next generation of scientific image data. *BMC Bioinformatics* 18:529, 2017.

Russel, S. S., Connolly Jr., H. C., and Krot, A. N., editors. *Chondrules: Records of Protoplanetary Disk Processes*. Cambridge Planetary Science. Cambridge University Press 450 p., 2018.

Russell, S. S. and Howard, L. 2013. The texture of a fine-grained calcium–aluminium-rich inclusion (CAI) in three dimensions and implications for early solar system condensation. *Geochimica et Cosmochimica Acta*, 116:52–62.

Shu, F. H., Shang, H., Gounelle, M., Glassgold, A. E., and Lee, T. 2001. The origin of chondrules and refractory inclusions in chondritic meteorites. *The Astrophysical Journal*, 548:1029–1050.

Spahr, D., Koch, T. E., Merges, D., Beck, A. A., Bolender, B., Carlsson, J. M., Christ, O., Fujita, S., Genzel, P.-T., Kerscher, J., Knautz, T., Lindner, M., Leber, D. M., Milman, V., Morgenroth, W., Wilde, F., Brenker, F. E., and Winkler, B. 2020. A Chondrule Formation Experiment Aboard the ISS: Experimental Set-up and Test Experiments. *Icarus*, 350:113898.

Steinpilz, T., Joeris, K., Jungmann, F., Wolf, D., Brendel, L., Teiser, J., Shinbrot, T., and Wurm, G. 2020. Electrical charging overcomes the bouncing barrier in planet formation. *Nature Physics*, 16:225–229.

Sugiura, N., Petaev, M., Kimura, M., Miyazaki, A., and Hiyagon, H. 01 2010. Nebular history of amoeboid olivine aggregates. *Meteoritics & Planetary Science*, 44:559–572.

Taillifet, E., Baillié, K., Charnoz, S., and Aléon, J. 2014. Origin of Refractory Inclusion Diversity by Turbulent Transport in the Inner Solar Nebula. In *45th Lunar and Planetary Science Conference*. (abstract #2086).

Tkalcec, B. J., Golabek, G. J., and Brenker, F. E. 2013. Solid-state plastic deformation in the dynamic interior of a differentiated asteroid. *Nature Geoscience*, 6:93–97.

Wark, D. and Boynton, W. V. 2001. The formation of rims on calcium-aluminum-rich inclusions: Step I—Flash heating. *Meteoritics & Planetary Science*, 36:1135–1166.

Wark, D. and Lovering, J. 1977. Marker events in the early evolution of the solar system: Evidence from rims on Ca-Al-rich inclusions in carbonaceous chondrites. *Lunar and Planetary Science Conference Proceedings*, 1:95–112.

Weidenschilling, S. J. 2003. Radial drift of particles in the solar nebula: Implications for planetesimal formation. *Icarus*, 165:438–442.

Wilde, F., Ogurreck, M., Greving, I., Hammel, J. U., Beckmann, F., Hipp, A., Lottermoser, L., Khokhriakov, I., Lytaev, P., Dose, T., Burmester, H., Müller, M., and Schreyer, A. 2016. Micro-CT at the imaging beamline P05 at PETRA III. *AIP Conference Proceeding*, 1741:030035.

Wurm, G. and Blum, J. 1998. Experiments on preplanetary dust aggregation. *Icarus*, 132:125–136.

Zhang, M., Clark, B., King, A. J., Russell, S. S., and Lin, Y. 2021. Shape and porosity of refractory inclusions in CV3 chondrites: A micro-computed tomography (µCT) study. *Meteoritics & Planetary Science*, 56: 500–514.

Zsom, A., Ormel, C. W., Güttler, C., Blum, J., and Dullemond, C. P. 2010. The outcome of protoplanetary dust growth: pebbles, boulders, or planetesimals? II. Introducing the bouncing barrier. *Astronomy & Astrophysics*, 513:A57.

CHAPTER 7

Publication IV

Formation of chondrule analogs aboard the International Space Station

Meteoritics & Planetary Science **56**:1669–1684

T. E. Koch[a], D. Spahr[a], B. J. Tkalcec[a], M. Lindner[a], D. Merges[a], F. Wilde[b], B. Winkler[a] and F. E. Brenker[a,c]

[a]Institute of Geosciences, Goethe-Universität Frankfurt, Altenhöferallee 1, 60438 Frankfurt, Germany

[b]Helmholtz-Zentrum Hereon, Max-Planck Strasse 1, 21502 Geesthacht, Germany

[c]Hawai'i Institute of Geophysics and Planetology, School of Ocean and Earth Science and Technology, University of Hawai'i at Mānoa, 1680 East-West Road, Honolulu, HI 96822, USA

Abstract

Chondrules are thought to play a crucial role in planet formation but the mechanisms leading to their formation are still a matter of unresolved discussion. So far, experiments designed to understand chondrule formation conditions have been carried out only under the influence of terrestrial gravity. In order to introduce more realistic conditions, we developed a chondrule formation experiment, which was carried out at long-term microgravity aboard the International Space Station (ISS). In this experiment, freely levitating forsterite (Mg_2SiO_4) dust particles were exposed to electric arc discharges, thus simulating chondrule formation via nebular lightning. The arc discharges were able to melt single dust particles completely which then crystallized with very high cooling rates of 10^5 K h^{-1}. The crystals in the spherules show a crystallographic preferred orientation of the [010] axes perpendicular to the spherule surface, similar to the preferred orientation observed in some natural chondrules. This microstructure is probably the result of crystallization under microgravity conditions. Furthermore, the spherules interacted with the surrounding gas during crystallization. We show that this type of experiment is able to form spherules, which show some similarities with the morphology of chondrules despite very short heating pulses and high cooling rates.

7.1 Introduction

The formation of chondrules is considered to be a fundamental step in the evolution of our Solar System and chondrules are often termed as the building blocks of the terrestrial planets (Bollard et al., 2017; Johansen et al., 2015). Besides their important role in planet formation, they contain information about their precursor material and the conditions and dynamics of the early protoplanetary disk (e.g. Tenner et al., 2013; Ushikubo et al., 280-295; Tenner et al., 2015; Schrader et al., 2018b; Marrocchi et al., 2019; Schrader et al., 2018a). However, the formation process of chondrules remains enigmatic despite numerous proposed formation theories (e.g. reviewed in Boss, 1996; Connolly Jr. and Jones, 2016; Desch et al., 2012; Russel et al., 2018). The challenge lies in developing a model in which the morphological, structural and chemical properties observed in chondrules result from a physically plausible formation mechanism (reviews in Desch and Cuzzi, 2000; Desch et al., 2012; Hubbard and Ebel, 2018). Several chondrule formation scenarios have been proposed, such as shock waves (e.g. Ciesla and Hood, 2002; Ciesla and Hood, 2002; Morris and Boley, 2018), collisions of planetesimals (Krot et al., 2005; Lichtenberg et al., 2018; Sanders and Scott, 2012), dissipation of magneto hydrodynamic turbulence (McNally et al., 2013) or nebular lightning (Desch and Cuzzi, 2000; Horányi et al., 1995), whereby some are considered more plausible than others (Desch et al., 2012). However, none of these theories is able to explain all features typical for a specific chondrule type by a single formation mechanism.

Experiments have been undertaken to test whether specific formation conditions lead to the formation of chondrules with a set of properties similar to those observed in natural samples, for example the different chondrule textures and chemical zoning in olivine crystals (e.g. Connolly Jr. et al., 1998; Hewins and Fox, 2004; Hewins et al., 2005; Jones et al., 2005; Jones et al., 2018; Villeneuve et al., 2015). One of the key factors involved in such experiments is the choice of the heat source. Furnace heating experiments, for example, have so far been significantly more successful in producing chondrule-like characteristics compared to flash-heating experiments (Güttler et al., 2008; Hewins et al., 2000; Poppe et al., 2010; Wdowiak, 1983) and have provided some constraints on the thermal evolution of chondrules. For example, porphyritic chondrules, which represent the most abundant chondrule type (e.g. Russel et al., 2018), are considered to be the result of incomplete melting followed by slow cooling at rates of 50–500 $\mathrm{K\,h^{-1}}$ (Jones et al., 2018 and references therein), whereas cryptocrystalline or radial chondrule textures are thought to be the result of heating above the liquidus and subsequent fast cooling with approx. 1000 $\mathrm{K\,h^{-1}}$ (Jones et al., 2018). Figure 7.1 shows a representative porphyritic chondrule and a cryptocrystalline chondrule, the different textures possibly result from different thermal histories.

Furthermore, interactions between the chondrule precursor material with the surrounding gas during chondrule formation are considered to be relevant for chondrule formation (Chaumard et al., 2018; Libourel et al., 2006; Libourel and Portail, 2018; Marrocchi and Libourel, 2013; Marrocchi and Chaussidon, 2015; Marrocchi et al., 2018, 2019; Piani et al., 2016; Tissandier et al., 2002; Villeneuve et al., 2015). Experiments on gas-melt interactions have successfully reproduced different chondrule characteristics pointing towards the need to go beyond models based on crystallization within closed systems (Tissandier et al., 2002; Villeneuve et al., 2015). Yet, these experiments were all unavoidably influenced by the Earth's gravity. In consequence, more realistic chondrule formation experiments must involve long-term microgravity conditions which are offered today only aboard the International Space Station (ISS). This environment brings several benefits. First, the sample material does not have to be statically mounted and single dust particles can serve as sample material instead of pressed pellets. Second, in microgravity the thermal evolution of the heated samples is not influenced by

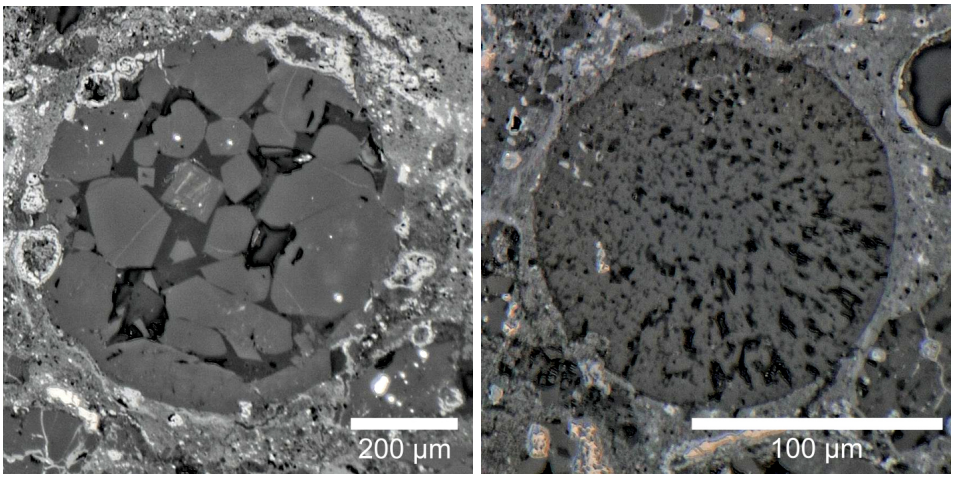

(a) (b)

Figure 7.1: Light microscopic images of different chondrule types from Northwest Africa 11542 (Gattacceca et al., 2019), which were probably formed under different thermal conditions. (*a*) A porphyritic olivine chondrule consisting of olivine crystals in mesostasis. (*b*) A cryptocrystalline chondrule.

thermally induced convection or prolonged contact of the sample with a container wall or sample holder. Furthermore, crystallization at microgravity probably avoids gravitationally-induced settling of crystals on one side of the sample (Radomsky and Hewins, 1990). Instead, the heated samples can cool and crystallize undisturbed while floating freely, similar to melt spherules in the Solar Nebula.

Although the theory of chondrule formation by lightning in the Solar Nebula has not been central to the debate in the last decade, there are many insights, which can be gained from an experiment that uses electrical discharges as heat source. First, chondrule formation by lightning can explain several chondrule characteristics, such as the chondrule-matrix complementarity paired with highly variable thermal histories of adjacent chondrules (Boss, 1996; Connolly Jr. and Jones, 2016; Desch et al., 2012). A recent study addressed the mechanism leading to lightning, and proposed the decay of ^{26}Al as a plausible charging mechanism (Johansen and Okuzumi, 2018), thus affirming that nebular lightning can provide the required amount of energy to form the estimated mass of chondrules of at least 1024 g (Desch and Cuzzi, 2000; Levy, 1988). Studies focusing on gas-melt interactions have questioned whether the formation of porphyritic chondrules requires slow cooling rates, and proposed faster cooling rates, which would be consistent with the cooling rate of chondrules being heated by an arc discharge (Libourel and Portail, 2018). The chemical zoning of Fe, Ca and Cr observed in chondrule olivine has been presented as an argument for slow cooling (Hewins et al., 2005; Jones, 1990; Jones et al., 2018), but recent experiments have produced porphyritic textures with Al and Ti zoning in olivines, similar to natural chondrules, with high cooling rates of 3000–6000 K h^{-1} (Greenwood and Herbst, 2021). This distribution is similar to Al-Ti zoning reported in the literature (Libourel and Portail, 2018; Marrocchi et al., 2018, 2019), thus substantially weakening the argument that slow cooling is required for the formation of porphyric chondrules.

Access to new commercially available payloads aboard the ISS enabled the development of a chondrule formation experiment at long-term microgravity with the acronym EXCISS (Experimental Chondrule formation aboard the ISS) (Spahr et al., 2020). The experimental set-up was designed to fit in a $10 \times 10 \times 15$ cm^3-sized experiment container and adhere to the strict constraints regarding technical components and power supply (Spahr et al., 2020). As

this type of experiment was to be performed at the ISS for the first time, the experimental conditions had to be as simple as possible but still reflect a realistic model system. In this experiment, freely floating Mg_2SiO_4 dust particles were exposed to arc discharges inside a glass sample chamber. In the past, experiments using lightning or similar flash-heating mechanisms (e.g. laser or plasma arcs) have not been very successful, either leading to the destruction of the samples or failing to reproduce chondrule textures (Blander et al., 1976; Güttler et al., 2008; Morlok et al., 2012; Poppe et al., 2010). However, arc discharge properties such as size, duration and discharge energy can be customized and we were able to modify the arc discharge generation technique in our experiment (Spahr et al., 2020) to produce less energetic, longer arc discharges compared to previous experiments (Güttler et al., 2008). A camera allowed the observation of the particles in real time and the sample material could be analyzed after sample return.
The proof-of-concept experiment presented here shows that scientifically useful results regarding chondrule formation, such as the response of dust particles to arc discharges, crystallization under microgravity conditions and the subsequent thermal evolution of chondrules, can be obtained under very tight technical constraints. In this article, we present the analysis of melt spherules formed in microgravity and discuss their relevance as chondrule analogs.

7.2 Methods & Materials

7.2.1 ISS experiments

The experimental set-up and the calibration of the arc discharges is described in Spahr et al. (2020). The experimental set-up was mounted inside a $10 \times 10 \times 15\,cm^3$-sized NanoRacks NanoLab, which was connected to the ISS by USB. The experiment was installed in the NanoRacks platform and the total run time of the experiment was 30 days. In total, 81 arc discharges with energies of 5–8 J and durations between 300 and 500 µs per discharge were induced. The sample chamber was manufactured from quartz glass and two tungsten electrodes with a diameter of 1 mm were fused into the glass on opposite sides. The sample chamber was filled with sample material and Argon atmosphere with 100 ± 1 mbar. The complete sample material remained in the sample chamber during the experiments. These experiments were filmed and the video material could be downloaded on a daily basis. Due to the low frame rate caused by the experimental set-up requirements, it is not possible to distinguish whether the particles melted inside the plasma channel or by thermal radiation.

7.2.2 Analytical procedure and sample preparation

Scanning electron microscopy (SEM) imaging was performed using a Phenom World ProX desktop SEM equipped with an electron backscatter detector (BSE) at the Geoscience Institute at the Goethe University. Energy dispersive X-ray spectroscopy (EDX) was carried out with an integrated silicon drift detector (SDD) for a semi-quantitative characterization of the chemical composition. The non-coated samples were measured under low vacuum conditions; the polished and carbon-coated samples were measured under high vacuum conditions. For imaging, we used an acceleration voltage of 10 kV while for EDX analysis a voltage of 15 kV was employed. Multiple BSE images were acquired with different focal planes and combined afterwards with the Helicon Focus 7 Pro (Kozub et al., 2018) software from Helicon. EDX data were analyzed using the Phenom Pro Suite software.
EBSD fabric analysis is especially suited to identify structural and textural properties of materials and is increasingly employed as an analytic tool to investigate the remnants of Solar Nebular processes in planetary materials (Bland et al., 2011; Tkalcec et al., 2013). EBSD was

performed at the Geoscience Institute at Goethe University Frankfurt with a Jeol scanning electron microscope JSM 6490. The SEM is equipped with a Nordlys II phosphor screen EBSD detector with Channel 5 software from Oxford Instruments and HKL Technology. EBSD was performed with an acceleration voltage of 15 kV, a working distance of 20 mm and a Si-wafer as calibrant. EBSD data was acquired by automated mapping performed at step sizes of 0.8–1 µm with low gain, 2×2 pixel binning, and a mean angular deviation (MAD) limit of <1.3°. Following data acquisition, no noise reduction at all was performed on the acquired EBSD data. Contoured pole figures are displayed as multiples of uniform density (m.u.d.), with a half width of 10°. The initial sample material as well as the experimental outcomes were embedded in Araldite epoxy resin, polished with Syton polish and thinly coated with carbon.
Synchrotron-based micro-CT was performed at PETRA III (DESY) in Hamburg, Germany. All data were collected on the micro tomography beamline P05 (Moosmann et al., 2014; Ogurreck et al., 2013; Wilde et al., 2016), operated by Helmholtz-Zentrum Hereon, using a 15 keV beam monochromatized by a double crystal monochromator. The images were acquired with a 24× magnification using a CMOS camera resulting in an approx. $1.8 \times 1.8\,\mathrm{mm}^2$ field of view. We used an acquisition time of 350 ms. A binning factor of 2×2 pixel resulted in a binned pixel size of approx. $0.61 \times 0.61\,\mathrm{mm}^2$. The samples were completely embedded in Araldite epoxy resin.

7.2.3 Initial sample material

The initial sample material consisted of well-characterized synthetic forsterite particles (Spahr et al., 2020). Figure 7.2a shows a focus-stacked SEM BSE image of a representative initial particle. Figure 7.2b shows several embedded and polished initial grains. The particles include numerous, evenly distributed, small pores. The grains are irregularly shaped with rough surfaces. A grain size analysis of the initial sample material was carried out with a random sampling of 849 grains using ImageJ (Rueden et al., 2017). Figure 7.2c shows a histogram of the longest dimension of the grains fitted with a normal distribution function. The mean diameter obtained from the fit is 126 µm and, due to the heterogeneity of the particle shapes, the distribution is rather broad ($\sigma = 23$). Figure 7.2d shows the correlation of the major to the minor ellipse axes, which again indicates the variability of the particle morphologies. EBSD analysis of the initial particles showed that the particles are fine grained, consisting of crystals having (circular equivalent) diameters of 5–10 µm, with a few exceptions where larger crystals >20 µm are present (Figs. 7.3a,b). Within each grain, the crystals are randomly oriented (Fig. 7.3c). The sample chamber was loaded with 30 mg of the sample material. Approximating the volume of a single grain by a sphere with a diameter of 126 µm and a porosity of approx. 10 vol%, the total number of particles is in the range of 10^4 particles.

7.2.4 Cooling rate determination

The cooling rates of chondrules melted by lightning are usually modelled by radiative cooling of a grey body (Eq. 7.1) (Morris and Desch, 2010). The temperature of the chondrule analogue after the arc discharge is given by the liquidus temperature of forsterite of 2163 K (Bowen and Schairer, 1925) and the temperature aboard the ISS is estimated to be 290 K. Equation 7.1 gives the change of the internal energy U of a radiating spherical grey body with time:

$$\frac{\partial U}{\partial t} = \epsilon \cdot \sigma \cdot A \cdot (T^4_{\mathrm{sample0}} - T^4_{\mathrm{ISS}}), \tag{7.1}$$

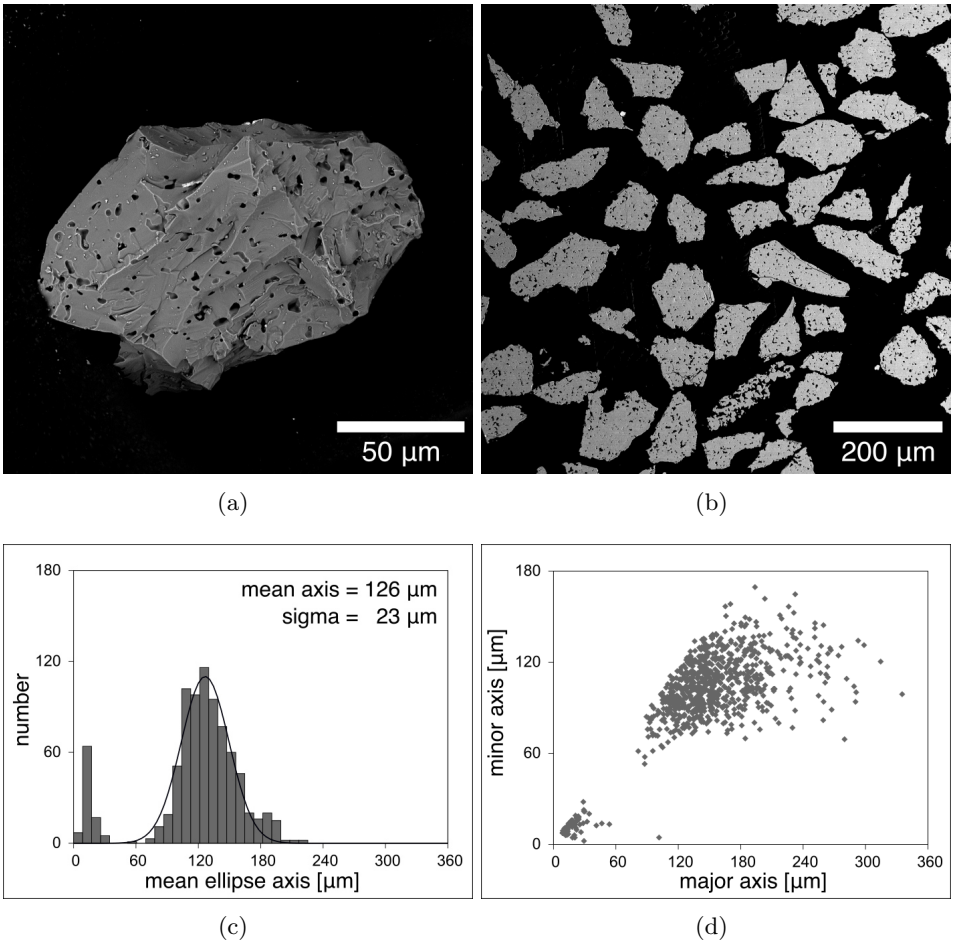

Figure 7.2: Initial sample material. (*a*) Focus-stacked representative porous initial dust particle used as starting material. (*b*) Polished grains of the initial starting material. The particles have highly heterogeneous morphologies and a large amount of evenly distributed small pores. (*c*) Histogram of the grain size distribution of a random sample containing 849 grains fitted with a normal distribution function. (*b*) Correlation between the minor and major axes of best-fit ellipses of the initial material.

Where U is the internal energy, t the time after the heating pulse in s, ϵ the emissivity (for reference, a black body has an emissivity of 1), σ the Stefan-Boltzmann constant, A the surface area of the spherule and T_{sample0} the temperature of the heated spherule at time 0 and T_{ISS} the temperature of the surrounding, both in K. ΔU for a short dt can be obtained using Equation (Eq. 7.2).

$$\Delta U = \epsilon \cdot \sigma \cdot A \cdot (T^4_{\text{sample}} - T^4_{\text{ISS}}) \cdot dt, \tag{7.2}$$

The change in U can also be described by means of the temperature dependent specific heat capacity $cp(T)$ in $\mathrm{J\,mol^{-1}\,K^{-1}}$, the change in Temperature of the spherule ΔT in K and the amount of substance in mol (Equation 7.3). The amount of substance n is calculated for different spherule sizes using the volume of the spherule, the density of forsterite ($3.275\,\mathrm{g\,cm^{-3}}$, and the molar mass of forsterite ($140.693\,\mathrm{g\,mol^{-1}}$).

$$U = c_p(T) \cdot n \cdot (\Delta T), \tag{7.3}$$

Combining Equation 7.2 and 7.3 gives an expression for the change of temperature of the spherule during a short time of radiation (Eq. 7.4).

$$\Delta T = \frac{\epsilon \cdot \sigma \cdot A \cdot (T^4_{\text{sample0}} - T^4_{\text{ISS}}) \cdot dt}{c_p(T) \cdot n}. \tag{7.4}$$

The resulting ΔT is subtracted from T_{sample0} to derive the new temperature of the spherule T_{sample1}. Using this new temperature, the calculations are iterated N times until T_{sampleN} is sufficiently close to T_{ISS} (291 K in this case). The specific heat capacity $c_p(T)$ in Equation 7.3 is calculated for each iteration step with the data from the data from the NIST Standard Reference Database (see NIST in reference section) .

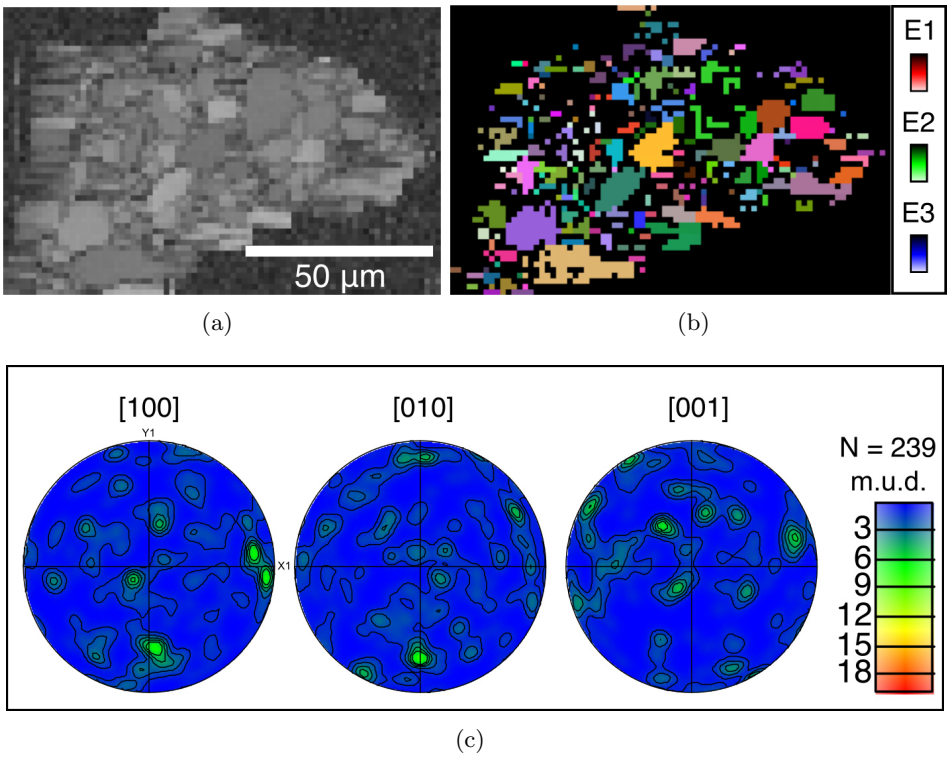

Figure 7.3: EBSD analysis of one typical polished initial sample grain from figure 2b. (*a*) Band contrast image. The particles are fine grained with most crystals having (circular equivalent) diameters of 5–10 µm with a few exceptions >20 µm. (*b*) All-Euler map of forsterite. (*c*) Pole figures showing the contoured data (bottom) based upon one point per grain, identifying 239 grains. The pole figures reveal a random orientation. Since no noise reduction was applied to the raw data, the few tight point maxima (green) are likely caused by duplication (non-adjacent points measured from the same grain but identified as individual grains) in areas where indexing was not continuous.

7.3 Results

7.3.1 Video analysis of the experiments

The videos and photographs downloaded from the ISS show that the first few arc discharges were induced while the space between the electrodes was empty. Then, when an electric field was applied prior to the next discharge, the particles agitated by the previous arc discharges formed an aggregate levitating between the electrodes (Fig. 7.4a). This aggregate was hit directly once by the ensuing arc discharge. The number of particles in the aggregates between the electrodes each time decreased strongly with ongoing arc discharges until their presence became an infrequent occurrence. In all, the space between the electrodes was empty in 70%

of the arc discharges. In total, 81 arc discharges were induced. The first noticeable change in particle morphology is observed after the fourth arc discharge. The number of transformed particles observed in the field of view increased with ongoing experimental duration. However, the actual process of transformation of individual particles could not be observed. Figure 7.4b shows an example of a melt spherule at a late stage of the experiment that may be a chondrule analogue.

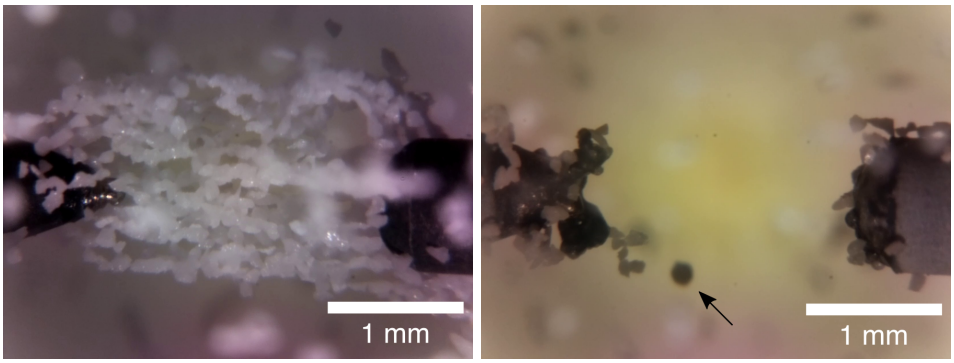

(a) (b)

Figure 7.4: Field of view of the sample chamber of the experiments aboard the ISS. (*a*) An aggregate of particles levitating between the electrodes prior to an arc discharge. (*b*) A melt spherule formed by arc discharge, levitating inside the sample chamber at a late stage of the experiments (black arrow).

7.3.2 SEM and CT analysis

After return of the sample chamber to Earth, the melt spherules formed during the experiment were studied with SEM combined with EBSD and synchrotron micro-CT. More than 90 newly formed objects were isolated from the sample chamber. Scanning electron microscopy and synchrotron micro-CT on these objects show nearly perfect, spherical shapes with smooth surfaces, very distinct from the rough, porous, angular and irregular shapes of the initial particles (Figs. 7.5a–c). SEM, EDX and optical observations show that tungsten, most likely sputtered from the electrodes, has interacted with the forsteritic melt and appears as bright lines on the spherule surface. During cooling and crystallization of forsterite, tungsten has precipitated along grain and subgrain boundaries, thus allowing a clear identification of the grain boundaries on the surface of the spherules (Figs. 7.5a–c). Micro-CT projections also showed the smooth surface on the spherical objects (Fig. 7.5d).
Cross-sections of some typical spherules were subsequently analyzed regarding their microstructure with SEM (Fig. 7.6). The melt spherules are nearly perfectly round with diameters ranging from 75–100 µm in size. The initial pore structure observed in the starting grains (Figs. 7.2a,b) has disappeared completely and instead a few larger voids have formed (Figs. 7.6a–d). Tungsten precipitations form a network of fine lines appear bright in the BSE images and are often arranged as bundles of parallel lamellae. In addition to the individual melt spherules, the experiments produced objects consisting of several fused spherules. Figure 5d shows a back scattered electron (BSE) image of a cross section of one of these fused objects. Beside melt zones, these aggregates often include still unmolten areas, as can be inferred from the pore structure, which is typical for the pristine material, with smooth interfaces between the molten and unmolten areas. A close up of a molten region shown in Fig. 7.6e shows the igneous texture with subhedral or elongated grains separated by a network of fine tungsten precipitations and containing a multitude of tiny inclusions. An ele-

mental EDX map displaying the distribution of tungsten confirms the tungsten composition of these white grain boundaries, lines and inclusions (Fig. 7.6f) and reveals that tungsten is also present in several triple junctions. The amount of tungsten incorporated in each spherule appears to vary from object to object, though this could also be an artifact due to sample preparation.

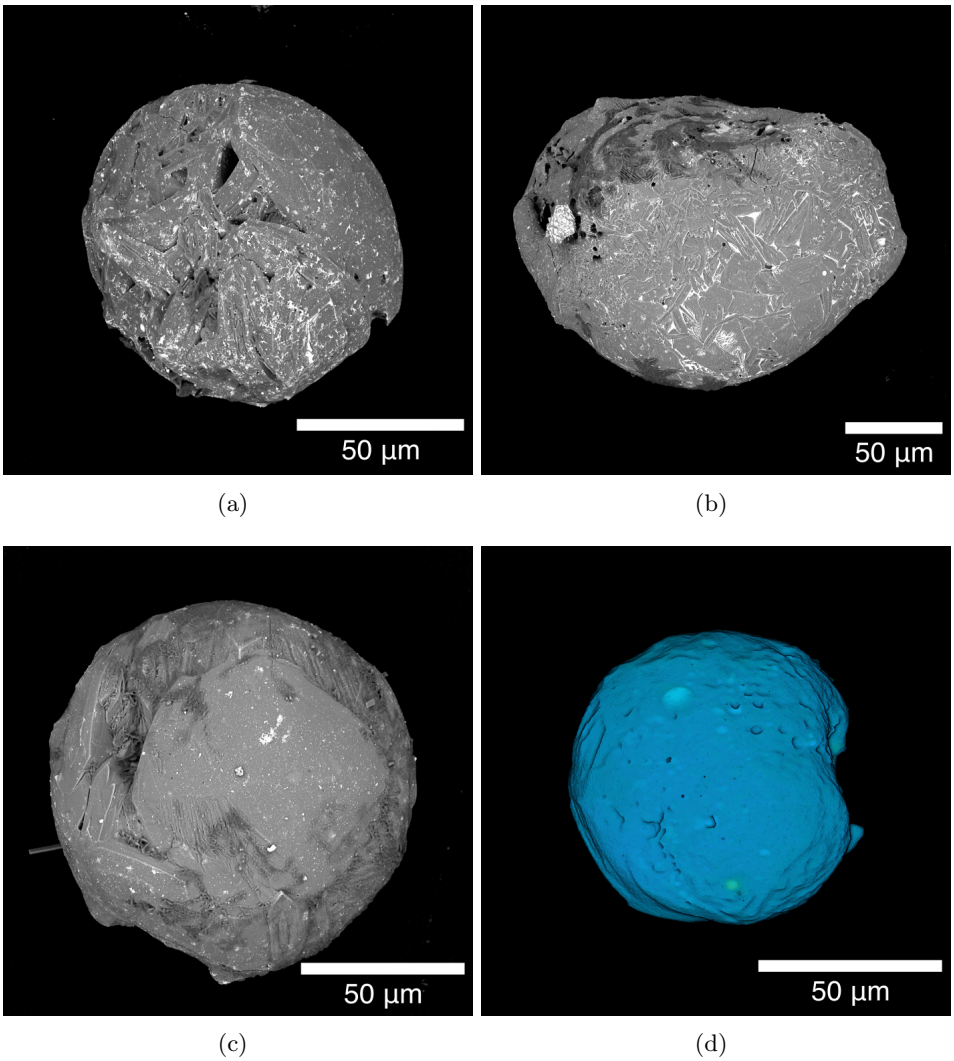

(a) (b)

(c) (d)

Figure 7.5: SEM BSE images and micro-CT projection of some exemplary melt spherules. (a, b, c) Focus-stacked BSE images of melt spherules. The shape and surface structure are completely transformed compared to the initial grains. The single grains are clearly visible. (*d*) Projections of a melt spherule obtained by synchrotron micro-CT.

7.3.3 EBSD fabric analysis

The melt spherules were studied by EBSD with regard to their crystallographic microstructure. Figure 7.7a shows a BSE image of a polished melt spherule. The band contrast image in Figure 7.7b reveals a range of crystal sizes between 5–20 µm and a shape-preferred orientation of most crystals with the longest axes extending parallel to the surface of the spherule. The crystals in areas with a higher tungsten abundance (right-hand side) are larger than those in regions with no visible tungsten precipitations (left-hand side). All indexed EBSD patterns

were assigned to the forsterite structure. The corresponding all Euler angle map is shown in Fig. 7.7c. Further, the pole figures reveal a well-defined crystallographic preferred orientation with the [010] axes perpendicular to the sphere surface (Fig. 7.7d) which is completely different from the random orientation of the crystals in the grains of the pristine sample material (Fig. 7.3).

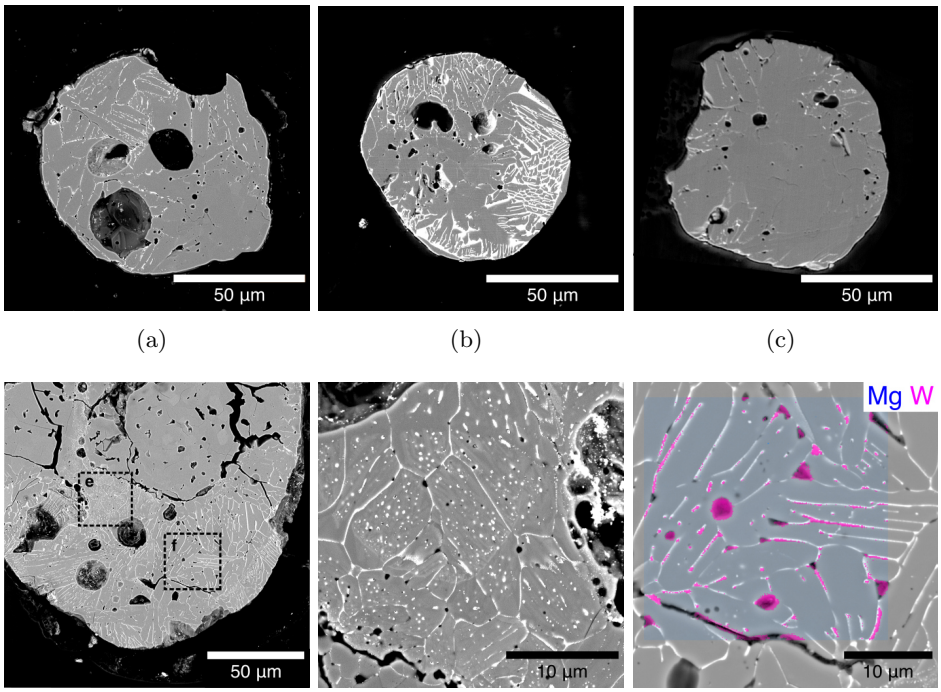

Figure 7.6: SEM BSE images of the melt spherules newly formed aboard the ISS. (a, b, c) Polished cross sections of example melt spherules. White lines are tungsten precipitations. Some spherules contain larger voids, which represent gas bubbles replacing the initial pore structure. (*d*) Close-up of an object containing both molten and unmolten areas, the latter showing the initial pore structure of the starting material. The molten area displays tungsten precipitations and larger gas bubbles. (*e*) Close-up of the left hand square marked in (*d*). The molten area shows an igneous texture with subhedral forsterite grains exhibiting straight grain boundaries. Tungsten not only precipitates along the grain boundaries but also appears as small tungsten inclusions. (*f*) Close-up of the right hand square marked in (*d*). The spatial distribution of Mg and W confirm that all bright lines in the BSE image are due to W.

The fused melt spherules shown in Figs. 7.6d–f were studied in greater detail. The BSE image in Figure 7.8a shows a cross section through the whole object with approximated dimensions of $185 \times 85\,\mu m^2$ in which an area was selected for further EBSD analysis (Fig. 7.8a, white box). The EBSD band contrast image in Figure 7.8b shows a noticeable difference in the texture between those parts that have experienced melting and the pristine material. EBSD analysis of an area of the sample, which displays a clear pore, structure (right-hand area of white box in Figs. 7.8a and 7.8c) reveals the microstructure of the initial sample material with forsterite grains in the size range of about 5–10 µm. This pristine material shows neither shape nor crystallographic preferred orientation (Fig. 7.8d). In contrast, EBSD analysis of the area without such pore structure (left hand area of white box in Figs. 7.8a and 7.8c) reveals a coarser grain size with forsterite grains averaging approximately 20 µm. The crystals of this area show a clear crystallographic preferred orientation of the [010] axes (Fig. 7.8e). The SEM BSE close-up image (Fig. 7.9a) reveals that the grains displayed in the EBSD phase map (Fig. 7.9b) include parallel forsterite lamellae separated by tungsten precipitation. The

misorientation between these lamellae is negligible (<0.5°) (Fig. 7.9c).

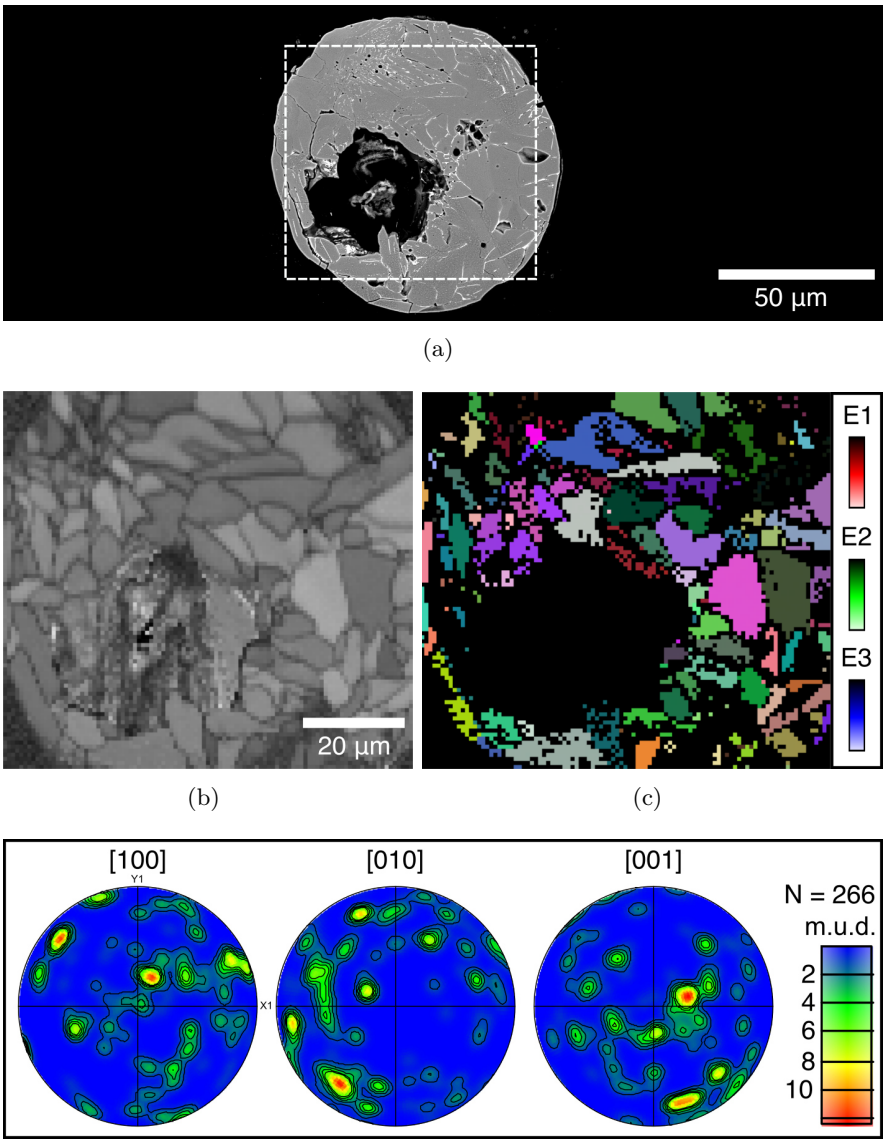

Figure 7.7: SEM and EBSD analysis of a representative melt spherule. (*a*) BSE image of the whole melt spherule with a diameter of 100(5) µm. The dashed square marks the area analyzed by EBSD. (*b*) Greyscale band contrast image visualizing the crystal sizes and morphologies. The grains sizes in the top left, W-poor part of the droplet are slightly smaller than in the right half. (*c*) EBSD all Euler angle map of forsterite. (*d*) Stereographic projections of EBSD data of the melt spherules. The data revealed a well-defined preferred orientation of the [010] axis perpendicular to the sphere surface.

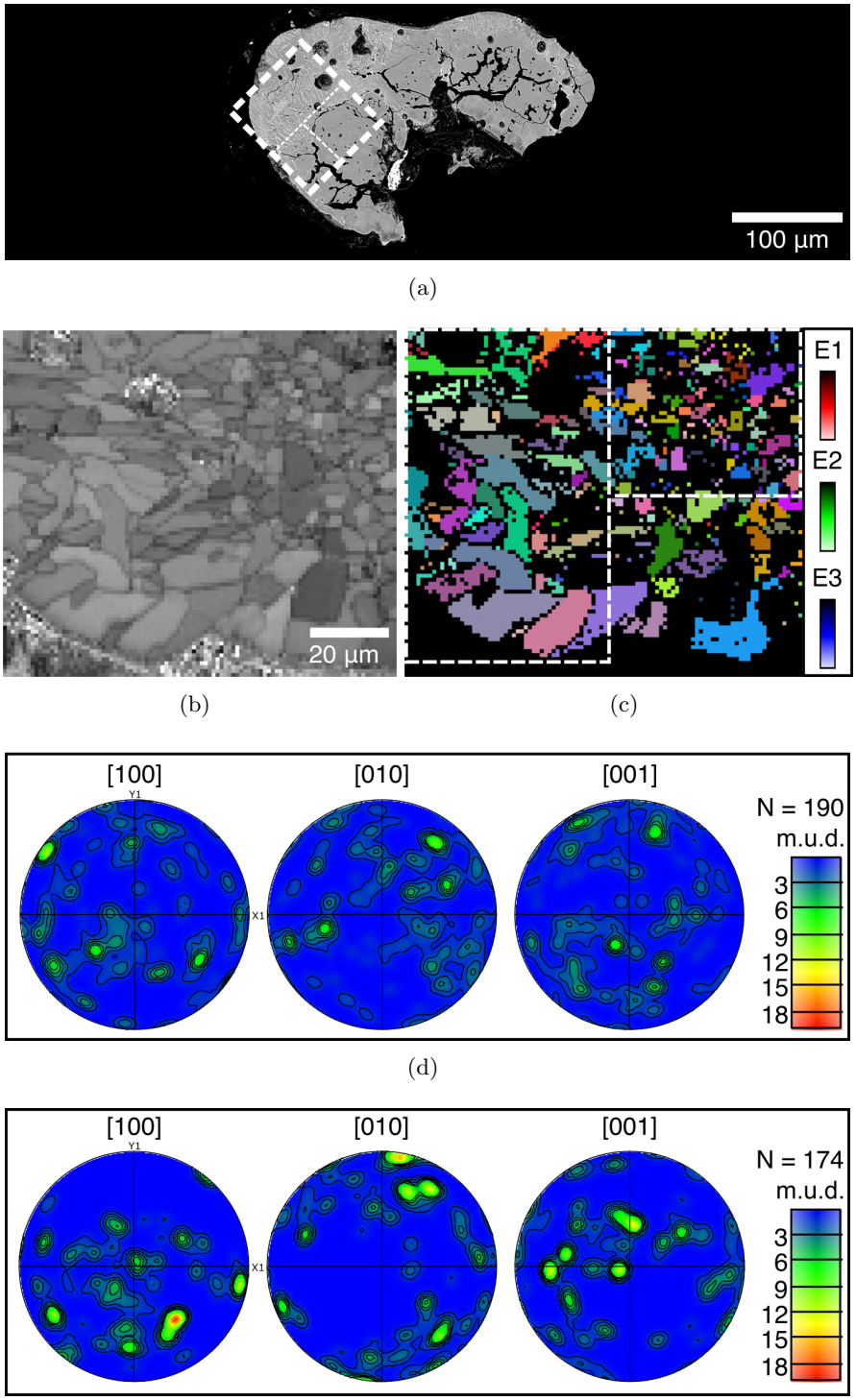

Figure 7.8: SEM and EBSD analysis of the object from Fig. 6d. (*a*) BSE image of the fused object consisting of molten and unmolten regions. The dashed square marks the area studied with EBSD. It consists of both an area with the initial pore structure and a molten, W-rich area. (*b*) The grey-scale band contrast image reveal the microstructure of the studied area. The grains sizes in the left, molten part of the droplet are substantially larger than in the right half that displays the initial pore structure. The crystals close to the rim of the object show an alignment of the longest crystal face perpendicular the surface. (*c*) EBSD all Euler angle map of forsterite of the area shown in (*b*). (*d*) Stereographic projections of EBSD data of the initial unmolten part (top right hand square marked in (*c*)) (*e*) Stereographic projections of EBSD data of the molten area (left hand square in (*c*)) show a similar well-defined alignment of the [010] axes perpendicular to the surface as observed for the melt spherule shown in Fig. 6.

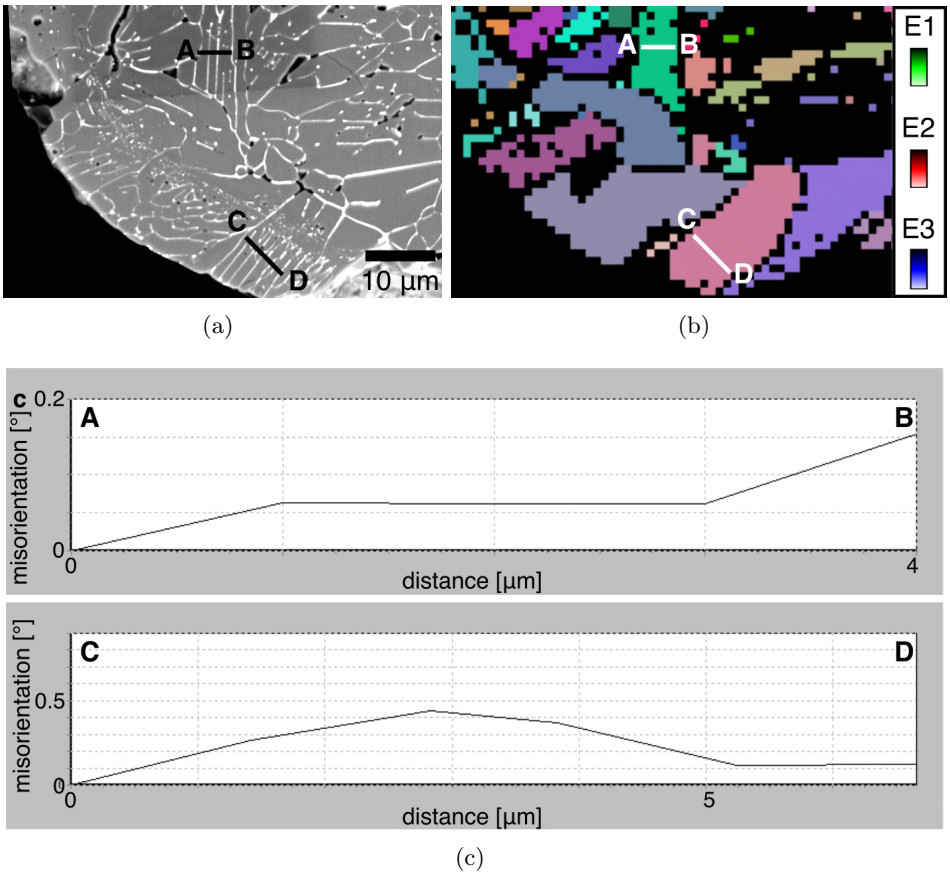

Figure 7.9: Misorientation profiles over grains with parallel tungsten lamellae. (*a*) A BSE close-up of the edge of the fused object consisting of molten and unmolten regions. The molten area shows a network of very fine, often parallel tungsten precipitations. (*b*) EBSD all Euler map displaying the grain boundaries reveals that the observed sets of parallel tungsten lamellae are intracrystal. (*c*) Misorientation profiles perpendicular to the intracrystal tungsten lamella marked in (*a*) and (*b*) showing very low misorientation angles <5° between the lamella in each set.

7.3.4 Cooling rates

The cooling rates were calculated in order to estimate the thermal evolution of the melt spherules after arc discharges. Figure 7.10a shows the temperature profiles of spherical objects with diameters corresponding to those of the melt spherules formed here (d = 80–200 µm). The resulting cooling rates are plotted in Figure 7.10b starting with a cooling rate of 10^7 K h^{-1} and decrease to $<10^4$ K h^{-1} within 40 s.

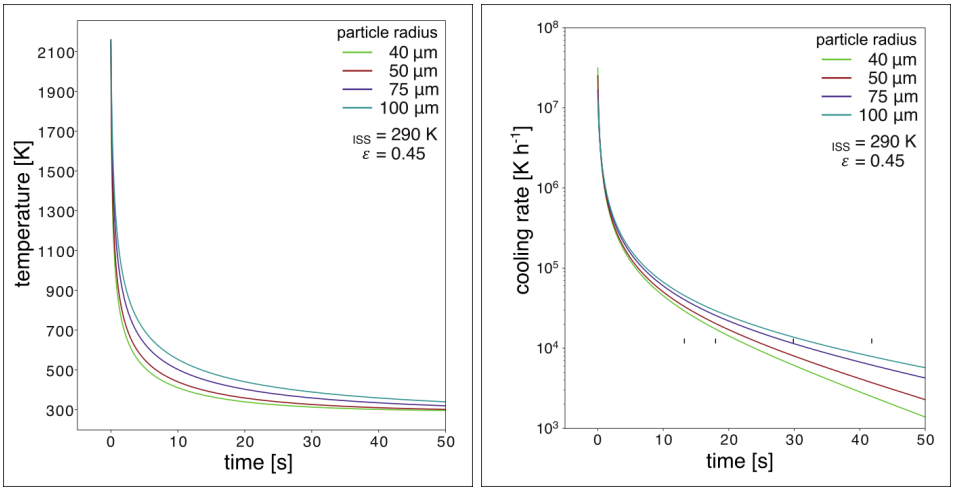

(a) (b)

Figure 7.10: Calculated cooling histories of the melt spherules after the arc discharge. (*a*) Temperature of the melt spherules plotted against time after arc discharge for different spherule diameters. (*b*) Corresponding cooling rates versus time after heating event.

7.4 Discussion

In our experiment, single dust particles in the size range of approximately 100–120 µm experienced complete melting by a heating pulse with a duration <500 µs and energies <8 J (Spahr et al., 2020) followed by rapid cooling. The melt spherules have a very narrow size distribution of approx. 80–100 µm despite the wider size distribution shown by the initial sample particles. However, the amount of formed spherules is not sufficient for a representative size distribution and for conclusions to be drawn between discharge energy and particle size.

The spherules often include spherical voids, but it is unclear if the voids are due to initial porosity or are the results of inefficient melting, the latter of which was discussed as reason for the formation of voids in previous arc-discharge experiments (Wdowiak, 1983). In our experiment, the porous starting material allowed us to easily distinguish between molten and unmolten parts but future experiments could benefit from using sample material with no pores in order to determine whether this material develops voids during this type of experiments. Although the microstructure of the melt spherules obtained here differs from that of natural chondrules, there are some similarities, which merit further discussion and can help to develop the next generation of chondrule formation experiments under microgravity. The microstructure of these melt spherules is dominated by relatively large forsterite crystals (approx. 20 µm) and few large spherical pores, which is clearly distinct from the microstructure of the initial particles. This implies that the complete particles were melted. Furthermore, crystallization resulted in a strong crystallographic preferred orientation of the [010] axes perpendicular to the spherule surface. This microstructure differs from that of spherules produced in previous flash-heating experiments, which mostly display a more radial texture (Blander et al., 1976; Mishra et al., 2020; Poppe et al., 2010). Recent crystallization experiments on Earth using laser heating of Mg_2SiO_4 spherules which were levitated on a gas jet led to the formation of a dendritic microstructure, which is clearly different from the fabric observed here (Mishra et al., 2020). Consequently, the observed microstructure seems to be the result of crystallization in microgravity without any contact to sample chamber walls,

which would imply that this feature probably cannot be observed in experiments on Earth. Preferred orientation of [010] has been observed in natural porphyritic and metal-rich porphyritic chondrules (Dodd and Teleky, 1967; Libourel and Portail, 2018) and also interpreted as the result of crystallization under microgravity conditions (Dodd and Teleky, 1967). The orientations of [100] and [001] of the synthetic samples differ from those of natural chondrules; however, known to the authors, there are no published comprehensive orientation analyzes of chondrules required for a detailed comparison.

The molten edge region of one spherule of the fused object in Figure 8 displays palisadic crystal morphologies which have been also observed in porphyritic chondrules (e.g. Libourel and Portail, 2018; Jacquet et al., 2021). However, the most important structural difference of the melt spherules compared to natural chondrules is the absence of glassy mesostasis, typical for natural porphyritic chondrules. This observation can likely be attributed to the use of pure forsterite as starting material and consequently, future experiments could benefit from a mixture of olivine and plagioclase as initial material.

Furthermore, we observed one object, which resemble in a broad way compound chondrules since it consists of two partially-molten spherules, and another one who seems to be the results of collisions of molten and initial material. However, their textures are not comparable to those of compound chondrules and incomplete melting is not typically observed in natural porphyritic chondrules. Some chondrules show evidence for repeated heating or chondrule recycling (Baecker et al., 2017; Jacquet et al., 2021; Krot et al., 2018; Schrader et al., 2018b; Villeneuve et al., 2020), which would also contribute to complete instead of partial melting. Whether half-melted particles transformed with repeated melting to completely molten particles could not be determined in our experiment. The limited spatial dimensions of the heating flash in our experiment caused only a very low amount of completely molten droplets and consequently the possibility of collisions between completely molten droplets was unlikely. Complete melting may have been prevented in many cases by the distance between a particle and the arc discharge or by large particle diameters. Due to the experimental conditions aboard the ISS, it was not possible to observe the distance between the particles and the arc discharge for specific samples. Future experiments could benefit from the usage of high-speed cameras.

In our experiment, the cooling rate of a single melt spherule is dominated by thermal radiation and is $>10^5$ $\mathrm{K\,h^{-1}}$ within the first seconds, which is in accordance with the cooling rates predicted for the nebular lightning hypothesis (Morris and Desch, 2010). The cooling rate is of special interest in chondrule formation experiments because it is interpreted to be responsible for the formation of the different chondrule textures (detailed review in Jones et al., 2018). High cooling rates have been one of the counterarguments against the formation of chondrules by nebular lightning or other flash-heating formation scenarios (Desch et al., 2012; Hewins et al., 2000), since they are not in according with the thermal path of the most common chondrule texture type, porphyritic chondrules. Consequently, there are two possibilities for future microgravity experiments: either change the thermal history by employing a new technical approach or work with high cooling rates and change the sample material. The latter is supported by the idea that the cooling rate is not one of the decisive factors for the formation of different chondrule texture types. For example, the cooling rate of spherules in our experiment is consistent with the results of experiments by Greenwood and Herbst (2021) who were able to reproduce porphyritic textures with chemical zoning with very high cooling rates. The forsterite crystals observed in our melt spherules formed by arc discharge aboard the ISS do not display chemical zoning since the starting material was pure forsterite, but this is an aspect which could be addressed in future experiments using more chemically complex starting material.

Another important parameter which may influence the chondrule formation is the interaction of melt with the surrounding gas (Baecker et al., 2017; Libourel and Portail, 2018; Libourel et al., 2006; Marrocchi and Chaussidon, 2015; Marrocchi et al., 2018; Tissandier et al., 2002; Villeneuve et al., 2015). The recent analytical work of Libourel and Portail (2018) and experiments from Villeneuve et al. (2015) proposed that the precursor material may have been heated well above the liquidus temperature and started crystallizing at high temperatures around 1800 K in reaction with the surrounding gas. The duration of the interaction lasted up to a few tens of minutes, with subsequent fast cooling at rates of up to 10^6 K h^{-1} (Libourel and Portail, 2018). They suggested that lightning and impact splash scenarios rather than shock waves seem better suited to realize the thermal history proposed in their model.
The melt spherules formed in the experiment also provide information about the incorporation of metal and gas-solid interactions during the experiment. There are different theories about the origin of Fe-Ni inclusions in chondrules. Libourel and Portail (2018) for example, concluded that liquid metal drops were incorporated into the chondrule melt during chondrule formation and served as nuclei for porphyritic textures, whereas other studies proposed that metal blebs are relicts of chondrule precursors (Marrocchi et al., 2019). The tungsten precipitation and inclusions observed in our melt spherules are due to tungsten evaporation from the electrodes prior to its interaction with the molten spherules. Although their incorporation is not directly comparable to the proposed origin of natural Fe-Ni inclusions in chondrules, they demonstrate an interaction of the complete spherule with the surrounding W-bearing gas at high temperatures during crystallization. Even though this period was much shorter (approx. several 100 µs) than the long-duration experiments on gas-melt interactions (Libourel and Portail, 2018; Villeneuve et al., 2015), it shows that interaction of gas and liquid is possible in this type of experiment and this topic could be studied with an improved experimental set-up.

7.5 Conclusion

We carried out the first chondrule formation experiment under long-term microgravity conditions aboard the ISS. We have shown, that freely floating Mg_2SiO_4 dust particles can be completely melted by arc discharges into melt spherules that can be considered to be chondrule analogs. Some micro-textural properties, such as crystal sizes and orientations, morphologies and metal inclusions, are very similar to those observed in natural chondrules. The cooling rates of the melt spherules in our experiments are much higher than the previously established cooling rates of the majority of chondrules, but consistent with recent results (e.g. Greenwood and Herbst, 2021), which implies that the experiment parameters of the experiment could be used for similar experiments. The absence of mesostasis in the experimentally formed spherules can be attributed to the restricted initial composition, which was pure Mg_2SiO_4. This clearly prevents a more detailed comparison of our samples to natural chondrules. Chondrule formation experiments under long-term microgravity conditions are still in a very early stage but our experiments have provided novel experimental constraints for the formation of the first solids formed and processed in the early few million years of our Solar System. As the feasibility of this experimental approach to study chondrule formation under long-term microgravity conditions is now established, more advanced experiments can be developed to study chemically more complex systems.

Acknowledgments

This project was realized with the help of A.A. Beck, O. Christ, P.-T. Genzel and D. Mederos Leber. We thank the Hackerspace Ffm e. V., especially S. Fujita and J. Kerscher, R. Haseitl and S. Matthies for the help with the technical implementation and the software development. We thank J. Weppler and the German Aerospace Center DLR for taking care of the organization of this project. We thank NanoRacks LLC and DreamUp for the payload opportunity. We also thank the astronauts aboard the ISS under the command of A. Gerst for the implementation of the experiment. Funding: We are grateful for financial support provided by the Dr. Rolf M. Schwiete Stiftung, the German Aerospace center DLR, NanoRacks LLC, DreamUp, Biovia, the BmWi (50JR1704) and DFG (BR2015/35-1; Wi1232/44-1), Nordlicht GmbH and ZEISS. We acknowledge DESY (Hamburg, Germany), a member of the Helmholtz Association HGF, for the provision of experimental facilities. Parts of this research were carried out at PETRA III. BW is grateful for support through the BIOVIA Science Ambassador program.

Bibliography

Baecker, B., Rubin, A. E., and Wasson, J. T. 2017. Secondary melting events in Semarkona chondrules revealed by compositional zoning in low-Ca pyroxene. *Geochimica et Cosmochimica Acta*, 211:256–279.

Bland, P. A., Howard, L. E., Prior, D. J., Wheeler, J., Hough, R. M., and Dyl, K. A. 2011. Earliest rock fabric formed in the Solar System preserved in a chondrule rim. *Nature Geoscience*, 4:244–247.

Blander, M., Planner, H. N., Keil, K., Nelson, L. S., and Richardson, N. L. 1976. The origin of chondrules: experimental investigation of metastable liquids in the system Mg_2SiO_4-SiO_2. *Geochimica et Cosmochimica Acta*, 40:889–896.

Bollard, J., Connelly, J. N., Whitehouse, M. J., Pringle, E. A., Bonal, L., Jørgensen, J. K., Nordlund, Å., Moynier, F., and Bizzarro, M. 2017. Early formation of planetary building blocks inferred from Pb isotopic ages of chondrules. *Science Advances*, 3.

Boss, A. P. 1996. A concise guide to chondrule formation models. In Hewins, R. H., Jones, R. H., and Scott, E. R. D., editors, *Chondrules and the Protoplanetary Disk*, pages 257–263.

Bowen, N. L. and Schairer, J. F. 1925. The system MgO-FeO-SiO_2. *American Journal Science*, 29:151–217.

Chaumard, N., Humayun, M., Zanda, B., and Hewins, R. H. 2018. Cooling rates of type I chondrules from Renazzo: Implications for chondrule formation. *Meteoritics & Planetary Science*, 53:984–1005.

Ciesla, F. J. and Hood, L. L. 2002. The nebular shock wave model for chondrule formation: Shock processing in a particle-gas suspension. *Icarus*, 158:281–293.

Connolly Jr., H. C. and Jones, R. H. 2016. Chondrules: The canonical and noncanonical views. *J. Geophys. Res.-Planets*, 121:1885–1899.

Connolly Jr., H. C., Jones, B. D., and Hewins, R. H. 1998. The flash melting of chondrules: an experimental investigation into the melting history and physical nature of chondrule precursors. *Geochimica et Cosmochimica Acta*, 62:2725–2735.

Desch, S. J. and Cuzzi, J. N. 2000. The generation of lightning in the solar nebula. *Icarus*, 143:87–105.

Desch, S. J., Morris, M. A., Connolly Jr., H. C., and Boss, A. P. 2012. The importance of experiments: Constraints on chondrule formation models. *Meteoritics & Planetary Science*, 47:1139–1156.

Dodd, R. T. and Teleky, L. S. 1967. Tpreferred orientation of olivine crystals in porphyritic chondrules. *Icarus*, 6:407–416.

Gattacceca, J., Bouvier, A., Grossman, J., Metzler, K., and Uehara, M. 2019. A systematic for oxygen isotopic variation in meteoritic chondrules. *Meteoritics & Planetary Science - The Meteoritical Bulletin*, 106:469–471.

Greenwood, J. P. and Herbst, W. 2021. New constraints on chondrule formation from experimental reproduction of aluminum and titanium zoning in chondrule olivine. In *52th Lunar and Planetary Science Conference*. (abstract #1617).

Güttler, C., Poppe, T., Wasson, J. T., and Blum, J. 2008. Exposing metal and silicate charges to electrical discharges: Did chondrules form by nebular lightning? *Icarus*, 195:504–510.

Hewins, R., Connolly Jr., H. C., and Libourel, G. 2005. Experimental constraints on chondrule formation. *Chondrites and the Protoplanetary Disk*, 341:286.

Hewins, R. H. and Fox, G. E. 2004. Chondrule textures and precursor grain size: an experimental study. *Geochimica et Cosmochimica Acta*, 68:917–926.

Hewins, R. H., Zanda, R. H., Horányi, M., Robertson, S., Den Hartog, D. J., and Fiksel, G. 2000. The trouble with flash heating. In *31st Lunar and Planetary Science Conference*. (abstract #1675).

Horányi, M., Morfill, G., Goertz, C. K., and Levy, E. H. 1995. Chondrule formation in lightning discharges. *Icarus*, 114:174–185.

Hubbard, A. and Ebel, D. S. 2018. Evaluating non-shock, non-collisional models for chondrule formation. In Russell, S. S., Connolly Jr., H. C., and Krot, A. N., editors, *Chondrules: Records of Protoplanetary Disk Processes*, Cambridge Planetary Science, page 400–426. Cambridge University Press.

Jacquet, E., Piralla, M., Kersaho, P., and Marrocchi, Y. 2021. Origin of isolated olivine grains in carbonaceous chondrites. *Meteoritics & Planetary Science*, 56:13–33.

Johansen, A. and Okuzumi, S. 2018. Harvesting the decay energy of ^{26}Al to drive lightning discharge in protoplanetary discs. *Astronomy and Astrophysics*, 609:1–22.

Johansen, A., Low, M.-M. M., Lacerda, P., and Bizzarro, M. 2015. Growth of asteroids, planetary embryos, and kuiper belt objects by chondrule accretion. *Science Advances*, 1:1–16.

Jones, R., Villeneuve, J., and Libourel, G. 2018. Thermal histories of chondrules. In Russell, S. S., Connolly Jr., H. C., and Krot, A. N., editors, *Chondrules: Records of Protoplanetary Disk Processes*, Cambridge Planetary Science, pages 57–90. Cambridge University Press.

Jones, R. H. 1990. Petrology and mineralogy of Type II, FeO-rich chondrules in Semarkona (LL3.0): Origin by closed-system fractional crystallization, with evidence for supercooling. *Geochimica et Cosmochimica Acta*, 54:1785–1802.

Jones, R. H., Grossman, J., and Rubin, A. 2005. Chemical, mineralogical and isotopic properties of chondrules: Clues to their origin. *Chondrites and the Protoplanetary Disk*, 341:251.

Kozub, D., Khmelik, V., Shapoval, J., Chentsov, V., Yatsenko, S., Litovchenko, B., and Starikh, V. Helicon Focus 7.0.2 Pro. Helicon Soft Ltd. Available: `https://www.heliconsoft.com/heliconsoft-products/helicon-focus/` [2018, Septemper 27]., 2018.

Krot, A. N., Amelin, Y., Cassen, P., and Meibom, A. 2005. Young chondrules in CB chondrites from a giant impact in the early solar system. *Nature*, 436:989–992.

Krot, A. N., Nagashima, K., Libourel, G., and Miller, K. E. 2018. Multiple mechanisms of transient heating events in the protoplanetary disk: Evidence from precursors of chondrules and igneous ca, al-rich inclusions. In Russell, S. S., Connolly Jr., H. C., and Krot, A. N., editors, *Chondrules: Records of Protoplanetary Disk Processes*, Cambridge Planetary Science, page 11–56. Cambridge University Press.

Levy, E. H. 1988. Energetics of chondrule formation. In Kerridge, J. F. and Matthews, M. S., editors, *Meteorites and the Early Solar System*, Cambridge Planetary Science, pages 697–711. Cambridge University Press.

Libourel, G. and Portail, M. 2018. Chondrules as direct thermochemical sensors of solar protoplanetary disk gas. *Science Advances*, 4:eaar3321.

Libourel, G., Krot, A. N., and Tissandier, L. 2006. Role of gas-melt interaction during chondrule formation. *Earth and Planetary Science Letters*, 251:232–240.

Lichtenberg, T., Golabek, G. J., Dullemond, C. P., Schönbächler, M., Gerya, T. V., and Meyer, M. R. 2018. Impact splash chondrule formation during planetesimal recycling. *Icarus*, 302:27–43.

Marrocchi, Y. and Chaussidon, M. 2015. A systematic for oxygen isotopic variation in meteoritic chondrules. *Earth and Planetary Science Letters*, 430:308–315.

Marrocchi, Y. and Libourel, G. 2013. Sulfur and sulfides in chondrules. *Geochimica et Cosmochimica Acta*, 119:117–136.

Marrocchi, Y., Villeneuve, J., Batanova, V., Piani, L., and Jacquet, E. 2018. Oxygen isotopic diversity of chondrule precursors and the nebular origin of chondrules. *Earth and Planetary Science Letters*, 496: 132–141.

Marrocchi, Y., Villeneuve, J., Jacquet, E., Piralla, M., and Chaussidon, M. 2019. Rapid condensation of the first solar system solids. *Proceedings of the National Academy of Sciences*, 116:23461–23466.

McNally, C. P., Hubbard, A., Mac Low, M.-M., Ebel, D. S., and D'Alessio, P. 2013. Mineral processing by short circuits in protoplanetary disks. *The Astrophysical Journal*, 767:L2.

Mishra, B., Manvar, P., Choudhury, K., Karagadde, S., and Srivastava, A. 2020. Experiments to understand crystallization of levitated high temperature silicate melt droplets under low vacuum conditions. *Scientific Reports*, 10:20910.

Moosmann, J., Ershov, A., Weinhardt, V., Baumbach, T., Prasad, M. S., LaBonne, C., Xiao, X., Kashef, J., and Hofmann, R. 2014. Time-lapse X-ray phase-contrast microtomography for *in vivo* imaging and analysis of morphogenesis. *Nature Protocols*, 9:294–304.

Morlok, A., Sutton, Y. C., Braithwaite, N. S. J., and Grady, M. M. 2012. Chondrules born in plasma? Simulation of gas-grain interaction using plasma arcs with applications to chondrule and cosmic spherule formation. *Meteoritics & Planetary Science*, 47:2269–2280.

Morris, M. and Boley, A. C. 2018. Formation of chondrules by shock waves. In Russell, S. S., Connolly Jr., H. C., and Krot, A. N., editors, *Chondrules: Records of Protoplanetary Disk Processes*, Cambridge Planetary Science, pages 375–399. Cambridge University Press.

Morris, M. A. and Desch, S. J. 2010. Thermal histories of chondrules in solar nebula shocks. *The Astrophysical Journal*, 722:1474–1494.

NIST. https://webbook.nist.gov/cgi/cbook.cgi?ID=C10034943&Units=SI&Mask=2&Type=JANAFS&Plot=on, 06th June 2020.

Ogurreck, M., Wilde, F., Herzen, J., Beckmann, F., Nazmov, V., Mohr, J., Haibel, A., Müller, M., and Schreyer, A. 2013. The nanotomography endstation at the PETRA III Imaging Beamline. *Journal of Physics: Conference Series*, 425:182002.

Piani, L., Marrocchi, Y., Libourel, G., and Tissandier, L. 2016. Magmatic sulfides in the porphyritic chondrules of EH enstatite chondrites. *Geochimica et Cosmochimica Acta*, 195:84–99.

Poppe, T., Güttler, C., and Springborn, T. 2010. Thermal metamorphoses of cosmic dust aggregates: Experiments by furnace, electrical gas discharge, and radiative heating. *Earth, Planets and Space*, 62:53–56.

Radomsky, P. M. and Hewins, R. H. 1990. Formation conditions of pyroxene-olivine and magnesian olivine chondrules. *Geochimica et Cosmochimica Acta*, 54:3475–3490.

Rueden, C. T., Schindelin, J., Hiner, M. C., DeZonia, B. E., Walter, A. E., Arena, E. T., and Eliceiri, K. W. ImageJ2: ImageJ for the next generation of scientific image data. *BMC Bioinformatics* 18:529, 2017.

Russel, S. S., Connolly Jr., H. C., and Krot, A. N., editors. *Chondrules: Records of Protoplanetary Disk Processes*. Cambridge Planetary Science. Cambridge University Press 450 p., 2018.

Sanders, I. S. and Scott, E. R. D. 2012. The origin of chondrules and chondrites: Debris from low-velocity impacts between molten planetesimals? *Meteoritics & Planetary Science*, 47:2170–2192.

Schrader, D. L., Nagashima, K., Davidson, J., McCoy, T. J., Ogliore, R. C., and Fu, R. R. 2018a. Outward migration of chondrule fragments in the early Solar System: O-isotopic evidence for rocky material crossing the Jupiter Gap? *Geochimica et Cosmochimica Acta*, 282:133–155.

Schrader, D. L., Nagashima, K., Waitukaitis, S. R., Davidson, J., McCoy, T. J., Connolly, H. C., and Lauretta, D. S. 2018b. The retention of dust in protoplanetary disks: Evidence from agglomeratic olivine chondrules from the outer Solar System. *Geochimica et Cosmochimica Acta*, 223:405–421.

Spahr, D., Koch, T. E., Merges, D., Beck, A. A., Bolender, B., Carlsson, J. M., Christ, O., Fujita, S., Genzel, P.-T., Kerscher, J., Knautz, T., Lindner, M., Leber, D. M., Milman, V., Morgenroth, W., Wilde, F., Brenker, F. E., and Winkler, B. 2020. A Chondrule Formation Experiment Aboard the ISS: Experimental Set-up and Test Experiments. *Icarus*, 350:113898.

Tenner, T. J., Nakashima, D., Ushikubo, T., Kita, N. T., and Weisberg, M. K. 2013. Oxygen isotope ratios of FeO-poor chondrules in CR3 chondrites: Influence of dust enrichment and H_2O during chondrule formation. *Geochimica et Cosmochimica Acta*, 148:228–250.

Tenner, T. J., Ushikubo, T., Kurahashi, E., Kita, N. T., and H., N. 2015. Oxygen isotope systematics of chondrule phenocrysts from the CO3.0 chondrite Yamato 81020: Evidence for two distinct oxygen isotope reservoirs. *Geochimica et Cosmochimica Acta*, 102:226–245.

Tissandier, L., Libourel, G., and Robert, F. 2002. Gas-melt interaction and their bearing on chondrule formation. *Meteoritics & Planetary Science*, 37:1377–1389.

Tkalcec, B. J., Golabek, G. J., and Brenker, F. E. 2013. Solid-state plastic deformation in the dynamic interior of a differentiated asteroid. *Nature Geoscience*, 6:93–97.

Ushikubo, T., Nakashima, D., Kimura, M., Tenner, T. J., and Kita, N. T. 280-295. Contemporaneous formation of chondrules in distinct oxygen isotope reservoirs. *Geochimica et Cosmochimica Acta*, 109:2013.

Villeneuve, J., Libourel, G., and Soulié, C. 2015. Relationships between type i and type ii chondrules: Implications on chondrule formation processes. *Geochimica et Cosmochimica Acta*, 160:277–305.

Villeneuve, J., Marrocchi, Y., and Jacquet, E. 2020. Silicon isotopic compositions of chondrule silicates in carbonaceous chondrites and the formation of primordial solids in the accretion disk. *Earth and Planetary Science Letters*, 542:116318.

Wdowiak, T. J. 1983. Experimental investigation of electrical discharge formation of chondrules. In King, E. A., editor, *Chondrules and their origins*, pages 279–283. Lunar and Planetary Institute, Houston.

Wilde, F., Ogurreck, M., Greving, I., Hammel, J. U., Beckmann, F., Hipp, A., Lottermoser, L., Khokhriakov, I., Lytaev, P., Dose, T., Burmester, H., Müller, M., and Schreyer, A. 2016. Micro-CT at the imaging beamline P05 at PETRA III. *AIP Conference Proceeding*, 1741:030035.

CHAPTER 8

Conclusion

In the framework of this thesis, an experiment which was focused on early Solar System particle behavior was carried out aboard the ISS. In this experiment, freely floating particles were exposed to electric fields and electric discharges. Several important observations and results which can be related to early Solar System processes could be obtained, which are also displayed in Figure 8.1:

A Particles that were agitated under microgravity conditions align in chains in an electric field with their longest axis parallel to the electric field lines. Electric fields could have influenced the inner structure of particle aggregates in the PPD and caused porosity reduction and compaction. Porosity reduction is important regarding the formation of dense early Solar System aggregates such as AOAs and plays an important role in the formation of planetesimals.

B Arc discharges induced the formation of fused aggregates, which have morphological characteristics comparable to fluffy-type CAIs, the oldest material of our Solar System. The fractal structures formed in the experiment are very stable, which implies that a small amount of melting could have stabilized the fractal structures of fluffy-type CAIs to survive transportation to the chondrite accretion region and chondrite parent body formation. Periodically repeated local (flash-)heating events with subsequent aggregation of particles could have been involved in CAI formation after their condensation.

C Arc discharges can melt freely floating particles completely which crystallize with a preferred orientation of the crystals perpendicular to the spherule surface which has been found in natural chondrules but differ from the results of experiments on Earth. The melt spherules show evidence for a complete interaction with the surrounding hot gas. Therefore, microgravity experiments with more advanced experimental parameters bear great potential for future chondrule formation experiments.

D Collisions of particles with different degrees of melting led to the formation of aggregates, which resemble igneous CAIs textures with relict grains, disk-like CAIs and Wark-Lovering rims.

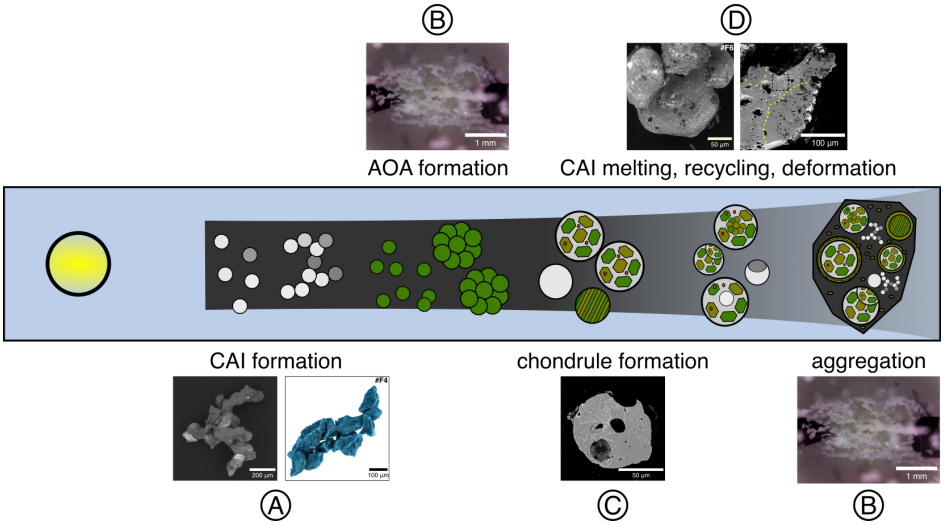

Figure 8.1: Schematic sketch of the most important milestones during the early evolution of the protoplanetary disk together with images from the experimental outcomes, which delivered new findings to understand these processes. (A) Formation of fractal aggregates which resemble the morphologies of fluffy type CAIs. (B) Alignment and orientation in electric fields which could have influenced the porosity of particle aggregates. (C) Arc discharges can melt dust particles to spherules which show some similarities to natural chondrules. (D) Collisions of particles with different degrees of melting can form aggregates which resemble objects such as compound CAIs and disk-shaped CAIs.

CHAPTER 9

Deutsche Zusammenfassung und Fazit

9.1 Zusammenfassung

Vor etwa 4.56 Ga bestand unser Sonnensystem aus Gas und Staubpartikeln, welche in Form einer Scheibe um unsere Protosonne zirkulierten. Diese Scheibe wird als protoplanetaren Scheibe (PPD) bezeichnet (z. B. Weidenschilling and Cuzzi, 2006; Dominik et al., 2007). In dieser Umgebung haben sich viele komplexe Prozesse abgespielt, z. B. Kondensation, Evaporation, Kollisionen von Partikeln, thermische überprägung und Schmelzprozesse, welche sehr wahrscheinlich zur Planetenbildung beigetragen haben (z. B. Russel et al.; Johansen et al., 2018; 2015).
Die Analyse von Meteoriten kann helfen, diese Prozesse aus dem frühen Sonnensystem zu rekonstruieren (z. B. Krot et al., 2009). Die wichtigsten Meteorite für diese Forschung stellen Chondrite dar (z. B. Krot et al., 2009). Diese spezielle Meteoritenart umfasst Bruchstücke von nicht differenzierten Mutterkörpern, welche allgemein als die Vorläufer der terrestrischen Planeten betrachtet werden. Ihre Hauptbestandteile sind Calcium-Aluminium-reiche Einschlüsse (CAIs), amöboide Olivine Aggregaten (AOAs), Chondren, Metalle und feinkörniges Material (z. B. Weisberg et al., 2006; Krot et al., 2009).
Das Wachstum von Objekten durch Aggregation ist einer der ersten Prozesse in der PPD und ist auch Teil weiterer wichtiger Entwicklungsschritte in der Planetenentstehung (Dominik et al., 2007; Blum and Wurm, 2008). Aggregation scheint auch oft mit chemischen Prozessen simultan aufzutreten. Ein Beispiel für die Kombination zwischen Aggregation mit weiteren Prozessen wie Evaporation, Kondensation und Aufschmelzung ist die Bildung von Calcium-Aluminium-reichen Einschlüssen (Krot, 2019). CAIs werden oft als das älteste Material unseres Sonnensystems bezeichnet und sie werden in unterschiedlichen Arten in Chondriten gefunden. Viele CAIs weisen fraktale Strukturen auf, welche in der Literatur als „fluffy-type“ CAIs bezeichnet werden (MacPherson and Grossman, 1984). Manche Studien schlussfolgerten, dass diese Aggregate sich schon während der Kondensation gebildet haben (Russell and Howard, 2013); andere erwägen die Bildung durch Kollisionen nach der Kondensation einzelner CAI Körner (Rubin, 2012). Auch ist es unklar, wie diese Strukturen den Transport innerhalb der PPD sowie die Einbettung in chondritische Mutterkörper und deren Verdichtung überlebten. Andere CAIs in Chondriten wurden vollständig aufgeschmolzen, sind umgeben von multimineralischen Rändern oder weisen eine Kombination dieser Eigenschaften auf (Aléon et al., 2013; Ivanova et al., 2015). Auch hier sind die genauen Umstände,

unter denen die Vielzahl von CAI Typen entstanden sind noch ungeklärt.
AOAs sind feinkörnige Aggregate welche vor allem aus Olivin bestehen und werden auch zu den refraktären Einschlüssen in Meteoriten gezählt (Krot et al., 2004). Sie sind wahrscheinlich durch Kondensation und Aggregation nach der CAI Bildung in größerer Distanz zur Sonne entstanden (Krot et al., 2004). Im Gegensatz zu CAIs wurden sie im Normalfall nicht aufgeschmolzen. Die „amöboide“ Morphologie von AOAs ist auch im Vergleich zu „fluffy-type“ CAIs deutlich weniger fraktal.
Die Bildung von Chondren stellt sehr wahrscheinlich einen weiteren, wichtigen Meilenstein in der Planetenentstehung dar (z. B. Bizzarro et al., 2017; Russel et al., 2018). Chondren sind kleine kugelige Objekte welche häufig in Chondriten vorkommen und auch als Bausteine unseres Sonnensystems bezeichnet werden. Gleichzeitig stellt die Bildung von Chondren eines der größten Mysterien in der Kosmochemie dar (Connolly Jr. and Jones, 2016). Die Textur von Chondren weist auf einen magmatischen Ursprung hin. Demnach müsste ein spezieller Mechanismus Chondrenvorläufer, möglicherweise CAIs und AOAs, aufgeschmolzen haben, welche dann unter komplexen Bedingungen kristallisierten (Krot et al., 2018). Bisher wurde jedoch kein Prozess gefunden, dessen Entstehung physikalisch plausibel erklärt werden kann und welcher Chondren mit den charakteristischen chemischen und texturellen Eigenschaften bilden würde. Es wurden bereits unzählige Theorien zur Bildung von Chondren vorgestellt, z. B. Schockwellen (z. B. Desch et al., 2005), elektrische Entladungen (z. B. Desch and Cuzzi, 2000), Kollisionen von Protoplaneten (z. B. Ebel et al., 2018), jedoch kann keine dieser Theorien alle Eigenschaften von Chondren erklären. Ein wichtiger Punkt, welcher von einem Entstehungsmechanismus erfüllt werden muss, ist die Rekonstruktion der thermischen Geschichte von Chondren (z. B. Jones et al., 2018). Bisher wurde angenommen, dass porphyrische Chondren, der häufigste Chondren-Typ, durch unvollständige Aufschmelzung und langsamer Abkühlung entstanden ist. Diese langsame Abkühlung kann z. B. nicht durch die Entstehung durch elektrische Entladungen in der PPD erfüllt werden. Andere Analysen und Experimente widersprechen jedoch der Annahme einer langsamen Abkühlrate und finden durchaus plausible Argumente für andere thermische Pfade (z. B. Greenwood and Herbst, 2021). Ein anderer Faktor, welcher die Chondrenbildung beeinflusst haben könnte, ist die Reaktion der Schmelze mit den umliegenden Gasen, welche wiederum andere thermische Entwicklungen und Abkühlraten voraussetzt (Villeneuve et al., 2015; Libourel and Portail, 2018).
Mit Hilfe von Experimenten können vermutete Prozesse und die Bedingungen in der PPD getestet werden (z. B. Desch et al., 2012). Experimente, die sich mit Partikelaggregation befassen sind in der Astrophysik bereits etabliert und werden auch regelmäßig in der Mikrogravitation durchgeführt (z. B. Blum and Wurm, 2008). Diese Experimente befassen sich mit der Struktur von Aggregaten, welche durch Kollisionen entstehen, mit den genauen Geschwindigkeiten, welche zu Wachstum und oder zu Zerstörung der Aggregate führen und mit der Porositätsentwicklung und Verdichtung von Aggregaten. Sie werden jedoch fast immer ohne das Einbeziehen kosmochemischer Zusammenhänge durchgeführt, jedoch zeigt die Analyse von Meteoriten, dass Aggregationsprozesse eng verknüpft mit kosmochemischen Prozessen aufgetreten sind.
Experimente zur Chondrenenstehung liefern wichtige Informationen über die thermische Evolution von Chondren und zu chemischen Reaktionen während ihrer Entstehung (z. B. Desch et al., 2012). Diese wurden aber bisher nur auf der Erde durchgeführt. In den bisher erfolgreichsten Experimenten wird ein Ursprungsmaterial in einem Ofen kontrolliert aufgeschmolzen und abgekühlt (z. B. Hewins et al., 2005). Gravitation beeinflusst viele dieser Experimente z. B. durch Kontakt zum Probencontainer. In manchen Experimenten wurde deshalb mit nicht statisch montierten Proben gearbeitet, welche z. B. durch elektrische Entladungen, Plasma arcs oder Laser geheizt wurden (Güttler et al., 2010; Morlok et al., 2012). Diese

Experimente haben bisher jedoch weniger erfolgreich chondren-ähnliche Texturen erzeugt.
Im Rahmen dieser Doktorarbeit wurde deshalb ein Experiment entwickelt, das ohne den Einfluss von Gravitation durchgeführt wurde und den astrophysikalischen Ansatz der Aggregationsexperimente mit Aufschmelzungsexperimenten verbindet. In diesem Experiment mit dem Akronym EXCISS (**Ex**perimental **C**hondrule Formation aboard the **ISS**), wurden freischwebende Mg_2SiO_4-Partikel elektrischen Feldern und elektrischen Entladungen ausgesetzt, um z. B. Aggregation von Partikeln und die Entstehung von Chondren zu simulieren. Das Experiment arbeitet dabei im Vergleich zu früheren Aggregationsexperimenten mit einer chemischen Verbindung, die der Zusammensetzung von Meteoriten ähnlicher ist als bisher verwendete SiO_4- oder Glasskugeln. Zusätzlich wurden die Eigenschaften der elektrischen Entladungen im Vergleich zu den bisherigen Experimenten mit elektrischen Entladungen angepasst, um bessere Ergebnisse zu erzielen. Das Experiment wurde insgesamt an 30 Tagen auf der ISS durchgeführt und gefilmt. Anschließend wurden die Proben an der Goethe-Universität mit verschiedenen analytischen Methoden untersucht.
Der experimentelle Aufbau sowie die Ergebnisse des Experiments wurden im Laufe dieser kumulativen Doktorarbeit in vier Publikationen in „peer-reviewed“ Zeitschriften veröffentlicht, welche im folgenden Text zusammengefasst werden.

Publikation I: A chondrule formation experiment aboard the ISS: Experimental set-up and test experiments

Dieser Artikel beschreibt den experimentellen Aufbau des EXCISS Experiments sowie die Probenpräparation und die Testexperimente auf der Erde.
Das Experiment wurde in einen etwa $10 \times 10 \times 15\,\mathrm{cm}^3$ großen Container der Firma NanoRacks eingebaut. Diese Container sind auf der ISS via USB mit der NanoRacks Plattform verbunden.
Der experimentelle Aufbau wird in unterschiedliche Einheiten untergliedert. Die „control“ Einheit ist für die Steuerung des Experiments und die Datenverwaltung zuständig. Die „power supply“ Einheit enthält Li-Ionen Akkus um eine durchgängige Stromversorgung zu gewährleisten sowie ausreichend Energie für die Entladungsexperimente zur Verfügung zu stellen. Die „arc generation“ Einheit ist für die Entstehung der elektrischen Entladungen zuständig. Sie ist direkt mit der Probenkammer verbunden, welche durch LEDs beleuchtet wird. Die Experimente werden durch eine Raspberry Pi Kamera ausgestattet mit einer speziellen Optik gefilmt.
Es wurden zwei unterschiedliche Probenkammern entwickelt. Probenkammer I wurde für Testexperimente sowie die Charakterisierung der Entladungen aus Vakuumflanschen gebaut. Sie kann mit unterschiedlichen Gasen und kontrolliertem Gasdruck gefüllt werden. So konnten Elektronendichte und Elektronentemperatur bestimmt werden.
Probenkammer II wurde für die Experimente auf der ISS konzipiert. Diese Probenkammer besteht aus Quarz-Glas mit zwei eingeschmolzenen Wolfram-Elektroden. Die Elektroden haben einen Durchmesser von 1 mm und sind in das Glas auf gegenüberliegenden Seiten eingeschmolzen. Der Abstand der Elektrodenspitzen innerhalb der Probenkammer beträgt etwa 2 mm. Probenkammer II wurde mit 100 ± 1 mbar Ar-Gas und 30 mg synthetischen Mg_2SiO_4 Partikeln geladen. Das Startmaterial wurden mit verschiedenen Techniken wie XRD, Raman-Spektroskopie und Synchrotron micro-CT untersucht. Die Partikel haben eine Größe von etwa 80–180 µm, sind eher eckig und zeigen eine relativ hohe Porosität durch kleine Poren.
Bisherige Experimente, welche mit elektrischen Entladungen Chondrenentstehung reproduzieren wollten, waren nicht erfolgreich und haben eher zur Zerstörung der Proben geführt. Deshalb wurde die „arc generation“ Einheit so entwickelt, dass sie im Vergleich zu anderen

Experimenten längere, niedriger energetische Entladungen erzeugt. Insgesamt können zwei unterschiedliche Entladungen ausgelöst werden. Die sogenannten „ignition sparks“ sind kurze (etwa 4 µs), niedrig energetische ($Q \ll 0.01\,\mathrm{J}$) Entladungen, welche durch eine Zündspule erzeugt werden und deren Energie nicht zum Schmelzen des Probenmaterials ausreicht.
Bei „arc discharges“ handelt es sich um längere Entladungen (ungefähr 300–400 µs) mit höherer Energie als „ignition sparks“ ($Q = 5$–$8\,\mathrm{J}$), die so Partikel aufschmelzen können. Sie werden erzeugt, indem zusätzlich nach der Induzierung von „ignition sparks“ durch die Zündspule Energie in den ionisierten Kanal geleitet wird, welche vorher in Kondensatoren gespeichert wurde.
Die Steuerung des Experiments läuft über Softwareupdates während eines täglichen Kommunikationszeitraums, in dem sowohl Daten heruntergeladen als auch neue Befehle zum Experiment gesendet werden können.
Im Rahmen der Entwicklung des experimentellen Aufbaus wurden Experimente am Boden durchgeführt, welche die Funktionsfähigkeit des Experiment inklusive Schmelzen und Verschmelzen der Probenpartikel bestätigten. Die so erzeugten Aggregate wurden mit Rasterelektronenmikroskopie (SEM) und Synchrotron micro-CT untersucht, um sie mit den Proben, welche auf der ISS erzeugt wurden zu vergleichen. Zusätzlich wurden im Rahmen dieses Artikels natürliche Chondren als Referenz für die erzeugten Proben mit Synchrotron micro-CT untersucht.

Publikation II: Mg_2SiO_4 particle aggregation aboard the ISS — Influence of electric fields on aggregation behavior, particle velocity and shape-preferred orientation

In diesem Artikel wurde das Verhalten von Partikeln in der Mikrogravitation unter dem Einfluss von elektrischen Feldern und nach elektrischen Entladungen untersucht.
Die Aggregation von Partikeln und die Porositätsreduzierung von Aggregaten in der PPD sind wichtige Entwicklungsschritte in der Entstehung von Planetesimalen (z. B. Dominik et al., 2007). Elektrostatische Effekte wurden bereits in anderen Studien als möglicher Einfluss auf die Aggregatbildung vorgestellt, z. B. bei der Aggregation von Chondren (Steinpilz et al., 2020). Diese Studien wurden durch das EXCISS Experiment ergänzt, indem das Verhalten von Partikeln in elektrischen Feldern und nach Entladungen in der Mikrogravitation beobachtet wurden.
Diese Experimente wurden in drei verschiedene Stadien unterteilt. Im ersten Teil des Experiments wurde die Probenkammer zuerst ohne äußere Einflüsse beobachtet und anschließend ein elektrisches Feld angelegt. In Teil II wurden „ignition sparks“ induziert und die Bewegung der Partikel analysiert. In Teil III wurde das Verhalten der Partikel nach „arc discharges“ beobachtet. Sowohl in Teil II als auch III war ein elektrisches Feld nach den Entladungen angelegt.
Die ersten Bilder von der ISS zeigen, dass im Bereich zwischen den Elektroden keine Partikel vorhanden waren. Als die Kondensatoren geladen wurden und so ein elektrisches Feld zwischen den Elektroden angelegt wurde, ist ein Aggregat aus Partikeln erschienen welches von den Elektroden angezogen wurde und sich zwischen ihnen positionierte. Die Größe des Aggregats lässt darauf schließen, dass es fast die Gesamtheit der Partikel in der Probenkammer enthält. Sobald das elektrische Feld verschwunden war, hat sich das Aggregat aus dem Sichtfeld bewegt.
In Stadium II wurden „ignition sparks“ ausgelöst während das Aggregat zwischen den Elektroden schwebt. Die Partikel, die sich im getroffenen Areal des Aggregates befanden, wurden in verschiedene Richtungen beschleunigt, der nicht getroffene Teil hat entweder das Sichtfeld als Ganzes verlassen oder sich nur um die Elektrode bewegt. Die Bewegungsrichtung der Par-

tikel war dabei von der Anziehung der Elektroden geprägt. Nach einigen „ignition sparks“ blieb der Bereich zwischen den Elektroden leer.
In Stadium III wurden zuerst hochenergetische „arc discharges“ ausgelöst, während der Bereich zwischen den Elektroden leer war. Dies führte zu starken, ungerichteten Partikelbewegungen in der Probenkammer. Die Partikelgeschwindigkeiten wurden danach exponentiell durch die Stoke‘s Gasreibung abgebremst. Das anschließende elektrische Feld zwischen den Elektroden hat dafür gesorgt, dass die freischwebenden Partikel angezogen wurden und sich entlang der Feldlinien in Ketten angeordnet haben. Auffällig dabei war, dass sich die Körner mit der Längsachse parallel der Feldlinien angeordnet haben. Die Bildung dieser Partikelketten lässt sich auf Dielektrophoresis zurückführen. Die elektrischen Felder haben dabei zur Induzierung einer Dipolachse parallel der Längsachse der Partikel geführt. Mit zunehmender Feldstärke haben sich die Partikelketten angenähert, bis sich ein relativ dichtes Aggregat gebildet hat.
Diese Beobachtungen lassen Rückschlüsse zu einigen Prozessen im frühen Sonnensystem zu. Zuerst, Aggregate sind relativ stabil gegenüber kleinen elektrischen Entladungen. Des Weiteren konnte gezeigt werden, dass Partikel, welche in elektrischen Feldern Aggregate bilden, sich schon mit einer Vorzugsorientierung anordnen. Partikelaggregate könnten sich demnach schon mit einer geringeren Porosität bilden als durch einfache Kollisionen. Elektrische Felder könnten zudem neben Kollisionen von Aggregaten, Gasreibung und Selbstgravitation (Dominik and Tielens, 1997; Dominik et al., 2007; Blum and Wurm, 2008) potentiell die innere Struktur von Aggregaten beeinflusst und zur Verdichtung beigetragen haben.

Publikation III: Formation of fused aggregates under long-term microgravity conditions aboard the ISS with implications for early Solar System particle aggregation

Nach dem Rücktransport des Experiments zur Goethe-Universität, wurde die Probenkammer geöffnet und das Material untersucht. In diesem Artikel wird die Bildung der verschmolzenen Aggregate im Experiment im Zusammenhang mit der Entstehung von Calcium-Aluminiumreichen Einschlüssen diskutiert.
CAIs gehören zum ältesten Material unseres Sonnensystems (Connelly et al., 2012). Sie werden in fast allen primitiven Meteoriten gefunden und kommen in sehr unterschiedlichen Typen mit unterschiedlichen chemischen Eigenschaften und unterschiedlichen Morphologien vor (z. B. MacPherson, 2003; Krot, 2019). Es ist jedoch noch unklar, welche Prozesse zur Bildung der unterschiedlichen CAI-Typen und Eigenschaften geführt haben und ob diese in einem Zusammenhang stehen (MacPherson, 2003; Rubin, 2012; Russell and Howard, 2013; Krot, 2019). Die Analyse der entstanden Aggregate kann bei dieser Fragestellung helfen.
Die Videoanalyse zeigt, dass sich schon mindestens nach dem vierten „arc discharge“ verschmolzene Aggregate gebildet haben. Aufgrund des beschränkten Sichtfeldes und der Bildrate konnte leider nicht nachvollzogen werden, welche Aggregate sich zu welchem Zeitpunkt gebildet haben. Das Probenmaterial aus der Probenkammer wurde mit dem Lichtmikroskop sowie mit Rasterelektronenmikroskopie (SEM), Elektronenrückstreubeugung (EBSD) und Synchrotron micro-CT untersucht.
Die Aggregate konnten zunächst anhand ihrer unterschiedlichen Morphologien in drei Gruppen eingeteilt werden: (1) längliche Aggregate, (2) Boomerang-förmige Aggregate und (3) stark verschmolzene Aggregate mit einem homogen erscheinendem, dichten Kern. Diese Aggregate wurden zuerst im Ganzen mit Synchrotron micro-CT und SEM analysiert. Die Aggregate bestehen aus bis zu 20 ursprünglichen Partikeln, welche unterschiedliche Grade von Aufschmelzung aufweisen. Ein analysiertes Aggregat besteht aus einer flachen Scheibe, in welcher sich von außen nicht mehr die ursprünglichen Körner erkennen lassen.
Einige Aggregate wurden angeschliffen, um die innere Mikrostruktur zu untersuchen. Auch

hier lässt sich erkennen, dass die Aggregate aus Partikeln bestehen, welche unterschiedlich stark aufgeschmolzen wurden. Einige Partikel wurden komplett aufgeschmolzen, wohingegen andere keine Anzeichen für Aufschmelzung zeigen. Manche Partikel und Aggregate zeigen nur eine Aufschmelzung der Ränder, während das Innere unverändert erscheint. Alle aufgeschmolzenen Bereiche enthalten Wolfram-Ausfällungen, welche entlang der Korngrenzen oder als kleine Einschlüsse innerhalb der Kristalle auftreten. Viele Körner bilden parallele Lamellen, welche durch feine Wolfram-Ausfällungen getrennt werden. Das Wolfram muss während des Kristallwachstums aus der Gasphase mit der Schmelze interagiert haben.
EBSD wurde verwendet, um die Korngrößen und kristallographische Orientierung der Kristalle in den ursprünglichen und in den aufgeschmolzenen Partikeln und Aggregaten zu untersuchen. EBSD am Rand eines Aggregats zeigt eine kristallographische Orientierung mit der [001] Achse senkrecht zur Oberfläche.
Die Berechnung der Kollisionszeiten mit Verwendung der Partikelgeschwindigkeiten welche in Publikation II ermittelt wurden führt zu der Erkenntnis, dass die Aggregatbildung innerhalb von maximal 0.5 s nach den elektrischen Entladungen stattgefunden hat.
Zur besseren Vergleichbarkeit der Morphologien der experimentell erzeugten Aggregate und natürlicher CAIs wurde eine CAI Stichprobe aus dem Meteoriten Northwest Africa 13656 analysiert. Dabei wurde festgestellt, dass sich alle verschiedenen, experimentell erzeugten Aggregatmorphologien auch unter den natürlichen CAIs finden lassen. Scheibenförmige CAIs wurden zudem in der Literatur diskutiert (Ivanova et al., 2008).
Das Verhältnis der längsten zu kürzesten Achse der länglichen Aggregate ist in der gleichen Größenordnung wie das der natürlicher CAIs im untersuchten Chondriten und CAIs in der Literatur (Zhang et al., 2021). Die Orientierung der Schmelzränder ist ähnlich der Orientierung von Wark-Lovering rims (Bolser et al., 2016). Die stark verschmolzenen Aggregate ähneln verschmolzenen, natürlichen CAIs (Aléon et al., 2013).
Diese Untersuchungen zeigen, dass Aggregation von teilweise aufgeschmolzenen Körnern nach kurzen Aufheizungsereignissen in der Schwerelosigkeit zu Aggregaten führt, welche wichtige morphologische Eigenschaften von natürlichen CAIs aufweisen. Auch hilft ein geringer Anteil von Aufschmelzung dabei die fraktalen Strukturen zu stabilisieren, sodass „fluffy“ CAIs den Transport vom inneren Teil der PPD bis zur Bildungsregion der Chondrite sowie die Aggregation von chondritischen Mutterkörpern und deren Verdichtung unbeschadet überstanden haben könnten.

Publikation IV: Formation of chondrule analogs aboard the International Space Station

In dieser Publikation wurden die Ergebnisse der Analysen der einzelnen Schmelzkugeln präsen- tiert und ihre Relevanz bezüglich Chondrenentstehungsexperimenten in der Mikrogravitation diskutiert.
Die Schmelzkugeln wurden zuerst ohne weitere Präparation mit dem Rasterelektronenmikroskop untersucht. Zudem wurden sie in Epoxidharz eingebettet und mit Synchrotron micro-CT analysiert. Diese Untersuchungen haben gezeigt, dass die äußere Morphologie der Proben der äußerlichen Erscheinung natürlicher Chondren sehr ähnelt.
Weitere Schmelzkugeln sowie ein Objekt, welches aus zwei teilweise aufgeschmolzenen Partikeln besteht, wurden in Epoxidharz eingebettet, angeschliffen und poliert. Diese Proben wurden anschließend mit SEM und EBSD untersucht. Die Mikrostruktur der Kügelchen ist im Vergleich zu den ursprünglichen Körnern vollständig verändert. Anstatt der ursprünglichen, gleichmäßig verteilten Poren sind stattdessen einige runde, deutlich größere Poren zu sehen. Die Proben zeigen ähnliche Wolfram-Ausfällungen wie die in Publikation III gezeigten Aggregate.

Die EBSD Analyse einer Schmelzkugel hat gezeigt, dass diese vollständig kristallin ist und in der Forsterit-Struktur kristallisiert ist. Sie zeigt eine starke Vorzugsorientierung der [010] Achse senkrecht zur Kugeloberfläche. Des Weiteren wurde ein Objekt untersucht, welches noch teilweise unverändertes Material beinhaltet. Auch hier wurde gezeigt, dass der geschmolzene Bereich eine Vorzugsorientierung der am schnellsten wachsenden Achse senkrecht zur Kugel- oberfläche hat. Dies wurde bereits in natürlichen Chondren beobachtet (Libourel and Portail, 2018). Da es sich bei dem Ausgangsmaterial um reines Mg_2SiO_4 handelte, konnten in dem Experiment keine porphyrischen Strukturen erzeugt werden, da sich keine Mesostasis bilden konnte. Zukünftige Experimente könnten von einer Mischung aus verschiedenen Mineralen profitieren, um so porphyrische Strukturen zu erzeugen. Das entstandene Gefüge zeigt im Vergleich zu ähnlichen Experimenten auf der Erde ein etwas anderes Kristallgefüge, welches gleichmäßig zur Kugeloberfläche kristallisiert ist und nicht ein seitlich gerichtetes Kristallwachstum zeigt (Radomsky and Hewins, 1990).
Des Weiteren wurden die Abkühlraten der Partikel im Experiment berechnet. Sie liegen im Bereich von 10^4–$10^7\,\mathrm{K\,h^{-1}}$ und entsprechen demnach den Abkühlraten, welche für Chondren angenommen werden, die durch elektrische Entladungen erzeugt wurden (Morris and Desch, 2010). Die Entstehung der Schmelzkugeln im Experiment, welche durch eine sehr schnelles, kurzes Aufschmelzen mit anschließender schneller Abkühlung charakterisiert wird, entspricht nicht den geläufigen Theorien, welche z. B. für porphyrische Chondren eine unvollständige Aufschmelzung und langsame Abkühlraten angeben. Jedoch wurde erst vor kurzem in einer neuen experimentellen Studie gezeigt (Greenwood and Herbst, 2021), dass porphyrische Chondren eventuell doch mit einer schnelleren Abkühlrate entstehen können.
Ein weiterer, möglicherweise entscheidender Prozess während der Entstehung von Chondren sind Wechselwirkungen der Schmelze mit dem umgebenem Gas (z. B. Libourel and Portail, 2018). Das Gas in der Probenkammer enthielt nach den Entladungen Wolfram, welches von den heißen Elektroden evaporiert ist. Die Schmelzkugeln zeigen, dass die komplette Schmelze mit dem umliegenden Wolfram-haltigem Gas interagiert hat. Dieser Prozess war jedoch nur sehr kurz und ist nicht unbedingt vergleichbar mit den umfangreichen Experimenten auf der Erde bezüglich dieser Thematik, zeigt jedoch auch das Potential von zukünftigen Experimenten in der Mikrogravitation.

9.2 Fazit

Im Rahmen dieser Doktorarbeit wurde ein Experiment durchgeführt, mit welchem neue Erkenntnisse über Prozesse aus dem frühen Sonnensystem gewonnen werden konnten. In diesem Experiment wurden Partikel elektrischen Feldern und elektrischen Entladungen ausgesetzt. Dabei wurden folgende wichtige Beobachtungen und Ergebnisse erzielt, welche auch in Figure 8.1 graphisch dargestellt werden:

A Partikel, welche in der Mikrogravitation in Bewegung versetzt wurden, sammeln sich im elektrischen Feldern in Ketten entlang der Feldlinien an. Dabei ist die Längsachse der Partikel ebenfalls parallel der Feldlinien ausgerichtet. Elektrische Felder könnten demnach in der PPD die innere Struktur und Porosität von Partikelaggregaten, wie z. B. in AOAs oder Planetesimalen beeinflusst haben.

B Aggregate, welche in der Schwerelosigkeit durch die Kollisionen aus teilweise angeschmol- zenen Partikel entstanden sind, zeigen die typischen Morphologien von „fluffy-type“ CAIs. Diese filligranen Aggregate wären stabil genug, um den Transport innerhalb der PPD sowie Einbettung in die chondritischen Mutterkörper und Verdichtung zu überstehen.

C Elektrische Entladungen können Partikel aufschmelzen, welche unter Mikrogravitation mit einer Vorzugsorientierung kristallisieren. Diese Mikrostruktur ähnelt natürlichen Chondren und unterscheiden sich von Experimenten auf der Erde. Außerdem zeigen diese Schmelzkugeln eine Interaktion mit dem umliegenden Gas. Die Ergebnisse zeigen, dass zukünftige Experimente zur Chondrenentstehung in der Mikrogravitation mit angepassten experimentellen Bedingungen zu realistischeren Ergebnissen führen können.

D Kollisionen von Partikeln mit unterschiedlichen Schmelzgraden können auch zur Bildung von Aggregaten führen, welche ähnlichkeiten mit sekundären CAI Eigenschaften aufweisen, wie z. B. Verschmelzung von CAIs, Wark-Lovering-Rändern oder Deformation zu flachen Scheiben.

Bibliography

Aléon, J., Marin-Carbonne, J., Taillifet, E., Mckeegan, K., Charnoz, S., and Baillie, K. 2013. Igneous CAI growth by coagulation and partial melting of smaller proto-CAIs: Insights from a compact type A CAI and from modeling. In *44th Lunar and Planetary Science Conference*. (abstract #2530).

Bizzarro, M., Connelly, J. N., and Krot, A. N. 2017. Chondrules: Ubiquitous chondritic solids tracking the evolution of the solar protoplanetary disk. In Pessah, M. and Gressel, O., editors, *Formation, Evolution, and Dynamics of Young Solar Systems*, pages 161–195, Cambridge, 2017. Springer International Publishing.

Blum, J. and Wurm, G. 2008. The growth mechanisms of macroscopic bodies in protoplanetary disks. *Annual Review of Astronomy and Astrophysics* 46:21–56.

Bolser, D., Zega, T. J., Asaduzzaman, A., Bringuier, S., Simon, S. B., Grossman, L., Thompson, M. S., and Domanik, K. J. 2016. Microstructural analysis of Wark-Lovering rims in the Allende and Axtell CV3 chondrites: Implications for high-temperature nebular processes. *Meteoritics & Planetary Science* 51: 743–756.

Connelly, J. N., Bizzarro, M., Krot, A. N., Nordlund, Å., Wielandt, D., and Ivanova, M. A. 2012. The absolute chronology and thermal processing of solids in the solar protoplanetary disk. *Science* 338:651–655.

Desch, S. J. and Cuzzi, J. N. 2000. The generation of lightning in the solar nebula. *Icarus* 143:87–105.

Desch, S. J., Morris, M. A., Connolly Jr., H. C., and Boss, A. P. 2012. The importance of experiments: Constraints on chondrule formation models. *Meteoritics & Planetary Science* 47:1139–1156.

Dominik, C. and Tielens, A. G. G. M. 1997. The physics of dust coagulation and the structure of dust aggregates in space. *The Astrophysical Journal* 480:647–673.

Ebel, D., Alexander, C., and Libourel, G. 2018. Formation of chondrules by planetesimal collisions. In Johnson, B. C., Ciesla, F. J., Dullemond, C. P., and Melosh, H. J., editors, *Chondrules: Records of Protoplanetary Disk Processes*, Cambridge Planetary Science, pages 343–360. Cambridge University Press.

Greenwood, J. P. and Herbst, W. 2021. New constraints on chondrule formation from experimental reproduction of aluminum and titanium zoning in chondrule olivine. In *52th Lunar and Planetary Science Conference*. (abstract #1617).

Hewins, R., Connolly Jr., H. C., and Libourel, G. 2005. Experimental constraints on chondrule formation. *Chondrites and the Protoplanetary Disk* 341:286.

Ivanova, M. A., Kononkova, N. N., Krot, A. N., Greenwood, R. C., Franchi, I. A., Verchovsky, A. B., Trieloff, M., Korochantseva, E. V., and Brandstätter, F. 2008. The Isheyevo meteorite: Mineralogy, petrology, bulk chemistry, oxygen, nitrogen, carbon isotopic compositions, and ^{40}Ar-^{39}Ar ages. *Meteoritics & Planetary Science* 43:915–940.

Ivanova, M. A., Lorenz, C. A., Krot, A. N., and MacPherson, G. J. 2015. A compound Ca-, Al-rich inclusion from CV3 chondrite Northwest Africa 3118: Implications for understanding processes during CAI formation. *Meteoritics & Planetary Science* 50:1512–1528.

Johansen, A., Low, M.-M. M., Lacerda, P., and Bizzarro, M. 2015. Growth of asteroids, planetary embryos, and kuiper belt objects by chondrule accretion. *Science Advances* 1:1–16.

Jones, R., Villeneuve, J., and Libourel, G. 2018. Thermal histories of chondrules. In Russell, S. S., Connolly Jr., H. C., and Krot, A. N., editors, *Chondrules: Records of Protoplanetary Disk Processes*, Cambridge Planetary Science, pages 57–90. Cambridge University Press.

Krot, A. N. 2019. Refractory inclusions in carbonaceous chondrites: Records of early solar system processes. *Meteoritics & Planetary Science* 54:1647–1691.

Krot, A. N., Petaev, M. I., Russell, S. S., Itoh, S., Fagan, T. J., Yurimoto, H., Chizmadia, L., Weisberg, M. K., Komatsu, M., Ulyanov, A. A., and Keil, K. 2004. Amoeboid olivine aggregates and related objects in carbonaceous chondrites: records of nebular and asteroid processes. *Geochemistry* 64:185–239.

Krot, A. N., Amelin, Y., Bland, P., Ciesla, F., Connelly, J., Davis, A. M., Huss, G. R., Hutcheon, I., Makide, K., Nagashima, K., Nyquist, L., Russell, S., Scott, E. R. D., Thrane, K., Yurimoto, H., and Yin, Q.-Z. 2009. Origin and chronology of chondritic components: A review. *Geochimica et Cosmochimica Acta* 73: 4963–4997.

Krot, A. N., Nagashima, K., Libourel, G., and Miller, K. E. 2018. Multiple mechanisms of transient heating events in the protoplanetary disk: Evidence from precursors of chondrules and igneous ca, al-rich inclusions. In Russell, S. S., Connolly Jr., H. C., and Krot, A. N., editors, *Chondrules: Records of Protoplanetary Disk Processes*, Cambridge Planetary Science, page 11–56. Cambridge University Press.

Libourel, G. and Portail, M. 2018. Chondrules as direct thermochemical sensors of solar protoplanetary disk gas. *Science Advances* 4:eaar3321.

Morlok, A., Sutton, Y. C., Braithwaite, N. S. J., and Grady, M. M. 2012. Chondrules born in plasma? Simulation of gas-grain interaction using plasma arcs with applications to chondrule and cosmic spherule formation. *Meteoritics & Planetary Science* 47:2269–2280.

Morris, M. A. and Desch, S. J. 2010. Thermal histories of chondrules in solar nebula shocks. *The Astrophysical Journal* 722:1474–1494.

Radomsky, P. M. and Hewins, R. H. 1990. Formation conditions of pyroxene-olivine and magnesian olivine chondrules. *Geochimica et Cosmochimica Acta* 54:3475–3490.

Rubin, A. 2012. A new model for the origin of Type-B and Fluffy Type-A CAIs: Analogies to remelted compound chondrules. *Meteoritics & Planetary Science* 47:1062–1074.

Russel, S. S., Connolly Jr., H. C., and Krot, A. N., editors. 2018. *Chondrules: Records of Protoplanetary Disk Processes*. Cambridge Planetary Science. Cambridge University Press 450 p.

Russell, S. S. and Howard, L. 2013. The texture of a fine-grained calcium–aluminium-rich inclusion (CAI) in three dimensions and implications for early solar system condensation. *Geochimica et Cosmochimica Acta* 116:52–62.

Steinpilz, T., Joeris, K., Jungmann, F., Wolf, D., Brendel, L., Teiser, J., Shinbrot, T., and Wurm, G. 2020. Electrical charging overcomes the bouncing barrier in planet formation. *Nature Physics* 16:225–229.

Villeneuve, J., Libourel, G., and Soulié, C. 2015. Relationships between type i and type ii chondrules: Implications on chondrule formation processes. *Geochimica et Cosmochimica Acta* 160:277–305.

Weisberg, M. K., McCoy, T. J., and Krot, A. N. 2006. Systematics and Evaluation of Meteorite Classification. In Lauretta, D. S. and McSween, H. Y., editors, *Meteorites and the Early Solar System II*, pages 19–52. University of Arizona Press.

Zhang, M., Clark, B., King, A. J., Russell, S. S., and Lin, Y. 2021. Shape and porosity of refractory inclusions in CV3 chondrites: A micro-computed tomography (µCT) study. *Meteoritics & Planetary Science* 56: 500–514.

Connolly Jr., H. C. and Jones, R. H. 2016. Chondrules: The canonical and noncanonical views. *J. Geophys. Res.-Planets* 121:1885–1899.

Desch, S. J., Ciesla, F. J., Hood, L. L., and Nakamoto, T. 2005. Heating of Chondritic Materials in Solar Nebula Shocks. In Krot, A. N., Scott, E. R. D., and Reipurth, B., editors, *Chondrites and the Protoplanetary Disk*, volume 341 of *Astronomical Society of the Pacific Conference Series*, pages 849–872.

Dominik, C., Blum, J., Cuzzi, J. N., and Wurm, G. 2007. Growth of dust as the initial step toward planet formation. In Reipurth, B., Jewitt, D., and Keil, K., editors, *Protostars and Planets V*, pages 257–263.

Güttler, C., Blum, J., Zsom, A., Ormel, C. W., and Dullemond, C. P. 2010. The outcome of protoplanetary dust growth: pebbles, boulders, or planetesimals? I. Mapping the zoo of laboratory collision experiments. *Astronomy & Astrophysics* 513:A56.

MacPherson, G. J. 2003. Calcium-Aluminum-rich Inclusions in Chondritic Meteorites. *Treatise on Geochemistry* 1:201–246.

MacPherson, G. J. and Grossman, L. 1984. "Fluffy" Type A Ca-, Al-rich inclusions in the Allende meteorite. *Geochimica et Cosmochimica Acta* 48:29–46.

Weidenschilling, S. J. and Cuzzi, J. N. 2006. Accretion dynamics and timescales: Relation to chondrites. In *Meteorites and the Early Solar System II*, pages 473–485. The University of Arizona Press.

Eidestattliche Erklärung

Ich erkläre hiermit, dass ich die vorgelegte Dissertation über *Experimental Study of Early Solar System Processes aboard the International Space Station (ISS)* selbständig angefertigt und mich anderer Hilfsmittel als der in ihr angegebenen nicht bedient habe, insbesondere, dass alle Entlehnungen aus anderen Schriften mit Angabe der betreffenden Schrift gekennzeichnet sind. Ich versichere, die Grundsätze der guten wissenschaftlichen Praxis beachtet, und nicht die Hilfe einer kommerziellen Promotionsvermittlung in Anspruch genommen zu haben

Ort, Datum	Unterschrift

Acknowledgements